

https://dspace.org/

Influence of copper on the corrosion and mechanical properties of Grade 4 titanium for biomedical applications

Hadebe, Nomsombuluko Dayanda Elizabeth

2022-12

University of the Witwatersrand, Johannesburg

https://hdl.handle.net/10539/41700

Hadebe, Nomsombuluko Dayanda Elizabeth. (2022). Influence of copper on the corrosion and mechanical properties of Grade 4 titanium for biomedical applications. [Master's dissertation, University of the Witwatersrand, Johannesburg]. https://hdl.handle.net/10539/41700

Downloaded from a DSpace repository. https://dspace.org/



UNIVERSITY OF THE
WITWATERSRAND,
JOHANNESBURG

Influence of copper on the corrosion and mechanical properties of Grade 4 titanium for biomedical applications

50:50 Report MSc REPORT

Prepared by

Nomsombuluko Dayanda Elizabeth Hadebe (1296452)

Submitted to

School of Chemical and Metallurgical Engineering, Faculty of Engineering and the Built Environment, University of the Witwatersrand, Johannesburg

Supervisors: Prof. Lesley Cornish, Prof. Lesley Chown, Ms Melanie Smit and

Dr Alain Mwamba

19 December 2022

DECLARATION

I declare that this research report is my own unaided work. It is being submitted for the Degree of Master of Science to the University of the Witwatersrand, Johannesburg. It has not been submitted before for any degree or examination to any University.



Nomsombuluko Dayanda Elizabeth Hadebe

Johannesburg, 19 December 2022

DEDICATION

To my mother Mangali Aletor Hadebe for paving the path of success for us.

ABSTRACT

This study assessed the effect of Ti_2Cu and its proportions on the corrosion resistance, and compared the results to Grade 4 commercially pure titanium. The Thermo-Calc program with the TTTI3 (Ti-alloy) database was used to predict the phases. Materials Studio software was used to model the crystal structures and XRD patterns of the phases of Ti-Cu alloys. Ti-Cu samples with 0, 5, 15, 25, 33, 40, 47 and 50 wt % Cu were produced. Composition, microstructures, phases, hardness and corrosion resistance were studied in the as-cast and annealed conditions (750° and 900°C water quenched).

The CP Ti samples comprised basket-weave acicular microstructures. The Ti-5Cu samples comprised lamellar (αTi) and Ti_2Cu phases. The Ti-15Cu, Ti-25Cu and Ti-33Cu alloys comprised (αTi) dendrites and sparse eutectic of Ti_2Cu and (αTi). The (βTi) dendrites decomposed to (αTi) and Ti_2Cu, and could not be retained due to insufficient fast quenching. The Ti-40Cu and Ti-47Cu samples had minor titanium oxide dendrites which solidified first and then Ti_2Cu nucleated on them and grew as dendrites, surrounded by the Ti_2Cu + TiCu eutectic. In the Ti-50Cu sample, TiCu was the true primary phase and grew as needles, and was subsequently surrounded by a coarse TiCu + Ti_2Cu eutectic. No Ti_3Cu phase was observed. The microstructures of the as-cast alloys agreed with the Cu-Ti phase diagram of Ansara et al. (2021) and Dyal Ukabhai et al. (2022) with the congruent formation of Ti_2Cu, as well as no Ti_3Cu. The addition of copper to titanium increased the hardness, while annealing decreased the hardness of the Ti-Cu alloys.

Addition of copper above 5 wt % Cu and annealing decreased the corrosion resistance of the samples, but since copper ions in liquid solutions promote the antimicrobial activity, some corrosion is necessary to allow the copper ions to be available. The corrosion tests showed that the corrosion rates obtained were very low, below 0.13 mm/y, which is an acceptable corrosion rate for biomaterial applications. Ti-5Cu showed the best corrosion resistance.

ACKNOWLEDGEMENTS

To God for making it all possible.

I wish to express my sincere thanks to my supervisor, Professor Lesley Cornish, for the support, encouragement and guidance received throughout the time span of this research. For giving me an opportunity to go to Sweden, Uppsala University. I will remain grateful to you for your effective mentorship, dedication and supervision. I cannot thank you enough.

Dr Lee Fowler, Professor Sussane Norgren, Professor Caroline Öhman-Mägi and Dr Nobom Hashe for their technical contribution.
Professor Lesley Chown for Themo-Calc™ and corrosion testing assistance.
Dr Maje Phasha for assistance with Material studio.
Mr Edson Muhuma for assistance casting the samples.
Ms Tondani Maitakhole and Ms Sibongile Masuku for lab assistance.
Mr Archie Corfield for assistance with SEM and XRD analysis.
Ms Melanie Smit and Dr Alain Mwamba for technical support.
Mr Andrew Mampuru, Mr Absalom Mabeba, Ms Dudu Nkomo and Ms Kiyaasha Ukabhai Dyal for their motivation and discussions when things got tough. All the Physical Metallurgy Group colleagues for their direct and indirect contribution to the completion of this project.

Mintek, DSI-NRF Centre of Excellence in Strong Materials and the School of Chemical and Metallurgical Engineering at the University of the Witwatersrand for their support in terms of facilities, financial assistance and permission to publish these results.
The Department of Science and Innovation (DSI) and the Advanced Metals Initiative (AMI) and the Ferrous Metals Development Network (FMDN) are gratefully acknowledged for providing support and funding.

Thanks to my parents and siblings for your love and support. Thanks to my partner Tsietsi Mononela for having my back always. Thanks to my children Ndumiso and Zethembiso for always seeing the best in me. I love and appreciate all of you.

TABLE OF CONTENTS

LIST OF FIGURES VIII

LIST OF TABLES XV

Chapter 1: INTRODUCTION 1

1.1. Background 1

1.2. Hypothesis 2

1.3. Problem Statement 3

1.4. Impact Statement 3

1.5. Research Objectives 3

Chapter 2: LITERATURE REVIEW 5

2.1. Introduction to titanium 5

2.1.1. The metallurgy of titanium 6

2.1.2. Alloying elements in titanium 7

2.1.3 Passivation of titanium 8

2.2. Titanium biocompatibility 10

2.2.1 Osseointegration 11

2.2.2 Effect of bacteria on dental implants 11

2.3. Ti-Cu alloys in biomedical applications 13

2.3.1 Microstructures of Ti-Cu alloys 15

2.3.2. Heat treatment of Ti-Cu alloys 20

2.4. Corrosion of dental implants 22

2.4.1 Uniform corrosion 24

2.4.2 Pitting corrosion 25

2.4.3 Galvanic corrosion 25

2.4.4 Fretting and erosion-corrosion 26

2.4.5 Microbial corrosion 26

2.4.6 Stress induced cracking 28

2.4.7 Crevice corrosion 28

2.5. Corrosion of Ti-Cu alloys 30

2.5.1 Corrosion testing and measurements 32

2.6. Mechanical properties of Ti-Cu alloys 33

Chapter 3: EXPERIMENTAL PROCEDURE 36
3.1. Material Selection 36
3.2. Melting 36
3.3. Heat Treatment 38
3.4. Modelling 39
3.4.1 Thermo-Calc™ 39
3.4.2 Materials Studio 39
3.5. Sample Analysis 40
3.5.1 Metallographic preparation 40
3.5.2 Chemical composition 41
3.5.3 Phase analysis 41
3.5.4 Vickers hardness 42
3.6. Corrosion Testing 42
3.6.1 Electrochemical Testing 42
3.6.2 Immersion Testing 43
3.7. Bacteria Testing 44
Chapter 4: RESULTS 46
4.1 Modelling 46
4.1.1 Thermo-Calc™ 46
4.1.2 Material Studio 54
4.2 Material Characterisation 59
4.3 Hardness Testing 90
4.4 Corrosion Testing 92
4.4.1 Electrochemical Testing 92
4.4.2 Immersion Testing 108
4.5 Bacteria Testing 111
Chapter 5: DISCUSSION 113
Chapter 6: CONCLUSIONS AND RECOMMENDATIONS 123

REFERENCES 125

APPENDIX A: Individual hardness measurements 137

APPENDIX B: Corrosion scans (two per condition) 138

APPENDIX C: List of publications from this work 146

List of Figures

Figure 2-1. O_2 content on the yield strength, UTS and ductility of CP Ti (Liu, et al., 2017).....6
Figure 2-2. Crystal structures of titanium (Gialanella & Malandruccolo, 2020).....6
Figure 2-3. Effect of alloying elements on phase diagrams of titanium alloys (Yang, 2005). ...7
Figure 2-4.Oxide growth mechanism on titanium (Hryniewicz, et al., 2011).....9
Figure 2-5. Pourbaix diagram for the Ti-H_2O system at 25°C (Bhola & Mishra, 2013).....10
Figure 2-6. Stages of biofilm formation in oral environment (Subramani, et al., 2009). 11
Figure 2-7. Dental implant with peri-implantitis (Uhlmann, et al., 2019). 13
Figure 2-8. Anti-bacterial mechanisms on the surface of a Ti-Cu implant (Li, et al., 2016). ...14
Figure 2-9. Cu-Ti phase diagram (Murray, 1987).....17
Figure 2-10. Cu-Ti phase diagram, showing "$CuTi_3$" (Okamoto, 2002). 17
Figure 2-11. Cu-Ti phase diagram (Ansara, et al., 2021).....18
Figure 2-12.Typical microstructure of the as-cast CP Ti (Kikuchi, et al., 2003). 19
Figure 2-13. Typical microstructure of the as-cast Ti-5Cu (Kikuchi, et al., 2003).....19
Figure 2-14. Typical microstructure of the as-cast Ti-10Cu (Kikuchi, et al., 2003).....19
Figure 2-15. Ti-3Cu alloy (a) As-forged and annealed, (e) Aged (Bao, et al., 2018). 20
Figure 2-16. Ti-3Cu alloy: (a) as-cast, (b) after solid solution treatment (Zhang, et al., 2016). 21
Figure 2-17. Ti-25Cu alloy samples at different conditions: (a) As-cast, (b) Annealed at 750°C for 90 h, (c) Annealed at 805°C, and (d) Annealed at 850°C (Zhan, et al., 2012). 22
Figure 2-18. Different forms of corrosion (Noumbissi, et al., 2019). 24
Figure 2-19. Mechanisms of microbial corrosion in Ti dental implants (Costa, et al., 2021)..28
Figure 2-20. Crevice corrosion in aqueous chloride media (Bhola et al., 2011).....29
Figure 2-21. Ti-Cu: (a) OCP, (b) Tafel curves (Liu, et al., 2014). 31
Figure 2-22. Anodic potentiodynamic curves of Ti-CP and Ti-xCu alloys in artificial saliva (Pina, et al., 2016). 32
Figure 2-23. Change in hardness with copper content in the Ti–Cu alloys (Liu, et al., 2014). 33
Figure 2-24. Micro-hardness of the Ti–Cu alloys (Zhang, et al., 2016).....34
Figure 3-1. Photograph of the button arc furnace used.....37

Figure 3-2. As-cast (~50 x ~30mm) Ti-5Cu alloy button (50g). 38
Figure 3-3. Photograph of the argon purging set-up. 38
Figure 3-4. Summary of the experiments conducted. 40
Figure 3-5. Photograph of the corrosion cell test set-up. 43
Figure 3-6. Photograph of the corrosion immersion test set-up. 44
Figure 4-1. Cu-Ti phase diagram drawn using Thermo-Calc with the TTTI3 database. 46
Figure 4-2. Phase proportions of CP Ti. 47
Figure 4-3. Phase proportions of Ti-5Cu. 48
Figure 4-4. Phase proportions of Ti-15Cu. 49
Figure 4-5. Phase proportions of Ti-25Cu. 50
Figure 4-6. Phase proportions of Ti-33Cu. 51
Figure 4-7. Phase proportions of Ti-40Cu. 52
Figure 4-8. Phase proportions of Ti-47Cu. 53
Figure 4-9. Phase proportions of Ti-50Cu. 54
Figure 4-10. Modelled HCP (αTi) phase: (a) crystal structure, and (b) XRD pattern. 55
Figure 4-11. Modelled BCC (βTi) phase: (a) crystal structure, and (b) XRD pattern. 56
Figure 4-12. Modelled Ti_2Cu intermetallic tetragonal phase: (a) crystal structure, and (b) XRD pattern. 57
Figure 4-13. Modelled Ti_3Cu intermetallic tetragonal phase: (a) crystal structure, and (b) XRD pattern. 58
Figure 4-14. Modelled TiCu intermetallic tetragonal phase: (a) crystal structure, and (b) XRD pattern. 59
Figure 4-15. Microstructures of as-cast CP Ti: (a) OM image, (b) SEM-BSE image, showing a Widmanstätten basket-weave structure of (αTi) inside the grains. 60
Figure 4-16. Microstructures of CP Ti heat treated at 750°C: (a) OM image, (b) SEM-BSE image, showing a Widmanstätten basket-weave structure of (αTi) inside the grains. 60
Figure 4-17. Microstructures of CP Ti heat treated at 900°C: (a) OM image, (b) SEM-BSE image, showing a Widmanstätten basket-weave structure of (αTi) inside the grains. 61
Figure 4-18. XRD pattern of as-cast CP Ti, showing (αTi) phase peaks. 62
Figure 4-19. XRD pattern of CP Ti heat treated at 750°C, showing (αTi) phase peaks. 62
Figure 4-20. XRD pattern of CP Ti heat treated at 900°C, showing (αTi) phase peaks. 62

Figure 4-21. Microstructures of as-cast Ti-5Cu: (a) OM image, showing (αTi) (light contrast) and Ti_2Cu (dark contrast), (b) SEM-BSE image, showing (αTi) (dark contrast) and Ti_2Cu (light contrast). 63
Figure 4-22. Microstructures of as-cast Ti-5Cu: (a) OM image, showing (αTi) (light contrast) and Ti_2Cu (dark contrast), (b) SEM-BSE image, showing (αTi) (dark contrast) and Ti_2Cu (light contrast). 64
Figure 4-23. Microstructures of as-cast Ti-5Cu: (a) OM image, showing (αTi) (light contrast) and Ti_2Cu (dark contrast), (b) SEM-BSE image, showing (αTi) (dark contrast) and Ti_2Cu (light contrast). 64
Figure 4-24. XRD pattern of as-cast Ti-5Cu, showing (αTi) and Ti_2Cu peaks. 65
Figure 4-25. XRD pattern of Ti-5Cu heat treated at 750°C, showing (αTi) and Ti_2Cu peaks.... 66
Figure 4-26. XRD pattern of Ti-5Cu heat treated at 900°C, showing (αTi) and Ti_2Cu peaks.... 66
Figure 4-27. Microstructures of Ti-15Cu as-cast: (a) OM image, (b) SEM-BSE image, showing (αTi) (dark contrast) and Ti_2Cu (light), and Ti oxide (darker contrast). 67
Figure 4-28. Microstructures of Ti-15Cu heat treated at 750°C: (a) OM image, (b) SEM-BSE image, (αTi) (dark contrast) and Ti_2Cu (light contrast). 68
Figure 4-29. Microstructures of Ti-15Cu heat treated at 900°C: (a) OM image, (b) SEM-BSE image, (αTi) (dark contrast) and Ti_2Cu (light contrast) and Ti oxide (darker contrast). 68
Figure 4-30. XRD pattern of as-cast Ti-15Cu, showing (αTi) and Ti_2Cu peaks. 70
Figure 4-31. XRD pattern of Ti-15Cu heat treated at 750°C, showing (αTi) and Ti_2Cu peaks. 70
Figure 4-32. XRD pattern of Ti-15Cu heat treated at 900°C, showing (αTi) and Ti_2Cu peaks. 70
Figure 4-33. Microstructures of Ti-25Cu as-cast: (a) OM image, (b) SEM-BSE image, showing (αTi) (dark contrast) and Ti_2Cu (light) and Ti oxide (darker contrast). 71
Figure 4-34. Microstructures of Ti-25Cu heat treated at 750°C: (a) OM image, (b) SEM-BSE image, showing (αTi) (dark contrast) and Ti_2Cu (light) and Ti oxide (darker contrast). 72
Figure 4-35. Microstructures of Ti-25Cu heat treated at 900°C: (a) OM image, (b) SEM-BSE image, showing (αTi) (dark contrast) and Ti_2Cu (light contrast) and Ti oxide (darker contrast). 72
Figure 4-36. XRD pattern of Ti-25Cu as-cast, showing (αTi) and Ti_2Cu peaks. 73
Figure 4-37. XRD pattern of Ti-25Cu heat treated at 750°C, showing (αTi) and Ti_2Cu peaks. 74
Figure 4-38. XRD pattern of Ti-25Cu heat treated at 900°C, showing (αTi) and Ti_2Cu peaks. 74

Figure 4-39. Microstructures of Ti-33Cu as-cast: (a) OM image, (b) SEM-BSE image, showing (αTi) (dark contrast) and Ti_2Cu (light contrast).....75
Figure 4-40. Microstructures of Ti-33Cu heat treated at 750°C: (a) OM image, (b) SEM-BSE image, showing (αTi) (dark contrast) and Ti_2Cu (light contrast).....75
Figure 4-41. Microstructures of Ti-33Cu heat treated at 900°C: (a) OM image, (b) SEM-BSE image, showing (αTi) (dark contrast), Ti_2Cu (light contrast) and oxide (darker contrast). 76
Figure 4-42. XRD pattern of Ti-33Cu as-cast, showing (αTi) and Ti_2Cu peaks. 77
Figure 4-43. XRD pattern of Ti-33Cu heat treated at 750°C, showing (αTi) and Ti_2Cu peaks. 77
Figure 4-44. XRD pattern of Ti-33Cu heat treated at 900°C, showing (αTi) and Ti_2Cu peaks. 78
Figure 4-45. Microstructures of Ti-40Cu as-cast: (a) OM image (b) SEM-BSE image, showing Ti oxides (dark contrast), Ti_2Cu (medium contrast) and TiCu (light contrast).....79
Figure 4-46. Microstructures of Ti-40Cu heat treated at 750°C: (a) OM image (b) SEM-BSE image, showing Ti oxides (dark contrast), Ti_2Cu (medium contrast) and TiCu (light contrast). 79
Figure 4-47. Microstructures of Ti-40Cu heat treated at 900°C: (a) OM image, (b) SEM-BSE image, showing Ti oxides (dark contrast), Ti_2Cu (medium contrast) and TiCu (light contrast). 80
Figure 4-48. XRD pattern of Ti-40Cu as-cast, showing Ti_2Cu and TiCu peaks.....81
Figure 4-49. XRD pattern of Ti-40Cu heat treated at 750°C, showing Ti_2Cu and TiCu peaks. .81
Figure 4-50. XRD pattern of Ti-40Cu heat treated at 900°C, showing Ti_2Cu and TiCu peaks. .82
Figure 4-51. Microstructures of Ti-47Cu as-cast: (a) OM image, showing Ti oxides (dark contrast), Ti_2Cu (light contrast) and TiCu (medium contrast) and (b) SEM-BSE image, showing Ti oxides (dark contrast), Ti_2Cu (medium contrast) and TiCu (light contrast).....83
Figure 4-52. Microstructures of Ti-47Cu heat treated at 750°C: (a) OM image, showing Ti oxides (dark contrast), Ti_2Cu (light contrast) and TiCu (medium contrast) and (b) SEM-BSE image, showing Ti oxides (dark contrast), Ti_2Cu (medium contrast) and TiCu (light contrast). 83
Figure 4-53. Microstructures of Ti-47Cu heat treated at 900°C: (a) OM image, showing Ti oxides (dark contrast), Ti_2Cu (light contrast) and TiCu (medium contrast) and (b) SEM-BSE image, showing Ti oxides (dark contrast), Ti_2Cu (medium contrast) and TiCu (light contrast). 84

Figure 4-54. XRD pattern of Ti-47Cu as-cast, showing Ti_2Cu and TiCu peaks.....85
Figure 4-55. XRD pattern of Ti-47Cu heat treated at 750°C, showing Ti_2Cu and TiCu peaks. .85
Figure 4-56. XRD pattern of Ti-47Cu heat treated at 900°C, showing Ti_2Cu and TiCu peaks. .86
Figure 4-57. Microstructures of Ti-50Cu as-cast: (a) OM image and (b) SEM-BSE image, showing Ti oxides (dark contrast), TiCu (light contrast) and Ti_2Cu (medium contrast).....87
Figure 4-58. Microstructures of Ti-50Cu heat treated at 750°C: (a) EPMA image and (b) OM image, showing Ti oxides (dark contrast), TiCu (light contrast) and Ti_2Cu (medium contrast). 87
Figure 4-59. Microstructures of Ti-50Cu heat treated at 900°C: (a) OM image and (b) SEM-BSE image, showing Ti oxides (dark contrast), TiCu (light contrast) and Ti_2Cu (medium contrast). 88
Figure 4-60. XRD pattern of Ti-50Cu as-cast, showing Ti_2Cu and TiCu peaks.....89
Figure 4-61. XRD pattern of Ti-50Cu heat treated at 750°C, showing Ti_2Cu and TiCu peaks. .89
Figure 4-62. XRD pattern of Ti-50Cu heat treated at 900°C, showing Ti_2Cu and TiCu peaks. .90
Figure 4-63.Vickers hardness as a function of nominal copper content of the as-cast and annealed Ti-Cu alloys. 91
Figure 4-64. OCP of CP Ti in PBS. 92
Figure 4-65. Potentiodynamic polarisation curves of CP Ti in PBS. 93
Figure 4-66. OCP of Ti-5Cu in PBS. 94
Figure 4-67. Potentiodynamic polarisation curves of Ti-5Cu in PBS. 95
Figure 4-68. OCP of Ti-15Cu in PBS. 96
Figure 4-69. Potentiodynamic polarisation curves of Ti-15Cu in PBS. 97
Figure 4-70. OCP of Ti-25Cu in PBS. 98
Figure 4-71. Potentiodynamic polarisation curves of Ti-25Cu in PBS. 99
Figure 4-72. OCP of Ti-33Cu in PBS. 100
Figure 4-73. Potentiodynamic polarisation curves of Ti-33Cu in PBS. 101
Figure 4-74. OCP of Ti-40Cu in PBS. 102
Figure 4-75. Potentiodynamic polarisation curves of Ti-40Cu in PBS. 103
Figure 4-76. OCP of Ti-47Cu in PBS. 104
Figure 4-77. Potentiodynamic polarisation curves of Ti-47Cu in PBS. 105
Figure 4-78. OCP of Ti-50Cu in PBS. 106

Figure 4-79. Potentiodynamic polarisation curves of Ti-50Cu in PBS. 107
Figure 4-80. Immersion test results for all the alloys. 108
Figure 4-81. As-cast alloys after 30 days exposure in PBS solution. 110
Figure 4-82. Alloys HT at 750°C after 30 days exposure in PBS solution. 110
Figure 4-83. Alloys HT at 900°C after 30 days exposure in PBS solution. 110
Figure 4-84. Antibacterial Rate (R) after 2 hours for the as-cast alloys. 111
Figure 4-85. Antibacterial Rate (R) after 6 hours for the as-cast alloys. 111
Figure 5-1. Effect of Ti_2Cu proportions on Vicker's hardness bar graph based on the samples. 116
Figure 5-2.OCP of all the as-cast alloys. 117
Figure 5-3. OCP of all the alloys annealed at 750°C. 118
Figure 5-4. OCP of all the alloys annealed at 900°C. 118
Figure 5-5. Summary of the corrosion rates: the green oval shows the lowest corrosion rates of Ti-5Cu and the red oval shows the highest corrosion rates of Ti-33Cu. 121
Figure 5-6. Effect of Ti_2Cu proportions on corrosion rates. 122
Figure B-0-1. OCP and potentiodynamic polarisation curves of CP Ti, as-cast in PBS. 138
Figure B-0-2. OCP and potentiodynamic polarisation curves of Ti-5Cu, as-cast in PBS. 138
Figure B-0-3. OCP and potentiodynamic polarisation curves of Ti-15Cu, as-cast in PBS. 138
Figure B-0-4. OCP and potentiodynamic polarisation curves of Ti-25Cu, as-cast in PBS. 139
Figure B-0-5. OCP and potentiodynamic polarisation curves of Ti-33Cu, as-cast in PBS. 139
Figure B-0-6. OCP and potentiodynamic polarisation curves of Ti-40Cu, as-cast in PBS. 139
Figure B-0-7. OCP and potentiodynamic polarisation curves of Ti-47Cu, as-cast in PBS. 140
Figure B-0-8. OCP and potentiodynamic polarisation curves of Ti-50Cu, as-cast in PBS. 140
Figure B-0-9. OCP and potentiodynamic polarisation curves of CP Ti HT at 750°C in PBS. 140
Figure B-0-10. OCP and potentiodynamic polarisation curves of Ti-5Cu HT at 750°C in PBS. 141
Figure B-0-11. OCP and potentiodynamic polarisation curves of Ti-15Cu HT at 750°C in PBS. 141
Figure B-0-12. OCP and potentiodynamic polarisation curves of Ti-25Cu HT at 750°C in PBS. 141

Figure B-0-13. OCP and potentiodynamic polarisation curves of Ti-33Cu HT at 750°C in PBS. 142
Figure B-0-14. OCP and potentiodynamic polarisation curves of Ti-40Cu HT at 750°C in PBS. 142
Figure B-0-15. OCP and potentiodynamic polarisation curves of Ti-47Cu HT at 750°C in PBS. 142
Figure B-0-16. OCP and potentiodynamic polarisation curves of Ti-50Cu HT at 750°C in PBS. 143
Figure B-0-17. OCP and potentiodynamic polarisation curves of CP Ti HT at 900°C in PBS..143
Figure B-0-18. OCP and potentiodynamic polarisation curves of Ti-5Cu HT at 900°C in PBS. 143
Figure B-0-19. OCP and potentiodynamic polarisation curves of Ti-15Cu HT at 900°C in PBS. 144
Figure B-0-20. OCP and potentiodynamic polarisation curves of Ti-25Cu HT at 900°C in PBS. 144
Figure B-0-21. OCP and potentiodynamic polarisation curves of Ti-33Cu HT at 900°C in PBS. 144
Figure B-0-22. OCP and potentiodynamic polarisation curves of Ti-40Cu HT at 900°C in PBS. 145
Figure B-0-23. OCP and potentiodynamic polarisation curves of Ti-47Cu HT at 900°C in PBS. 145
Figure B-0-24. OCP and potentiodynamic polarisation curves of Ti-50Cu HT at 900°C in PBS. 145

List of Tables

Table 2-1. Phase stabilising alloying elements (Olsson, 2008). 7
Table 2-2. Intermetallic phases identified for the Ti-Cu system (Okamoto, 2002). 15
Table 2-3. Phase transformations in the Ti-Cu system (Murray, 1987).....16
Table 3-1. Chemical compositions of titanium and copper (wt %) starting materials. 36
Table 3-2. Ti-Cu casting compositions. 37
Table 3-3. Etching reagent used for the Ti-Cu samples. 41
Table 3-4. Chemical composition of the PBS solution. 42
Table 4-1. Phase transformations in Ti-Cu system drawn with Thermo-Calc and TTTI3 database.....47
Table 4-2. Thermo-Calc^{TM} results of CP Ti. 47
Table 4-3. Thermo-Calc^{TM} results of Ti-5Cu. 48
Table 4-4. Thermo-Calc^{TM} results of Ti-15Cu. 49
Table 4-5. Thermo-Calc^{TM} results of Ti-25Cu. 50
Table 4-6. Thermo-Calc^{TM} results of Ti-33Cu. 51
Table 4-7. Thermo-Calc^{TM} results of Ti-40Cu. 52
Table 4-8. Thermo-Calc^{TM} results of Ti-47Cu. 53
Table 4-9. Thermo-Calc^{TM} results of Ti-50Cu. 54
Table 4-10. EPMA results for CP Ti. 61
Table 4-11. XRD phase proportions of CP Ti. 63
Table 4-12. EPMA results for Ti-5Cu. 65
Table 4-13. XRD phase proportions of Ti-5Cu.....66
Table 4-14. EPMA results for Ti-15Cu. 69
Table 4-15. XRD phase proportions of Ti-15Cu.....71
Table 4-16. EPMA results for Ti-25Cu. 73
Table 4-17. XRD phase proportions of Ti-25Cu.....74
Table 4-18. EPMA results for Ti-33Cu. 76
Table 4-19. XRD phase proportions of Ti-33Cu.....78
Table 4-20. EPMA results for Ti-40Cu. 80

Table 4-21. XRD phase proportions of Ti-40Cu.....82
Table 4-22. EPMA results for Ti-47Cu. 84
Table 4-23. XRD phase proportions of Ti-47Cu.....86
Table 4-24. EPMA results for Ti-50Cu. 88
Table 4-25. XRD phase proportions of Ti-50Cu.....90
Table 4-26. Hardness results of the alloys. 91
Table 4-27. Corrosion tests results for CP Ti in PBS. 93
Table 4-28. Corrosion tests results for Ti-5Cu. 95
Table 4-29. Corrosion tests results for Ti-15Cu. 97
Table 4-30. Corrosion tests results for Ti-25Cu in PBS. 99
Table 4-31. Corrosion tests results for Ti-33Cu. 101
Table 4-32. Corrosion tests results for Ti-40Cu. 103
Table 4-33. Corrosion tests results for Ti-47Cu. 105
Table 4-34. Corrosion tests results for Ti-50Cu. 107
Table 4-35. Immersion test corrosion results of the alloys, after 720 h. 109
Table 4-36. Antibacterial rate of the alloys as-cast. 112

Chapter 1: INTRODUCTION

1.1. Background

South Africa is among the top producers of titanium ore in the world (Refiloe, 2008; Maphango, 2012). Rather than simply exporting the ore, efforts are being made to set up a robust titanium industry in the country (Roux, et al., 2020). Beneficiating titanium would result in less expensive titanium products being manufactured from local raw materials and this could become a large source of revenue and job creation (Roux, et al., 2020). For South Africa, mineral resource beneficiation is very important and is part of the national development plan (Adams, 2013).

Producing titanium biomaterials locally is part of materials beneficiating. Biomaterials are used to manufacture implants to replace a lost or a sickly biological structure to restore its form and functionality (Geetha, et al., 2009). For materials to be considered for implant applications, they need to have acceptable mechanical properties, chemical properties, corrosion resistance, osseointegration (the apparent direct attachment or connection of osseous tissue to an inert alloplastic material), biocompatibility, be free of toxic elements and not corrode noticeably or cause inflammation in the human body (Geetha, et al., 2009). Commercially pure titanium (CP Ti) and titanium alloys have been widely used in orthopaedic and dental implant applications (Liu, et al., 2017). In addition to good mechanical strength, chemical stability and successful osseointegration, CP Ti is used in dentistry applications due to its high strength-to-weight ratio and resistance to corrosion (Prasad, et al., 2015). However, the disadvantages of CP Ti include poor wear resistance, low mechanical strength and mechanical properties that are difficult to improve without reducing biocompatibility (Elias, et al., 2015).

Corrosion of titanium dental implants is considered a trigger factor for peri-implantitis and it causes the implants to fail (Rodrigues, et al., 2013). Peri-implantitis is an inflammatory disease affecting the surrounding tissues of the implant, especially the bone, and is caused by the attachment of pathogenic biofilms on the implant surface and peri-implant tissues, resulting

in bone loss and destruction of soft tissues (Schminke, et al., 2015). Possible lead bacteria of peri-implantitis, such as *Porphyromonas gingivalis*, *Prevotella intermedia*, and *Aggregatibacter actinomycetemcomitans*, are associated with biofilm formation on dental implants (Schminke, et al., 2015).

In the last decade, surfaces able to withstand bacteria adhesion and antimicrobial agents/antibiotics carriers have been developed to avoid implant-related infections (Romanò, et al., 2015). Avoiding bacterial adhesion onto the implant surface can be achieved by applying hydrophilic coatings such as hyaluronic acid or poly-N-vinylpyrrolidone, which was successful in reducing *Staphylococcus epidermidis* adhesion (Francolini & Donelli, 2010). The disadvantage of the hydrophilic coatings is their inability to prevent protein adhesion onto the implants, which may result in an impaired optimal integration in the adjacent tissue. The use of antibiotics to disrupt the biofilm can be challenging, due to the complex protective structure the biofilm possesses, and it often resists antibiotics, which are beyond the minimal inhibitory concentration (MIC). MIC is defined as the lowest concentration of an antimicrobial that will inhibit the visible growth of a microorganism after overnight incubation (Andrews, 2001). The concentration of antibiotics needed to disrupt a biofilm can range from 100 to 1000 times the MIC needed to kill planktonic cells (Janus, et al., 2015). The long-term use of high doses may also result in risky side-effects and bacteria resistance (Llor & Bjerrum, 2014). Thus, silver has been suggested as an alternative, because of its low toxicity and good biocompatibility with human cells, and long-term antibacterial activity due to sustained ion release and low bacterial resistance. However, silver may lead to DNA damage (Bruellhoff, et al., 2010). As an alternative option to silver, copper can be used because of antibacterial properties (Zhang, et al., 2021).

1.2. Hypothesis

Copper-bearing titanium alloys exhibit excellent antibacterial properties due to the Ti_2Cu intermetallic phase formed. The redistribution of copper and size distribution of Ti_2Cu precipitates caused by heat treatment, such as annealing and ageing, could significantly improve the mechanical properties, corrosion resistance and antibacterial rate.

1.3. Problem Statement

Although it has been reported that titanium alloyed with small amounts of copper has adequate biocompatibility and corrosion resistance for dental use, much is still unknown (Corrêa, et al., 2015). The objective of this project was to characterise Ti-Cu alloys at different compositions, such as 5, 15, 25, 33, 40, 47 and 50 wt% copper in Grade 4 titanium.

1.4. Impact Statement

Copper-bearing titanium alloys have exhibited excellent antibacterial properties (Liu, et al., 2017; Zhang, et al., 2021). Although Ti-Cu alloys have high corrosion resistance due to TiO_2 formed on the surfaces, they are not immune to corrosion. Corrosion of titanium dental implants is associated with implant failure and is considered as a trigger factor for peri-implantitis. This research addressed the addition of copper to titanium Grade 4 studying the compositions, heat treatments and impacts on mechanical properties, corrosion and antibacterial effects, which then provided an opportunity for optimization of the final alloy. As part of minerals beneficiation, manufacturing of Ti-Cu alloy dental implants from local raw materials could become a large source of revenue and job creation.

1.5. Research Objectives

The aim of this research was to investigate the effect of copper additions on Grade 4 titanium, focusing on corrosion resistance and hardness properties to assess the effect of the amount of Ti_2Cu and its distribution on corrosion resistance and the antimicrobial properties. This was done to obtain information which would aid the understanding of the properties of titanium alloys with copper for potential dental prosthetic applications.

The research objectives were:

- To characterise the copper and titanium used as starting materials.
- To produce as-cast samples by adding 5, 15, 25, 33, 40, 47 and 50 wt% copper to Grade 4 titanium, and then anneal the alloys at 750°C and 900°C for two hours, followed by

water quenching. Annealing at these temperatures and fast quenching was done to obtain microstructures such as (βTi), (αTi) + Ti_2Cu, transformed (βTi) + Ti_2Cu and Ti_2Cu + TiCu and to homogeneously distribute the Ti_2Cu precipitates. These temperatures were decided because at 750°C, titanium has a α phase while 900°C is above the 882°C where titanium is β.

- To assess the microstructure and hardness of both as-cast and annealed Ti-Cu alloys, compared to Titanium Grade 4.

- To define the corrosion of the Ti-Cu alloys in phosphate buffer saline (PBS), a simulated physiological solution, and compare to Titanium Grade 4. PBS is a phosphate buffer, prepared from sodium phosphate, potassium phosphate and sodium chloride, where the pH is maintained by a phosphate-phosphoric acid equilibrium.

Chapter 2: LITERATURE REVIEW

2.1. Introduction to titanium

The initial application of titanium in dentistry occurred accidentally in 1965, when the Swedish doctor Per-Ingvar Brånemark was investigating the blood microcirculation in rabbit tibiae using observational cameras made of titanium (Jorge, et al., 2013). He noticed that the titanium cameras and the bone were perfectly integrated, without any rejection, making it difficult for the cameras to be removed (Jorge, et al., 2012). The use of titanium and its alloys for medical and dental applications has much increased in recent years. Titanium has been the material of choice in several branches of dentistry, due to its excellent characteristics such as biocompatibility, osseointegration, high wear and corrosion resistance, low compatibility issues and high strength. Thus, recent attention has been directed towards further development of this material. Titanium also has a modulus of elasticity which is similar to that of the bone (10-30GPa); this prevents bone resorption and achieves good bone remodelling (Prasad, et al., 2015; Niinomi, et al., 2016). Titanium has been proposed as an alternative to 316L stainless steel and Co-Cr alloys owing to better biocompatibility and corrosion resistance, since stainless steels and Co-Cr alloys usually contain some harmful elements, such as nickel, cobalt and chromium (Li, et al., 2014).

Titanium is a light, strong, shiny, naturally corrosion-resistant transition metal and has a high melting point of 1670°C. The American Society of Testing Materials (ASTM) defines CP Ti as being available in four different grades (Grades 1-4) that are based on the removal of small amounts of oxygen, nitrogen, hydrogen, iron and carbon during purification procedures, where each grade has different physical and mechanical properties (Özcan & Hämmerle, 2012). Grade 4 CP Ti, which is of interest for this project, has an oxygen content of 0.4 wt%, and the highest strength with moderate formability compared to Grades 1, 2 and 3, as shown in Figure 2-1 (Liu, et al., 2017). Titanium implants are made from Grade 4 CP Ti because it has the highest strength of the CP Ti grades.

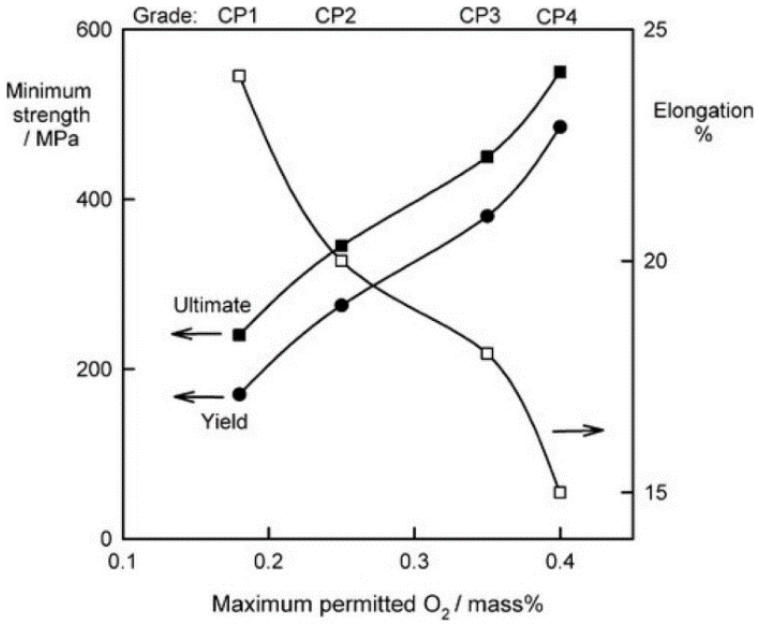


Figure 2-1. O_2 content on the yield strength, UTS and ductility of CP Ti (Liu, et al., 2017).

2.1.1. The metallurgy of titanium

Titanium is a metal which has two phases, α and β, as shown in Figure 2-2. Below 882°C, pure titanium has a hexagonal closed packed (HCP) lattice, while at 882°C it transforms into a body centred cubic (BCC) lattice (Han, et al., 2018). Titanium alloys are generally classified as α, α + β, and β-type alloys. Young's moduli of α and α + β-Titanium alloys such as CP Ti and Ti-6Al-4V are higher than those of β-type titanium alloys (Li, et al., 2014). Therefore, β-type titanium alloys are considered more advantageous for the development of titanium alloys with low Young's modulus for biomedical applications.

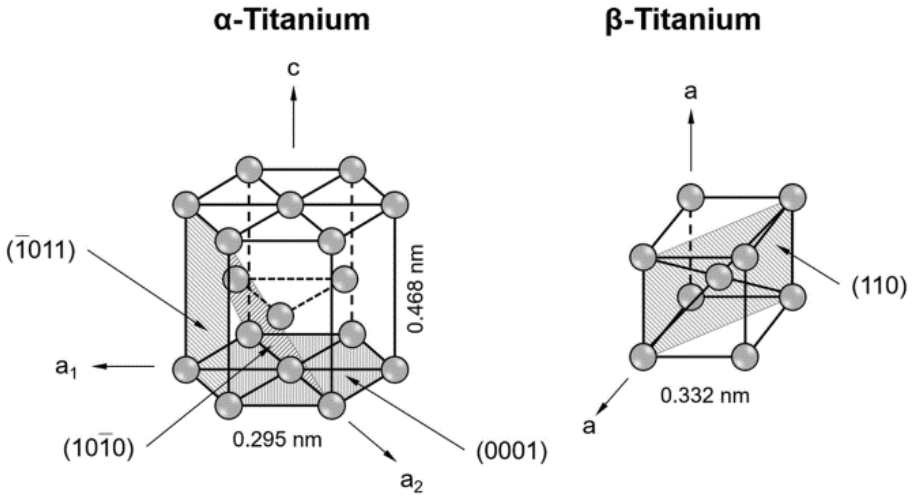


Figure 2-2. Crystal structures of titanium (Gialanella & Malandruccolo, 2020).

2.1.2. Alloying elements in titanium

The alloying elements in titanium can be classified into α or β-stabilising elements, depending on their influence on α/β transformation temperature (Yang, 2005). The substitutional element of aluminium and the interstitial elements of oxygen, nitrogen and carbon are all strong α-stabilisers. These elements can increase the transus temperature with increasing solute contents. There are two types of β-stabilisers: β-eutectoid and β-isomorphous. β-eutectoid stabilisers, such as iron, manganese, cobalt, nickel, silicon, hydrogen, copper and chromium, which promotes eutectoid behaviour and are compound formers. β-isomorphous stabilisers, such as molybdenum, vanadium, tungsten and niobium, are soluble in β-titanium and their alloys crystallise as β at room temperature (Yang, 2005; Olsson, 2008; Geetha, et al., 2009). Additionally, there are other elements like zirconium and tin called neutral elements, because of their very slight influence on the transformation temperature. Table 2-1 and Figure 2-3 show the alloying elements and their stabilising effect on phases.

Table 2-1. Phase stabilising alloying elements (Olsson, 2008).

Stabilising	**Elements**							
β-eutectoid stabilisers	Mn	Fe	Ni	Co	Cu	Cr	Si	H
β-isomorphous	V	Mo	W	Ni	Ta			
α-stabilisers	N	Ca	Al	O	Ga			
Neutral	Zr	Sn						

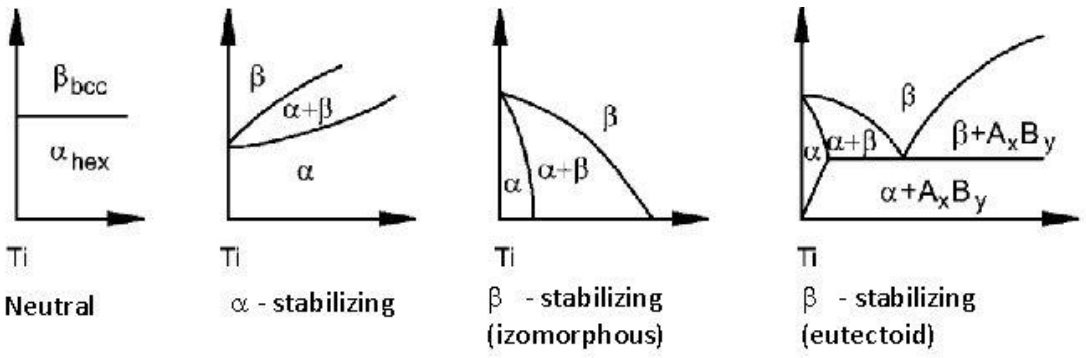


Figure 2-3. Effect of alloying elements on phase diagrams of titanium alloys (Yang, 2005).

2.1.3 Passivation of titanium

When titanium is exposed to air or water, it spontaneously forms a titanium dioxide (TiO_2) surface layer, which makes it biocompatible. This formation of this oxide film is referred to as passivation because the highly dynamic oxide layers subsequently act as a barrier to protect the underlying metallic titanium from further exposure and chemical reactions, such as corrosion (Prasad, et al., 2015). This passive film is composed of three layers: titanium oxide (TiO) layer which is the first layer adjacent to metallic titanium, titanium(III) oxide (Ti_2O_3) which is a middle layer and the anatase TiO_2 layer which is in contact with the environment (Gemelli & Camargo, 2007).

At room temperature, TiO_2 is the thickest layer and is responsible for the integration between the implant and the human bone (Gemelli & Camargo, 2007). This amorphous or low crystalline 4–6 nm thickness TiO_2 layer forms on the surface within nanoseconds of exposure to air or oxidising solutions (Fais, et al., 2012). The formation of the TiO_2 titanium occurs according to Equation 2-1 and Equation 2-2 (Prasad, et al., 2015):

$$\boldsymbol{Ti + O_2 \rightarrow TiO_2} \qquad \text{Equation 2-1}$$

$$\boldsymbol{Ti + 2H_2O \rightarrow TiO_2 + 4H^+ + 4e^-} \qquad \text{Equation 2-2}$$

According to Hryniewicz (2011), the oxide formation begins with adsorption of oxygen onto the titanium surface to create an oxide monolayer. This is followed by the tunnelling of oxygen through the titanium oxide to the titanium surface. For oxide formation to continue, titanium and oxygen need to be in contact, therefore oxygen ions move through the oxide film to the titanium surface to form new oxide layers; this mechanism is referred to as growth at constant field (Prasad, et al., 2015). Figure 2-4 shows an oxide growth mechanism on titanium (Hryniewicz, et al., 2011). Although titanium and its alloys have high corrosion resistance, due to the TiO_2, they are not immune to corrosion.

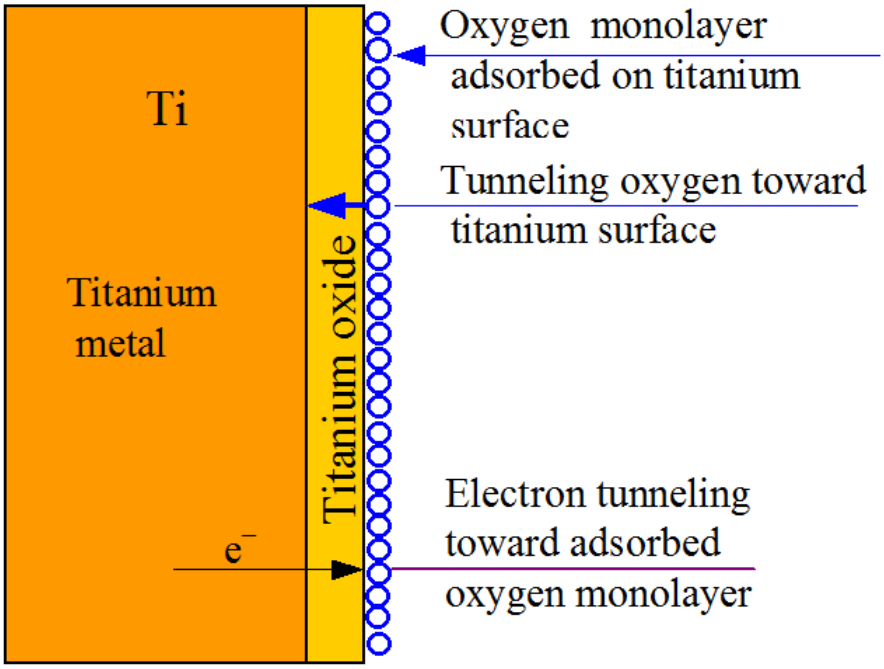


Figure 2-4.Oxide growth mechanism on titanium (Hryniewicz, et al., 2011).

Figure 2-5 shows the Pourbaix (potential-pH) diagram for the titanium water system at 25°C (Bhola, et al., 2011). It illustrates the broad range around which the passive TiO_2 film is stable, based on thermodynamic (free energy) considerations. Oxide stability over the full pH scale is indicated over a wide range of highly oxidizing to mildly reducing potentials. Under reducing acidic conditions, the oxide film breaks down and the corrosion of titanium implant surface occurs. Under strongly reducing (cathodic) conditions, titanium hydride formation is predicted. This range of oxide film stability and passivation is relatively insensitive to the presence of chlorides, explaining the high innate resistance of titanium to aqueous chloride environments.

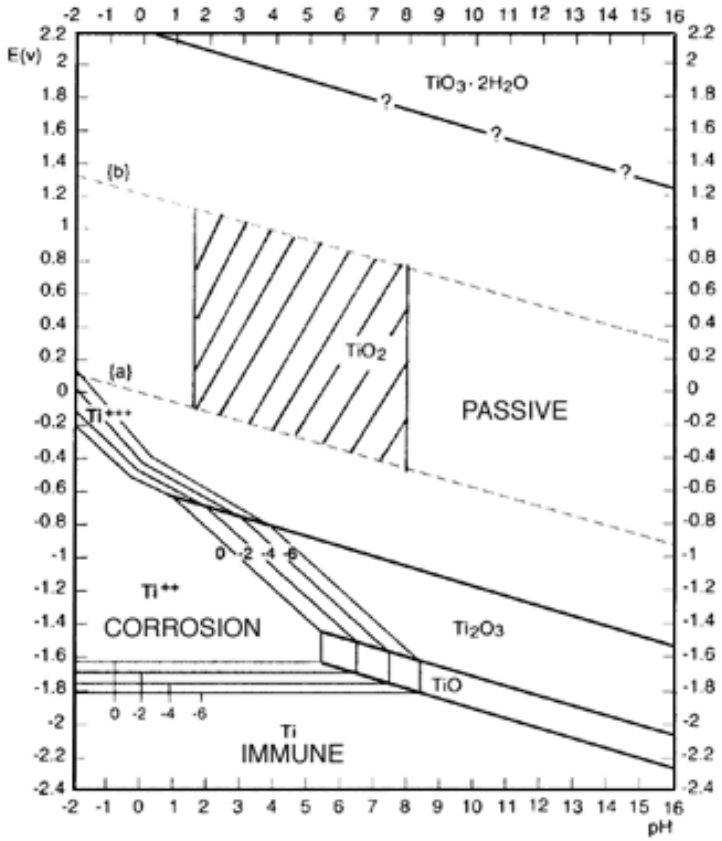


Figure 2-5. Pourbaix diagram for the Ti-H_2O system at 25°C (Bhola & Mishra, 2013).

2.2. Titanium biocompatibility

Biocompatibility is a term used to describe the property of a material being compatible with living tissue (Veritas, n.d.). Ideally, for a material to be biocompatible, it should not be harmful to any oral tissues, gingiva, mucosa, pulp or bone. Furthermore, the material should not contain toxic, leachable or diffusible substances that can be absorbed into the circulatory system, which may result in systemic responses such as teratogenic (defects in the human embryo or fetus) or carcinogenic (formation of cancer) effects (Swetha, et al., 2015). An ideal bone implant material is defined as having a biocompatible chemical composition to avoid adverse tissue reaction, excellent corrosion resistance in the physiological limits, acceptable strength, a high resistance to wear and a modulus of elasticity similar to that of bone to minimise bone resorption around the implant (Schmidt, et al., 2001; Ananth, et al., 2015). The two main factors that influence the biocompatibility of a material are the host response induced by the material and the material's degradation in the body environment.

2.2.1 Osseointegration

An implant is considered osseointegrated when it is reliably and predictably incorporated into the living bone under all normal loading. Titanium is good for osseointegration because it naturally forms a thin protective oxide film on its surface that can eventually transform into calcium phosphate apatite that then binds chemically with the bone which is good for osseointegration (Gosavi, et al., 2013; Monsees, 2016). The surface condition or roughening the surface of the implants improves osseointegration.

2.2.2 Effect of bacteria on dental implants

Bacteria can result in formation of a biofilm on implants. Biofilms formed on tooth surfaces are termed dental plaque. The formation of the plaque biofilm in the oral cavity occurs in multiple stages, as shown in Figure 2-6 (Subramani, et al., 2009).

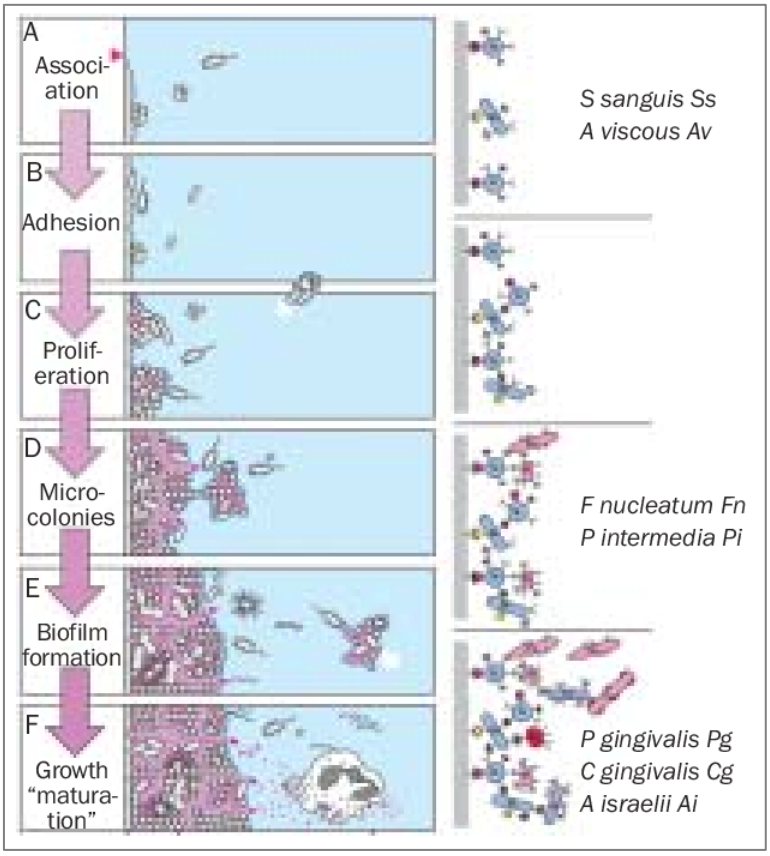


Figure 2-6. Stages of biofilm formation in oral environment (Subramani, et al., 2009).

The biofilms in the oral cavity consist of complex microbial communities embedded in a matrix of polymers, primarily of bacterial and salivary origin (Bowen, et al., 2018). The well-developed biofilms on dental implant surfaces and prosthetic restoration become the main source of microbes causing peri-implantitis (Subramani, et al., 2009). Peri-implantitis is characterised by severe inflammation, resulting in significant destruction of bone and the implant, as shown in Figure 2-7. Uhlmann (2019) reviewed peri-implant disease occurrence, focusing on studies spanning a minimum of 5 years. Schminke (2015) reported that approximately 30% of patients with dental implants developed peri-implantitis, while Mishler (2014) reported that the prevalence of peri-implantitis in dental applications was 10% of implants and 20% of patients. This indicates that the prevention of bacterial-related infection remains a major challenge for the delivery of quality medical care, and the problem results in a high rate of morbidity, thereby significantly increasing health care costs.

Once the peri-implantitis occurs, the patients may be required to make use of nonsurgical or surgical treatment (Prathapachandra & Suresh, 2012). Bao (2018) reported that many researchers have found that surface modification of titanium alloys could attain good antibacterial properties, although surface coatings were susceptible to exfoliation, so the antibacterial effect was greatly reduced over time. Therefore, alloying titanium with antimicrobial elements has attracted much attention worldwide due to the potential longer-term antibacterial property, good wear resistance, and good corrosion resistance (Zhang, et al., 2014; Bao, et al., 2018).

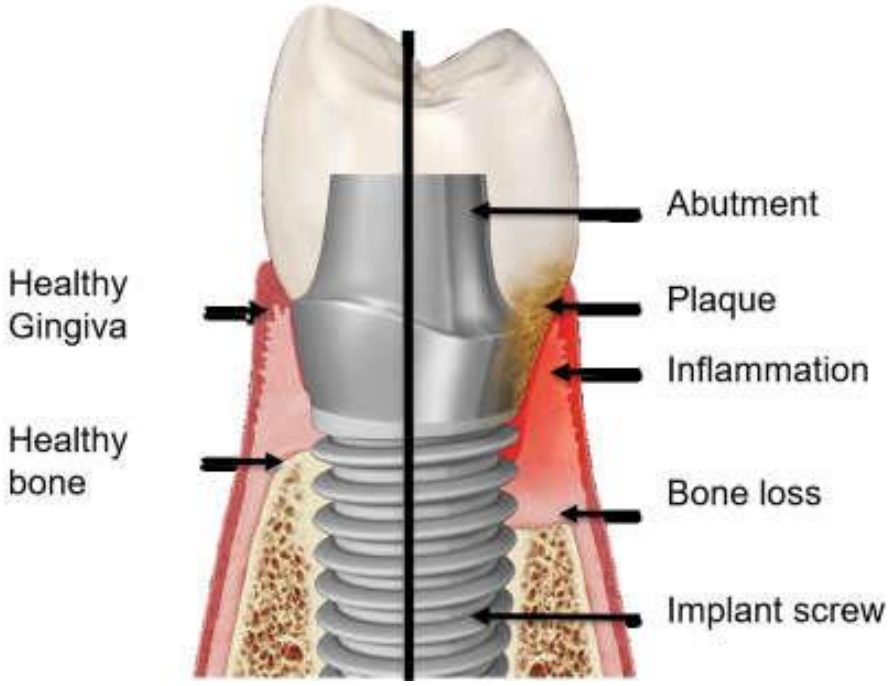


Figure 2-7. Dental implant with peri-implantitis (Uhlmann, et al., 2019).

2.3. Ti-Cu alloys in biomedical applications

Copper-bearing titanium alloys have exhibited excellent antibacterial properties (Liu, et al., 2017; Zhang, et al., 2021). Shirai (2009) first reported that titanium alloys containing 1 wt% Cu and 5 wt% Cu had antimicrobial activity and substantially reduced the incidence of pin tract infection (a common problem with external fixation and any other implant that breaks the skin barrier). Zhang (2016) reported that Ti-copper alloys with 1 and 5 wt% Cu showed antibacterial properties with an antibacterial rate of about 30% compared with CP Ti (unspecified). Further research showed that the copper content influenced the antibacterial rate and only the alloys with 5 wt% or higher copper had a strong and stable antibacterial rates (>99% antibacterial rate) against *Staphylococcus aureus* and *Escherichia coli*, which indicated that the copper content in Ti-Cu alloys must be at least 5 wt% to obtain a strong and stable antibacterial property (Bao, et al., 2018). High copper ion concentration normally resulted in a high antibacterial rate. However, excess copper intake causes stomach upset, nausea and diarrhoea, and can lead to tissue injury and disease (Bao, et al., 2018). Therefore, the World Health Organization has stated a copper limit of 2–3mg/day (Fowler, et al., 2019).

The mechanism by which Ti-Cu alloys kill bacteria is still unknown, but Cu ions are believed to play a role in killing at a distance from the surface (Fowler, et al., 2019). It is hypothesised that the Cu ions produce reactive oxygen species (ROS), which rupture the cell walls of bacteria, and occurs according to the Fenton chemistry reaction (Equation 2-3) where Cu reacts with hydrogen peroxide (H_2O_2) to produce hydroxyl products. The H_2O_2 is excreted by oral bacteria (Ryan & Kleinberg, 1995).

Fenton Chemistry reaction $Cu^{+} + H_2O_2 \rightarrow Cu^{2+} + OH^{-} + OH$ Equation 2-3

The Cu ions have also shown an ability to prohibit expression of biofilm forming enzymes such as *agr* and *sae* in *Staphylococcus aureus* (Li, et al., 2016; Fowler, et al., 2019). While these bacteria might be vulnerable to ROS, they can scavenge H_2O_2, thus limiting hydroxyl production and surviving copper-induced stresses (Baker, et al., 2010; Fowler, et al., 2019). Figure 2-8 shows the anti-bacterial mechanisms on the surface of Ti-Cu implant (Li, et al., 2016).

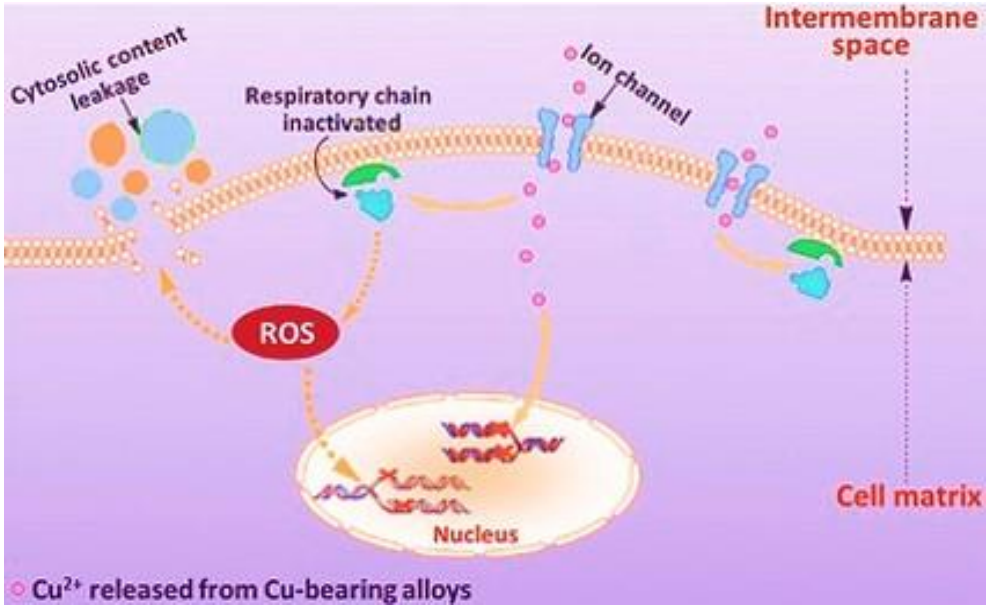


Figure 2-8. Anti-bacterial mechanisms on the surface of a Ti-Cu implant (Li, et al., 2016).

2.3.1 Microstructures of Ti-Cu alloys

Alloying titanium with copper results in the precipitation of intermetallic phases. Intermetallic phases are defined as solid phases involving two or more metallic or semi-metallic elements which have an ordered structure and a well-defined and fixed stoichiometry (Jiang, et al., 2018). Intermetallic phases have a high melting point and are generally brittle at room temperature. Table 2-2 shows the intermetallic phases identified for the Ti-Cu system (Okamoto, 2002).

Table 2-2. Intermetallic phases identified for the Ti-Cu system (Okamoto, 2002).

Phase	Pearson symbol	Space group	Prototype
Ti_3Cu	*oP*	*Pbam*	-
Ti_2Cu	*tI*6	*I4/mmm*	$MoSi_2$
CuTi	*tP*4	*P*4/*nmm*	γ TiCu
Ti_3Cu_4	*tI*14	*I*4/*mmm*	-
Ti_2Cu_3	*tP*10	*P*4/*mmm*	n/a
$TiCu_2$	*oC*12	*Amm*2	Au_2V
β-$TiCu_4$	*oP*20	*Pnma*	AuZr
α-$TiCu_4$	*tI*10	*I*4/*m*	$MoNi_4$

The existence of the phase Ti_3Cu is controversial. Earlier, Karlsson (1951) reported the possible existence of Ti_3Cu at 25 and 27.5 at. % Cu, which was not accepted by Murray (1987) as a stable phase. However, Canale & Servant (2002) revised the complete Cu-Ti phase diagram by thermodynamic assessment, taking into account the Ti_3Cu phase (after finding it experimentally) and concluded that Ti_3Cu phase exists as a stable phase at 76 at. %Ti to 78 at. %Ti. Figure 2-9 and shows the phase diagram by Murray (1987) and Figure 2-10 shows a version by Okamoto (2002). Brice (2015) reported the existence of Ti_3Cu at 3-4 wt% Cu step quenched at 600°C, 650°C and 750°C, and at 13-14 wt% Cu step quenched at 650°C and 750°C. Ansara et al. (2021) also published the Cu-Ti phase diagram showing a congruent formation of Ti_2Cu without Ti_3Cu, as shown in Figure 2-11. Zhan et al. (2012) indicated that the Ti_3Cu phase existed at 500°C. They reported that that the Ti_3Cu phase is stable, but is difficult to

obtain, and it is difficult to distinguish between the Ti_2Cu and Ti_3Cu phases by XRD patterns because their peak positions are similar in the range of $20° \leq 2\theta \leq 60°$. The only differences are that Ti_2Cu has a 44% intensity peak at $2\theta = 19.094°$ and a 14% intensity peak at $2\theta = 36.717°$ (Mueller & Knott, 1963), whereas Ti_3Cu has a 15% intensity peak at $2\theta = 24.845°$ and a 6% intensity peak at $2\theta = 35.424°$ (Karlsson, 1951). Except for the 44% intensity peak Ti_2Cu, the other differentiating peaks have very small intensities, and are likely to be lost in the background. Table 2-3 shows the Ti-Cu system's phase transformations in the area of interest for this project taken from Murray's phase diagram (Murray, 1987).

Table 2-3. Phase transformations in the Ti-Cu system (Murray, 1987).

Transformation	**Compositions (at.% Cu)**			**Temperature (°C)**	**Type**
Pure component					
β-Ti ⇌ α-Ti	0			882	-
L ⇌ β-Ti	0			1670	-
Phases					
(βTi) + L ⇌ Ti_2Cu	13.5	36.5	33.3	1005	Peritectic
(βTi) ⇌ (α-Ti) + Ti_2Cu (Zhan, et al., 2012)	5.4	1.6	33.3	790±5	Eutectoid
L ⇌ Ti_2Cu + TiCu	43	33.3	48	960±5	Eutectic
TiCu + L ⇌ Ti_3Cu_4	52	62.5	57.1	925±10	Peritectic

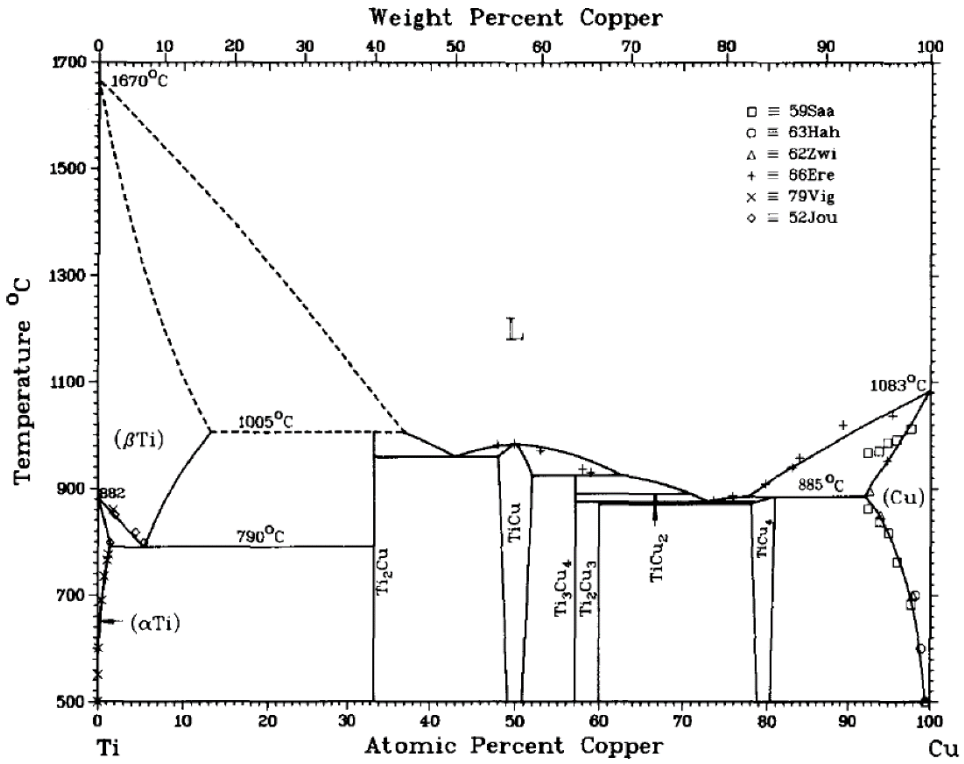


Figure 2-9. Cu-Ti phase diagram (Murray, 1987).

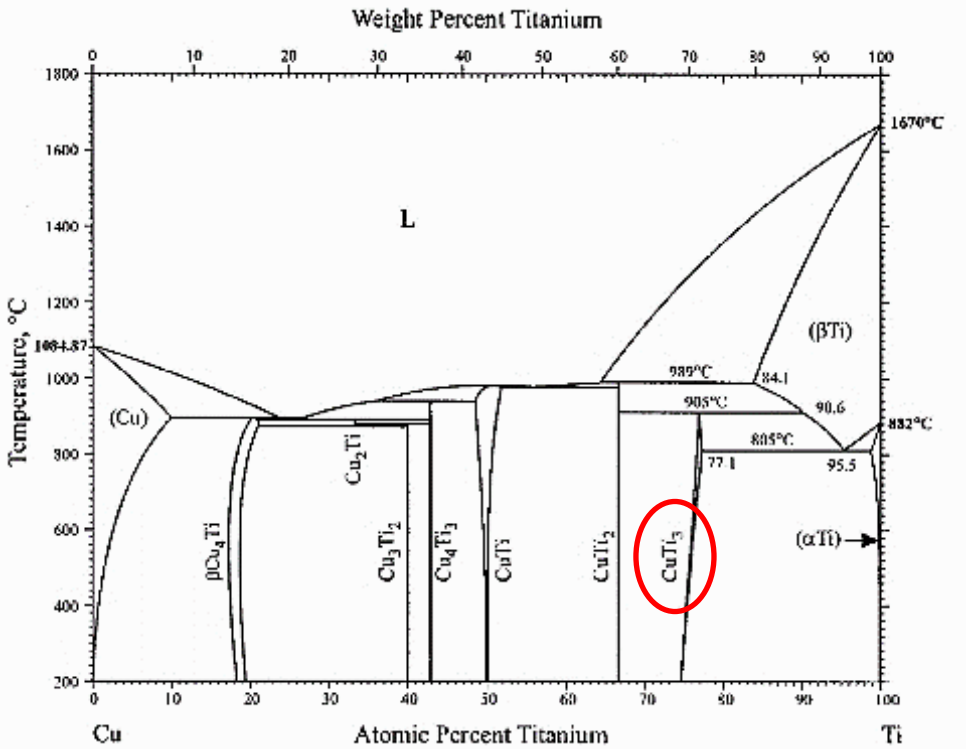


Figure 2-10. Cu-Ti phase diagram, showing "$CuTi_3$" (Okamoto, 2002).

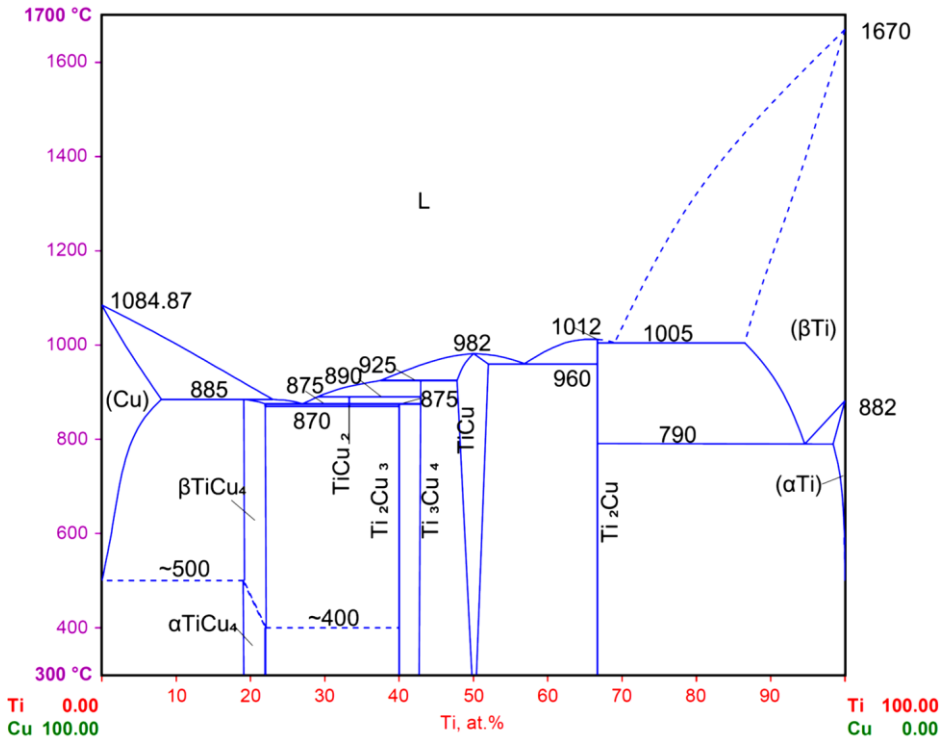


Figure 2-11. Cu-Ti phase diagram (Ansara, et al., 2021).

Titanium-rich alloys exhibit three types of microstructures: α, α+β and β. By alloying with β-stabilizing elements such as copper, the reactivity of titanium can be reduced, the melting point can also be lowered, thus facilitating the casting process. At an addition of 2 – 40 wt% copper, Ti-Cu alloys may show distinct microstructures, e.g., eutectoid, hyper- and hypo-eutectoid microstructures, and this allows the possibility for the mechanical behaviour of Ti-Cu alloys to be adjusted by controlling the fraction and distribution of Ti_2Cu precipitation (Xu, et al., 2020). Kikuchi (2003) indicated that the as-cast microstructure of CP Ti (Figure 2-12) had a typical Widmanstätten, basket-weave structure of acicular (αTi), Ti-5Cu (Figure 2-13) had a typical hypo-eutectoid structure which included primary precipitates of (αTi) and eutectoid (lamellae of (αTi) and Ti_2Cu) that transformed from (βTi) at the eutectoid temperature, while Ti-10Cu (Figure 2-14) had a eutectoid structure since 10 wt% Cu is close to 7 wt% (eutectoid point).

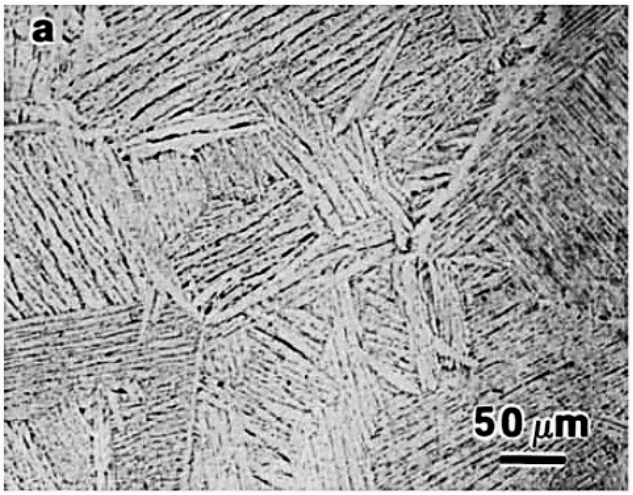


Figure 2-12.Typical microstructure of the as-cast CP Ti (Kikuchi, et al., 2003).

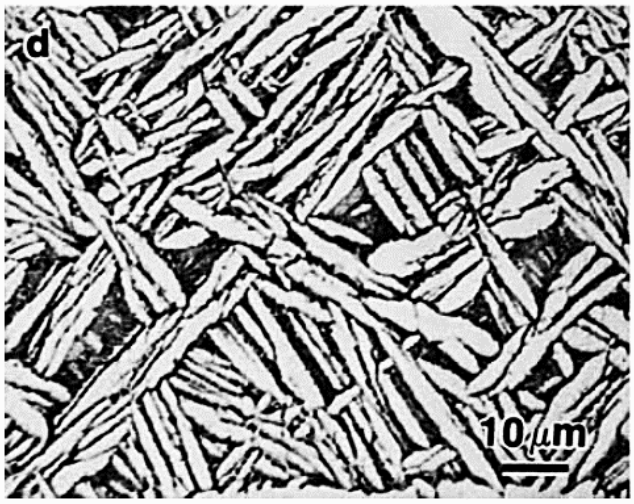


Figure 2-13. Typical microstructure of the as-cast Ti-5Cu (Kikuchi, et al., 2003).

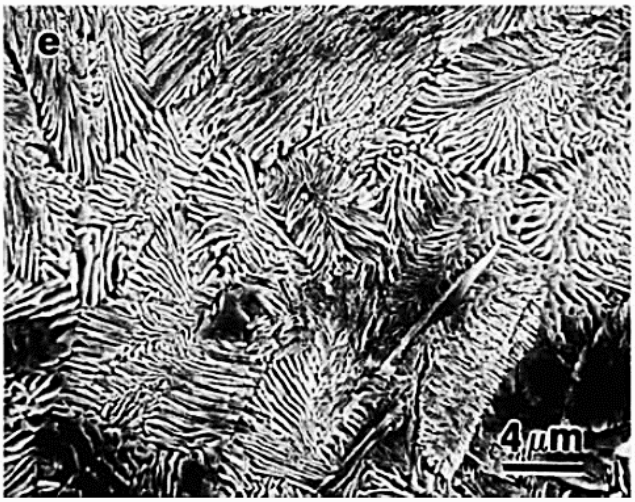


Figure 2-14. Typical microstructure of the as-cast Ti-10Cu (Kikuchi, et al., 2003).

2.3.2. Heat treatment of Ti-Cu alloys

Heat treatment, such as annealing and ageing, could significantly improve the mechanical properties, corrosion resistance and antibacterial rate due to the redistribution of copper and size distribution of Ti_2Cu precipitates. Bao (2018) reported a Ti-3Cu alloy, where a high temperature treatment (at 900°C/5 h + 400°C/24 h + 475°C/12 h) contributed to high strength but low plasticity, due to solid solution of copper and coarsening of grains. The aged (at 900°C/5 h + 400°C/24 h + 475°C/12 h) samples provided high tensile strengths (850 MPa, 900MPa and 880MPa) and strong antibacterial properties (antibacterial rates increased significantly to 91.32 %, 98.54 % and 99.32 %) due to the precipitation of Ti_2Cu. Figure 2-15 shows the Ti-3Cu alloy at different heat treatments (Bao, et al., 2018).

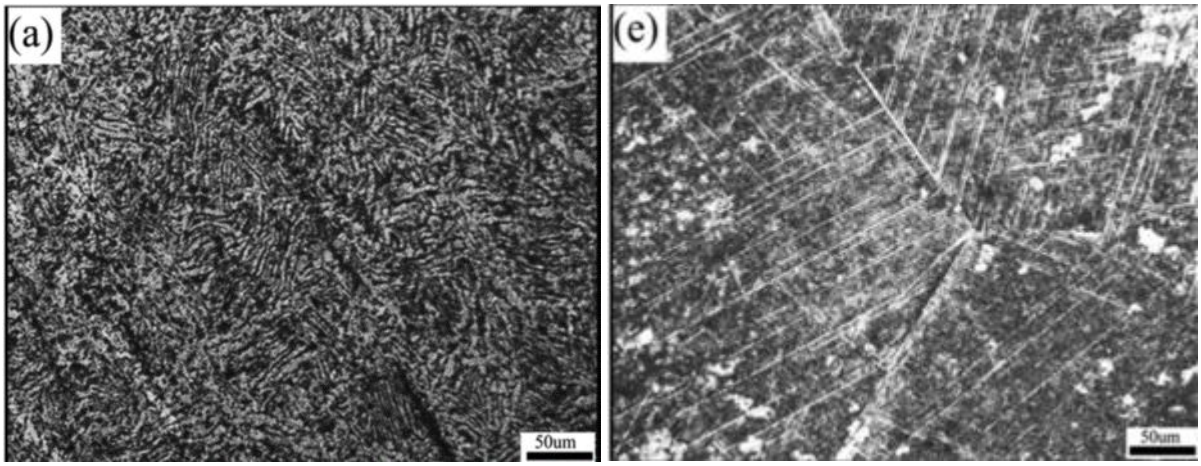


Figure 2-15. Ti-3Cu alloy (a) As-forged and annealed, (e) Aged (Bao, et al., 2018).

Zhang (2016) reported that the as-cast Ti–Cu alloys showed a low antibacterial rate, about 30%. With increasing Cu content, the antibacterial rate changed slightly, from 33% for Ti–2Cu (AC) to 35% for Ti–3Cu (AC) and to 36% Ti–4Cu (AC). After heat treatment (900°C/3 h + 400°C/12 h), the antibacterial rates increased significantly to 77.85%, 90.33% and 92.57%, for Ti–2Cu, Ti–3Cu and Ti–4Cu alloys, respectively. It was demonstrated that homogeneous distribution and a fine Ti_2Cu phase played a very important role in the mechanical, anticorrosion and antibacterial properties. The as-cast microstructures had a thin lamellar structure with wide grain boundaries, as shown in Figure 2-16(a). After solid solution treatment (at 900°C/3 h), the grain boundaries and grains became narrower than those in the as-cast samples and a typical acicular martensite was found, as shown in Figure 2-16(b).

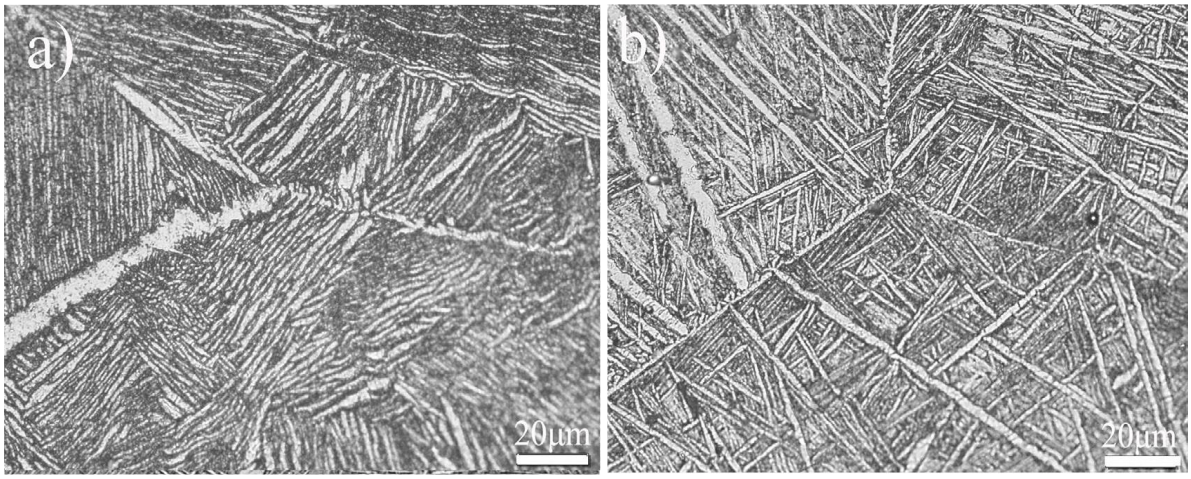


Figure 2-16. Ti-3Cu alloy: (a) as-cast, (b) after solid solution treatment (Zhang, et al., 2016).

Zhan et al. (2012) reported that the as-cast Ti-25Cu microstructure comprised two phases Ti_{ss} (solid solution) (dark) and Ti_2Cu (light), as shown in Figure 2-17(a). After annealing at 750°C for 90 h, Ti_3Cu precipitated in the dendritic Ti_{ss} phase and Ti_2Cu existed at the matrix. The annealing time was too short to obtain an equilibrium microstructure, which consisted of (αTi) and Ti_3Cu, as shown in Figure 2-17(b). Since the annealing time was too short to form an equilibrated microstructure of (αTi) and Ti_3Cu, three phases were detected at room temperature. Zhan et al. (2012) reported that this suggested that the eutectoid decomposition of (βTi) into (αTi) and Ti_3Cu occured very quickly under the high cooling rate through ice water quenching or liquid nitrogen quenching. After annealing at 805°C and 850°C Ti_3Cu was not observed; only Ti_{ss} and Ti_2Cu phases were observed in the microstructure, as shown in Figure 2-17(c and d). Therefore, Zhan et al. (2012) concluded that the formation of Ti_3Cu is controlled by the annealing temperature.

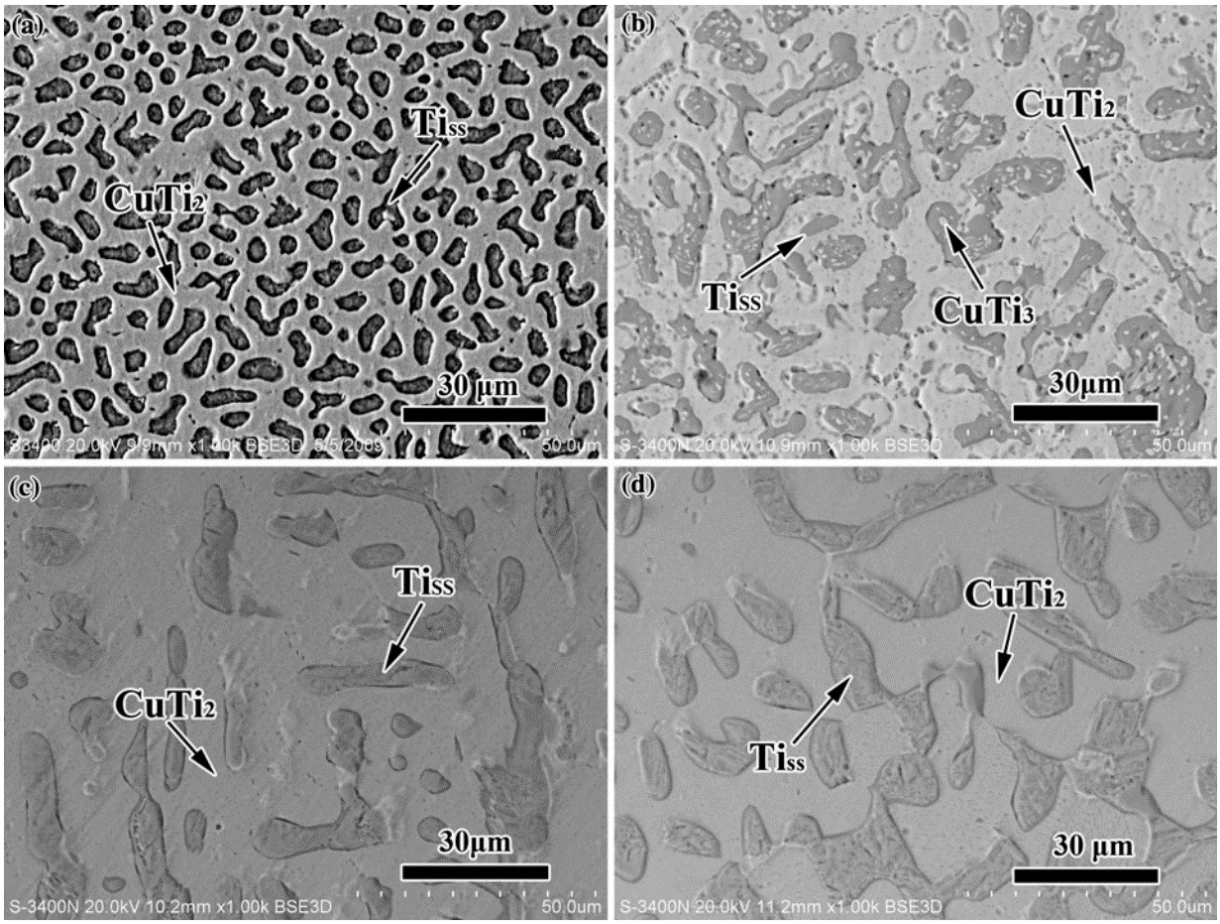


Figure 2-17. Ti-25Cu alloy samples at different conditions: (a) As-cast, (b) Annealed at 750°C for 90 h, (c) Annealed at 805°C, and (d) Annealed at 850°C (Zhan, et al., 2012).

2.4. Corrosion of dental implants

One of the challenges experienced in biomaterial applications is the degradation of the alloys caused by corrosion. The main causes of corrosion are: saliva amount, quality and temperature, protein, pH, plaque, chemical and physical properties of liquids, food and oral health conditions (Manam, et al., 2017). Saliva has several viruses, bacteria, yeast and fungi which can have products, such as organic acids and enzymes, epithelial cells, food debris, and components from gingival crevicular fluid (Chaturvedi, 2009). Therefore, corrosion by electrochemical attack is a concern, particularly when metallic implants, metallic fillings, or orthodontic appliances are placed in the hostile electrolytic environment provided by the human mouth (Chaturvedi, 2009).

The corrosion resistance can be considered a fundamental requirement of biomaterial components and is associated with ion release of the metallic species. The corrosion product or dissolved metal ions can either build up in tissues next to the implant or may be transferred to the other body parts (Okazaki & Gotoh, 2005). These metallic ions can be harmful, can reduce human life expectancy and can also cause pain or swelling in the region of the implant in the absence of infection (Adya, et al., 2017).

The features that determine how and why dental materials corrode are:

1. Oxidation and reduction reactions.
2. Factors that physically impede or prevent corrosion from taking place (formation of a metal oxide passive film on a metal surface).

There are two types of corrosive reactions, chemical and electrochemical. In chemical corrosion (dry corrosion), there is a direct combination of metallic and non-metallic elements to yield a chemical compound through oxidation, halogenation, or sulfurization reactions. Electrochemical corrosion (wet corrosion) requires the presence of water or some other fluid electrolyte. The different forms of corrosion are shown in Figure 2-18 (Noumbissi, et al., 2019).



Figure 2-18. Different forms of corrosion (Noumbissi, et al., 2019).

There are several types of corrosion commonly experienced in the oral cavity which are described below.

2.4.1 Uniform corrosion

Uniform corrosion is usually the most common type of corrosion. It is uniform across the metal surface, although at times in aqueous body fluids such as phosphate buffer saline (a phosphate buffer prepared from sodium phosphate, potassium phosphate and sodium chloride, Ringer's lactate (a type of isotonic, crystalloid fluid classified as a balanced or buffered solution used for fluid replacement) (Naseem, et al., 2020) and normal saline (prescription medicine used for fluid and electrolyte replenishment for intravenous administration) (Stoppler, 2016)). The corroded surface may take a mottled form, with a severely roughened metal surface that resembles localised attack (Bhola, et al., 2011). At high temperatures (>70°C) in highly acidic environments due to consumption of hot, spicy and sticky foods, general corrosion is a concern (Bhola, et al., 2011).

2.4.2 Pitting corrosion

Pitting corrosion is an extremely localised attack caused by the breakdown of the passivating oxide film (an ultra-thin film of a protective material), resulting in pits on the surface of the metal. It can be enhanced by the presence of proteins in the tissue fluid and serum (Hansen, 2008). The reduction in pH and increase in the concentration of chloride ions are two essential factors in the initiation and propagation of pitting corrosion. When the acidity increases with time, the passive layer of the alloy dissolves and local corrosion is accelerated. A titanium implant surface (due to protective oxide films) exhibits anodic pitting potentials that are very high (greater than 1V) compared to other biomaterials used (iron, steel, cobalt-chromium alloys etc.). Thus, pitting corrosion is of little concern in the oral environment for titanium alloys (Bhola, et al., 2011).

2.4.3 Galvanic corrosion

In dentistry applications, galvanic corrosion occurs when two or more dental prosthetic devices with dissimilar alloys come into contact while subjected to oral liquids like saliva, other liquids in the mouth and the bone and tissue fluids. It is caused by the difference in corrosion potentials in a flow of electric current between the alloys. This results in a formation of a galvanic cell which causes an increase in the corrosion rate of the anode while enhancing the amount of ion metal released (Zohdi, et al., 2012). The galvanic current passes not only through the metal/metal contacts, but also through the tissues, which may cause pain.

The electrochemical cell will have two electrodes as shown in Equation 2-4 to Equation 2-9 (Adya, et al., 2017; Bhola, et al., 2011). When these two dissimilar metals with different electrode potentials come in contact in the presence of a corrosive electrolyte, a potential is generated. The net result is a chemical reaction with oxidation occurring at the anode and reduction occurring at the cathode, the electronic exchange occurs through the contact and ionic exchange occurs through the electrolyte (Zohdi, et al., 2012). If a base metal alloy superstructure is provided over the titanium implant, the less noble metal alloy forms the anode and the more noble titanium alloy is protected as a cathode. The electronic exchange occurs through the metallic contact and ionic contact occurs through saliva, mucosa, tissue and bone fluids. Though the hydrogen evolution at the implant surface may further

complicate the situation by pressure under the prosthesis and hydrogen embrittlement of the implant surface (Bhola, et al., 2011).

1.	Oxidation (Anode):	$M \rightarrow M^{n+} + ne^{-1}$	Equation 2-4
2.	Reduction (Cathode):	$2H^{+} + 2^{e-} \rightarrow H_2$	Equation 2-5
		$4H^{+} + 4^{e-} + O_2 \rightarrow 2H_2O$	Equation 2-6
		$2H_2O + 2^{e-} \rightarrow H_2 + 2OH^{-}$	Equation 2-7
		$2H_2O + 4^{e-} + O_2 \rightarrow 4OH$	Equation 2-8
		$M^{n+} + e^{-} \rightarrow M^{(n-1)+}$	Equation 2-9

2.4.4 Fretting and erosion-corrosion

Fretting corrosion is caused by a combination of corrosive fluid (saliva with several enzymes and food particles) and velocity in the oral environment. The mechanical component of fretting is due to the rubbing movement which disrupts the passive layer and removes metal particles. This action stimulates the chemical activities at the surface, leading to oxidation or active corrosion, or re-passivation because of the electro-chemical aspect of the process (Eliaz, 2019).

2.4.5 Microbial corrosion

Microbiologically induced corrosion has been defined and widely accepted as corrosion damage initiated or aggravated due to the direct or indirect activities of microorganisms colonizing the materials surfaces (Liu, et al., 2016; Costa, et al., 2021). These microorganisms colonise and accumulate to form biofilms. Oral biofilms are assumed to change the implant's electrochemical environment, leading to disruption of the TiO_2 layer. This is hypothesised based on two main mechanisms (Costa, et al., 2021):

1. Bacteria can significantly reduce the peri-implant (the extra piece added artificially) micro environment pH by producing organic acids during fermentable carbohydrate catabolism. This low pH creates a favourable environment for pitting attacks.
2. Microbial accumulation on the dental implant can promote differential oxygen exposure on the titanium surface. As a result, the less aerated zones act as the anode and undergo crevice corrosion, thereby mitigating the reformation of the oxide layer.

Both these unfavourable conditions initiate metal dissolution and surface deterioration. Among the bacteria present in the oral cavity, *Streptococcus mutans* is a powerful corrosive microorganism because of its capacity to release lactic acid and grow in acidic environments. Although *S. mutans* is not directly responsible for implant-related infections, this important pathogen promotes quick co-aggregation with periodontopathogen bacteria due to reduced oxygen content related to the biofilm accumulation and extracellular polymeric substances (EPS) formation (Costa, et al., 2021). These EPSs are natural polymers of high molecular weight secreted by microorganisms into their environment (Liu, et al., 2016).

Figure 2-19 shows a representation of the microbial corrosion mechanism and Equation 2-10 to Equation 2-12 show the titanium oxidation reactions (Costa, et al., 2021). The biofilm that covers a titanium implant surface is a cathodic area, and the exposed titanium is an anodic area, which forms galvanic corrosion. These anodic and cathodic regions are produced by converting the biofilm covered implant surface into an electrode, which increases the corrosion rate due to the high chemical reactivity of the titanium material.

$TiO_2 + H_2O + H^+ = Ti(OH)^{3+}$	(exposed surface)	Equation 2-10
$4H^+ + O_2 + 4^e = 2H_2O$	(cathode region)	Equation 2-11
$Ti + H_2O = TiO^{2+} + 2H^+ + 4e$	(anode region)	Equation 2-12

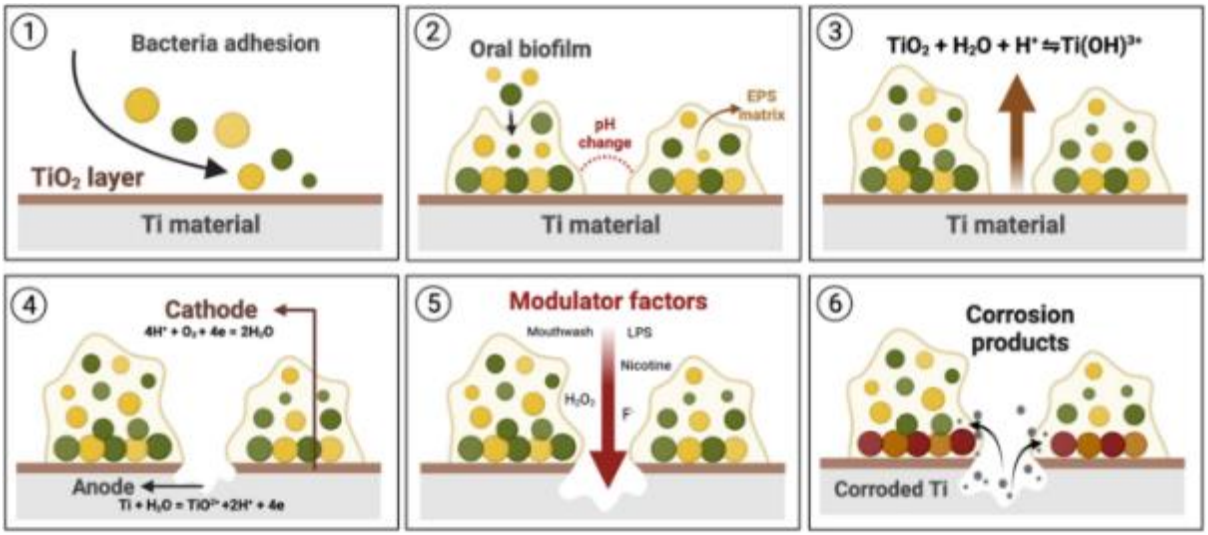


Figure 2-19. Mechanisms of microbial corrosion in Ti dental implants (Costa, et al., 2021).

2.4.6 Stress induced cracking

Stress-corrosion cracking refers to cracking caused by a combination of tensile stress and a specific corrosive medium. During chewing, dental implants are subjected to heavy compressive shear and bending forces. Also, rubbing of surfaces sometimes results in localised deformation. Thus, an electrolytic cell is formed between the stressed and unstressed metal portions. Eliaz (2019) reported that grain boundaries of stressed metal were most vulnerable to corrosion.

2.4.7 Crevice corrosion

Crevice corrosion occurs between two close surfaces or in constricted places where oxygen exchange is not available. The reduction in pH and increase in the concentration of chloride ions are two essential factors in the initiation and propagation of this type of corrosion (Adya, et al., 2017). Titanium alloy implants may be subjected to localised crevice attack while exposed to short time periods of hot (>70°C) chloride, bromide, iodide, fluoride or sulphate-containing solutions. Titanium chlorides formed within the crevice are unstable and tend to hydrolyse, forming hydrochloric acid (HCl) and titanium oxide/hydroxide corrosion products. Since there are small, restricted volumes of solution within the tight implant-superstructure crevice (the portion of a dental implant that attaches to its implant substructure and to a fixed or removable dental prosthesis to support or retain that prosthesis), low crevice pH levels (0-1) with high H^+ ions concentration can develop. These local reducing acidic conditions can

result in severe and rapid localised active corrosion within the crevices, depending on alloy resistance, temperature, and redox potential of the surrounding crevicular fluid (Bhola, et al., 2011). The mechanism of crevice corrosion for titanium in aqueous chloride media is shown in Figure 2-20 (Bhola, et al., 2011). The overall reaction consists of the dissolving of metal M and the reduction of oxygen to hydroxide ions as shown in Equations 2-13 and 2-14. The reactions initially occur at the entire surface and inside the crevice. The fluid inside the crevice becomes depleted of oxygen when it remains stagnant. The lower oxygen content in the crevice helps to form an anodic region at the metal surface. The metal surface in contact with the trapped moisture exposed to air forms a cathode. An excess of positively charged ions occurs in the crevice, causing the stagnant solution to become acidic. To compensate for the excess of positive ions, chloride ions in the fluid migrate into the crevice causing a local and small galvanic cell to be created (Mouritz, 2012). The metal chlorides hydrolyze in water, forming an insoluble hydroxide and an acid as shown in Equation 2-15. Crevice corrosion is therefore an autocatalytic process (Bhola, et al., 2011; Khoshnaw & Gubner, 2022).

$$M \longrightarrow M^{+} + e \qquad \text{(Oxidation)} \qquad \text{Equation 2-13}$$

$$O_2 + 2H_2O + 4e \longrightarrow 4OH^{-} \qquad \text{(Reduction)} \qquad \text{Equation 2-14}$$

$$M^{+}Cl^{-} + H_2O \longrightarrow MOH\downarrow + H^{+}\,Cl^{-} \qquad \text{Equation 2-15}$$

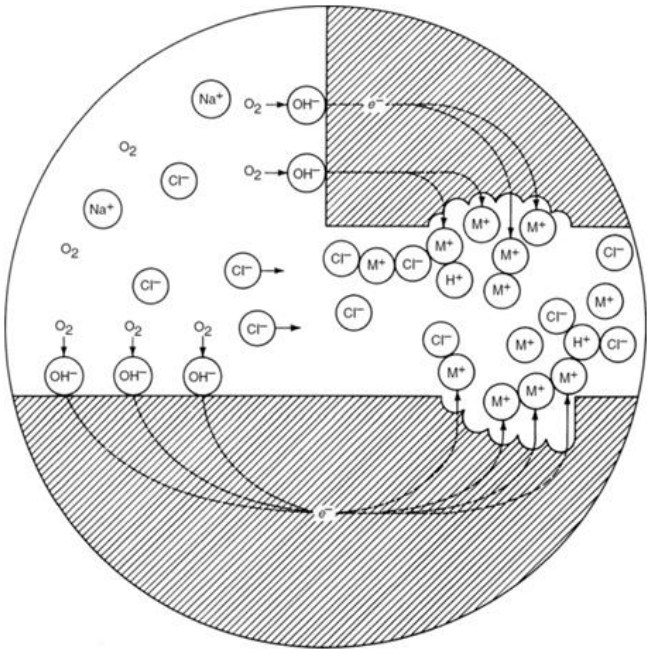


Figure 2-20. Crevice corrosion in aqueous chloride media (Bhola et al., 2011).

2.5. Corrosion of Ti-Cu alloys

For biomedical application, low corrosion rate is always desired. The corrosion resistance of Ti-Cu alloys is a very important characteristic for biomedical applications (Zhang, et al., 2016). While alloying titanium with high copper content can provide stronger antibacterial activity and high strength, it can also deteriorate the ductility and corrosion resistance, including generating a cytotoxic effect (Wang, et al., 2019). The increase of copper increases the volumetric fraction of Ti_2Cu intermetallic particles. Wang et al. (2019) reported that the eutectoid transformation and the resulting microstructure (αTi) + Ti_2Cu plays important role in the corrosion behaviour of Ti-Cu alloys due to different corrosion potential between the phases of the eutectic mixture. Bao et al. (2018) reported that the formation of the intermetallic compound Ti_2Cu produced an "envelope effect" which prevented the alloy from corrosive liquid contact and then strengthened the corrosion resistance of the alloy. Osório, et al. (2010 and 2012) reported that although the Ti_2Cu intermetallic compounds and the αTi phase constitute galvanic couples, a fine microstructure provides an "enveloping effect", modifying the cathode/anode area ratio between these phases which could minimise the galvanic effects and improve the corrosion resistance. Wang et al. (2019) also reported that the Ti-5Cu with a microstructure of αTi + Ti_2Cu and transformed αTi possessed significantly improved corrosion resistance, while Ti-5Cu with a microstructure αTi + transformed βTi showed an increase in corrosion rate when compared to CP Ti (no grade mentioned). They mentioned that the Ti_2Cu precipitates are nobler than both αTi matrix and eutectoid Ti-rich phase. They also mentioned that annealing for 1 hour at 740°C and 910°C resulted in homogeneously distributed Ti_2Cu precipitates "enveloping" the Ti-rich (less-noble) phase, and hence showed a better corrosion resistance. Takada et al. (2001) reported no significant difference in corrosion resistance between Ti-Cu alloys with copper concentrations up to 30% compared to CP Ti (no grade mentioned). Liu, et al. (2014) reported than the open circuit potential (OCP) of the Ti−Cu alloys were nobler, while the corrosion current densities were lower than the values of CP Ti. The calculated corrosion rates indicated that Ti–Cu alloys

exhibited lower corrosion rates than CP Ti, indicating that the addition of copper could slightly improve the biocorrosion resistance of titanium, Figure 2-21 (Liu, et al., 2014).

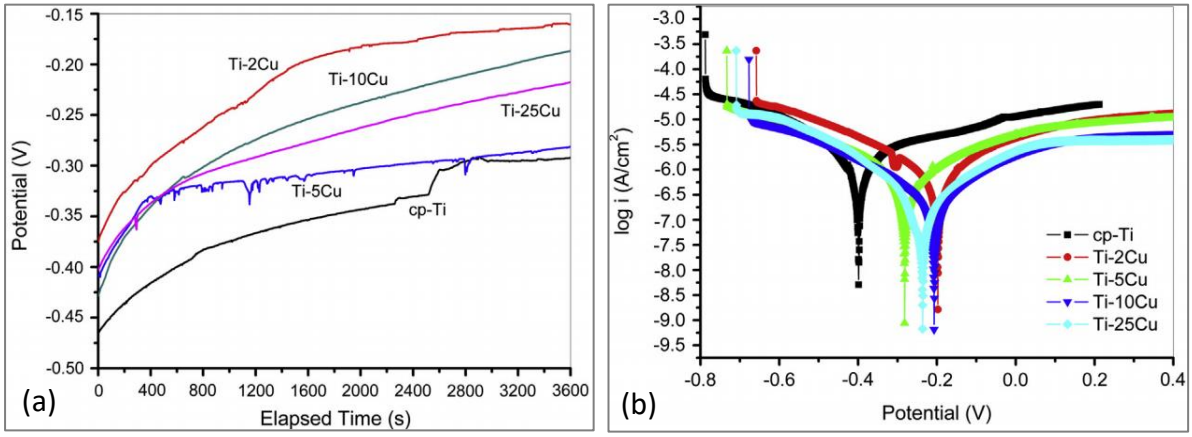


Figure 2-21. Ti-Cu: (a) OCP, (b) Tafel curves (Liu, et al., 2014).

Studies have been performed on effects of microstructure, composition and heat treatment on mechanical properties, corrosion behaviour, antibacterial properties and cell biocompatibility of solid Ti_2Cu alloys used for biomedical applications (Li, et al., 2017). Pina (2016) reported that CP Ti showed the highest chemical reactivity on its surface in artificial saliva in good agreement with the highest current densities obtained in the potentiodynamic curves at selected potentials. This indicated that alloying with 3 wt % copper improved the corrosion resistance of the alloy compared to pure titanium. However, a higher copper content increased the cathodic and anodic reactivity of the alloy surface as shown in Figure 2-22.

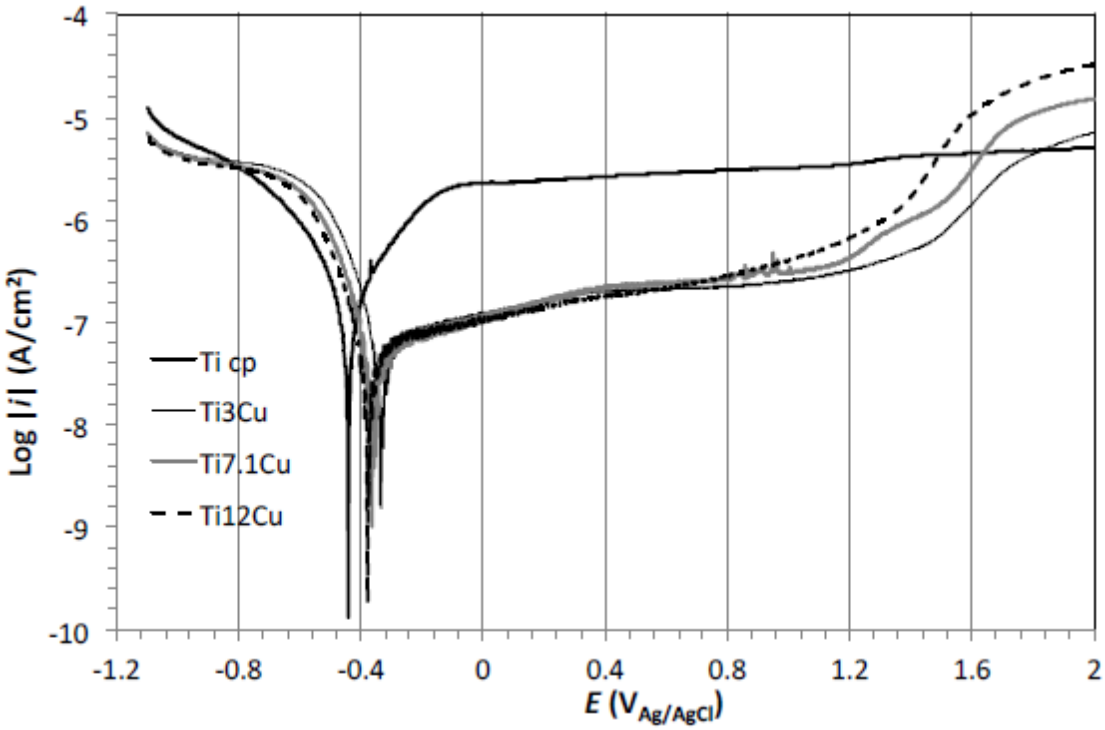


Figure 2-22. Anodic potentiodynamic curves of Ti-CP and Ti-xCu alloys in artificial saliva (Pina, et al., 2016).

2.5.1 Corrosion testing and measurements

The corrosion resistance of implant materials can be evaluated by several methods in the laboratory, by quantitative electrochemical measurements in simulated body fluids (*in vitro*) or quantitative measurements of implantation of devices into experimental animals (*in vivo*) (Hansen, 2008). The *in vitro* testing is usually the first step of testing followed by *in vivo* testing.

Uniform corrosion for titanium implants can be determined from weight loss data (increase or decrease in weight depending upon the environment and by products in accordance to ASTM G1 & G31), dimensional changes (shape, size, appearance) and electrochemical methods (anodic and cathodic polarization, cyclic voltammetry and electrochemical impedance measurements). Pitting corrosion can be measured by using the guiding principles under the American Standards for Testing of Materials G3 & G5, electrochemical techniques involving potentiostatic and potentiodynamic testing.

2.6. Mechanical properties of Ti-Cu alloys

Hardness and work hardening play vital roles in biomaterial implants due to their ability to increase the resistance against wear and corrosive effects of body fluids. Undesirable work hardening of Ti and Ti-based alloys with increased hardness occur during machining processes such as milling and drilling (Khorasani, et al., 2015). For a material to be biocompatible it must have a density as low as that of bone, high mechanical strength and fatigue resistance, low elastic modulus and good wear resistance (Oldani & Dominguez, 2012). The copper content in the titanium alloys significantly influences the mechanical properties, such as elongation, Young's modulus and hardness (Liu, et al., 2014). Some Ti–Cu alloys might have superior mechanical properties than CP Ti which could be explained by solid solution strengthening of the titanium and fine precipitation of intermetallic compounds (Liu, et al., 2017). Zhang, et al. (2016) reported that homogeneously dispersed and fine Ti_2Cu particles would significantly enhance the hardness and mechanical strength, but reduce the ductility. Liu, et al. (2014) reported that the hardness increased with the increasing copper content and reached a high value of 55 HRC at 5 wt% Cu. Further increase in Cu content did not change the hardness significantly, and a slight drop was found in the hardness at 10 wt% Cu as shown in Figure 2-23 (Liu, et al., 2014).

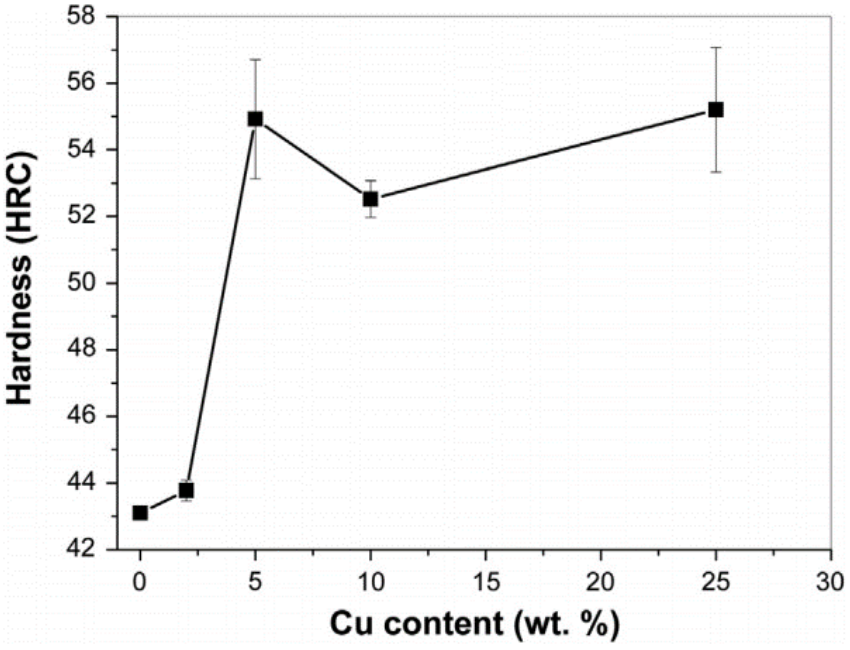


Figure 2-23. Change in hardness with copper content in the Ti–Cu alloys (Liu, et al., 2014).

Zhang et al. (2016) reported that with increasing the copper content (x = 2, 3 and 4 wt %), the micro-hardness increased significantly at all conditions (as-cast, solid solution treatment (T4) at 900°C for 3 hours and ageing treatment (T6) at 400°C for 12 h). The hardness increased from 203.7 HV (2 wt % Cu) to 247.8 HV (3 wt % Cu) and to 262.0 HV (4 wt % Cu) for the as-cast Ti–Cu, indicating that the Cu content enhanced the hardness. They also reported an increase in hardness after both heat treatments indicating that heat treatment could significantly enhance the hardness of the Ti–Cu alloy, especially the solid solution treatment, Figure 2-24.

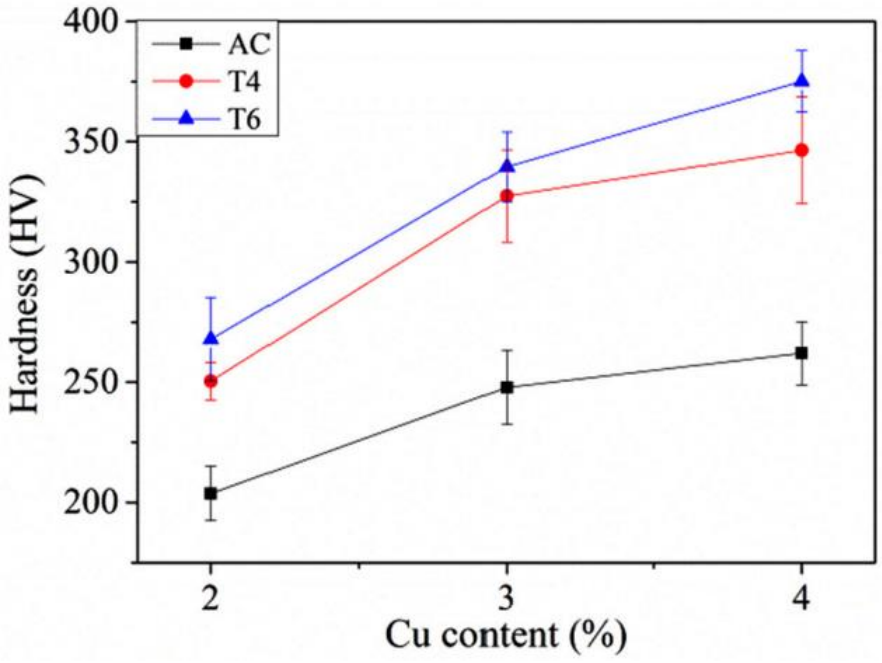


Figure 2-24. Micro-hardness of the Ti–Cu alloys (Zhang, et al., 2016).

Although the antibacterial effect of copper additions is superior compared to silver (Codita et al., 2010), Zhang et al. (2019) investigated alloying titanium with copper and found inconsistencies in the literature regarding the required copper content and the mechanisms that resulted in bacterial reduction. The antibacterial property is associated with preferential copper ion release from the Ti-Cu alloys due to the galvanic corrosion between phases with copper and the titanium matrix (Osório, et al. (2010, 2012). This shows that although Ti-Cu alloys are considered to have high corrosion resistance they are not immune to corrosion. The mechanical properties are also important and should be considered, since implants

experience mechanical loading *in vivo*. When titanium is alloyed with copper the intermetallic compound Ti_2Cu forms, which can result in brittleness (Unosson, et al. 2013). However, Ti_2Cu plays an important role in strong antibacterial behaviour therefore heat treatment, such as annealing and ageing, could also significantly improve the mechanical properties, corrosion resistance and antibacterial rate by redistributing copper and changing the size distribution of the Ti_2Cu precipitates (Bao et al. 2018). This interrelationship between choices of compositions and heat treatments, and their impacts on mechanical properties and antibacterial effects, provided an opportunity for optimization of the final alloy. Therefore, the objective of this project was to characterise Ti-Cu alloys at different compositions: 5, 15, 25, 33, 40, 47 and 50 wt% copper in Grade 4 titanium. This study assessed the effect of the Ti_2Cu compound and its proportions on the corrosion resistance, and compared them to the commercial pure titanium (Grade 4), which is currently commonly used as a material for dental screws.

Chapter 3: EXPERIMENTAL PROCEDURE

3.1. Material Selection

Titanium has been a material of choice in several disciplines of dentistry, and for this study Grade 4 CP Ti was selected due to its highest tensile strength and yield strength compared to Grades 1 to 3. High purity copper (SAE CA110) was also selected for alloying. Table 3-1 shows the chemical composition of both CP Ti and copper. Titanium was in form of a 15 mm diameter rod and was procured from Multi Alloys (Pty) Ltd., while copper was in plate form (3 mm thick) and procured from Meglan Trading CC.

Table 3-1. Chemical compositions of titanium and copper (wt %) starting materials.

Elements	Grade 4 CP Ti (wt %)	SAE CA110 Copper (wt %)
Nitrogen (N)	0.05	-
Carbon (C)	0.08	-
Oxygen (O)	0.4	0.04
Iron (Fe)	0.5	-
Silver (Ag)	-	0.05
Hydrogen (H)	0.015	-
Titanium (Ti)	98.96	-
Copper (Cu)	-	99.91

3.2. Melting

Eight 50g castings were manufactured using the Mintek button arc furnace. The samples (six samples at a time) were melted by a high-energy arc at high temperatures and water cooled via copper hearth. A pure titanium button was used an oxygen getter and was melted before melting the Ti-Cu alloys to prevent remaining oxygen in the chamber from reacting with the molten metal. Prior to melting the chamber was flushed five times with high purity argon. The argon gas was of 99.999% purity with oxygen ≤ 2 ppmv. The alloys were melted five times, turned over and re-melted to ensure homogenisation since the button arc furnace cannot stir the samples during melting to promote homogeneity. The melting points of titanium and

copper may lead to inhomogeneity due to their differences (1670°C for titanium and 1083°C for copper (Massalski, et al., 1991)). Table 3-2 shows the compositions of the castings. Figure 3-1 shows the button arc furnace and Figure 3-2 shows a typical as-cast button. After melting, the buttons were weighed to ascertain any loss.

Table 3-2. Ti-Cu casting compositions.

Titanium (g)	Copper (g)	Ti-Cu Alloy (wt %)
50	-	CP Ti
47.5	2.5	5Cu
42.5	7.5	15Cu
37.5	12.5	25Cu
33.5	16.5	33Cu
30	20	40Cu
26.5	23.5	47Cu
25	25	50Cu



Figure 3-1. Photograph of the button arc furnace used.

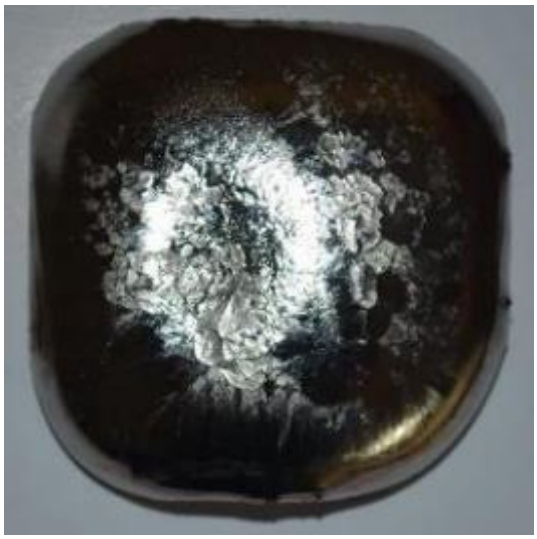


Figure 3-2. As-cast (~50 x ~30mm) Ti-5Cu alloy button (50g).

3.3. Heat Treatment

All samples were put in a vacuumed and sealed quartz ampoules (each sample on its own) at a pressure of 1.333 mbar argon to prevent oxygen from reacting with the samples. The gas was not dried or purified further. The evacuation and backfilling procedure was performed three times. Annealing was performed at 750°C and 900°C for two hours in a conventional furnace followed by a fast water quench (by crushing the ampoules on quenching). Figure 3-3 shows the quartz ampoule sealing preparation.

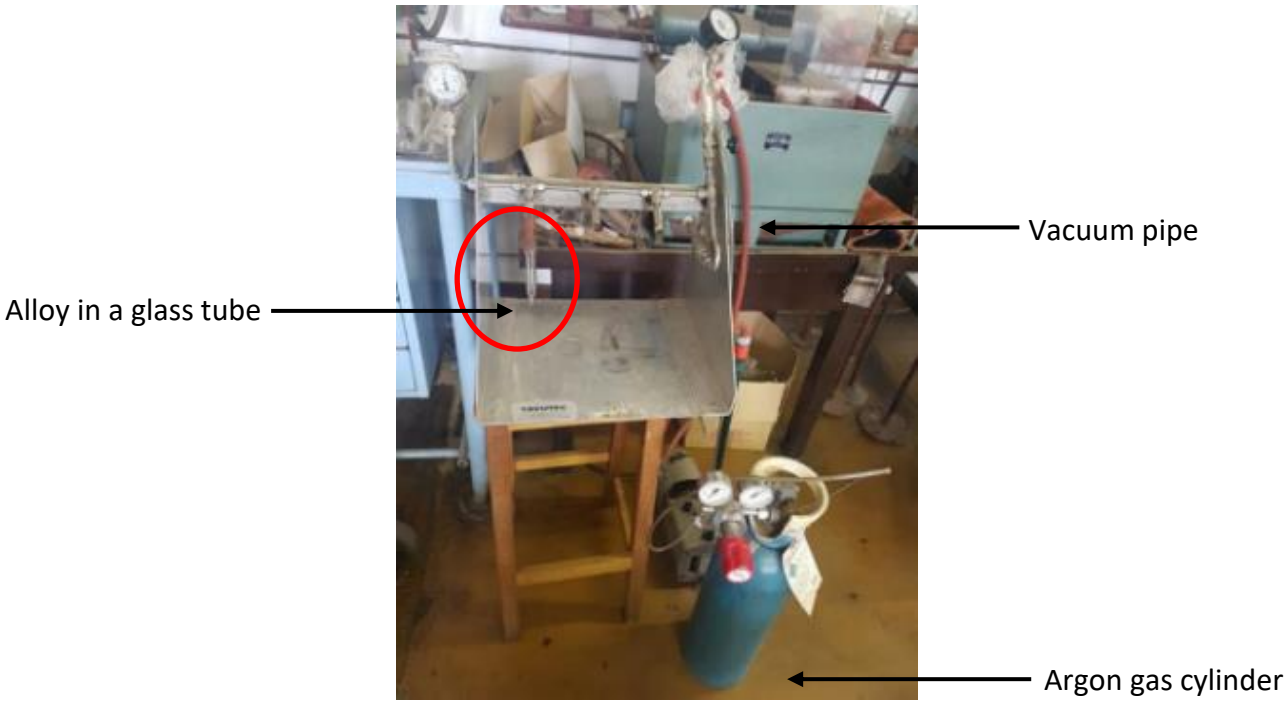


Figure 3-3. Photograph of the argon purging set-up.

3.4. Modelling

3.4.1 Thermo-Calc™

The Thermo-Calc program (v.2020b, Thermo-Calc Software AB, Stockholm, Sweden) with thermodynamic database TTTI3 (database which was available) was used to draw the phase diagram and to predict the equilibrium phases expected as a function of temperature for the different alloy compositions.

3.4.2 Materials Studio

A CASTEP module integrated within the Materials Studio software package was employed to carry out geometry optimization calculations to find the ground state crystal structures (Segall, et al., 2002). It is based on density functional theory (DFT) formalism and employs the plane-wave basis set to treat valence electrons and pseudopotentials to approximate the potential field of ion cores including nuclei and tightly bond core electrons (Hohenberg & Kohn, 1964; Kohn & Sham, 1965). The generalized gradient approximation (GGA) in the scheme of Perdew-Burke-Ernzerhof (PBE) was chosen to describe the electronic exchange-correlation interaction (Perdew, et al., 1996). The choice of PBE form of GGA was informed by its level of robustness and accuracy (Smeets & Kroes, 2021). Geometry optimisation calculations were carried out using fast Vanderbilt-type ultrasoft pseudopotentials (US) (Vanderbilt, 1990). Maximum plane wave cut-off energy of 650 eV and set of special k-points determined from the Monkhorst–Pack scheme (Monkhorst & Pack, 1976) were used. All the equilibrium crystal structures were obtained via geometry optimization in the Brayden-Fletcher-Goldfarb-Shanno (BFGS) minimization scheme (Fischer & Almlof, 1992). The convergence criterion of less than 1×10^{-5} eV/atom, the maximum residual forces of 0.03 eV/Å, maximum residual bulk stress of 0.05GPa and maximum atomic displacement of 1×10-3Å were utilized. The simulated XRD patterns were derived using the Reflex powder diffraction module.

3.5. Sample Analysis

Figure 3-4 shows a summary of the sample analysis performed on the samples.

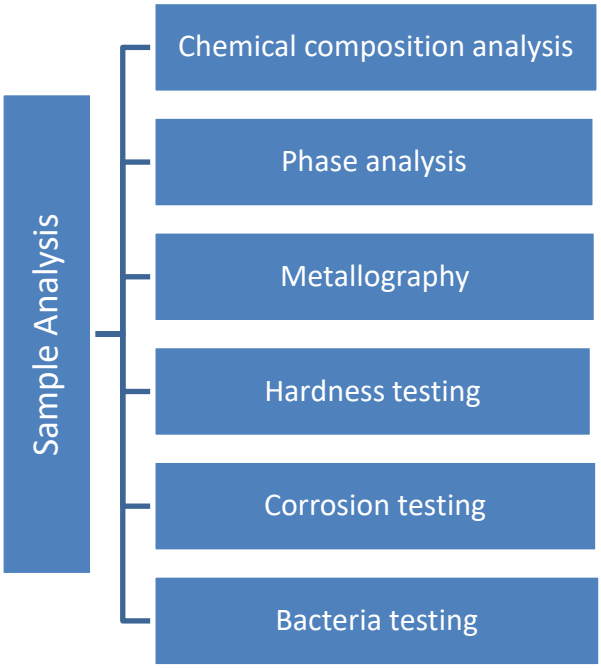


Figure 3-4. Summary of the experiments conducted.

3.5.1 Metallographic preparation

Cutting and mounting

The samples were sectioned using a Struers Discotom-60 machine. A Corundum-D300 disk from IMP Scientific & Precision (Pty) Ltd. was used for cutting. The cutting was performed while cooling with water to prevent overheating the samples, which may have changed the microstructure. For the ease of handling during examination, the samples were hot mounted in a blue epoxy resin using a Struers LaboPress-3 machine.

Grinding and polishing

The samples were ground and polished using a Struers Rotopoll-11 machine. The samples were ground from a 60 grit rough to 1200 grit fine silicon carbide paper to remove the

scratches and obtain a flat surface. The samples were polished from 6 to 1 µm surface finish to obtain a mirror finish.

Etching

The as-polished samples were etched using Keller's etchant as shown in Table 3-3. Keller's reagent reveals grain boundary contrast and precipitates in several wrought alloys (Vander Voort, 1999).

Table 3-3. Etching reagent used for the Ti-Cu samples.

Etchant	**Chemicals (ml)**			
Keller's reagent	Hydrofluoric acid (HF)	Hydrochloric acid (HCl)	Nitric acid (HNO_3)	Distilled water (H_2O)
	2	3	5	190

Optical microscopy

Metallography was performed on all the samples using a DSX-510 optical microscope. The samples were studied from the edge to the centre, taking representative images to ascertain the homogeneity. The images were taken at 555x to 1109x.

3.5.2 Chemical composition

Chemical composition and microstructures were analysed using a JEOL 8230 electron probe microanalyser, with a combination of up to 5 wavelength dispersive X-ray spectrometers (WDS) and an energy dispersive X-ray spectrometer (EDS). Analyses were performed at 20 kV, 30 nA, and calibrated using pure metal reference standards. Oxygen was not measured.

3.5.3 Phase analysis

X-ray diffraction (XRD) was performed on the samples using a Bruker D8 Advance powder diffractometer with a Linxeye detector and Fe filtered Co-K alpha radiation. The method made use of the net intensity of the main peaks of the phases, and identification was based on the crystal structure of phases that occur in amounts of >3 mass %. The limitation with the XRD is

that the amorphous phases were not detected and the phases specified may not necessarily reflect the actual composition of phases identified.

3.5.4 Vickers hardness

Hardness measurements were performed using an Emcotest Duravision Vickers hardness machine. Five measurements were performed randomly on the surfaces of all the samples using the load of 10kg. These measurements were averaged.

3.6. Corrosion Testing

Corrosion testing was performed on all samples at 37±1°C in a phosphate buffered saline (PBS) solution at a pH of 7.4. Table 3-4 shows the chemical composition of the PBS solution.

Table 3-4. Chemical composition of the PBS solution.

Solution	**Chemicals (g/L)**			
PBS	Sodium chloride (NaCl)	Potassium chloride (KCl)	Sodium hydrogen phosphate (Na_2HPO_4)	Potassium dihydrogen phosphate (KH_2PO_4)
	8.0	0.2	1.44	0.24

3.6.1 Electrochemical Testing

Potentiodynamic polarisation

Potentiodynamic tests were undertaken according to the ASTM Standard (ASTMG5, 2013). A PC-driven ACM Instruments AutoTafel potentiostat was used to perform the electrochemical tests. Two graphite rods acted as counter-electrodes and a Haber-Luggin capillary made the junction with a saturated calomel reference electrode (SCE) as shown in Figure 3-5. All potential values were measured with respect to the SCE. Nitrogen was bubbled continuously during testing to remove all the oxygen and maintain an anaerobic condition.

After each sample was immersed in the solution, the open circuit potential against (OCP) time curve was recorded for up to 2 hours to determine the OCP. When the potential had reached a sufficiently stable value at 2 hours, a cyclic polarisation scan was recorded from –250 mV to

1500 mV at a scanning speed of 10 mV/min. The scan direction was not reversed. The corrosion rates were then calculated using Equation 3-1.

$$CR = I_{corr} K EW / D A \qquad \text{Equation 3-1}$$

where: CR = The corrosion rates

I_{corr} = The corrosion current in amperes

K = A constant that defines the units for the corrosion rate

EW = The equivalent weight in grams/equivalent

D = Density in grams/cm³

A = Area of the sample in cm².

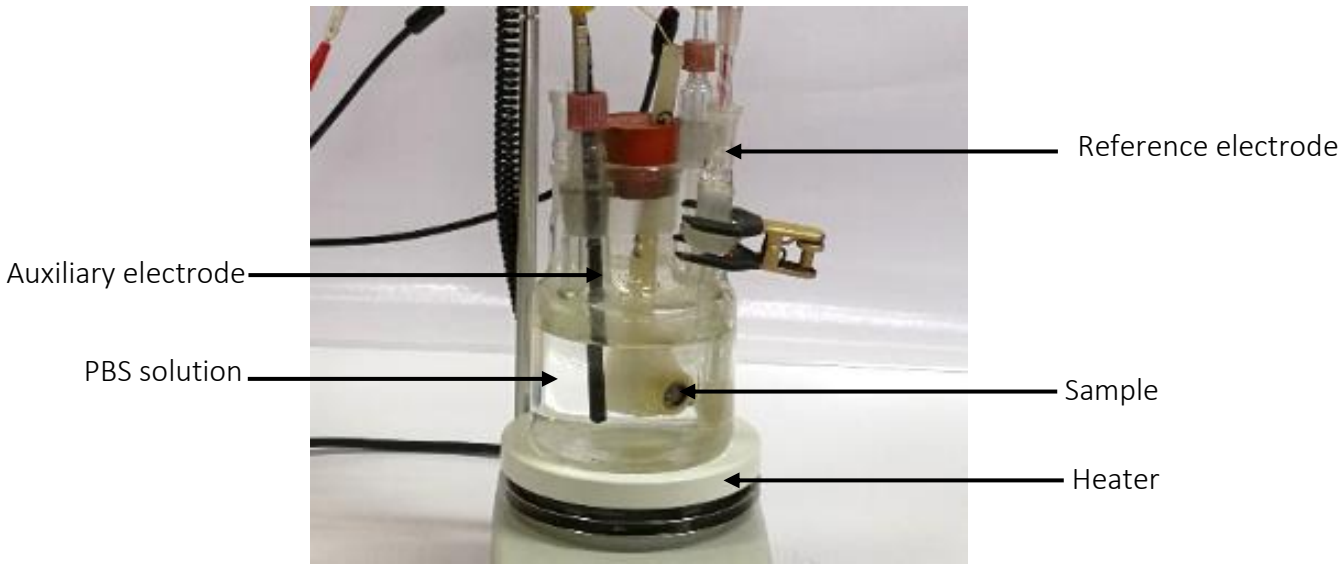


Figure 3-5. Photograph of the corrosion cell test set-up.

3.6.2 Immersion Testing

The immersion test was performed according to NACE Standard (ASTM NACE TM0169/G31—12a, 2012**)**. All the samples were exposed fully immersed in separate beakers to prevent contamination. The tests were performed for 30 days while maintaining the temperature at 37°C with the aid of a water bath as shown in Figure 3-6. The corrosion rates were calculated according to Equation 3-2.

Weight gain (g/cm^2) = $\Delta W/A$ Equation 3-2

where:

ΔW = Initial weight – after weight

A = sample area exposed to solution (cm^2).

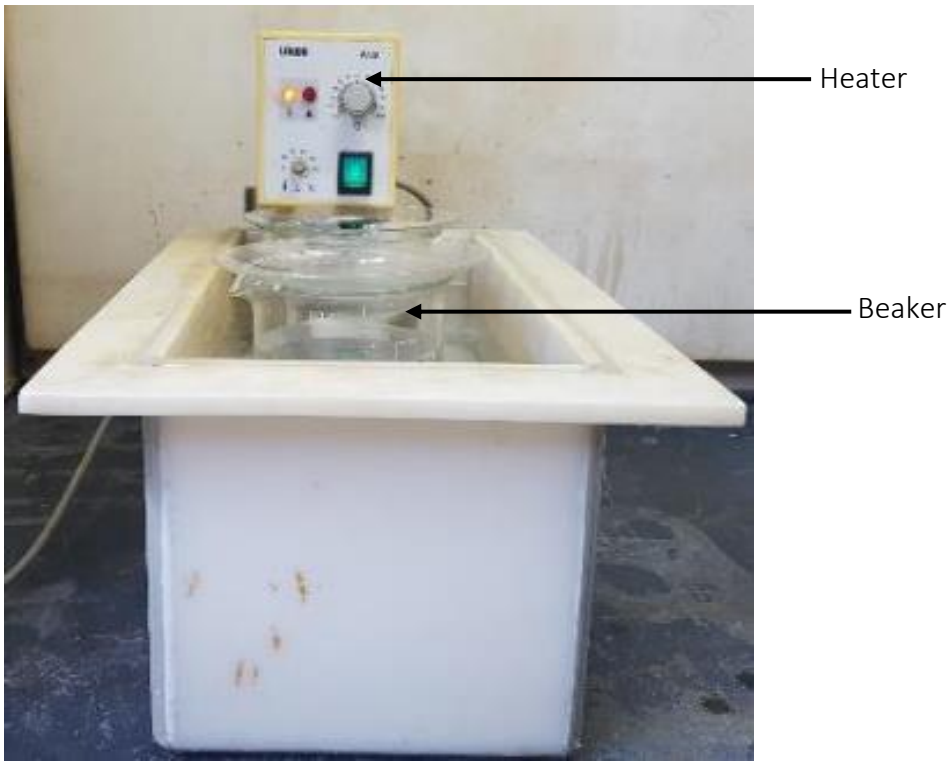


Figure 3-6. Photograph of the corrosion immersion test set-up.

3.7. Bacteria Testing

The bacteria tests were performed at Uppsala University, Sweden. They were performed on CP Ti, Ti-5Cu, Ti-15Cu and Ti-25Cu alloys. The other alloys were too brittle, and cracked during sample preparation. All the glassware was sterilised at 121°C for 15 min in the autoclave. The bacteria used was *Staphylococcus epidermidis* (XEN43), a genetically modified *S. epidermidis* 1457 strain with bioluminescent properties induced by introduction of the luxABCDE genes within the bacterial genome (Fowler, et al., 2019). The bacteria direct contact test used was developed by Weiss et al. (1996). The test was only run for 6 hours instead of 18 hours due to

time constraints. Ten micro-litres of bacterial agar were incubated with 10 ml of Tryptic Soy Broth (TSB, Fluke-Sigma 5 Aldrich) at 37°C for 12 hours. After incubation, the bacteria were centrifuged and tested in a UV spectrophotometer (Shimadzu – Model UV -1800) to ensure an optical density of 1.0 ca ($1x10^6$ bacteria) at a wavelength of 600 nm.

Three samples (diameter of 5 mm and thickness of 1 mm) of each Ti-Cu alloy were tested. Each sample was placed at the bottom of the well of a white opaque flat-bottomed 96-well plate (VWR North America, Pennsylvania, USA) and 10 µL of the prepared solution was seeded on the sample surface, followed by evaporation at 37°C for 30 min (ensuring contact of bacteria to the surface). Thereafter, 170 mL of Tryptic soy broth (TSB) was carefully added to each well. The luminescence of the bacteria was recorded hourly for 6 hours to study the bacterial growth over time on a Hidex Plate CHAMELEON V (425-106 Multilabel counter, Turku, Finland) with Mikrowin software (version 4.34, Mikrotek Laborsysteme GmbH). The relative luminescence from the bacteria was used to calculate the antibacterial rate (R) of the alloys, according to Equation 3-3.

$$\mathbf{R} = (N_{control} - N_{sample} / N_{control}) \times 100 \qquad \text{Equation 3-3}$$

where:

$N_{control}$ = relative luminescence of the CP-Ti sample,

N_{sample} = relative luminescence of the Ti-Cu alloys.

Chapter 4: RESULTS

4.1 Modelling

4.1.1 Thermo-Calc™

Before melting the samples, Thermo-Calc™ software was used to draw the phase diagram to show the expected phases. Figure 4-1 shows the phase diagram and Table 4-1 shows the reactions at different temperatures. The phase diagram showed incongruent formation of Ti_2Cu by a peritectic reaction. No Ti_3Cu phase was present.

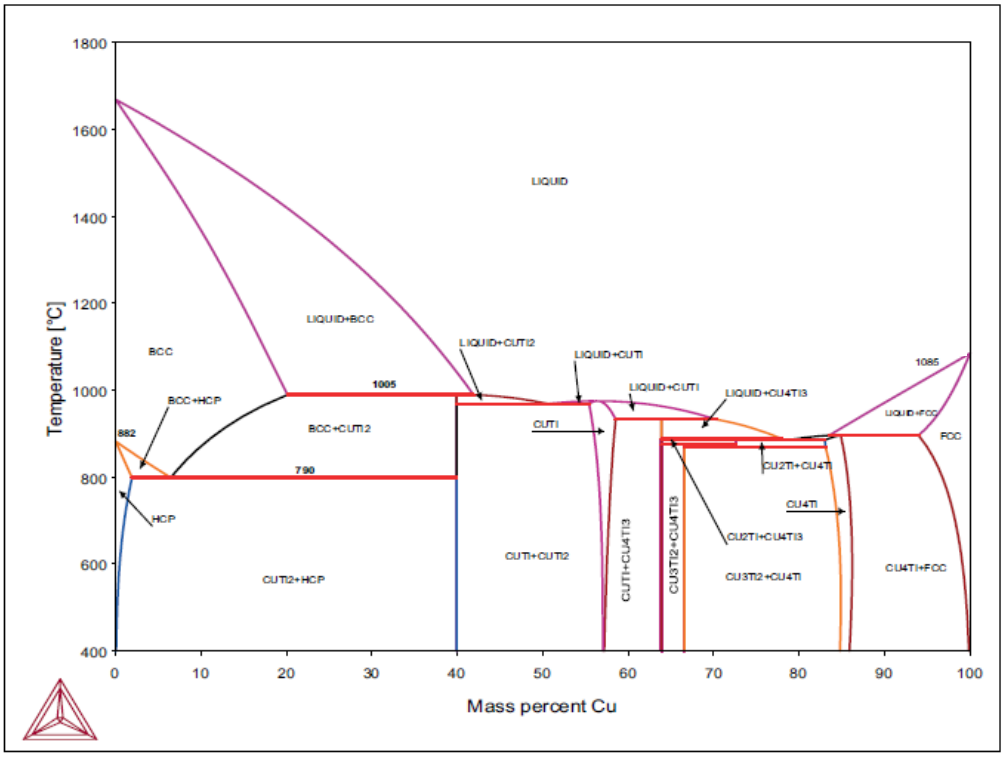


Figure 4-1. Cu-Ti phase diagram drawn using Thermo-Calc with the TTTI3 database.

Table 4-1. Phase transformations in Ti-Cu system drawn with Thermo-Calc and TTTI3 database.

Transformation	Compositions (wt% Cu)			Temperature (°C)
(βTi) ⇌ (αTi)	0			882
L ⇌ (βTi)	0			1670
L + (βTi) ⇌ + Ti_2Cu	41.7	19.4	39.9	1005
(βTi) ⇌ (αTi) + Ti_2Cu	6.7	1.8	39.9	790
L ⇌ Ti_2Cu + TiCu	50	39.9	55.3	972

The amount phases (mol) at 750°C and 900°C were obtained from the Thermo-Calc software for different compositions Thermo-Calc predicted the equilibrium phases: liquid, BCC (βTi), HCP (αTi), Ti_2Cu and TiCu. For CP Ti Thermo-Calc™ predicted liquid, BCC (βTi) and HCP (αTi) phases, as shown in Figure 4-2. CP Ti comprised BCC (αTi) at 900°C and HCP (βTi) at 750°C, as shown in Table 4-2.

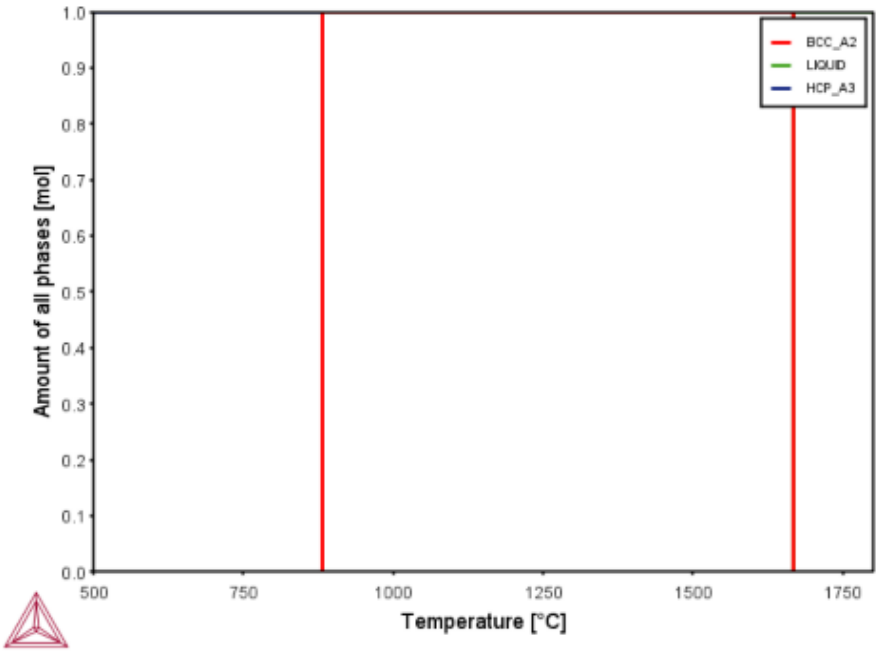


Figure 4-2. Phase proportions of CP Ti.

Table 4-2. Thermo-Calc™ results of CP Ti.

Alloy	Temperature (°C)	Phases (mol)	
		(αTi) HCP	(βTi) BCC
CP Ti	900	-	1.00
	750	1.00	-

Thermo-Calc™ predicted liquid, BCC (βTi), HCP (αTi) and Ti_2Cu phases for Ti-5Cu, as shown in Figure 4-3. Ti-5Cu comprised BCC (βTi) at 900°C and HCP (αTi) + Ti_2Cu at 750°C, as shown in Table 4-3.

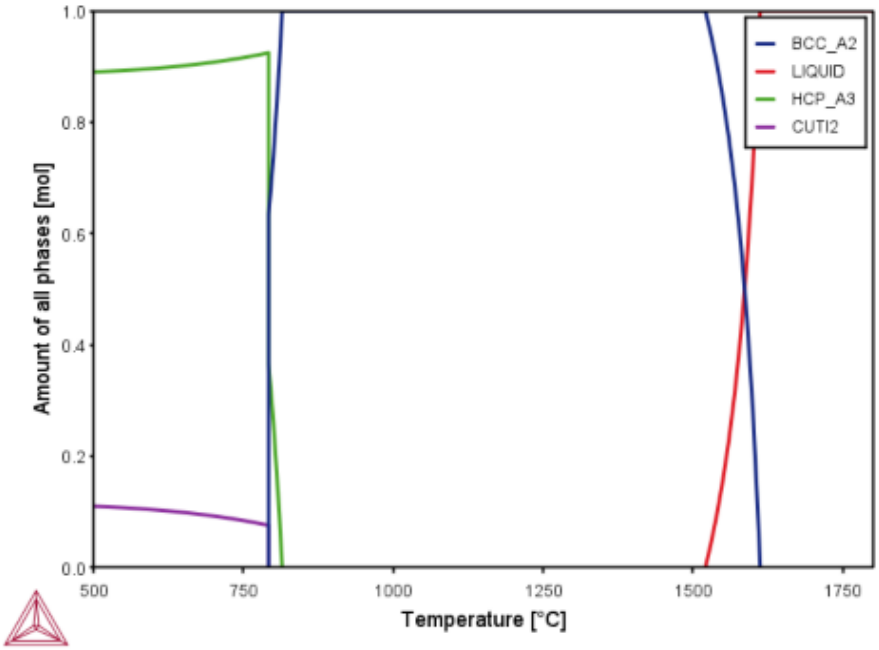


Figure 4-3. Phase proportions of Ti-5Cu.

Table 4-3. Thermo-Calc™ results of Ti-5Cu.

Alloy	Temperature (°C)	Phases (mol)		
		(αTi) HCP	(βTi) BCC	Ti_2Cu
Ti-5Cu	900	-	1.00	-
	750	0.92	-	0.08

Thermo-Calc™ predicted liquid, BCC (βTi), HCP (αTi) and intermetallic Ti_2Cu phases for Ti-15Cu similar to Ti-5Cu but the mole fractions of the phases were different, as shown in Figure 4-4. Ti-15Cu comprised BCC (βTi) + Ti_2Cu at 900°C and HCP (αTi) + Ti_2Cu at 750°C, as shown in Table 4-4.

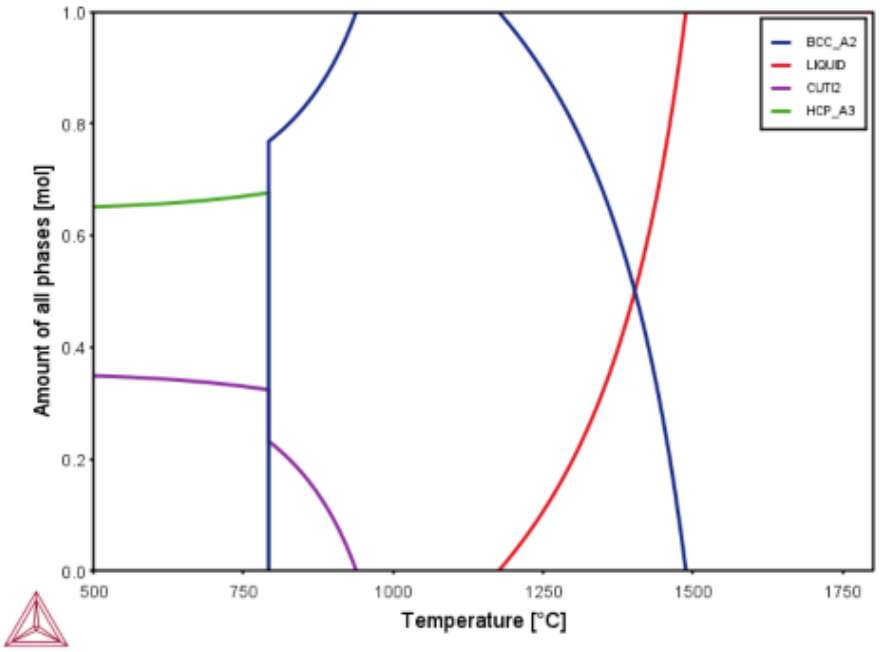


Figure 4-4. Phase proportions of Ti-15Cu.

Table 4-4. Thermo-Calc™ results of Ti-15Cu.

Alloy	Temperature (°C)	Phases (mol)		
		(αTi) HCP	(βTi) BCC	Ti_2Cu
Ti-15Cu	900	-	0.91	0.09
	750	0.67	-	0.33

Thermo-Calc™ predicted liquid, BCC (βTi), HCP (αTi) and intermetallic Ti_2Cu phases for Ti-25Cu, similar to Ti-5Cu and Ti-15Cu but the mole fractions of the phases were different, as shown in Figure 4-5. Ti-25Cu comprised BCC (βTi) + Ti_2Cu at 900°C and HCP (αTi) + Ti_2Cu at 750°C, as shown in Table 4-5.

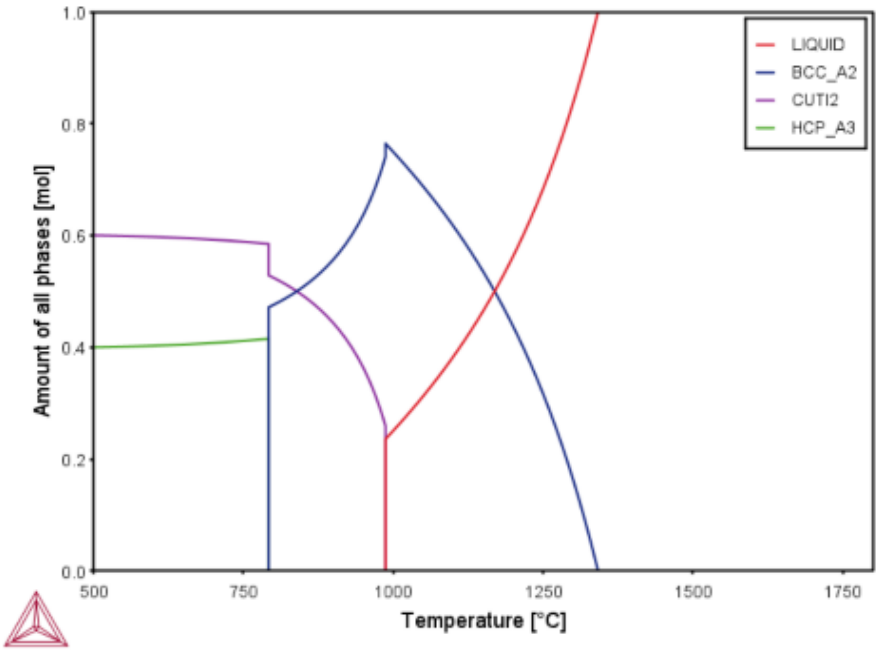


Figure 4-5. Phase proportions of Ti-25Cu.

Table 4-5. Thermo-Calc™ results of Ti-25Cu.

Alloy	Temperature (°C)	Phases (mol)		
		(αTi) HCP	(βTi) BCC	Ti_2Cu
Ti-25Cu	900	-	0.56	0.44
	750	0.42	-	0.58

Thermo-Calc™ predicted liquid, BCC (βTi), HCP (αTi) and intermetallic Ti_2Cu phases for Ti-33Cu, similar to Ti-5Cu, Ti-15Cu and Ti-25Cu, but the mole fractions of the phases were different, as shown in Figure 4-6. Ti-33Cu comprised BCC (βTi) + Ti_2Cu at 900°C and HCP (αTi) + Ti_2Cu at 750°C, as shown in Table 4-6.

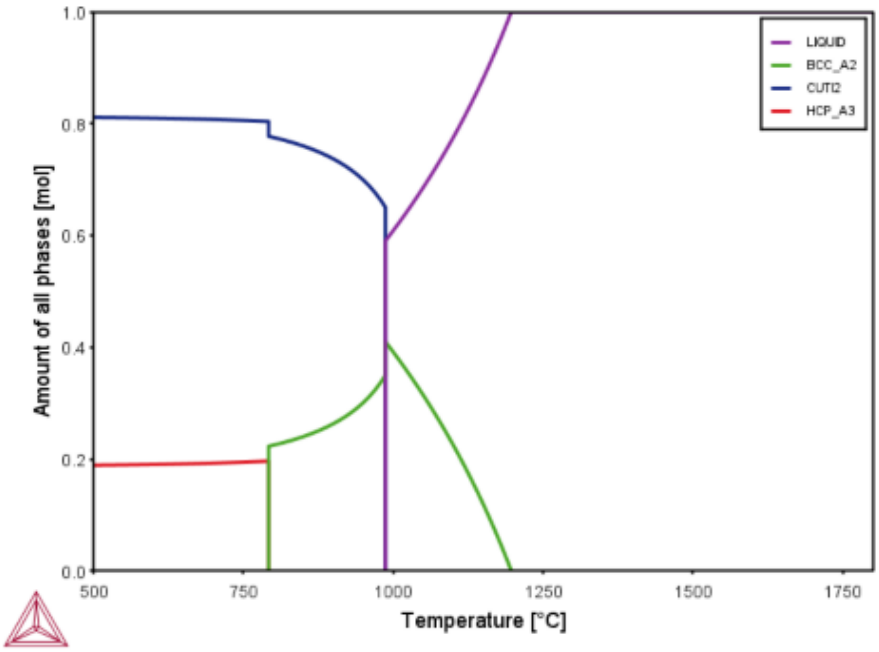


Figure 4-6. Phase proportions of Ti-33Cu.

Table 4-6. Thermo-Calc™ results of Ti-33Cu.

Alloy	Temperature (°C)	Phases (mol)		
		(αTi) HCP	(βTi) BCC	Ti_2Cu
Ti-33Cu	900	-	0.26	0.74
	750	0.19	-	0.81

Thermo-Calc™ predicted liquid, BCC (βTi), HCP (αTi) and intermetallic Ti_2Cu phases for Ti-40Cu, similar to Ti-5Cu, Ti-15Cu, Ti-25Cu and Ti-33Cu, but the mole fractions of the phases were different, as shown in Figure 4-7. Ti-40Cu comprised Ti_2Cu and TiCu at both 900°C and 750°C, as shown in Table 4-7.

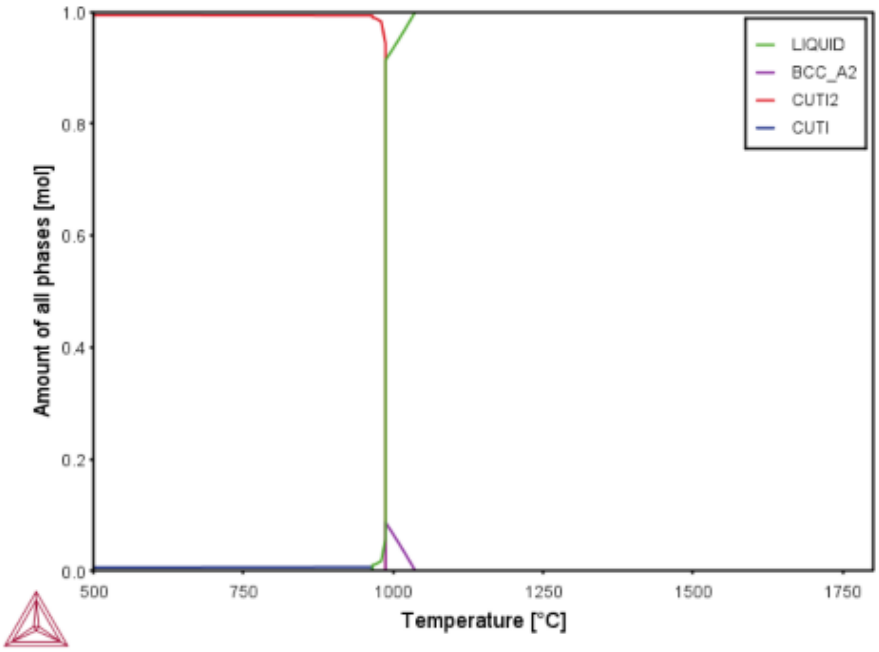


Figure 4-7. Phase proportions of Ti-40Cu.

Table 4-7. Thermo-Calc™ results of Ti-40Cu.

Alloy	Temperature (°C)	Phases (mol)	
		Ti_2Cu	TiCu
Ti-40Cu	900	0.99	0.01
	750	0.99	0.01

Thermo-Calc™ predicted liquid, Ti_2Cu and TiCu intermetallic phases for Ti-47Cu. Figure 4-8 shows the mole fractions of phases as a function of temperature. Ti-47Cu comprised Ti_2Cu and TiCu at both 900°C and 750°C, as shown in Table 4-8.

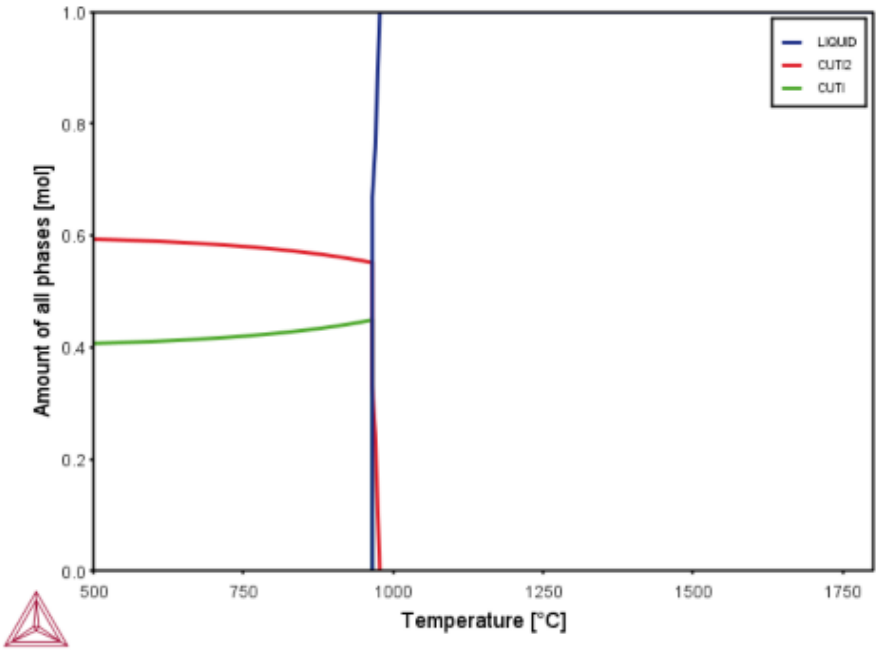


Figure 4-8. Phase proportions of Ti-47Cu.

Table 4-8. Thermo-Calc™ results of Ti-47Cu.

Alloy	Temperature (°C)	Phases (mol)	
		Ti_2Cu	TiCu
Ti-47Cu	900	0.56	0.44
	750	0.58	0.42

Thermo-Calc™ predicted liquid, Ti_2Cu and TiCu intermetallic phases for Ti-50Cu, similar to Ti-47Cu but the mole fractions of the phases were different. Figure 4-9 shows the mole fractions of phases as a function of temperature for Ti-50Cu. Ti-50Cu comprised Ti_2Cu and TiCu at both 900°C and 750°C, as shown in Table 4-9.

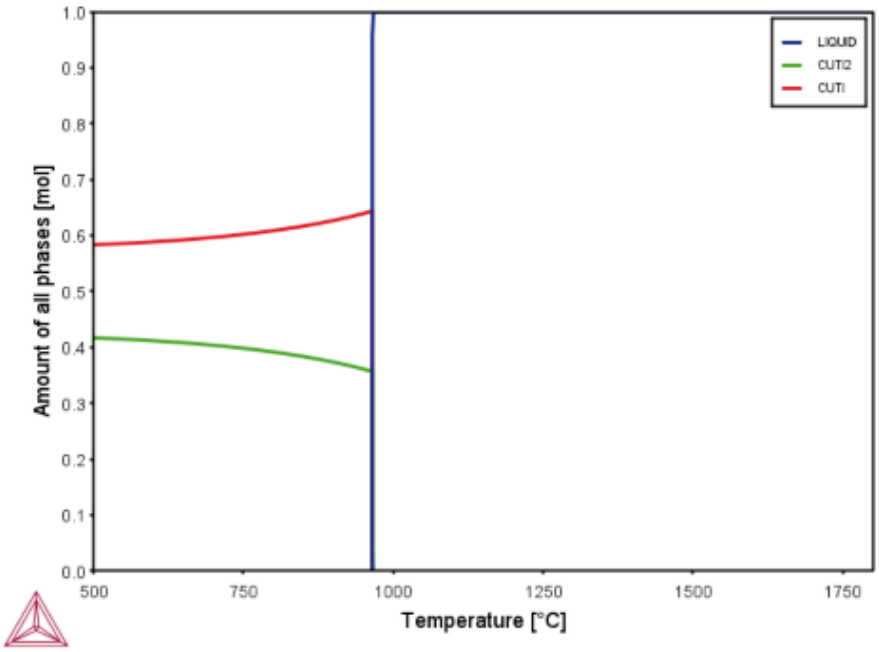


Figure 4-9. Phase proportions of Ti-50Cu.

Table 4-9. Thermo-Calc™ results of Ti-50Cu.

Alloy	Temperature (°C)	Phases (mol)	
		Ti_2Cu	TiCu
Ti-50Cu	900	0.38	0.62
	750	0.40	0.60

4.1.2 Material Studio

The CASTEP and XRD reflex module for powder diffraction was used to model the crystal structures and XRD patterns of the phases. The major peaks observed for alpha HCP αTi phase were at 2Θ = 41°, 45°, 46°, 77°, 83° and 85° with the third peak being the most intense. The alpha phase did not have a peak at 2Θ = 63° but around 2Θ = 60° , as shown in Figure 4-10. The beta BCC (βTi) phase had a major peak 2Θ = 45° and other peaks were at 2Θ = 62.5° and 77°, as shown in Figure 4-11. HCP (αTi) and BCC (βTi) phases had some similar peaks at 2Θ = 45° and 77° and BCC (βTi) had few peaks compared to HCP (αTi). Intermetallic tetragonal Ti_2Cu also had the first major peak at 2Θ = 45° and second one at 2Θ = 50°, as shown in Figure

4-12. The first minor peak of the intermetallic tetragonal Ti_3Cu phase was around 2Θ = 29°, while the most intense peaks were at 2Θ = 46° and 52.5°, as shown in Figure 4-13. The first minor peak of the intermetallic tetragonal TiCu phase was around 2Θ = 20°, while the most intense peaks were at 2Θ = 48° and 49°. The minor peak around 2Θ = 61.5°, as shown in Figure 4-14. Ti_2Cu and Ti_3Cu peaks were very different: Ti_2Cu had a first peak at 2Θ = 22.5° while Ti_3Cu had it at 2Θ = 29°. Ti_2Cu had the highest peak at 2Θ = 45.5° and other peaks at 2Θ = 49.5°, 55.5°, 69.0°, 75° and 83° while Ti_3Cu had at the highest peak at 2Θ = 46° and the other peaks were at 52.5°, 68.0°, 77.0° and 87.0°.

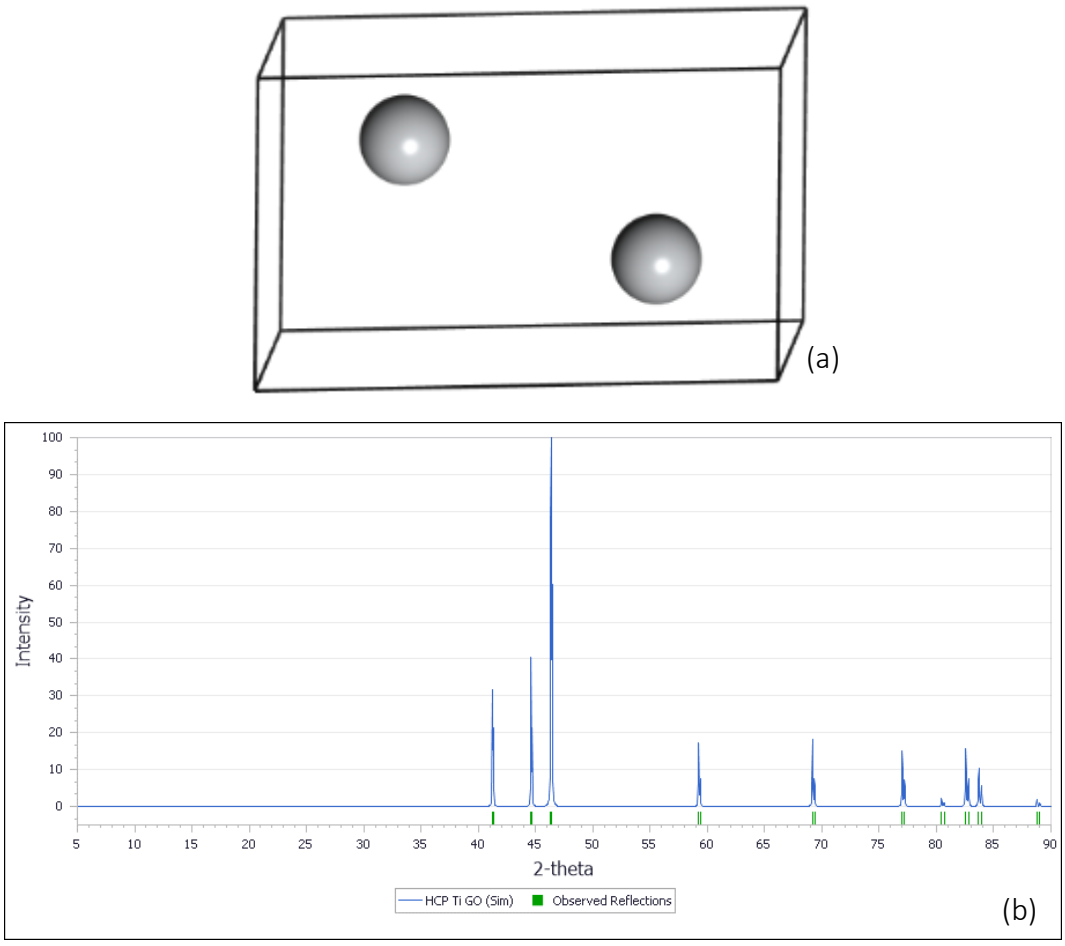


Figure 4-10. Modelled HCP (αTi) phase: (a) crystal structure, and (b) XRD pattern.

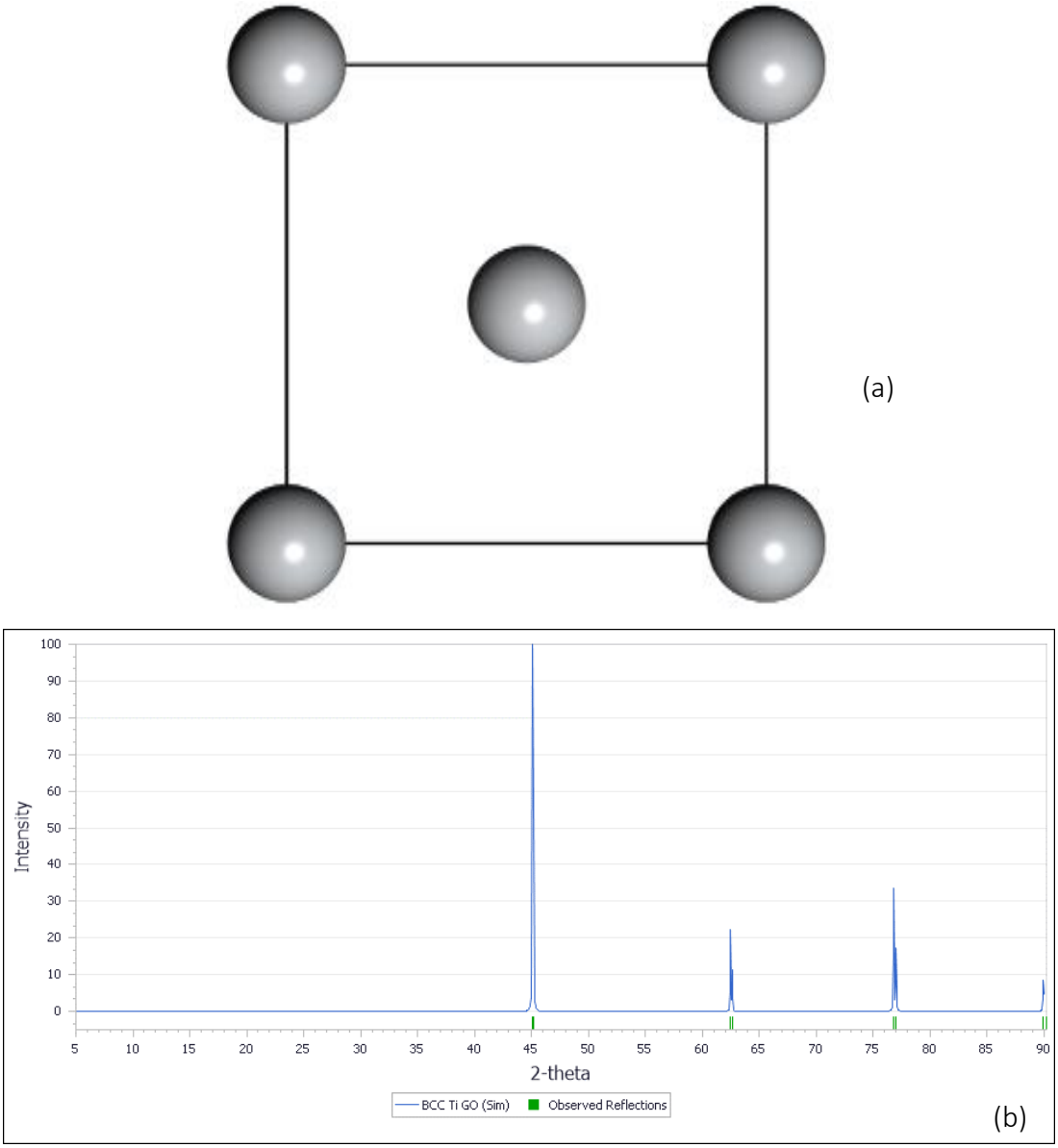


Figure 4-11. Modelled BCC (βTi) phase: (a) crystal structure, and (b) XRD pattern.

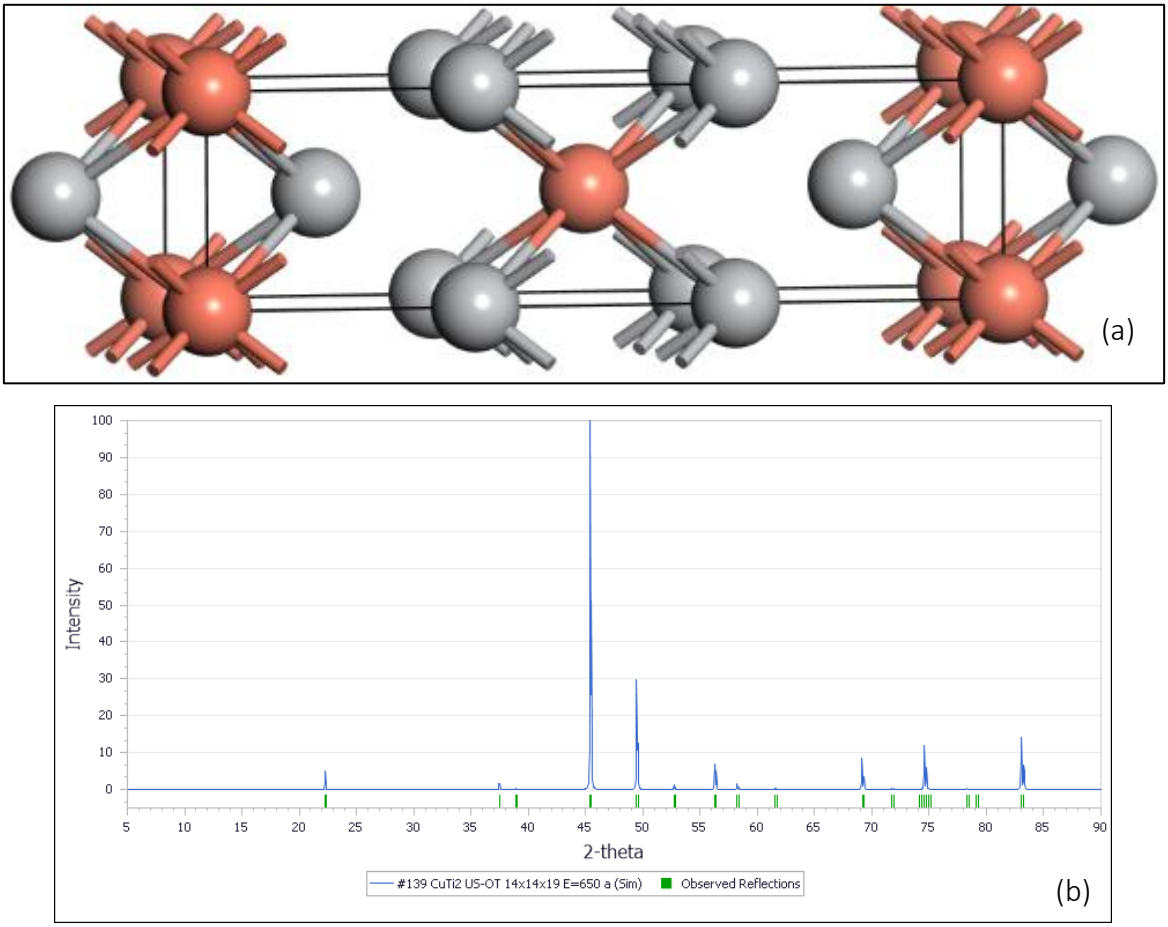
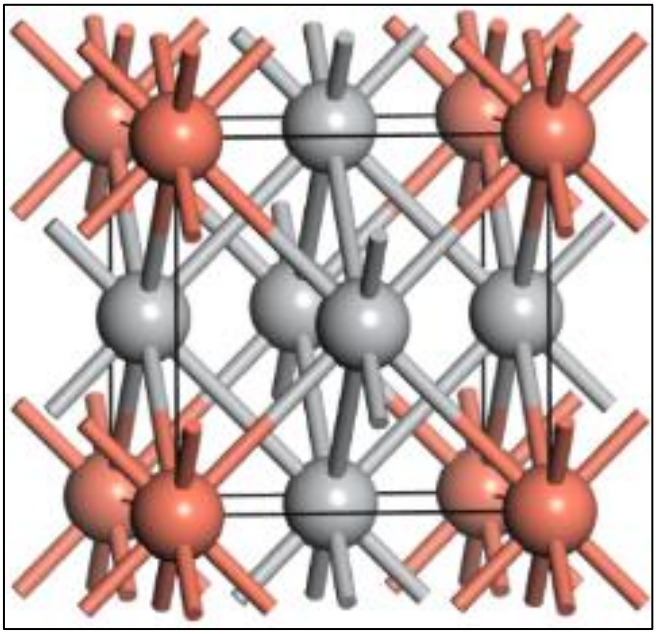
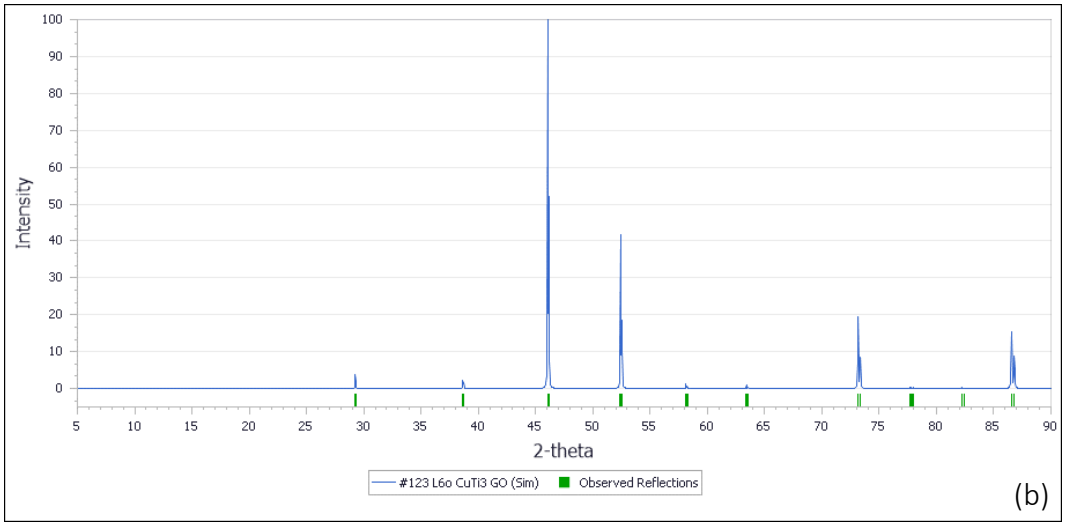


Figure 4-12. Modelled Ti_2Cu intermetallic tetragonal phase: (a) crystal structure, and (b) XRD pattern.



(a)



(b)

Figure 4-13. Modelled Ti_3Cu intermetallic tetragonal phase: (a) crystal structure, and (b) XRD pattern.

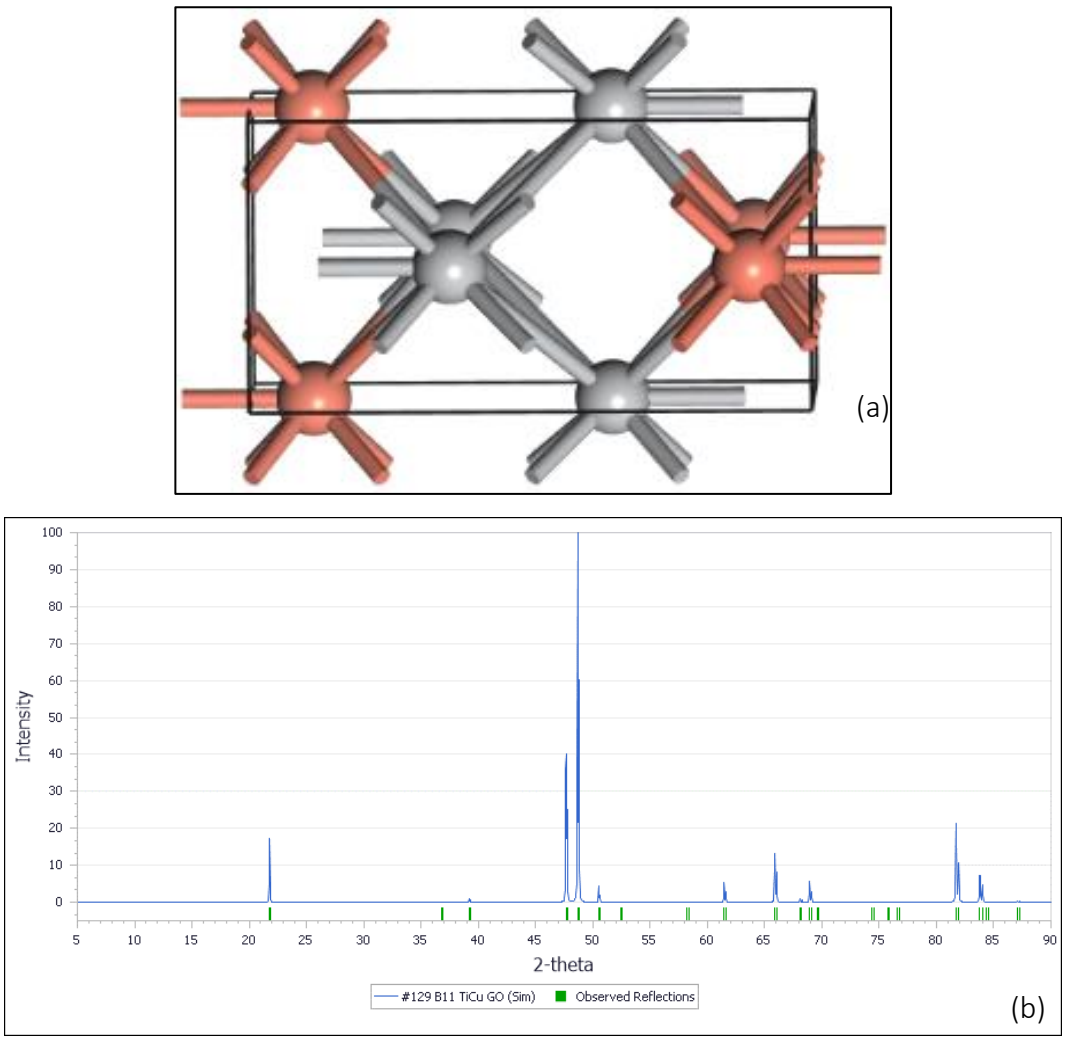


Figure 4-14. Modelled TiCu intermetallic tetragonal phase: (a) crystal structure, and (b) XRD pattern.

4.2 Material Characterisation

4.2.1 CP Ti

Microstructure and composition

Figure 4-15 to Figure 4-17 show OM and SEM-BSE images of CP Ti in the as-cast and annealed conditions. The microstructure was a typical Widmanstätten basket-weave structure of (αTi) which had grown inside the prior β grains. The annealed samples also showed a Widmanstätten structure. The average composition results are given in Table 4-10, showing that the CP Ti was 100% titanium.

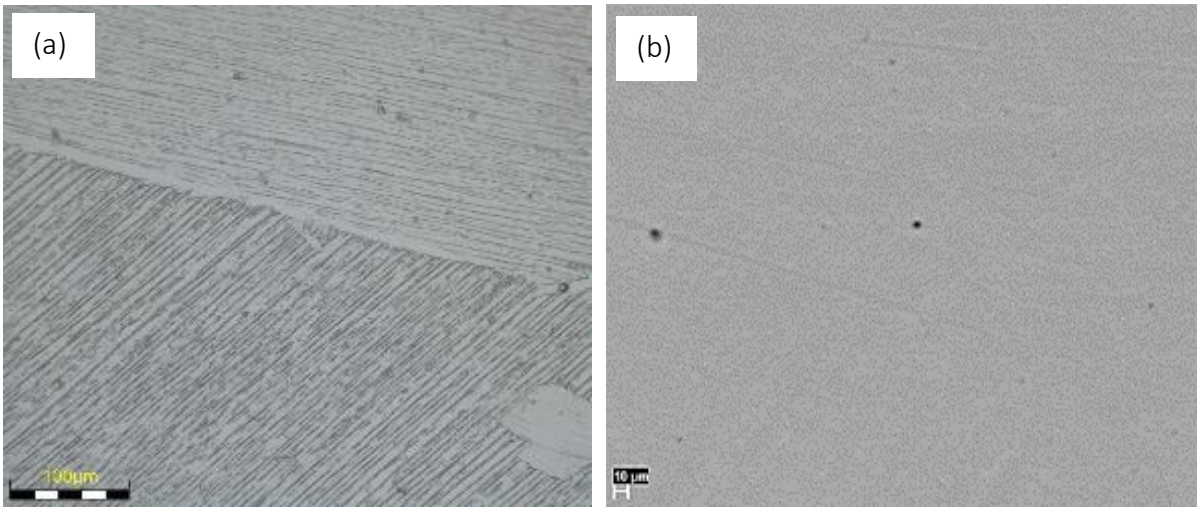


Figure 4-15. Microstructures of as-cast CP Ti: (a) OM image, (b) SEM-BSE image, showing a Widmanstätten basket-weave structure of (αTi) inside the grains.

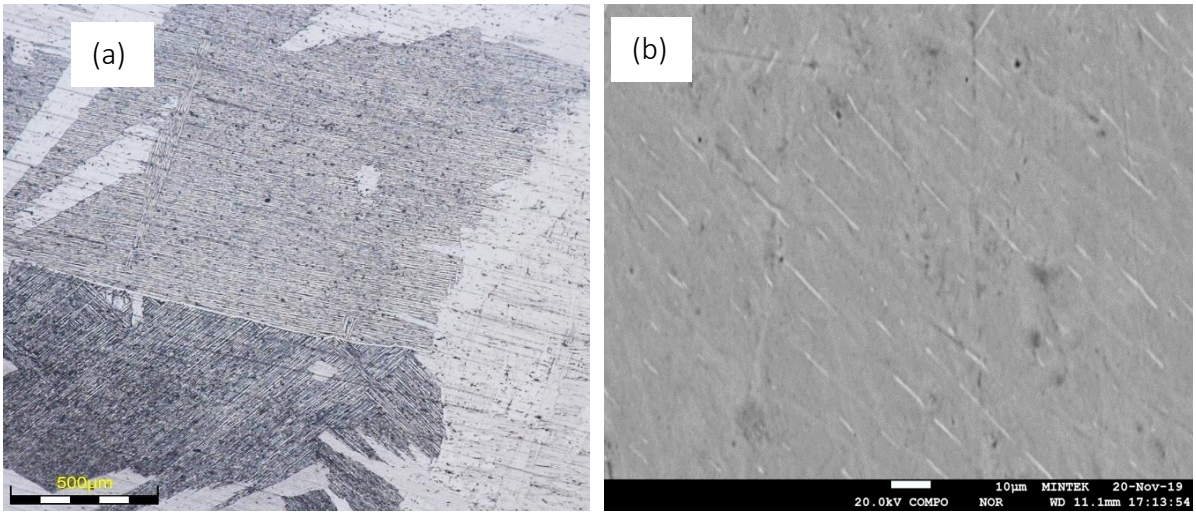


Figure 4-16. Microstructures of CP Ti heat treated at 750°C: (a) OM image, (b) SEM-BSE image, showing a Widmanstätten basket-weave structure of (αTi) inside the grains.

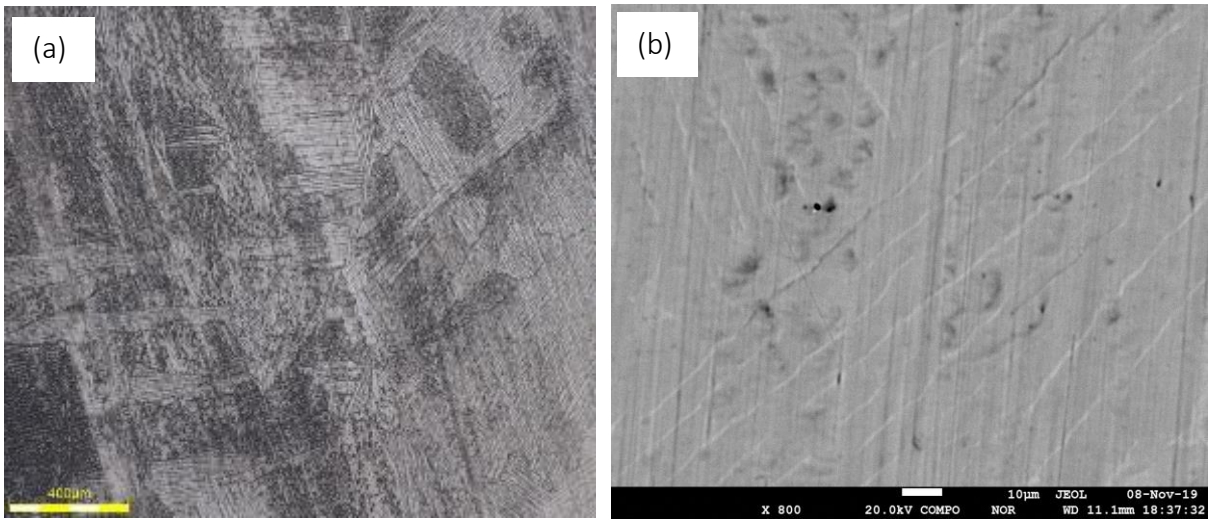


Figure 4-17. Microstructures of CP Ti heat treated at 900°C: (a) OM image, (b) SEM-BSE image, showing a Widmanstätten basket-weave structure of (αTi) inside the grains.

Table 4-10. EPMA results for CP Ti.

Alloy		**Area**	**Phases (wt %)**	
			Ti	**Cu**
CP Ti	**As-cast**	Overall	100	-
	750°C		100	-
	900°C		100	-

Phase analysis

Figure 4-18 to Figure 4-20 show the XRD patterns of as-cast and annealed CP Ti, indicating only single-phase (αTi). The (αTi) phase had peaks at 2Θ = 40.9°, 44.9°, 47.0°, 62.4° and 74.6° with the second peak being the most intense for the as-cast and the third peak being the most intense for the annealed samples. The results are shown in Table 4-11.

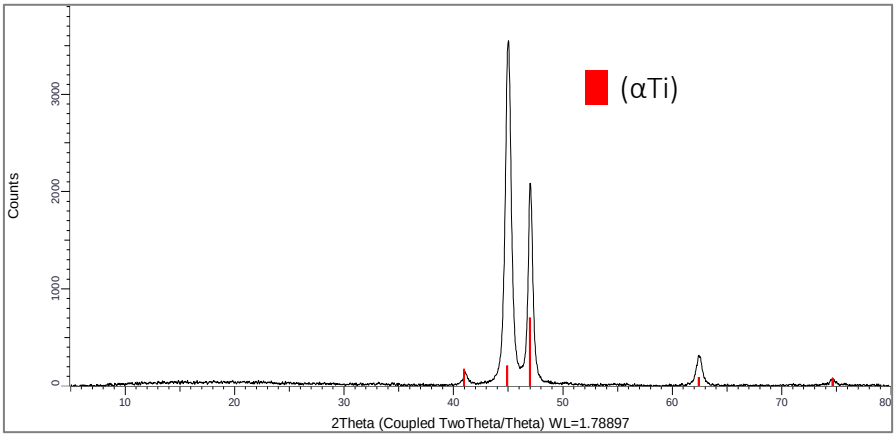


Figure 4-18. XRD pattern of as-cast CP Ti, showing (αTi) phase peaks.

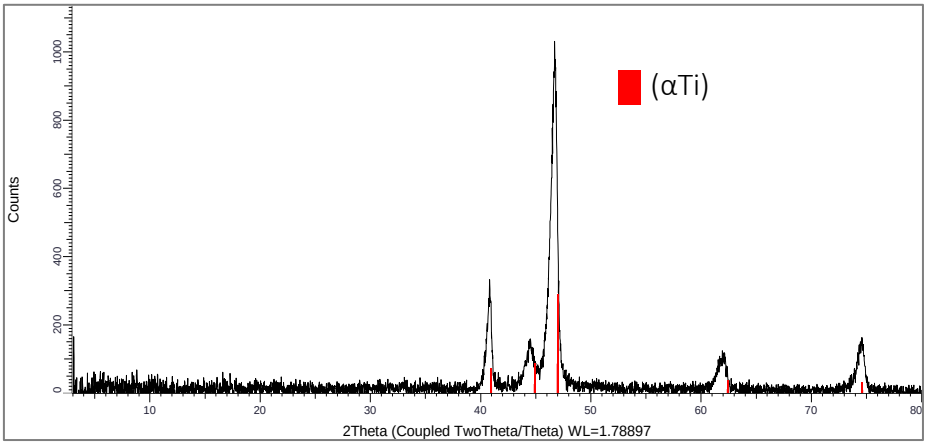


Figure 4-19. XRD pattern of CP Ti heat treated at 750°C, showing (αTi) phase peaks.

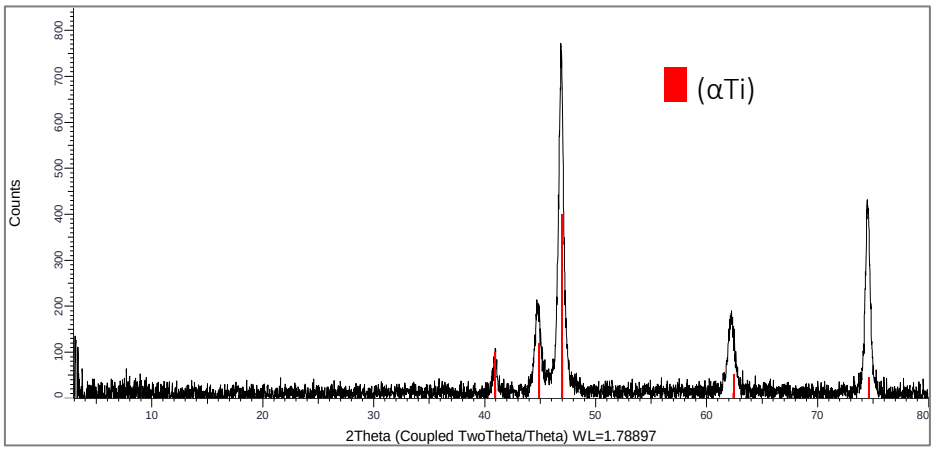


Figure 4-20. XRD pattern of CP Ti heat treated at 900°C, showing (αTi) phase peaks.

Table 4-11. XRD phase proportions of CP Ti.

Alloy		Phase proportions (wt %)	
CP Ti	**As-cast**	(αTi)	100±0.0
	750°C		
	900°C		

4.2.2 Ti-5Cu

Microstructure and composition

Figure 4-21 to Figure 4-23 show the OM and SEM-BSE images of as-cast and annealed Ti-5Cu. The as-cast and annealed at 750°C alloys comprised a dark (αTi) matrix and light Ti_2Cu precipitates, while the alloys annealed at 900°C had (αTi) surrounded by (αTi) + Ti_2Cu. The EDX analysis indicated that the dark phase was (αTi), and light phase was Ti_2Cu, with analyses that also include the surrounding (αTi) because the Ti_2Cu was so fine. Thus, the Ti_2Cu analyses has less Cu than they should have done. The average composition results are given in Table 4-12. The errors observed for the Ti-5Cu sample annealed at 750°C were due to the titanium oxide observed in Figure 4-22.

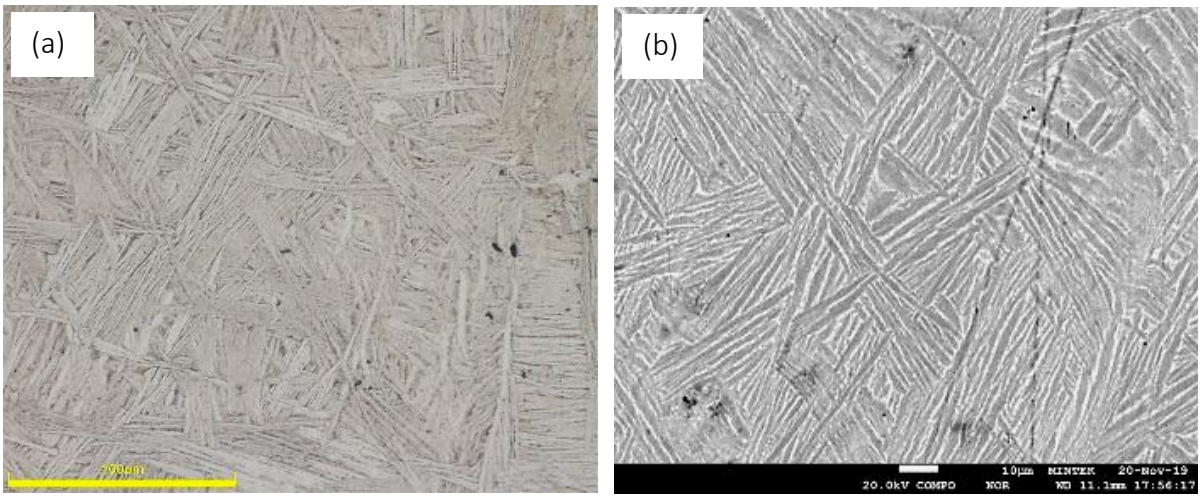


Figure 4-21**.** Microstructures of as-cast Ti-5Cu: (a) OM image, showing (αTi) (light contrast) and Ti_2Cu (dark contrast), (b) SEM-BSE image, showing (αTi) (dark contrast) and Ti_2Cu (light contrast).

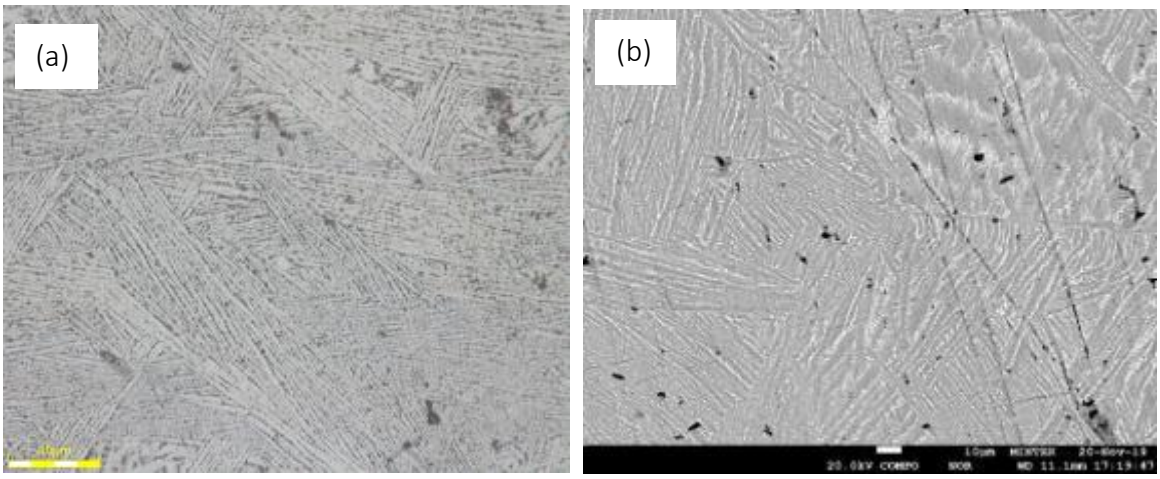


Figure 4-22**.** Microstructures of as-cast Ti-5Cu: (a) OM image, showing (αTi) (light contrast) and Ti_2Cu (dark contrast), (b) SEM-BSE image, showing (αTi) (dark contrast) and Ti_2Cu (light contrast).

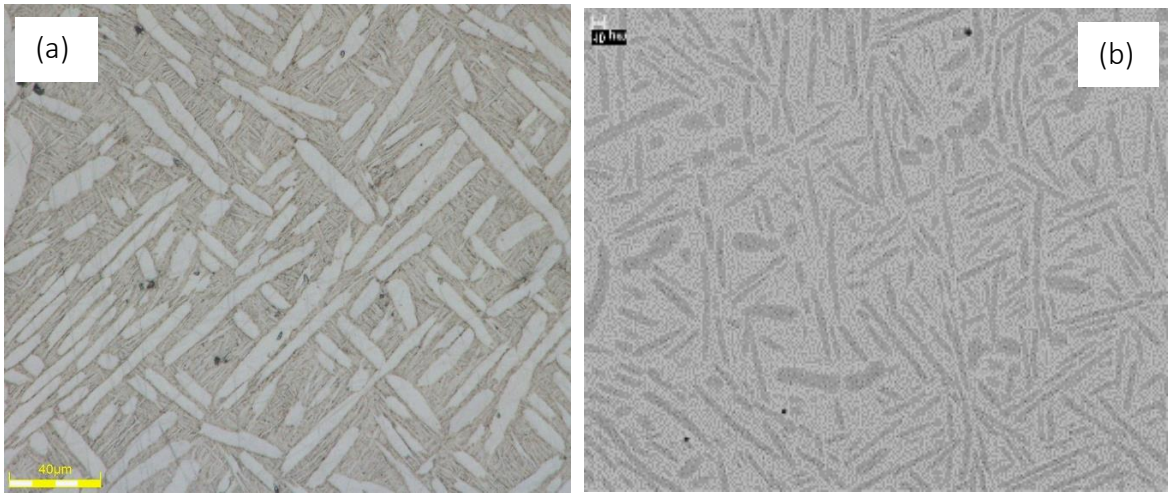


Figure 4-23**.** Microstructures of as-cast Ti-5Cu: (a) OM image, showing (αTi) (light contrast) and Ti_2Cu (dark contrast), (b) SEM-BSE image, showing (αTi) (dark contrast) and Ti_2Cu (light contrast).

Table 4-12. EPMA results for Ti-5Cu.

Alloy		Area	Phase	Composition (wt%)	
				Ti	Cu
Ti-5Cu	As-cast	Overall	-	65.4±0.9	4.6±0.9
		Dark contrast	(αTi)	97.7±0.7	2.3±0.5
		Light contrast	Ti_2Cu	93.8±0.9	6.2±0.9
	750°C	Overall	-	94.8±0.5	5.2±0.5
		Light contrast	Ti_2Cu	89.5±4.6	10.5±4.2
		Dark contrast	(αTi)	97.8±1.1	2.2±1.1
	900°C	Overall	-	95.3±0.8	4.7±1.0
		Dark contrast	(αTi)	97.3±0.6	2.7±0.9
		Light contrast	Ti_2Cu	93.2±0.6	6.8±2.1

Phase analysis

Figure 4-24 to Figure 4-26 show the XRD patterns of as-cast and annealed Ti-5Cu. XRD results showed two phases: (αTi) and Ti_2Cu. The (αTi) phase had peaks at 2Θ = 40.9°, 44.9°, 47.0°, 62.4° and 74.6° with the third peak being the most intense for all the samples. The Ti_2Cu phase had peaks at 2Θ = 19.0° (barely discernible in the background), 2Θ = 46.0°, 51.0°, 59.5° and 75.0°. The phase proportions derived from XRD are given in Table 4-13.

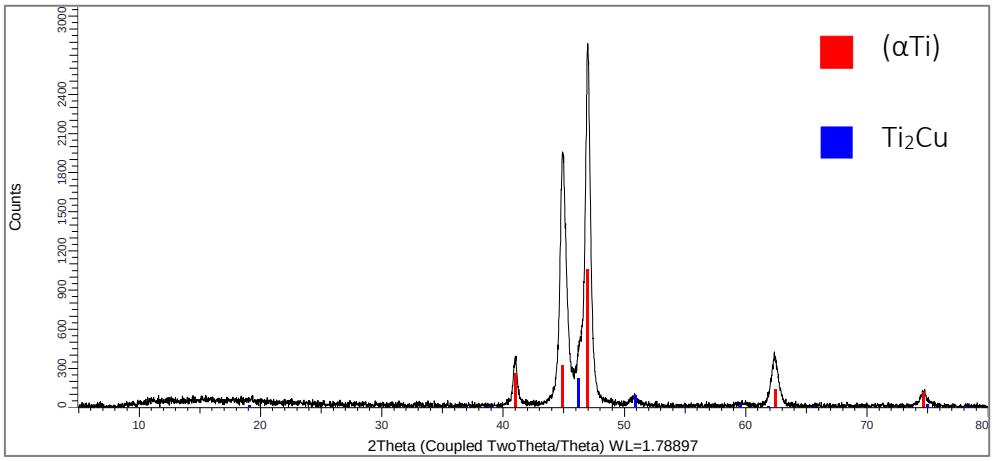


Figure 4-24. XRD pattern of as-cast Ti-5Cu, showing (αTi) and Ti_2Cu peaks.

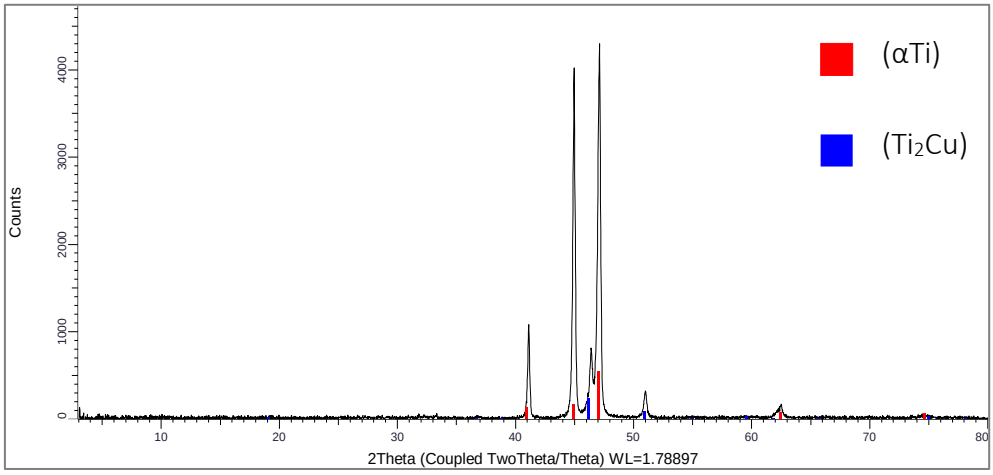


Figure 4-25. XRD pattern of Ti-5Cu heat treated at 750°C, showing (αTi) and Ti_2Cu peaks.

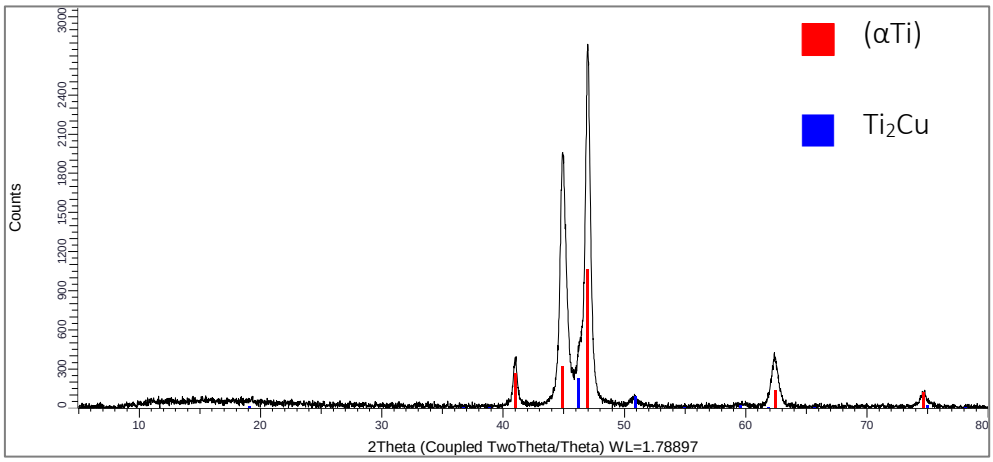


Figure 4-26. XRD pattern of Ti-5Cu heat treated at 900°C, showing (αTi) and Ti_2Cu peaks.

Table 4-13. XRD phase proportions of Ti-5Cu.

Alloy		**Phases proportions (wt %)**	
		(αTi)	**Ti_2Cu**
Ti-5Cu	**As-cast**	86	14
	750°C	84	16
	900°C	81	19

4.2.3 Ti-15Cu

Microstructure and composition

Figure 4-27 to Figure 4-29 show the OM and SEM-BSE images of as-cast and annealed Ti-15Cu. The alloys comprised (αTi) dendrites (dark contrast) and Ti_2Cu (light contrast). EDX analyses indicated that the dark contrast phase was (αTi), the light phase was Ti_2Cu and the darkest phase was Ti oxide. The Ti_2Cu precipitates became coarser with increased annealing temperature. The average EDX composition results are given in Table 4-14. The high errors for the overall of Ti-15Cu annealed at 750°C was due to the titanium oxide observed on Figure 4 29.

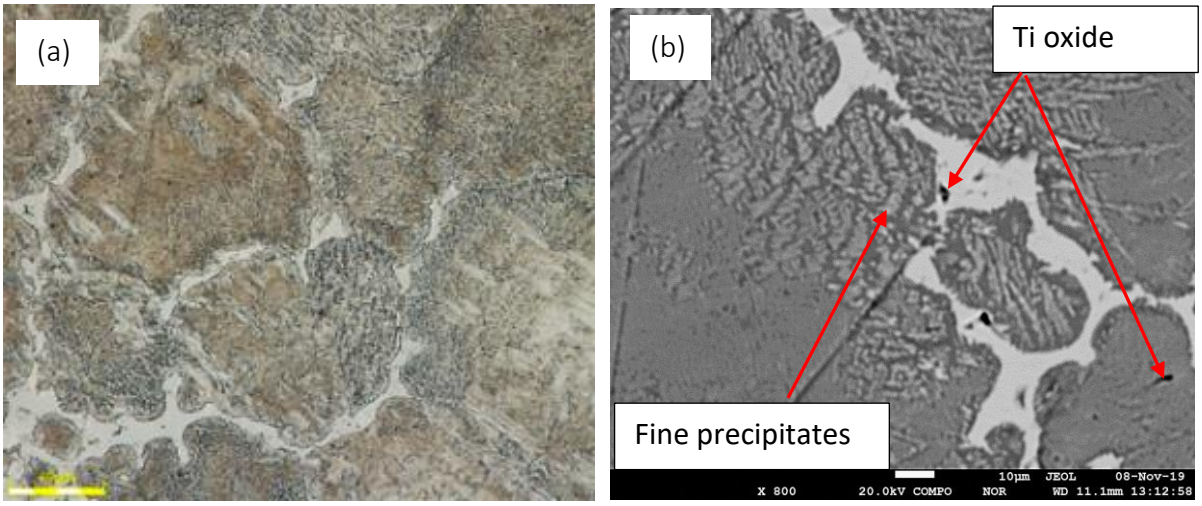


Figure 4-27. Microstructures of Ti-15Cu as-cast: (a) OM image, (b) SEM-BSE image, showing (αTi) (dark contrast) and Ti_2Cu (light), and Ti oxide (darker contrast).

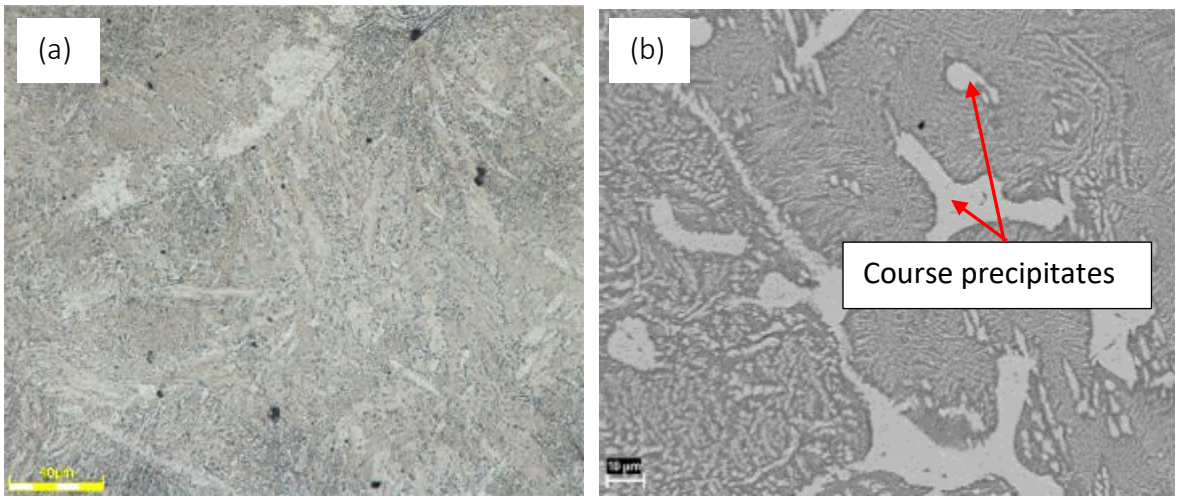


Figure 4-28. Microstructures of Ti-15Cu heat treated at 750°C: (a) OM image, (b) SEM-BSE image, (αTi) (dark contrast) and Ti_2Cu (light contrast).

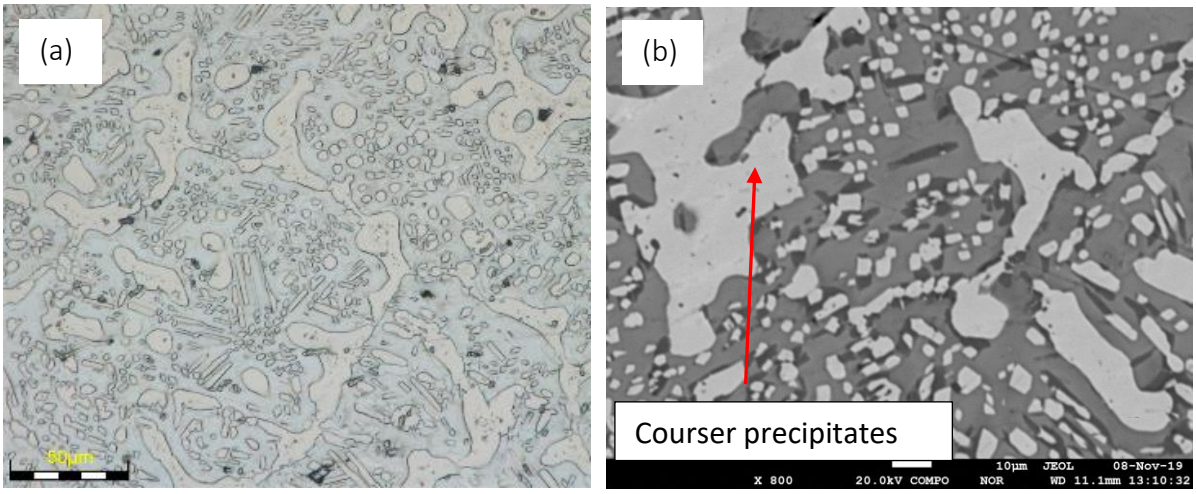


Figure 4-29. Microstructures of Ti-15Cu heat treated at 900°C: (a) OM image, (b) SEM-BSE image, (αTi) (dark contrast) and Ti_2Cu (light contrast) and Ti oxide (darker contrast).

Table 4-14. EPMA results for Ti-15Cu.

Alloy		Area	Phases	Composition (wt %)	
				Ti	Cu
Ti-15Cu	As-cast	Overall	-	85.3±1.1	14.7±1.0
		Dark contrast	(αTi)	87.1±1.6	12.9±2.0
		Light contrast	Ti_2Cu	63.1±1.4	36.9±1.1
		Darker contrast	Ti oxide	97.0±0.8	3.0±0.5
		Precipitates	-	83.8±0.7	16.2±0.6
	750°C	Overall	-	85.5±1.5	14.5±1.5
		Dark contrast	(αTi)	91.5±0.9	8.5±0.6
		Light contrast	Ti_2Cu	61.8±0.8	38.2±0.7
		Precipitates	-	65.8±1.0	34.2±1.1
	900°C	Overall	-	84.5±8.1	15.5±8.4
		Dark contrast	(αTi)	90.7±0.2	9.3±0.1
		Darker contrast	Ti oxide	98.0±0.4	2.0±0.3
		Light contrast	Ti_2Cu	61.5±0.2	38.5±0.4
		Coarse precipitates	-	64±0.1	36±0.1

Phase analysis

Figure 4-30 to Figure 4-32 show the XRDs patterns of as-cast and annealed Ti-15Cu, showing two phases: (αTi) and Ti_2Cu intermetallic phase. The (αTi) phase had peaks at 2Θ = 40.9°, 44.9°, 47.0°, 62.4° and 74.6° with the third peak being the most intense for all the alloys. The Ti_2Cu phase had peaks at 2Θ = 19.0°, 46.0°, 51.0°, 59.5° and 75.0°. The phase proportions are given in Table 4-15.

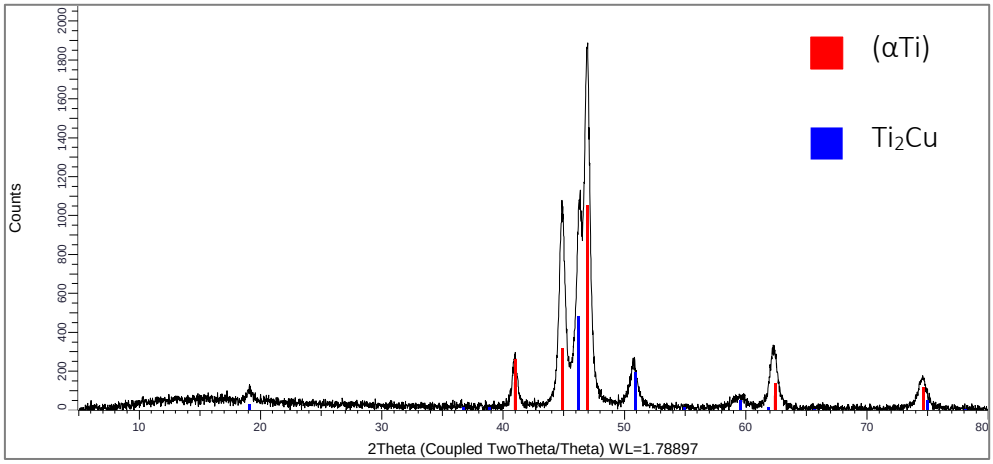


Figure 4-30. XRD pattern of as-cast Ti-15Cu, showing (αTi) and Ti_2Cu peaks.

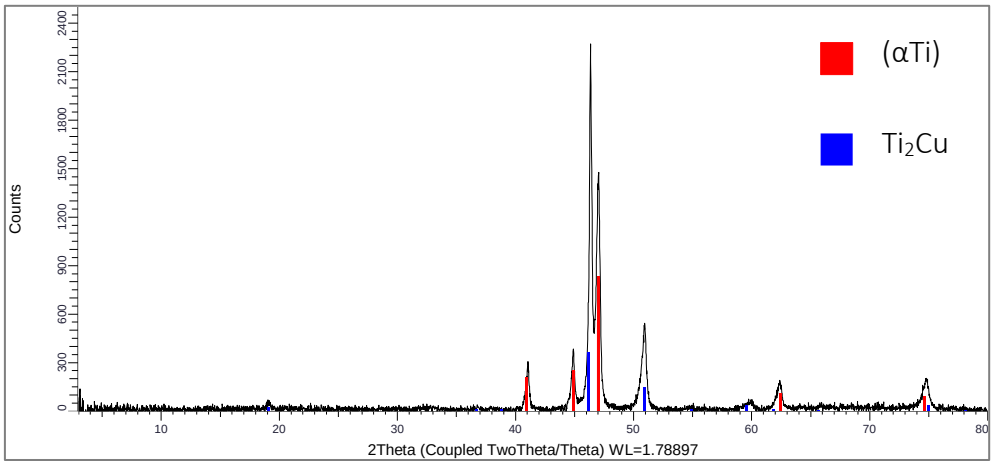


Figure 4-31. XRD pattern of Ti-15Cu heat treated at 750°C, showing (αTi) and Ti_2Cu peaks.

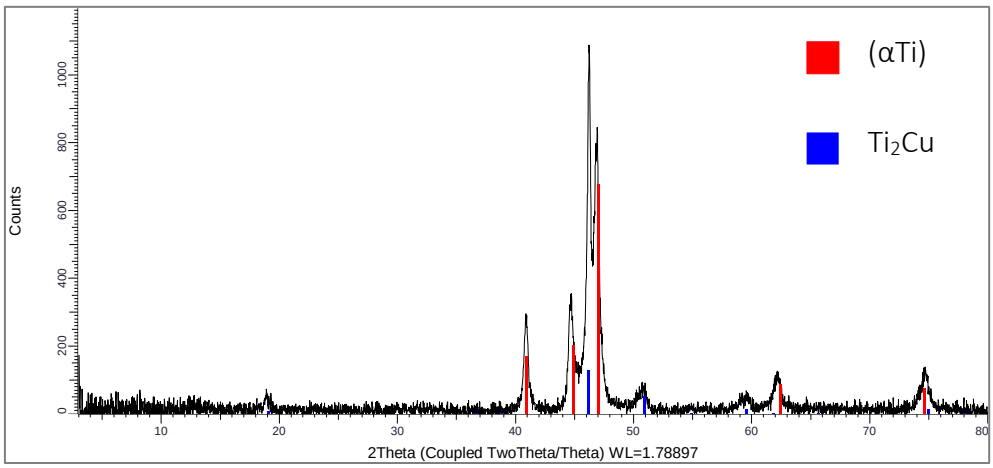


Figure 4-32. XRD pattern of Ti-15Cu heat treated at 900°C, showing (αTi) and Ti_2Cu peaks.

Table 4-15. XRD phase proportions of Ti-15Cu.

Alloy		Phase proportions (wt %)	
		(αTi)	Ti_2Cu
Ti-15Cu	As-cast	75	25
	750°C	75	25
	900°C	88	12

4.2.4 Ti-25Cu

Microstructure and composition

Figure 4-33 to Figure 4-35 show the OM and SEM-BSE images of as-cast and annealed Ti-25Cu. The alloys had originally comprised (βTi) dendrites which formed first, followed by the light regions (mixture of Ti_2Cu and (βTi)), which surrounded the dendrites and was a sparse eutectic. The (βTi) dendrites decomposed to (αTi) (dark contrast) and Ti_2Cu (light contrast). Some darker Ti oxides were observed in the dendrites. After annealing at 900°C, the light precipitates formed within the dendrites. The Ti_2Cu precipitates became coarser with increased annealing temperature. The average EDX composition results are given in Table 4-16.

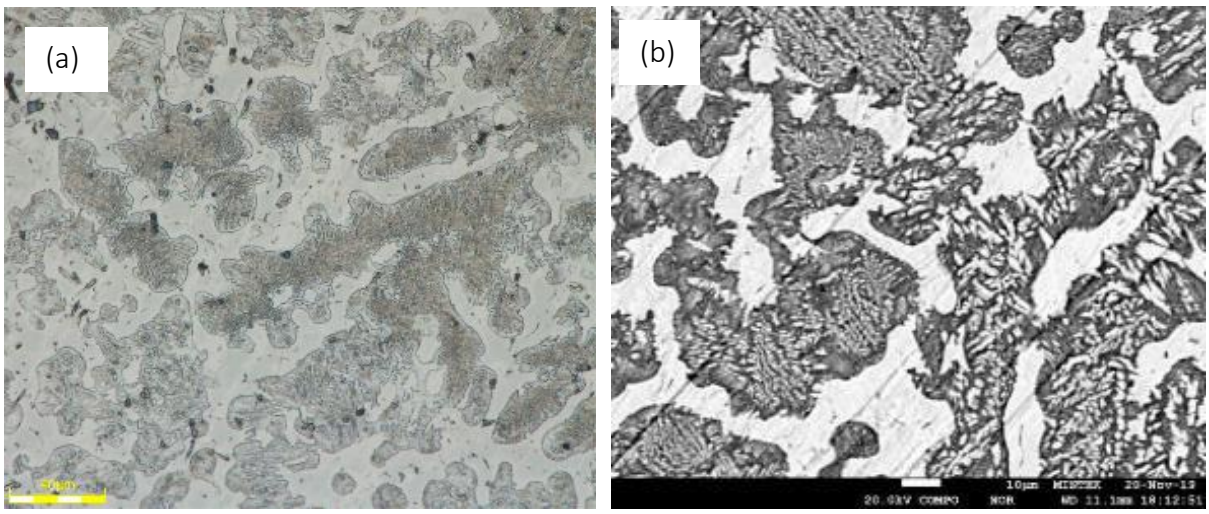


Figure 4-33**.** Microstructures of Ti-25Cu as-cast: (a) OM image, (b) SEM-BSE image, showing (αTi) (dark contrast) and Ti_2Cu (light) and Ti oxide (darker contrast).

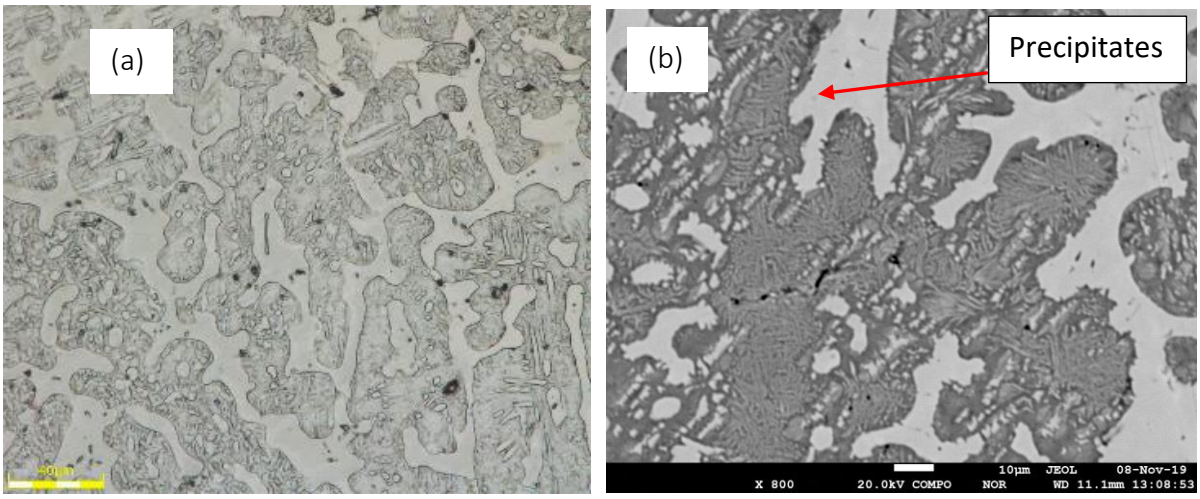


Figure 4-34**.** Microstructures of Ti-25Cu heat treated at 750°C: (a) OM image, (b) SEM-BSE image, showing (αTi) (dark contrast) and Ti_2Cu (light) and Ti oxide (darker contrast).

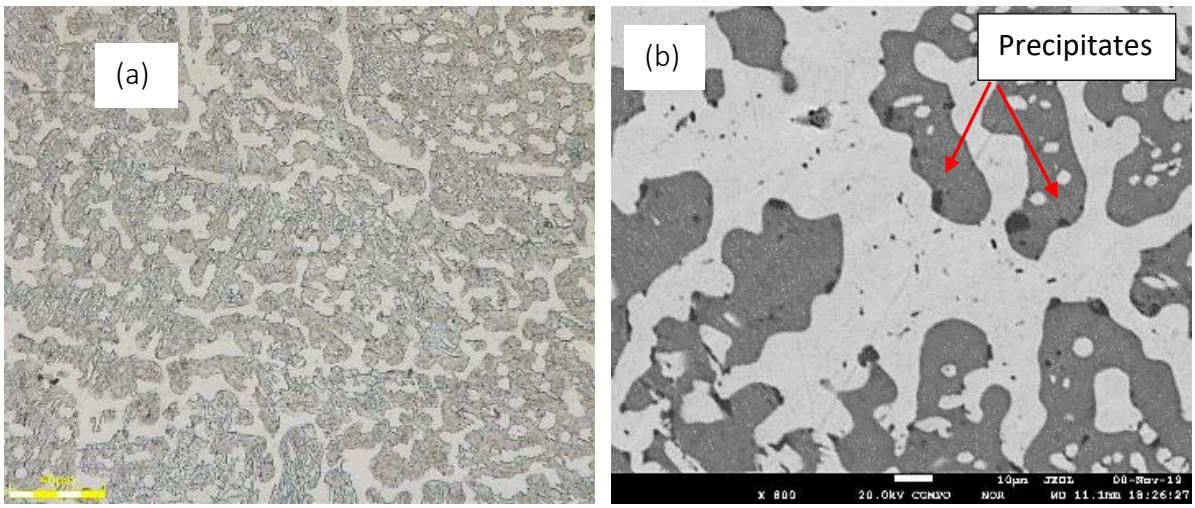


Figure 4-35**.** Microstructures of Ti-25Cu heat treated at 900°C: (a) OM image, (b) SEM-BSE image, showing (αTi) (dark contrast) and Ti_2Cu (light contrast) and Ti oxide (darker contrast).

Table 4-16. EPMA results for Ti-25Cu.

Alloy		Area	Phase	Composition (wt %)	
				Ti	Cu
Ti-25Cu	As-cast	Overall	-	73.8±2.0	26.2± 2.0
		Dark contrast	(αTi)	88.7±0.03	11.3±0.1
		Light contrast	Ti_2Cu	63.0±1.0	37.0±0.9
		Darker contrast	Ti oxide	96.0±0.8	4.0±0.1
	750°C	Overall	-	75.3±2.0	24.7± 1.8
		Dark contrast	(αTi)	84.8±3.3	15.2±3.2
		Light contrast	Ti_2Cu	61.1±1.7	38.9±0.6
		Precipitates	-	81.4±2.1	18.6±1.1
	900°C	Overall	-	75.1±3.0	24.9± 3.8
		Dark contrast	(αTi)	88.0±2.1	12.0±1.7
		Light contrast	Ti_2Cu	62.0±0.2	38.0±0.1
		Precipitates	-	81.9±2.1	18.1±1.5
		Darker contrast	Ti oxide	Too small to analyse	

Phase analysis

Figure 4-36 to Figure 4-38 shows the XRD patterns of as-cast and annealed of Ti-25Cu. The (αTi) phase had peaks at 2Θ = 40.9°, 44.9°, 47.0°, 62.4° and 74.6° with the third peak being the most intense for all the samples. The Ti_2Cu phase had peaks at 2Θ = 19.0°, 46.0°, 51.0°, 59.5° and 75.0°. The average phase proportions are given in Table 4-17.

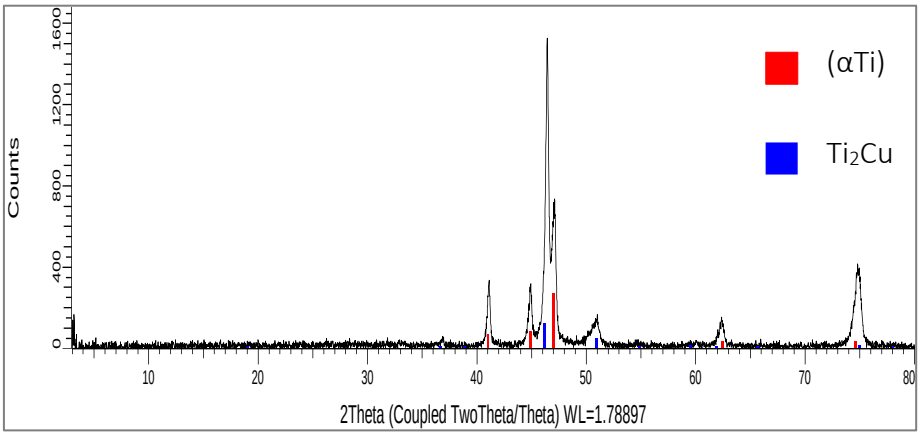


Figure 4-36**.** XRD pattern of Ti-25Cu as-cast, showing (αTi) and Ti_2Cu peaks.

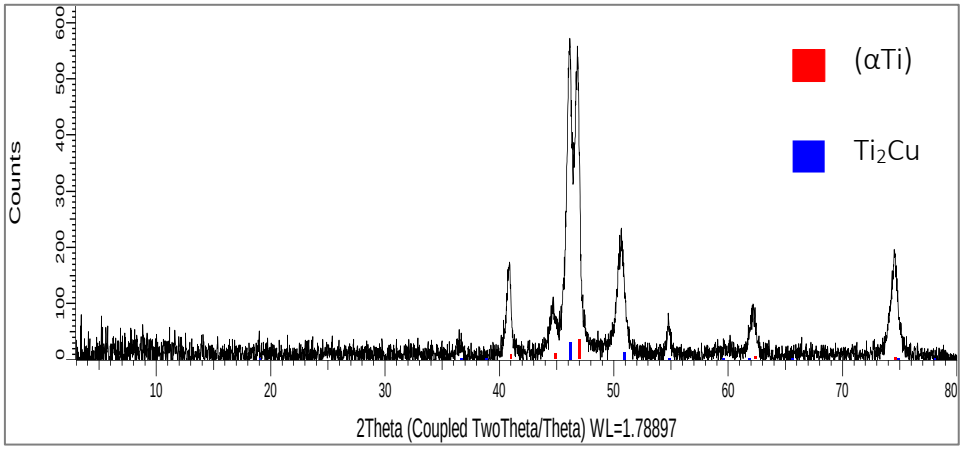


Figure 4-37. XRD pattern of Ti-25Cu heat treated at 750°C, showing (αTi) and Ti_2Cu peaks.

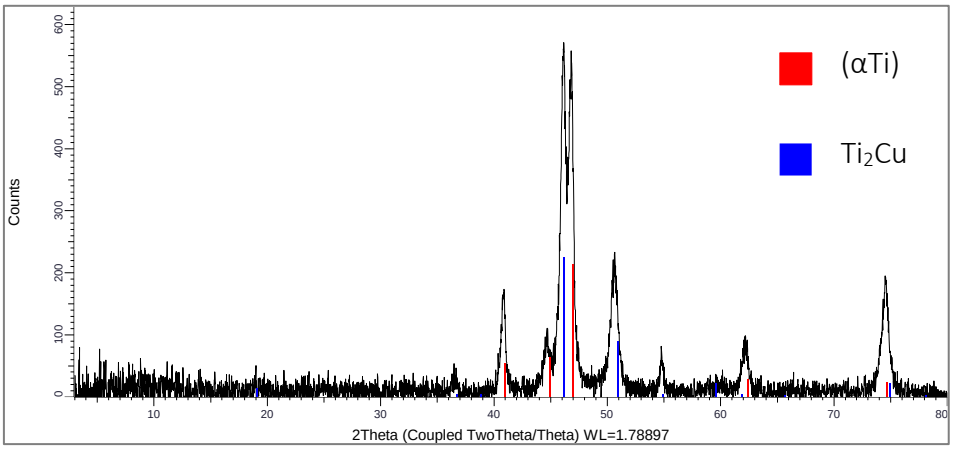


Figure 4-38. XRD pattern of Ti-25Cu heat treated at 900°C, showing (αTi) and Ti_2Cu peaks.

Table 4-17. XRD phase proportions of Ti-25Cu.

Alloy		**Phases (wt %)**	
		(αTi)	**Ti_2Cu**
Ti-25Cu	**As-cast**	58	35
	750°C	61	39
	900°C	56	44

4.2.5 Ti-33Cu

Microstructure and composition

Figure 4-39 to Figure 4-41 show the OM and SEM-BSE images of as-cast and annealed Ti-33Cu. The alloys comprised dark contrast (αTi) dendrites which had transformed from (βTi) surrounded by Ti_2Cu (light contrast). The dendrites were fewer and smaller with more Ti_2Cu (light contrast) than in lower Cu content samples. After annealing at 900°C, the dendrites were coarser and the darker Ti oxides were observed in the dendrites. The average composition results are given in Table 4-18.

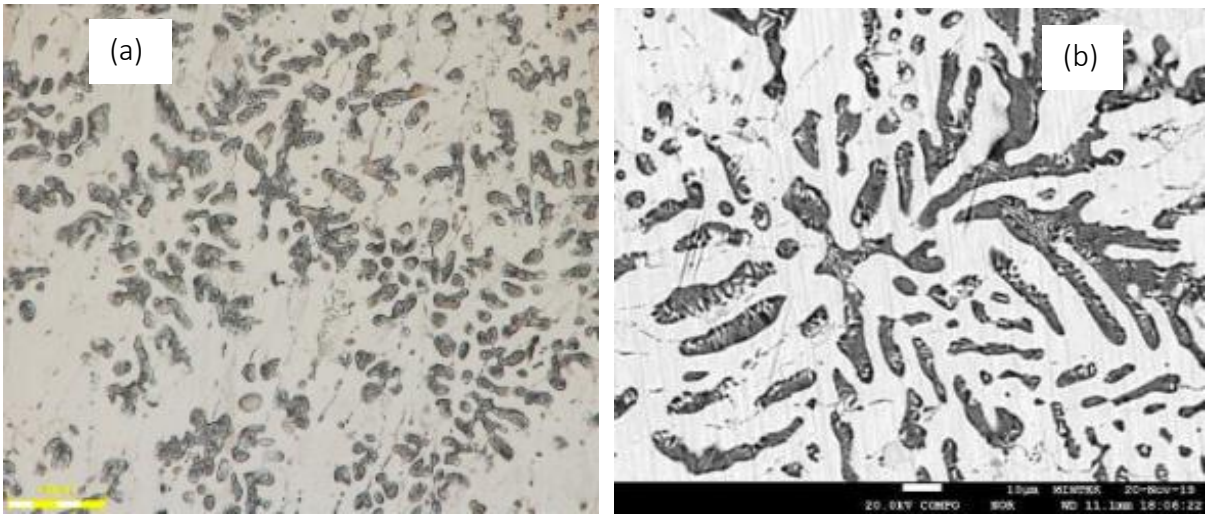


Figure 4-39**.** Microstructures of Ti-33Cu as-cast: (a) OM image, (b) SEM-BSE image, showing (αTi) (dark contrast) and Ti_2Cu (light contrast).

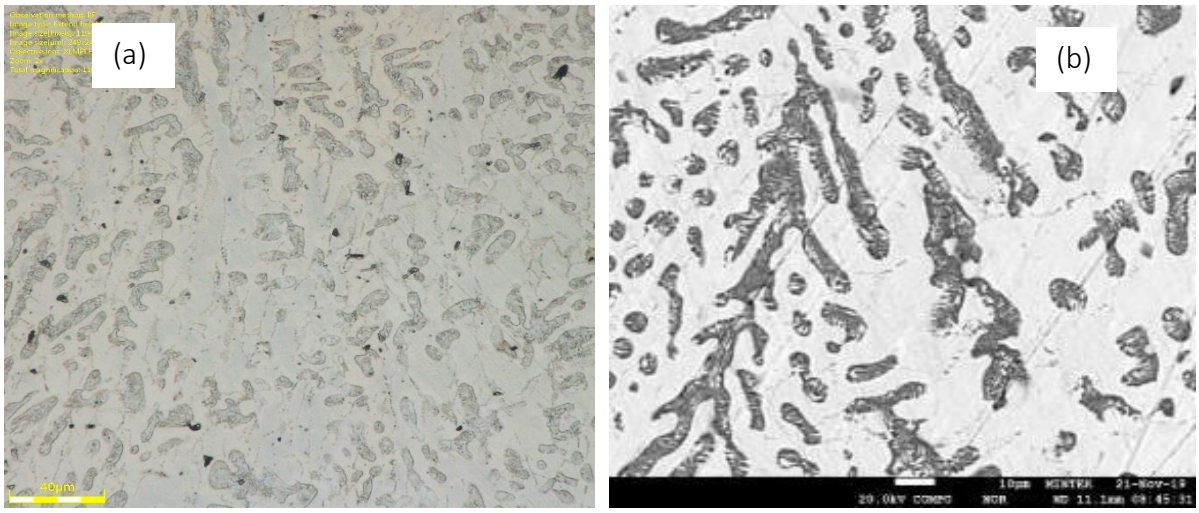


Figure 4-40**.** Microstructures of Ti-33Cu heat treated at 750°C: (a) OM image, (b) SEM-BSE image, showing (αTi) (dark contrast) and Ti_2Cu (light contrast).

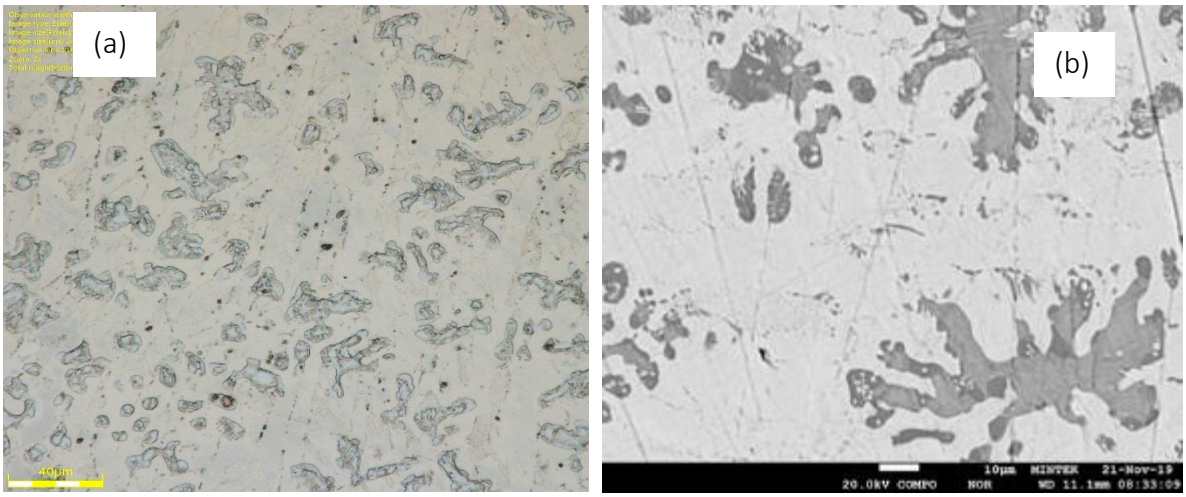


Figure 4-41**.** Microstructures of Ti-33Cu heat treated at 900°C: (a) OM image, (b) SEM-BSE image, showing (αTi) (dark contrast), Ti_2Cu (light contrast) and oxide (darker contrast).

Table 4-18. EPMA results for Ti-33Cu.

Alloy		**Area**	**Phases**	**Composition (wt %)**	
				Ti	**Cu**
Ti-33Cu	**As-cast**	Overall	-	66.6 ±3.1	33.4±3.0
		Dark contrast	(αTi)	87.6±0.7	12.4±1.4
		Light contrast	Ti_2Cu	60.8±0.9	39.2±0.9
	750°C	Overall	-	67.5±8.1	32.5±8.8
		Dark contrast	(αTi)	88.4±1.7	11.6±1.7
		Light contrast	Ti_2Cu	60.7±0.6	39.3±0.6
	900°C	Overall	-	66.0±8.1	34.0±8.0
		Dark contrast	(αTi)	87.0±1.5	13.0±1.1
		Light contrast	Ti_2Cu	61.4±1.0	38.6±0.4
		Darker contrast	Ti oxide	96.7±0.8	3.3±0.7

Phases

Figure 4-42 to Figure 4-44 show the XRD patterns of as-cast and annealed of Ti-33Cu. The (αTi) phase had peaks at 2Θ = 40.9°, 44.9°, 47.0°, 62.4° and 74.6°. The Ti_2Cu phase had peaks at 2Θ = 19.0°, 36.5°, 46.0°, 51.0°, 59.5° and 75.0° with the third peak being the most intense for all the alloys. The phase proportions are given in Table 4-19.

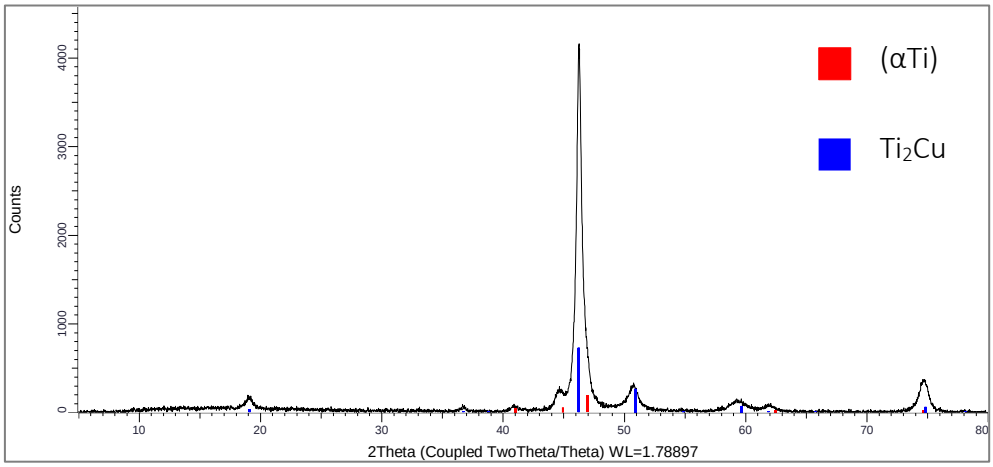


Figure 4-42**.** XRD pattern of Ti-33Cu as-cast, showing (αTi) and Ti_2Cu peaks.

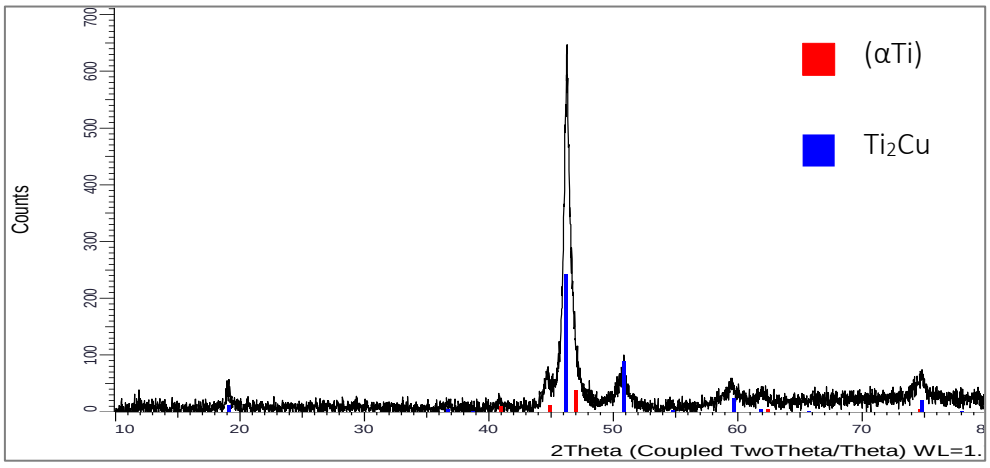


Figure 4-43**.** XRD pattern of Ti-33Cu heat treated at 750°C, showing (αTi) and Ti_2Cu peaks.

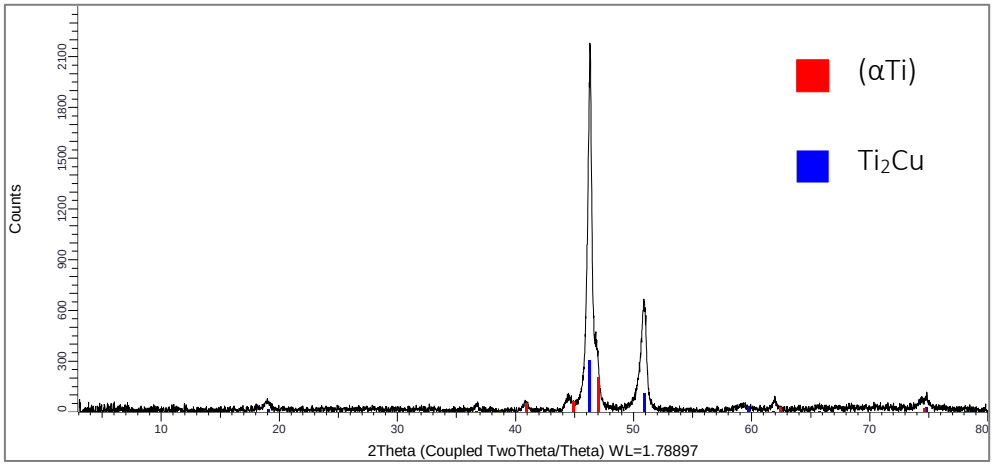


Figure 4-44**.** XRD pattern of Ti-33Cu heat treated at 900°C, showing (αTi) and Ti_2Cu peaks.

Table 4-19. XRD phase proportions of Ti-33Cu.

Alloy		**Phases (wt %)**	
		(αTi)	**Ti_2Cu**
Ti-33Cu	**As-cast**	28	72
	750°C	45	55
	900°C	9	91

4.2.6 Ti-40Cu

Microstructure and composition

Figure 4-45 to Figure 4-47 show the OM and SEM-BSE images of as-cast and annealed of Ti-40Cu. The microstructures comprised Ti_2Cu dendrites (medium contrast), which were surrounded by TiCu (light contrast), and Ti oxides (dark contrast) were also observed. The average composition results are given in Table 4-20. From the EDX analysis, the dark phase had less copper than the light phase. The large errors observed in the overall for Ti-15Cu annealed at 750°C was due to the titanium oxide observed on Figure 4-47.

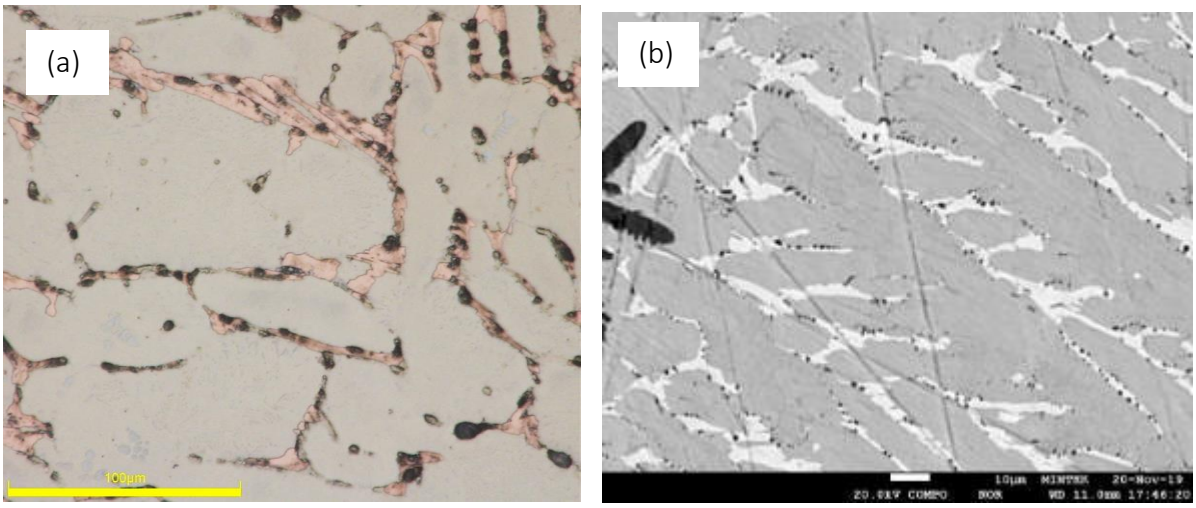


Figure 4-45**.** Microstructures of Ti-40Cu as-cast: (a) OM image (b) SEM-BSE image, showing Ti oxides (dark contrast), Ti_2Cu (medium contrast) and TiCu (light contrast).

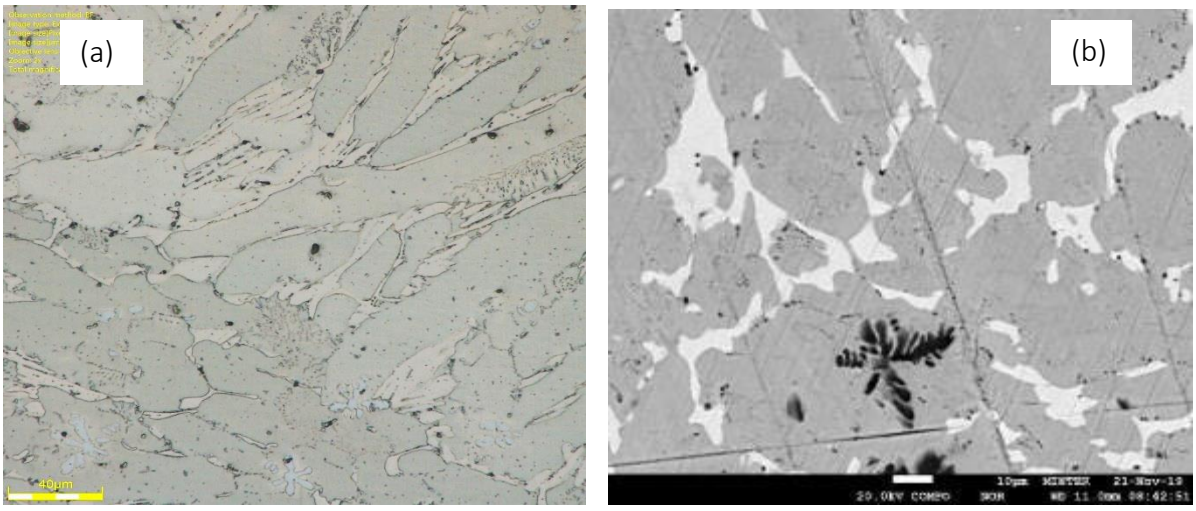


Figure 4-46. Microstructures of Ti-40Cu heat treated at 750°C: (a) OM image (b) SEM-BSE image, showing Ti oxides (dark contrast), Ti_2Cu (medium contrast) and TiCu (light contrast).

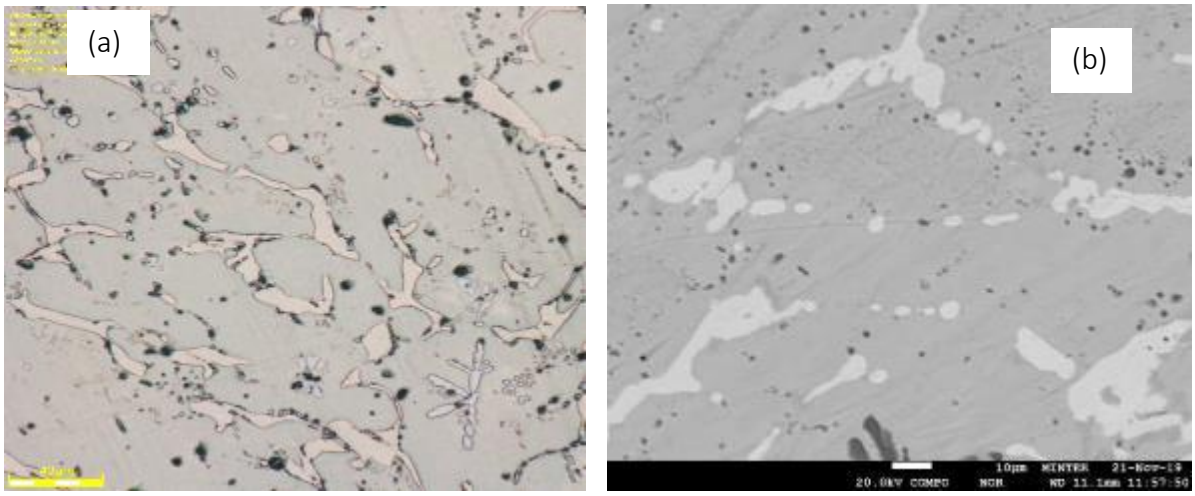


Figure 4-47**.** Microstructures of Ti-40Cu heat treated at 900°C: (a) OM image, (b) SEM-BSE image, showing Ti oxides (dark contrast), Ti_2Cu (medium contrast) and TiCu (light contrast).

Table 4-20. EPMA results for Ti-40Cu.

Alloy		**Area**	**Phases**	**Composition (wt %)**	
				Ti	**Cu**
Ti-40Cu	**As-cast**	Overall	-	60.5±6.2	39.5±8.2
		Medium contrast	Ti_2Cu	61.4±4.9	38.6±0.9
		Light contrast	TiCu	43.8±0.1	56.2±0.1
		Dark contrast	Ti oxide	97.0±0.9	3.0±0.4
	750°C	Overall	-	60.1±6.2	39.9±6.2
		Medium contrast	Ti_2Cu	60.8±0.6	39.2±0.7
		Light contrast	TiCu	43.7±0.2	56.3±0.3
		Dark contrast	Ti oxide	96.4±0.9	3.6±1.3
	900°C	Overall	-	60.5±8.1	39.5±8.2
		Medium contrast	Ti_2Cu	61.3±1.0	38.7±0.9
		Light contrast	TiCu	43.8±0.3	56.2±0.1
		Dark contrast	Ti oxide	89.0±0.2	11.0±0.1

Phases

Figure 4-48 to Figure 4-50 show the XRD patterns of as-cast and annealed Ti-40Cu. XRD patterns showed two intermetallic phases, Ti_2Cu and TiCu. The Ti_2Cu phase had peaks at 2Θ = 19.0°, 36.5°, 46.0°, 51.0°, 59.5° and 75.0° with the third peak being the most intense for all the samples. The TiCu phase had peaks at 2Θ = 17.5°, 48.0°, 49.0°, 65.0° and 70.0°. The phase proportions are given in Table 4-21.

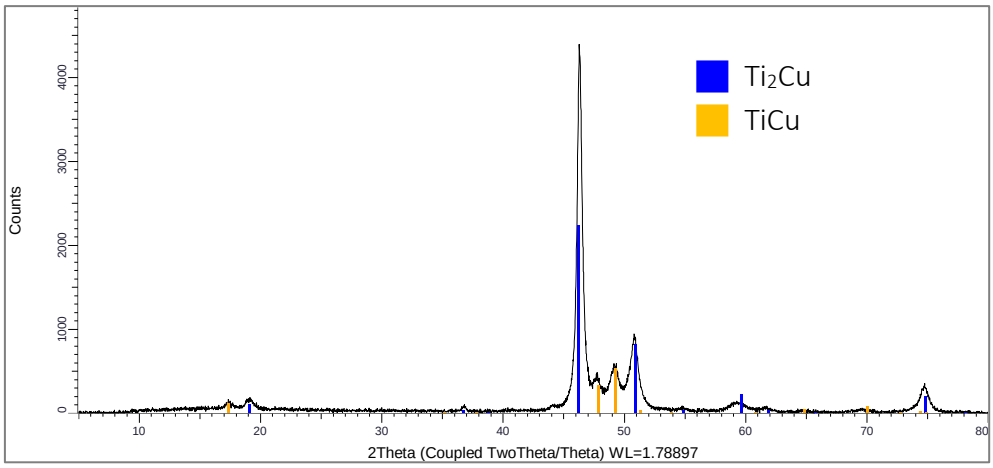


Figure 4-48**.** XRD pattern of Ti-40Cu as-cast, showing Ti_2Cu and TiCu peaks.

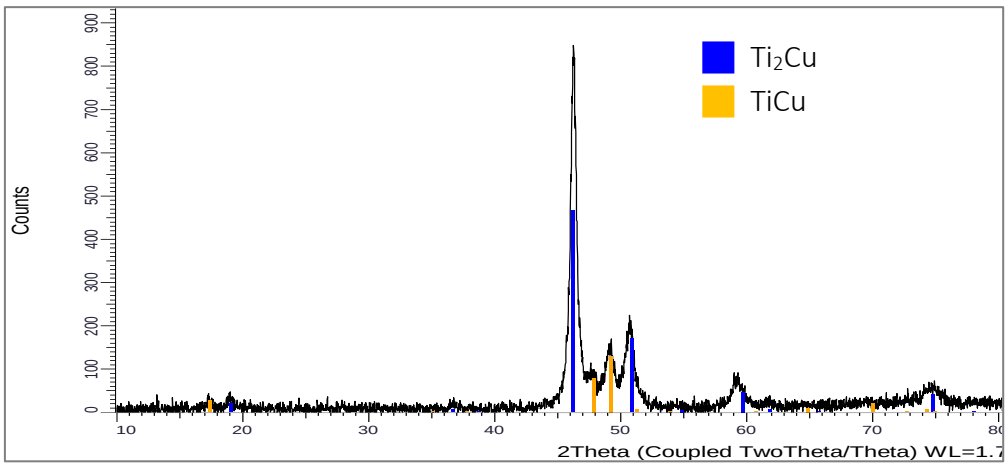


Figure 4-49**.** XRD pattern of Ti-40Cu heat treated at 750°C, showing Ti_2Cu and TiCu peaks.

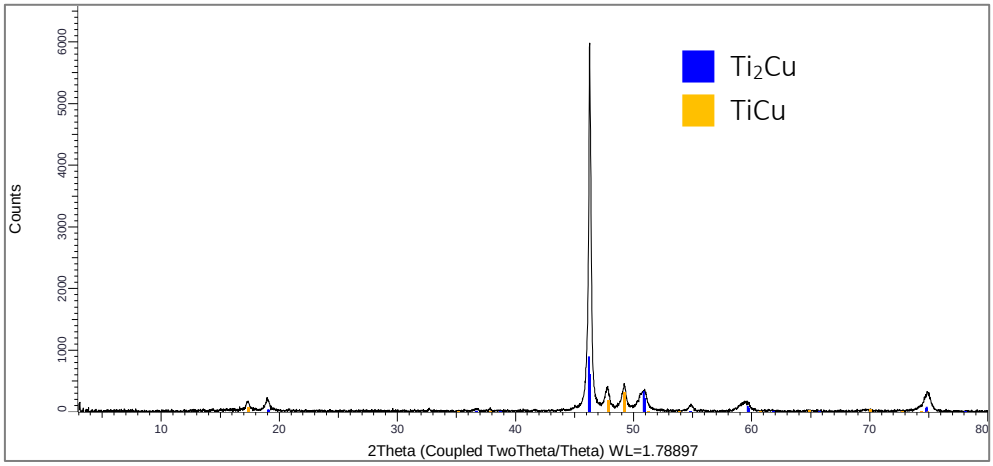


Figure 4-50**.** XRD pattern of Ti-40Cu heat treated at 900°C, showing Ti_2Cu and TiCu peaks.

Table 4-21. XRD phase proportions of Ti-40Cu.

Alloy		**Phases (wt %)**	
		Ti_2Cu	**TiCu**
Ti-40Cu	**As-cast**	80	20
	750°C	78	22
	900°C	65	35

4.2.7 Ti-47Cu

Microstructure and composition

Figure 4-51 to Figure 4-53 show the OM and SEM-BSE images of as-cast and annealed Ti-47Cu. The microstructures comprised Ti_2Cu dendrites (medium contrast), surrounded by TiCu (light contrast) and a Ti_2Cu + TiCu eutectic. The eutectic became more coarse with annealing. The EDX results showed Ti_2Cu as medium contrast and TiCu as light contrast. Black oxides were also observed. The average compositions are given in Table 4-22. The standard deviations for the annealed samples were very high, indicating that the samples were not homogeneous.

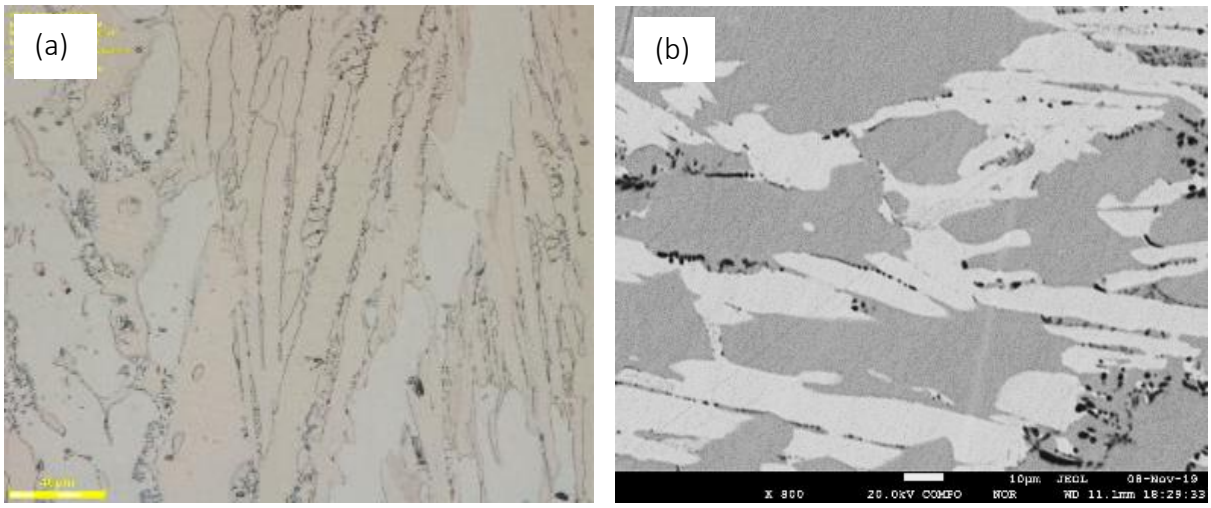


Figure 4-51**.** Microstructures of Ti-47Cu as-cast: (a) OM image, showing Ti oxides (dark contrast), Ti_2Cu (light contrast) and TiCu (medium contrast) and (b) SEM-BSE image, showing Ti oxides (dark contrast), Ti_2Cu (medium contrast) and TiCu (light contrast).

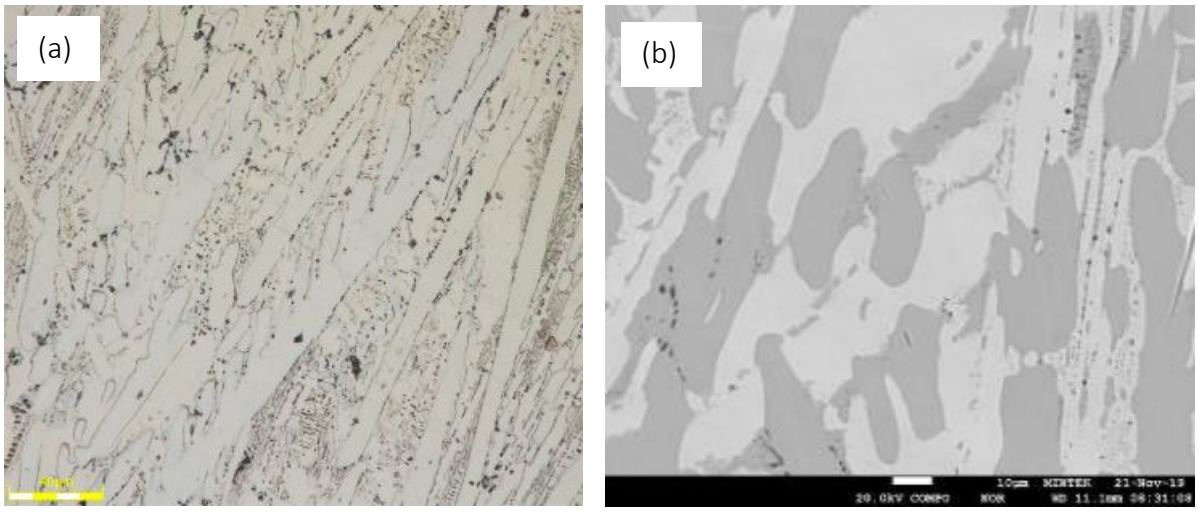


Figure 4-52**.** Microstructures of Ti-47Cu heat treated at 750°C: (a) OM image, showing Ti oxides (dark contrast), Ti_2Cu (light contrast) and TiCu (medium contrast) and (b) SEM-BSE image, showing Ti oxides (dark contrast), Ti_2Cu (medium contrast) and TiCu (light contrast).

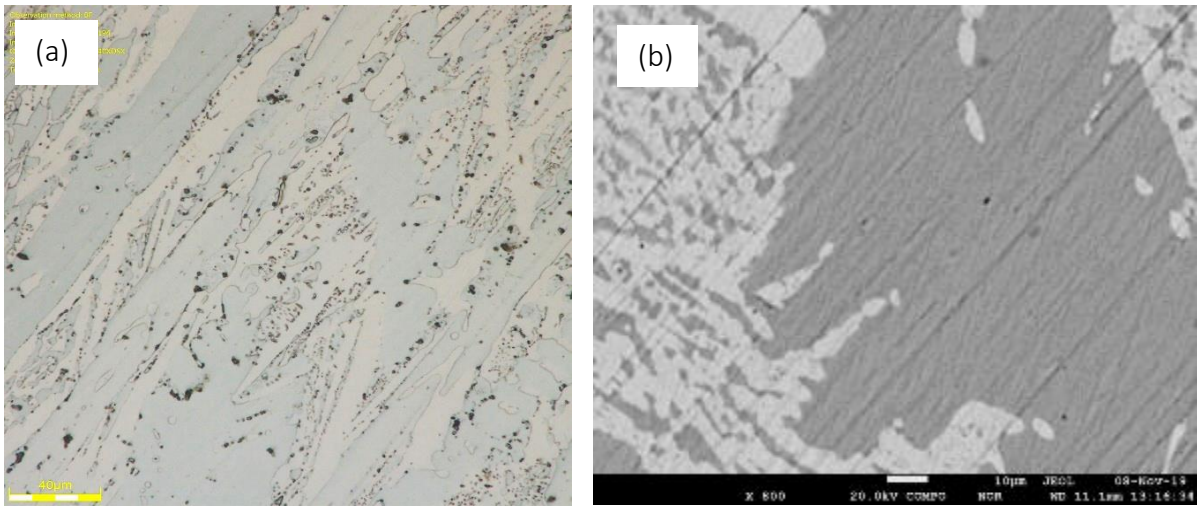


Figure 4-53**.** Microstructures of Ti-47Cu heat treated at 900°C: (a) OM image, showing Ti oxides (dark contrast), Ti_2Cu (light contrast) and TiCu (medium contrast) and (b) SEM-BSE image, showing Ti oxides (dark contrast), Ti_2Cu (medium contrast) and TiCu (light contrast).

Table 4-22. EPMA results for Ti-47Cu.

Alloy		**Area**	**Phases**	**Composition (wt %)**	
				Ti	**Cu**
Ti-47Cu	**As-cast**	Overall	-	53.0±2.3	47.0±2.4
		Medium contrast	Ti_2Cu	60.3±1.7	39.7±1.8
		Light contrast	TiCu	45.7±0.6	54.3±0.7
		Dark contrast	Ti oxide	97.1±0.8	2.9±0.5
	750°C	Overall	-	52.6±7.5	47.4±7.1
		Medium contrast	Ti_2Cu	60.7±0.1	39.9±0.1
		Light contrast	TiCu	43.1±0.1	56.6±0.1
		Dark contrast	Ti oxide	98.1±0.2	1.9±0.2
	900°C	Overall	-	53.0±8.6	47.0±8.6
		Medium contrast	Ti_2Cu	60.9±0.1	39.1±0.2
		Light contrast	TiCu	44.8±0.4	55.2±0.6

Phases

Figure 4-54 to Figure 4-56 show the XRD patterns of as-cast and annealed Ti-47Cu. XRD results showed two intermetallic phases: Ti_2Cu and TiCu. The Ti_2Cu phase had peaks at 2Θ = 19.0°, 36.5°, 46.0°, 51.0°, 59.5° and 75.0° with the third peak being the most intense for all the alloys. The TiCu phase had peaks at 2Θ = 17.5°, 48.0°, 49.0°, 65.0° and 70.0°. The phase proportion results are given in Table 4-23.

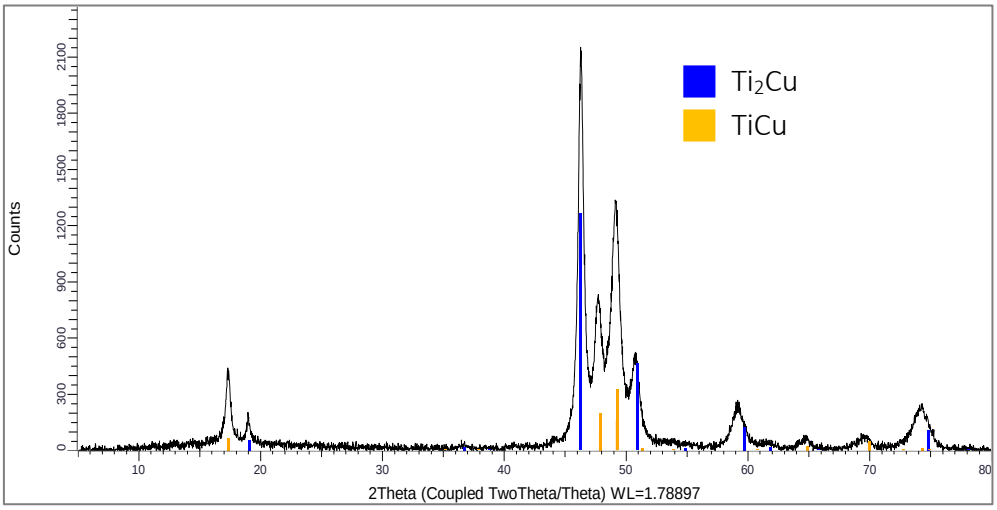


Figure 4-54. XRD pattern of Ti-47Cu as-cast, showing Ti_2Cu and TiCu peaks.

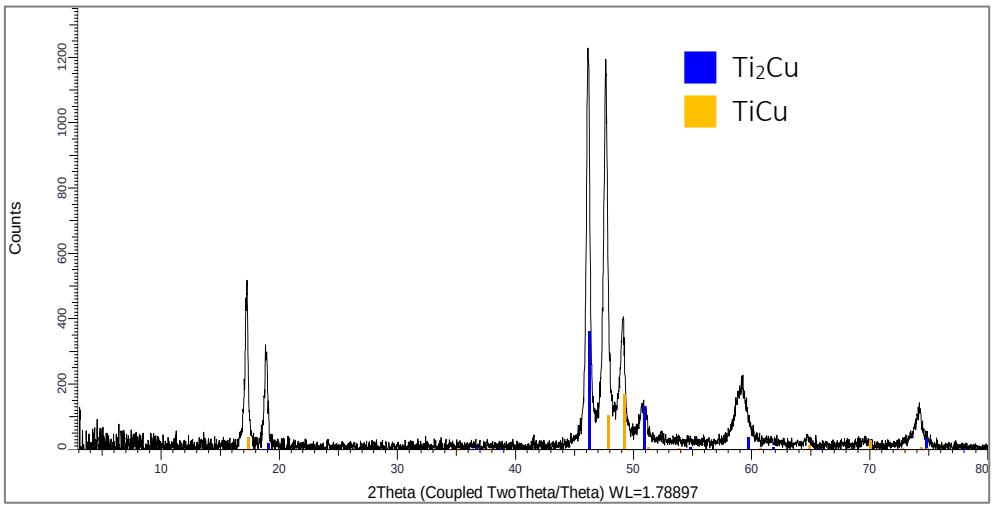


Figure 4-55. XRD pattern of Ti-47Cu heat treated at 750°C, showing Ti_2Cu and TiCu peaks.

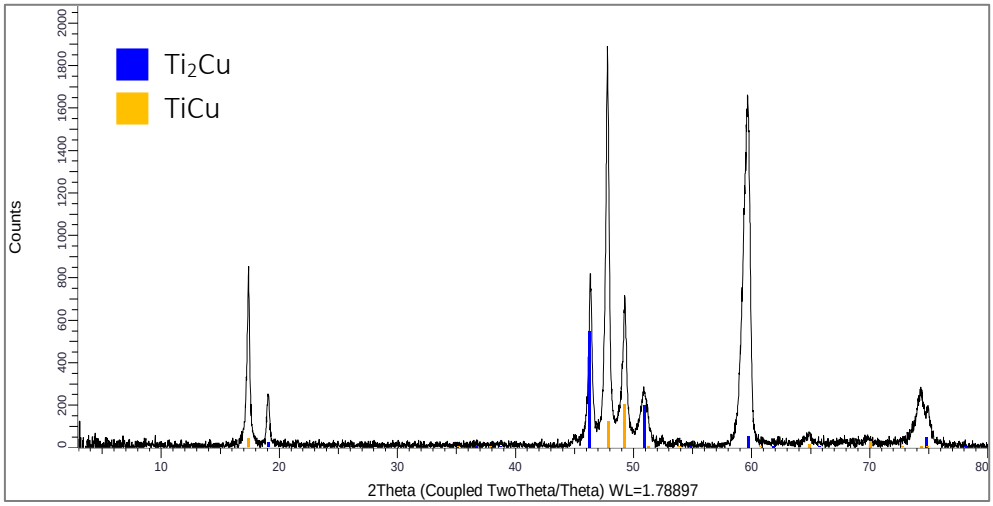


Figure 4-56. XRD pattern of Ti-47Cu heat treated at 900°C, showing Ti_2Cu and TiCu peaks.

Table 4-23. XRD phase proportions of Ti-47Cu.

Alloy		**Phases (wt %)**	
		Ti_2Cu	**TiCu**
Ti-47Cu	**As-cast**	79	21
	750°C	67	33
	900°C	72	28

4.2.8 Ti-50Cu

Microstructure and composition

Figure 4-57 to Figure 4-59 show the OM and SEM-BSE images of Ti-50Cu as-cast and annealed. Ti-50Cu is a eutectic alloy. The microstructure comprised primary TiCu needles (light contrast) surrounded by a eutectic of Ti_2Cu (medium contrast) and TiCu. Ti oxides were also observed. Annealing the samples coarsened the eutectic. The average EDX composition results are given in Table 4-24. The standard deviations for the as-cast samples were high, indicating that the samples were not homogeneous.

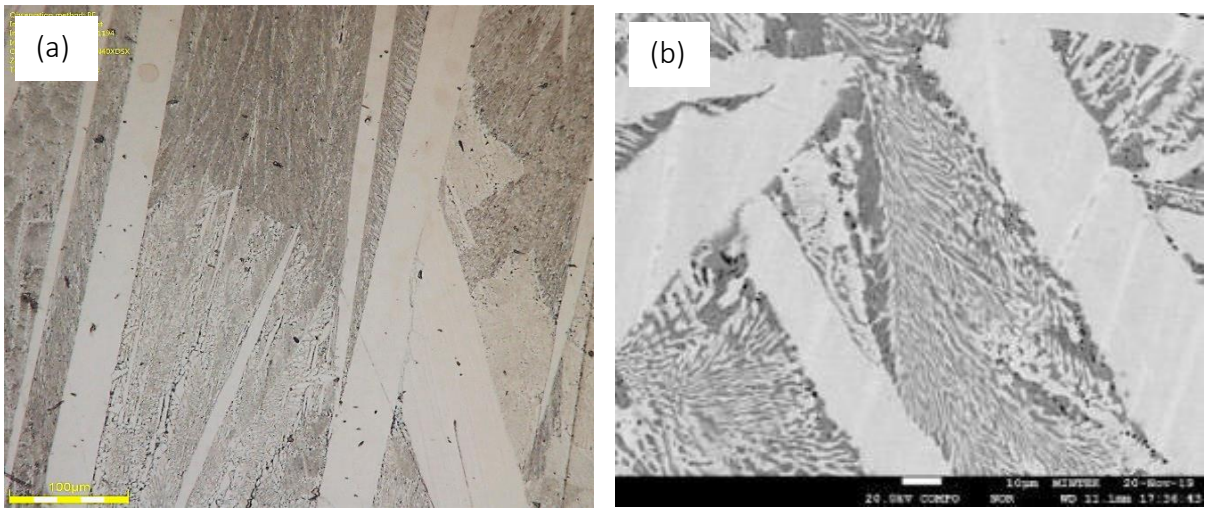


Figure 4-57**.** Microstructures of Ti-50Cu as-cast: (a) OM image and (b) SEM-BSE image, showing Ti oxides (dark contrast), TiCu (light contrast) and Ti_2Cu (medium contrast).

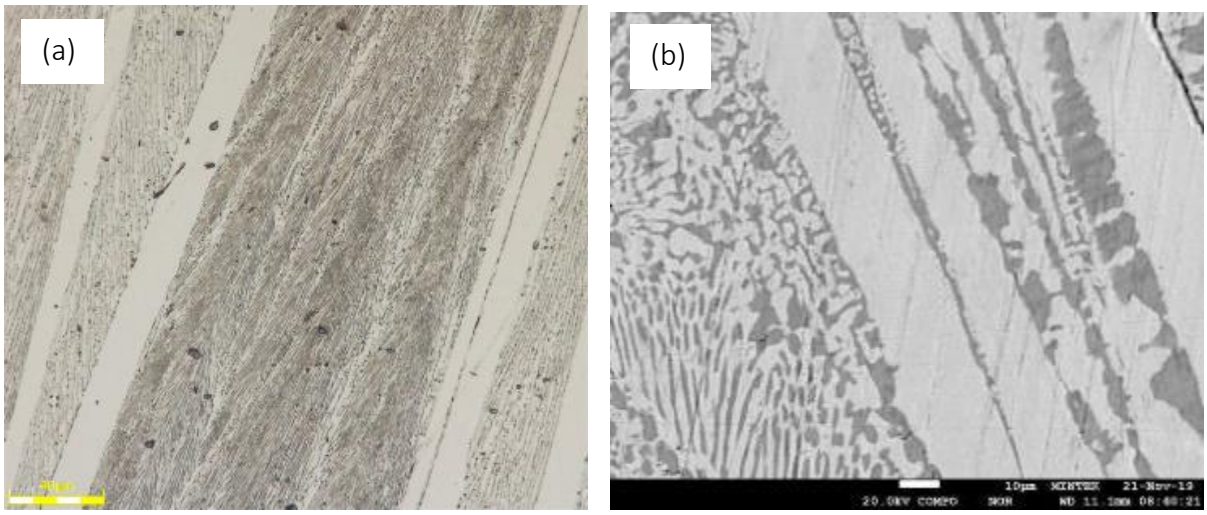


Figure 4-58**.** Microstructures of Ti-50Cu heat treated at 750°C: (a) EPMA image and (b) OM image, showing Ti oxides (dark contrast), TiCu (light contrast) and Ti_2Cu (medium contrast).

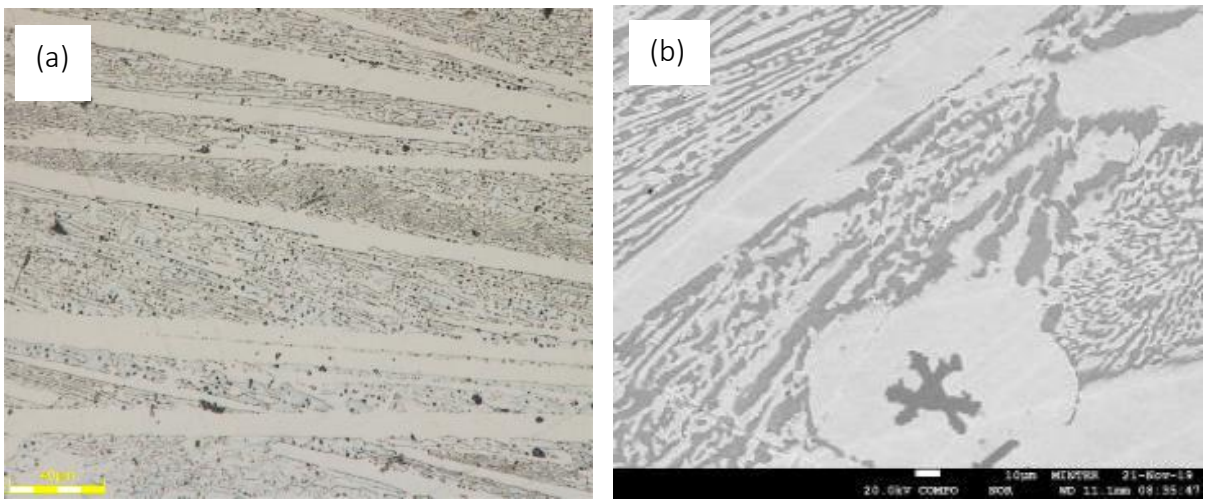


Figure 4-59**.** Microstructures of Ti-50Cu heat treated at 900°C: (a) OM image and (b) SEM-BSE image, showing Ti oxides (dark contrast), TiCu (light contrast) and Ti_2Cu (medium contrast).

Table 4-24. EPMA results for Ti-50Cu.

Alloy		**Area**	**Phase**	**Composition (wt %)**	
				Ti	**Cu**
Ti-50Cu	**As-cast**	Overall	-	50.4±6.1	49.6±6.2
		Medium contrast	Ti_2Cu	61.6±7.9	38.4±0.9
		Light contrast	TiCu	43.2±6.8	56.8±6.8
		Dark contrast	Ti oxide	60.5±0.6	39.5±0.5
	750°C	Overall	-	50.9±6.2	49.1±6.0
		Medium contrast	Ti_2Cu	60.2±0.2	39.8±0.2
		Light contrast	TiCu	43.3±0.2	56.7±0.1
	900°C	Overall	-	51.0±1.0	49.0±1.0
		Medium contrast	Ti_2Cu	59.8±0.7	40.2±1.1
		Light contrast	TiCu	44.2±2.2	55.8±2.1

Phases

Figure 4-60 to Figure 4-62 show the XRD patterns of Ti-50Cu, as-cast and annealed. XRD results showed two intermetallic phases Ti_2Cu and TiCu. The Ti_2Cu phase had peaks at 2Θ = 19.0°, 36.5°, 46.0°, 51.0°, 59.5° and 75.0° with the third peak being the most intense for all the samples. The TiCu phase had peaks at 2Θ = 17.5°, 48.0°, 49.0°, 51.1°, 65.0° and 70.0°. The phase proportions are given in Table 4-25.

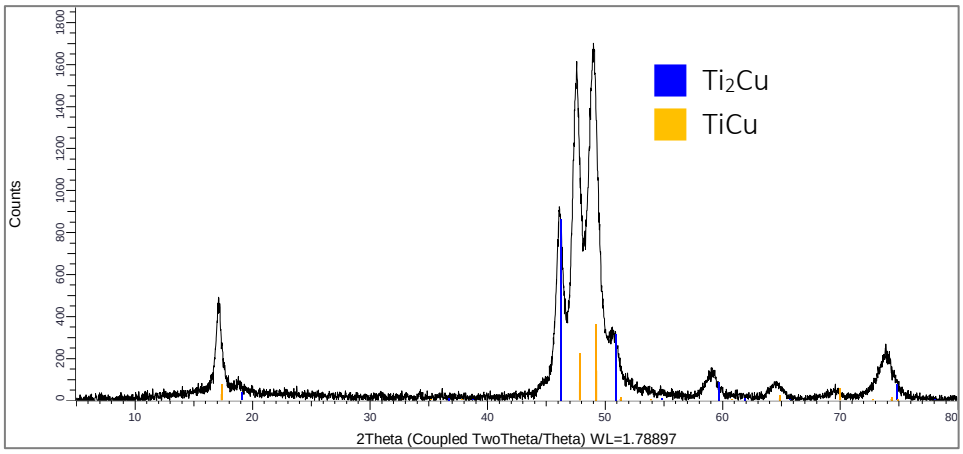


Figure 4-60**.** XRD pattern of Ti-50Cu as-cast, showing Ti_2Cu and TiCu peaks.

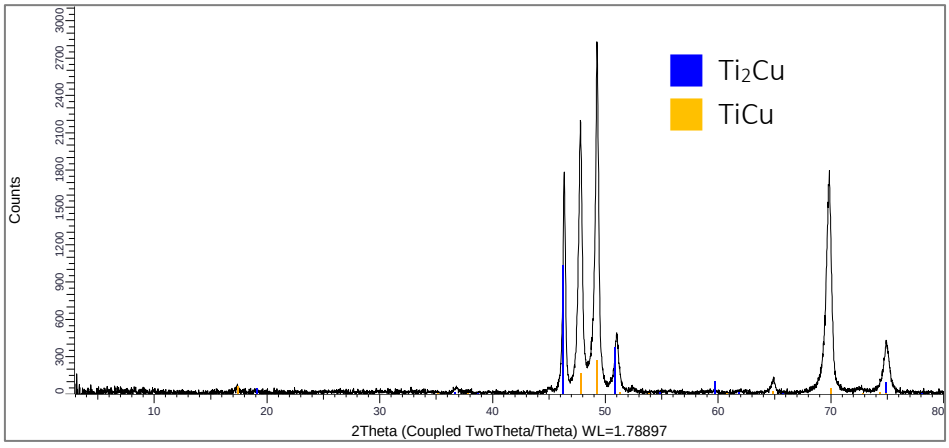


Figure 4-61**.** XRD pattern of Ti-50Cu heat treated at 750°C, showing Ti_2Cu and TiCu peaks.

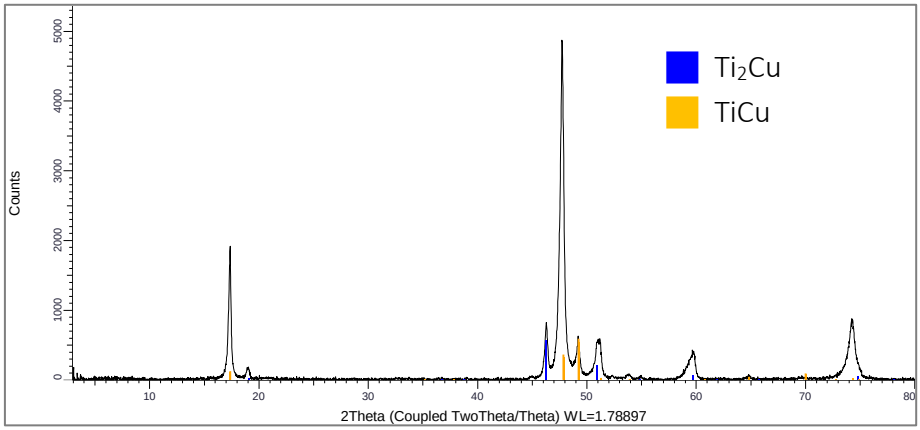


Figure 4-62**.** XRD pattern of Ti-50Cu heat treated at 900°C, showing Ti_2Cu and TiCu peaks.

Table 4-25. XRD phase proportions of Ti-50Cu.

Alloy		**Phases (wt %)**	
		Ti_2Cu	**TiCu**
Ti-50Cu	**As-cast**	70	30
	750°C	79	21
	900°C	51	49

4.3 Hardness Testing

The addition of copper to titanium increased the hardness of the alloys. The as-cast hardness increased and reached a peak value of 450±4 HV_{10} at Ti-25Cu and then almost remained constant although a slight drop was observed, with a sharp decrease to the value of 353±10 HV_{10} at Ti-33Cu. For the annealed samples, the hardness increased and reached the highest value of 359±32 Hv_{10} for the samples annealed at 750°C and 300±51 Hv_{10} for the samples annealed at 900°C and then a slight decrease was observed. The standard deviation for the samples was very high; this could indicate that the samples were not homogeneous. Annealing decreased the hardness of the alloys. The as-cast samples had the highest hardness while the samples annealed at 900°C showed the lowest hardness. Table 4-26 and Figure 4-63 shows the hardness results.

Table 4-26. Hardness results of the alloys.

Alloy	Hardness (HV_{10}) Average		
	As-cast	750°C	900°C
CP Ti	250±5	200±29	180±9
Ti-5Cu	307±24	286±31	210±19
Ti-15Cu	385±9	359±32	300±51
Ti-25Cu	450±4	317±20	300±5
Ti-33Cu	353±10	308±11	290±16
Ti-40Cu	432±20	286±24	280±21
Ti-47Cu	437±19	287±24	268±23
Ti-50Cu	430±5	287±9	270±39

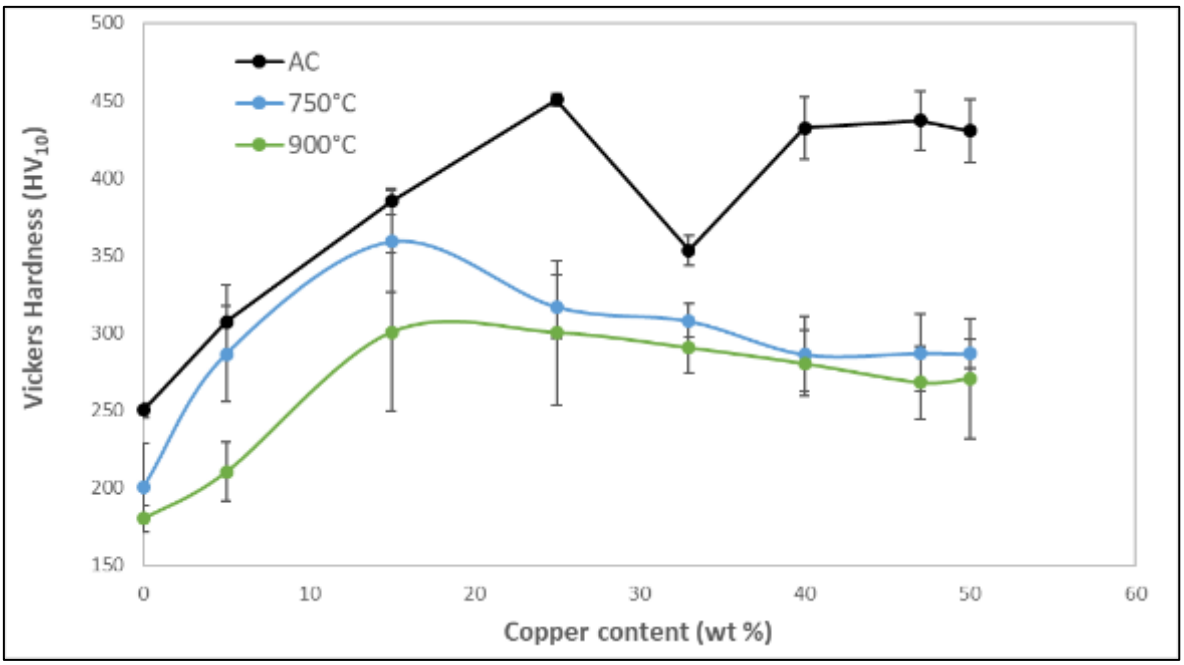


Figure 4-63.Vickers hardness as a function of nominal copper content of the as-cast and annealed Ti-Cu alloys.

4.4 Corrosion Testing

4.4.1 Electrochemical Testing

4.3.1 CP Ti

Figure 4-64 and Figure 4-65 show the OCP and potentiodynamic polarisation curves in the PBS solution. The potential for all alloys initially decreased and then increased at approximately 500 s until the passive film reached its limiting protective capacity after which it stabilised. The sample heat treated at 750°C shifted the potential towards the noble direction (due to quick formation of the passive film) of while the sample heat treated at 900°C was less noble when compared to the as-cast sample, as shown Figure 4-64. A long passivation stage was observed in the potentiodynamic polarisation curves, as shown in Figure 4-65. The heat treated sample showed an increase in corrosion rates Table 4-27 shows the OCP and potentiodynamic polarisation results.

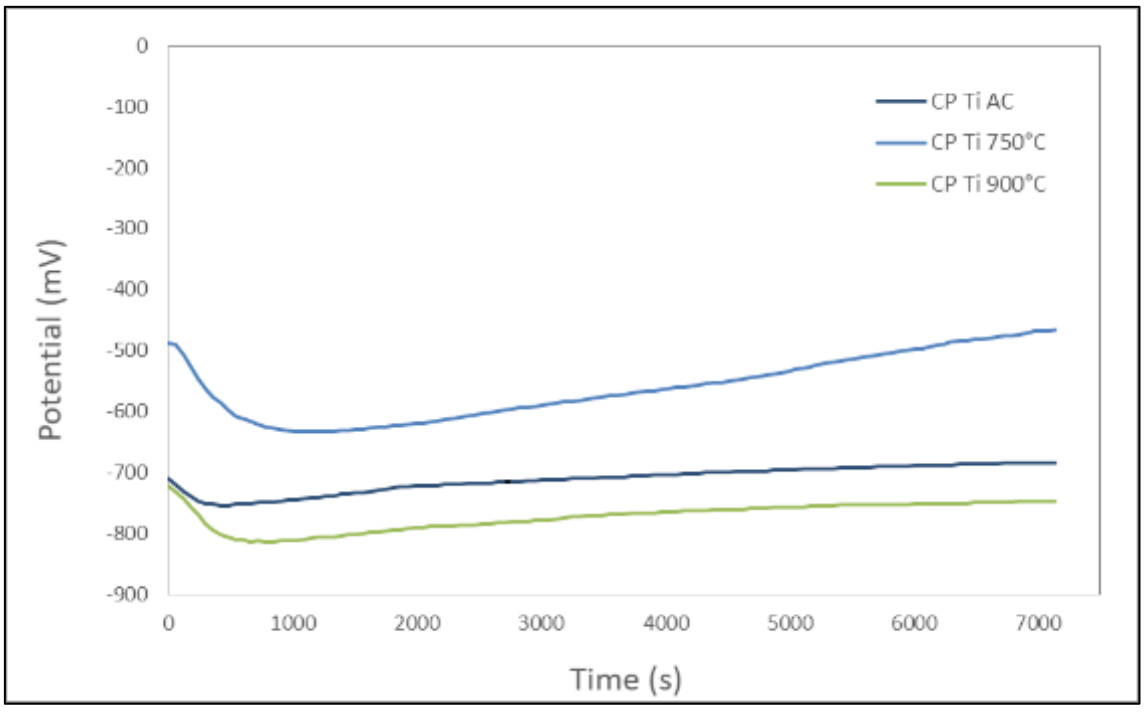


Figure 4-64. OCP of CP Ti in PBS.

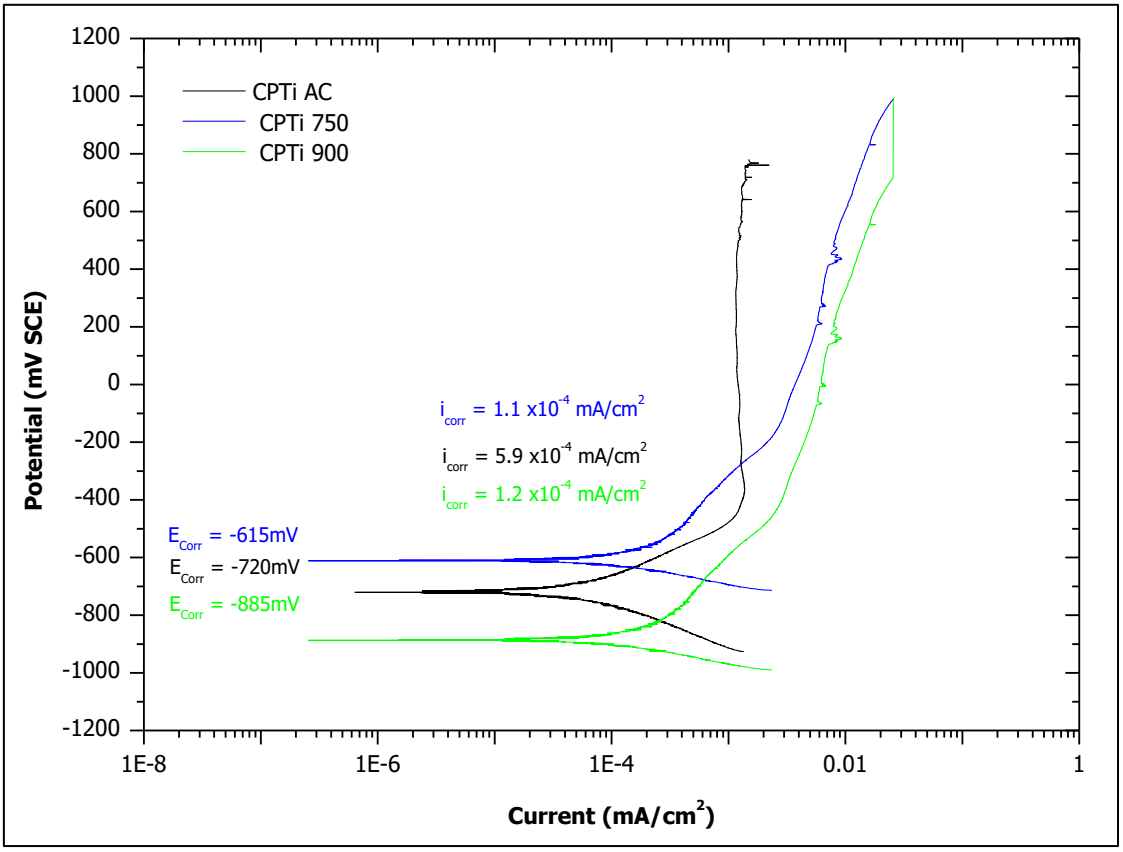


Figure 4-65. Potentiodynamic polarisation curves of CP Ti in PBS.

Table 4-27. Corrosion tests results for CP Ti in PBS.

Alloy		OCP (mV)	E_{Corr} (mV SCE)	I_{corr} (mA/cm²)	Corrosion Rates (mm/y)	
					Individual	Average
CP Ti	As-cast	-684	-720	$6.4X10^{-05}$	0.00058	0.00059±0.000019
		-675	-681	$6.7X10^{-05}$	0.00060	
	750°C	-466	-614	$1.1X10^{-04}$	0.00099	0.00113±0.000190
		-297	-441	$1.4X10^{-04}$	0.00126	
	900°C	-748	-885	$1.2X10^{-04}$	0.00108	0.00108±0.000000
		-761	-904	$1.2X10^{-04}$	0.00108	

4.3.2 Ti-5Cu

Figure 4-66 and Figure 4-67 show the OCP and potentiodynamic polarisation curves in the PBS solution. The potential for the as-cast and heat treated at 900°C samples initially decreased and then increased until the passive film reached its limiting protective capacity after which it stabilised, while the heat treated at 750°C alloy initially increased and then stabilised (due to the quick formation of a passive film). The sample heat treated at 750°C shifted the potential towards the noble direction while the sample heat treated at 900°C and the as-cast sample were less noble, as shown Figure 4-66. A long passivation stage was observed in the potentiodynamic polarisation curves, as shown in Figure 4-67. The heat treated samples showed decreased corrosion rates compared to as-cast. Table 4-28 shows the OCP and potentiodynamic polarisation results.

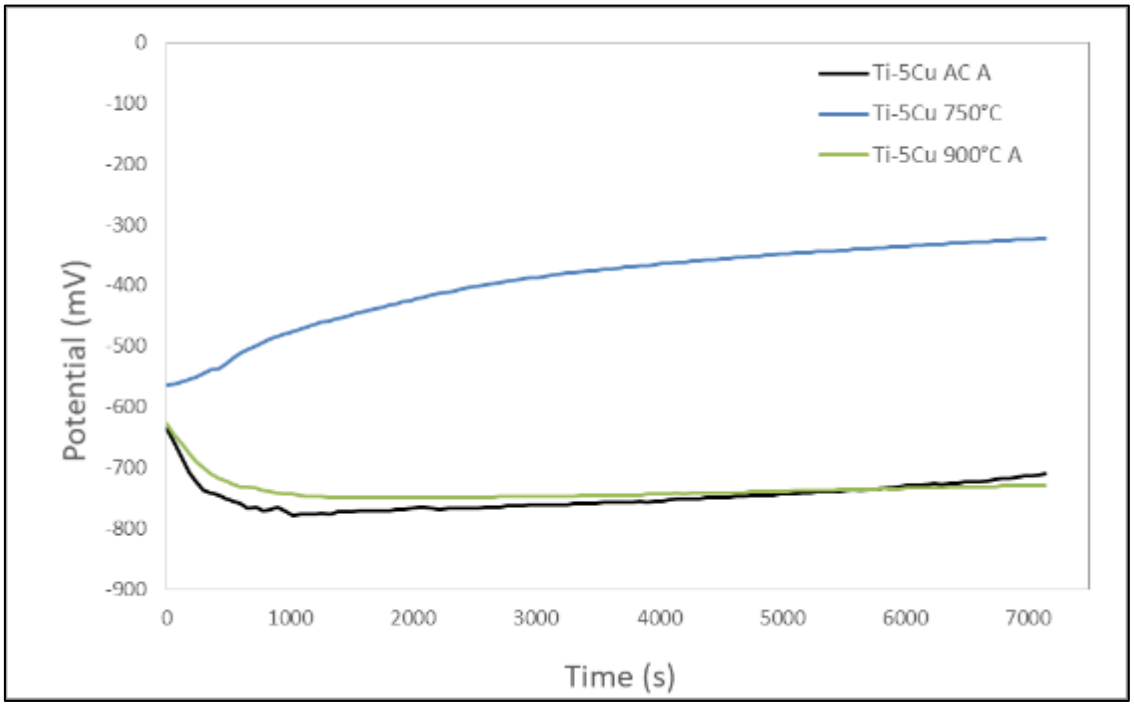


Figure 4-66. OCP of Ti-5Cu in PBS.

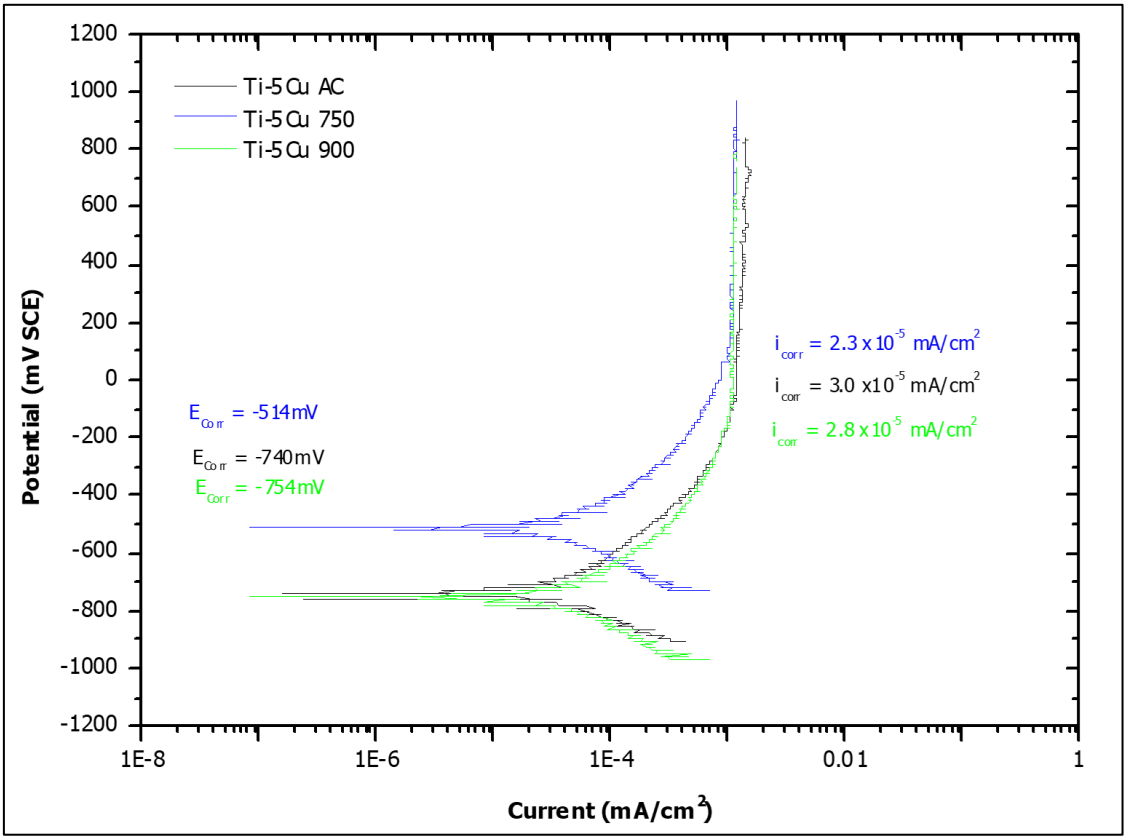


Figure 4-67. Potentiodynamic polarisation curves of Ti-5Cu in PBS.

Table 4-28. Corrosion tests results for Ti-5Cu.

Alloy		OCP (mV)	E_{Corr} (mV SCE)	I_{corr} (mA/cm²)	Corrosion Rates (mm/y)	
					Individual	Average
Ti-5Cu	As-cast	-711	-710	$3.0X10^{-05}$	0.00027	0.00027±0.000000
		-659	-740	$3.0X^{-05}$	0.00027	
	750°C	-491	-514	$2.3X10^{-05}$	0.00021	0.00023±0.000038
		-323	-349	$2.9X^{-05}$	0.00026	
	900°C	-729	-754	$2.8X10^{-05}$	0.00025	0.00027±0.000019
		-374	-398	$3.1X10^{-05}$	0.00028	

4.3.3 Ti-15Cu

Figure 4-68 and Figure 4-69 show the OCP and potentiodynamic polarisation curves in the PBS solution. The sample heat treated at 750°C shifted the potential towards the noble direction while the sample heat treated at 900°C and the as-cast sample were less noble, as shown Figure 4-69. A long passivation stage was observed in the potentiodynamic polarisation curves indicating that good passivation protection occurred, as shown in Figure 4-69. The heat treated samples showed increased corrosion rates when compared to the as-cast sample. Table 4-29 shows the OCP and potentiodynamic polarisation results.

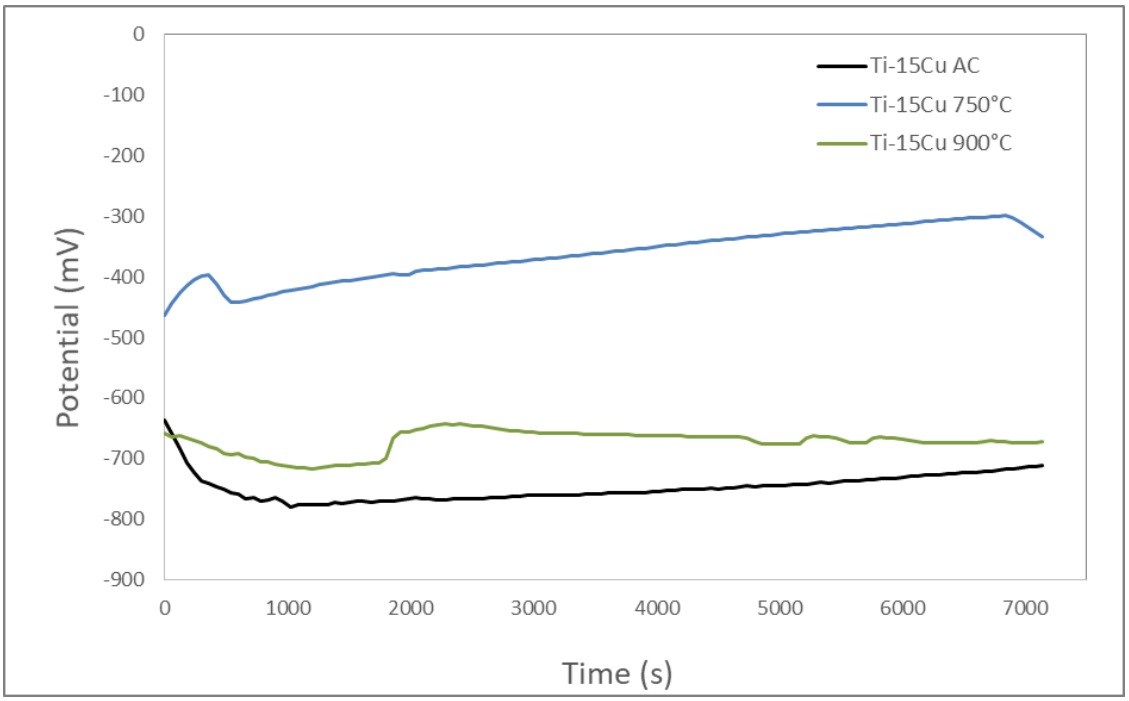


Figure 4-68. OCP of Ti-15Cu in PBS.

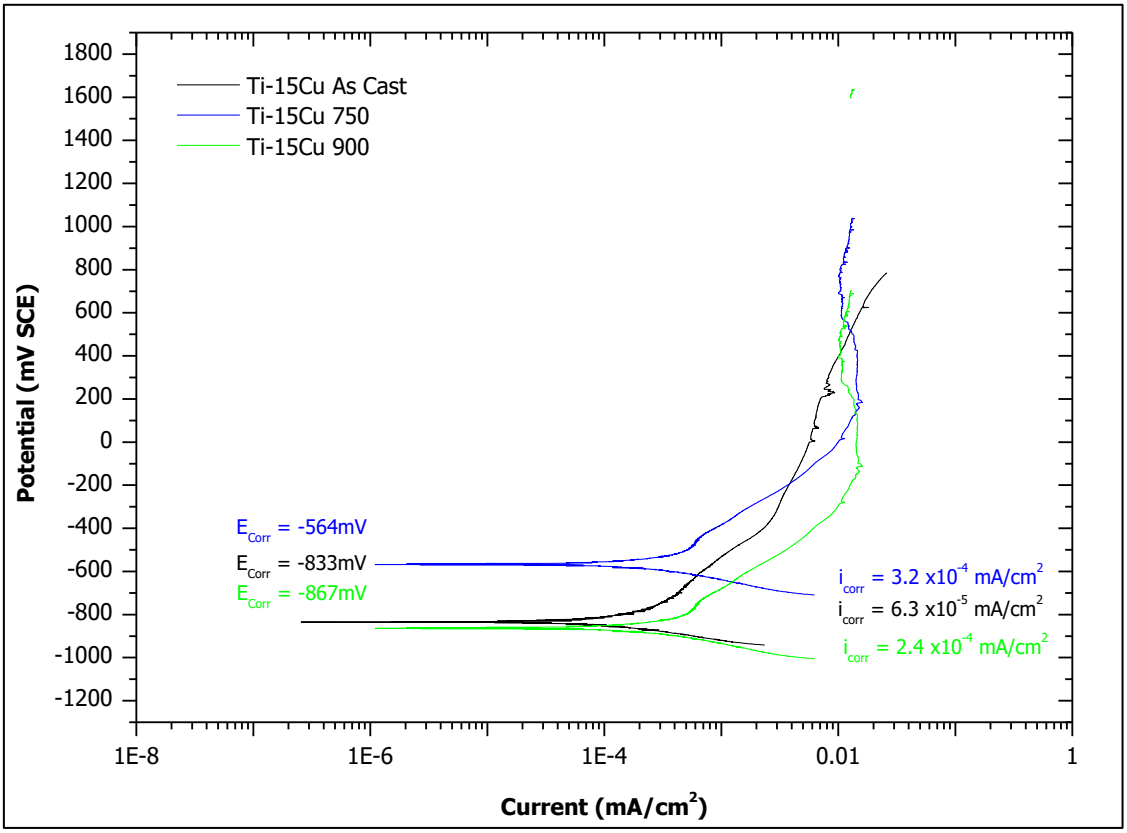


Figure 4-69. Potentiodynamic polarisation curves of Ti-15Cu in PBS.

Table 4-29. Corrosion tests results for Ti-15Cu.

Alloy		OCP (mV)	E_{Corr} (mV SCE)	I_{corr} (mA/cm²)	Corrosion Rates (mm/y)	
					Individual	Average
Ti-15Cu	As-cast	-709	-833	$6.3X10^{-05}$	0.00070	0.00063±0.000096
		-401	-814	$7.8X10^{-05}$	0.00057	
	750°C	-491	-567	$2.8X10^{-04}$	0.00252	0.00265±0.000000
		-450	-650	$3.1X10^{-04}$	0.00279	
	900°C	-729	-867	$2.1X10^{-04}$	0.00189	0.00203±0.000191
		-762	-770	$2.4X10^{-04}$	0.00216	

4.3.4 Ti-25Cu

Figure 4-70 and Figure 4-71 show the OCP and potentiodynamic polarisation curves in the PBS solution. The sample heat treated at 750°C shifted the potential towards the noble direction while the sample heat treated at 900°C was less noble when compared to the as-cast sample, as shown in Figure 4-70. A long passivation stage was observed in the potentiodynamic polarisation curves indicating that good passivation protection formed, as shown in Figure 4-71. The sample heat treated at 900°C showed an increase in corrosion rate, while that heat treated at 750°C showed a slight decrease when compared to the as-cast sample Table 4-30 shows the OCP and potentiodynamic polarisation results.

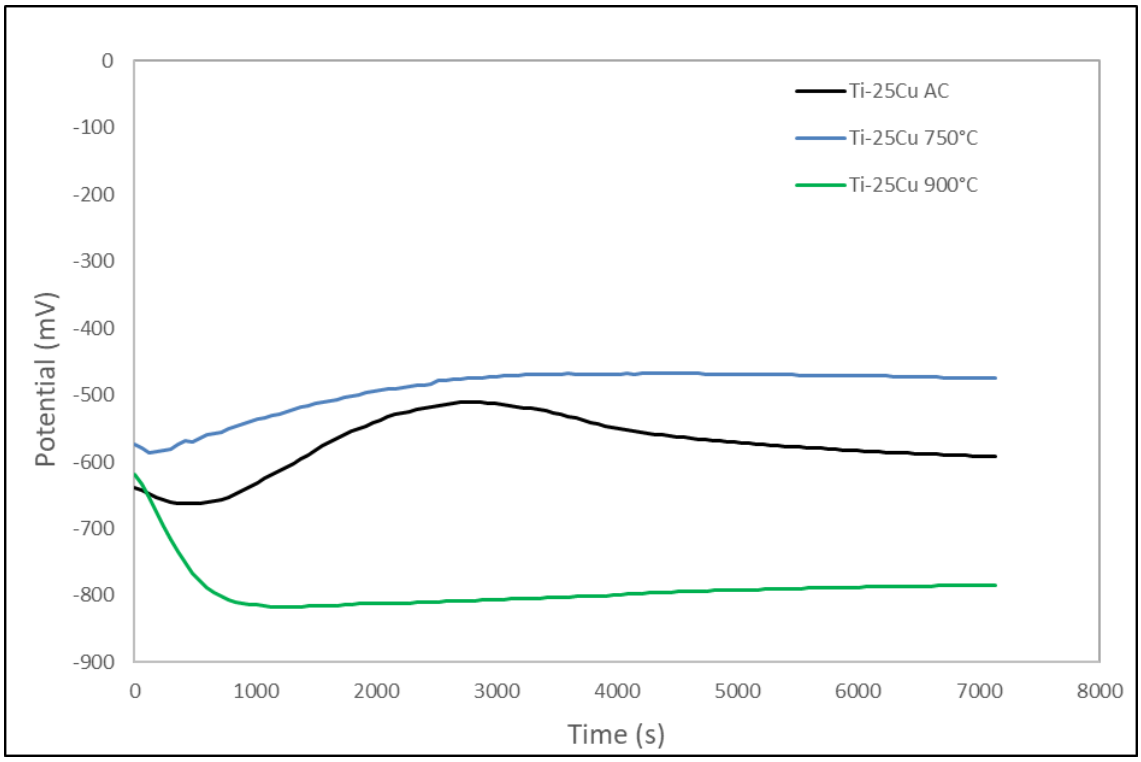


Figure 4-70. OCP of Ti-25Cu in PBS.

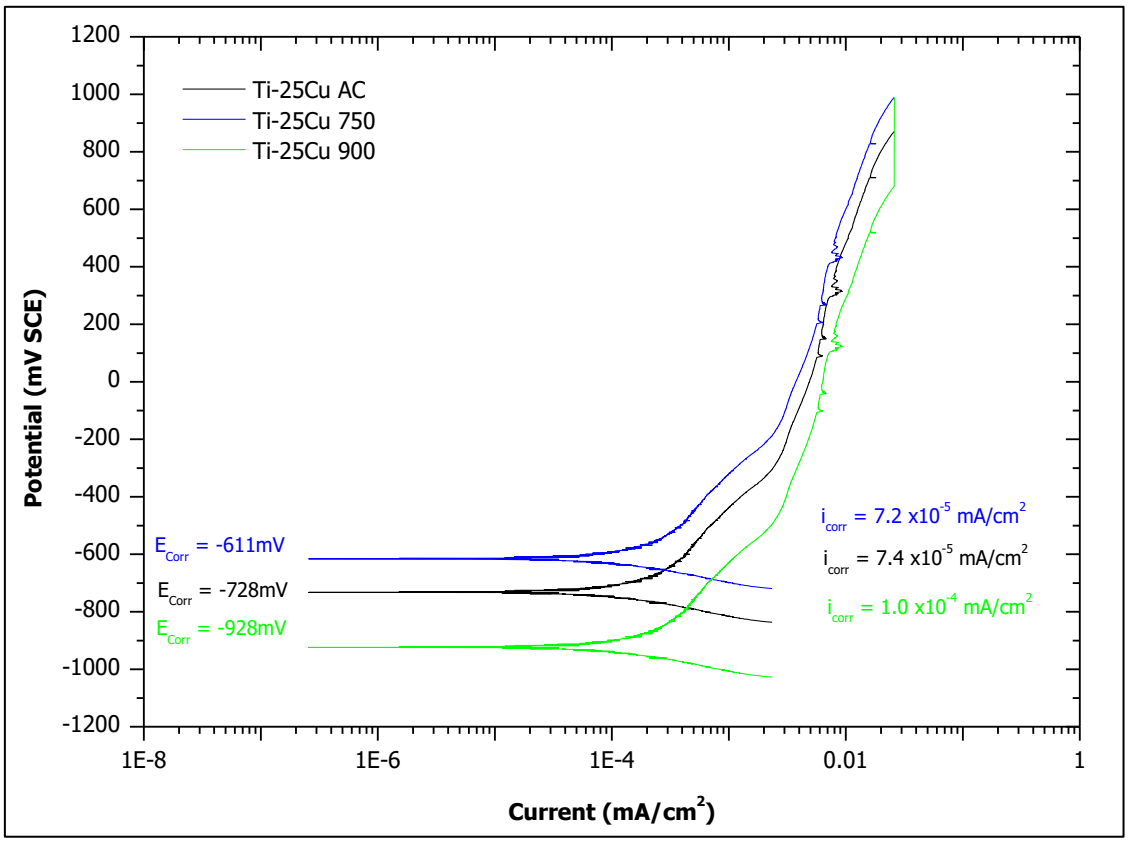


Figure 4-71. Potentiodynamic polarisation curves of Ti-25Cu in PBS.

Table 4-30. Corrosion tests results for Ti-25Cu in PBS.

Alloy		OCP (mV)	E_{Corr} (mV SCE)	I_{corr} (mA/cm²)	Corrosion Rates (mm/y)	
					Individual	Average
Ti-25Cu	As-cast	-571	-728	$7.4X10^{-05}$	0.00061	0.00064±0.000038
		-592	-718	$6.8X10^{-05}$	0.00067	
	750°C	-333	-611	$7.2X10^{-05}$	0.00065	0.00065±0.000045
		-460	-429	$7.9\ X10^{-05}$	0.00071	
	900°C	-792	-928	$1.0X10^{-04}$	0.00090	0.00090±0.000000
		-784	-928	$1.0X10^{-04}$	0.00090	

4.3.5 Ti-33Cu

Figure 4-72 and Figure 4-73 show the OCP and potentiodynamic polarisation curves in the PBS solution. The sample heat treated at 900°C was less noble compared to both the as-cast and heat treated at 750°C samples, as shown in Figure 4-72. A long passivation stage was observed in the potentiodynamic polarisation curves indicating that good passivation protection occurred, as shown in Figure 4-73. The heat treated samples showed an order of magnitude increase of corrosion rates compared to the as-cast sample. Table 4-31 shows the OCP and potentiodynamic polarisation results.

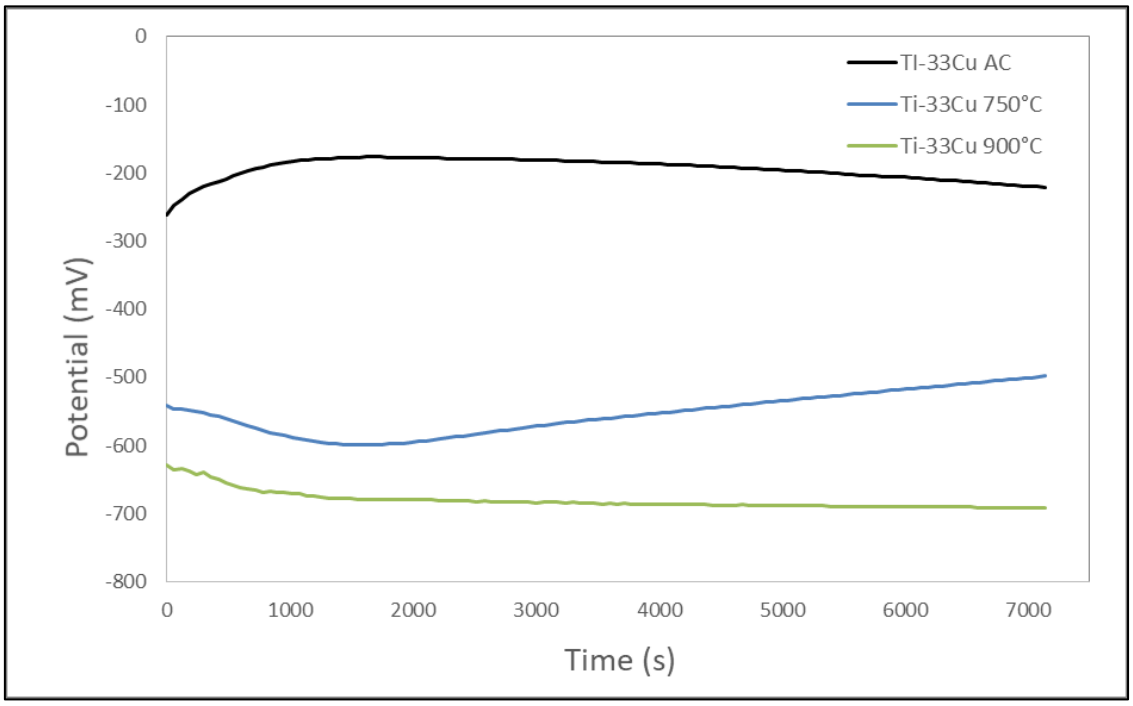


Figure 4-72. OCP of Ti-33Cu in PBS.

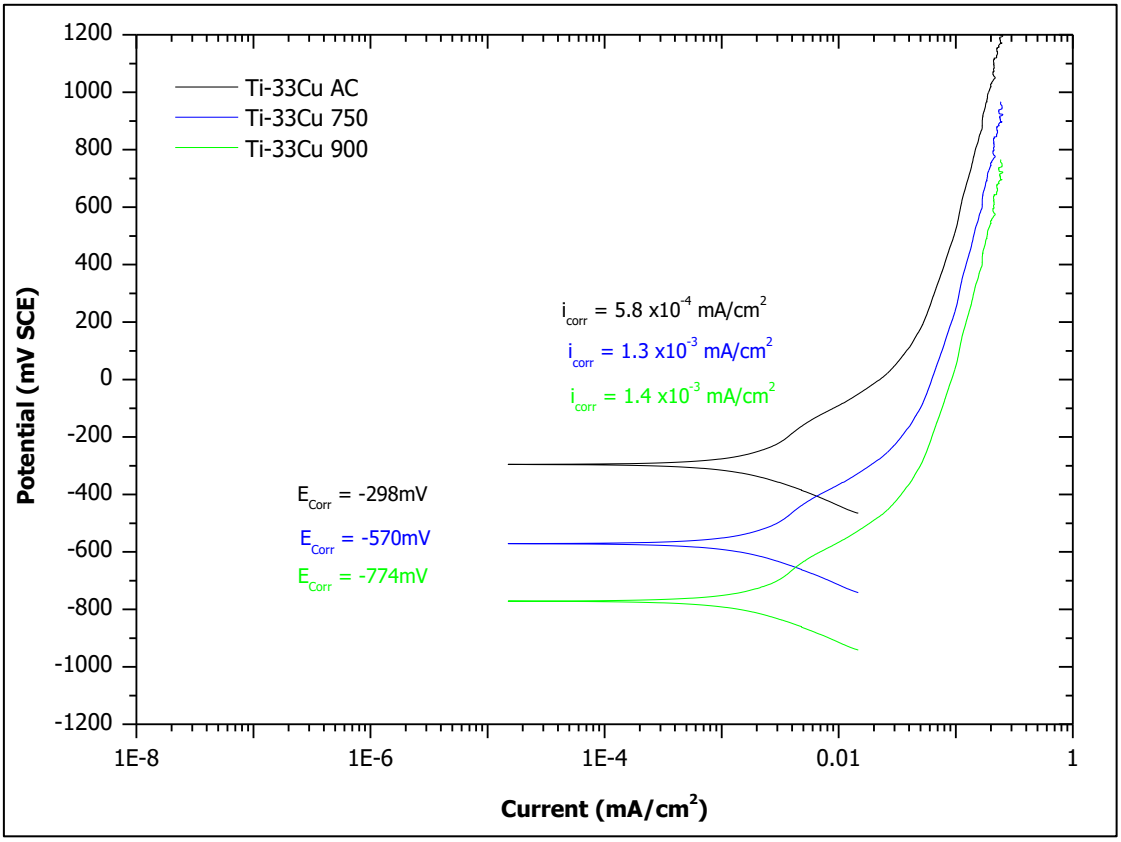


Figure 4-73. Potentiodynamic polarisation curves of Ti-33Cu in PBS.

Table 4-31. Corrosion tests results for Ti-33Cu.

Alloy		OCP (mV)	E_{Corr} (mV SCE)	I_{corr} (mA/cm²)	Corrosion Rates (mm/y)	
					Individual	Average
Ti-33Cu	As-cast	-221	-298	5.8X10^{-04}	0.00522	0.00500±0.000318
		-184	-230	5.3X10^{-04}	0.00477	
	750°C	-498	-570	1.3X10^{-03}	0.01170	0.01170±0.000000
		-486	-570	1.3X10^{-03}	0.01170	
	900°C	-784	-774	1.4X10^{-03}	0.01260	0.01260±0.000000
		-778	-860	1.4X10^{-03}	0.01260	

4.3.6 Ti-40Cu

Figure 4-74 and Figure 4-75 show the OCP and potentiodynamic polarisation curves in the PBS solution. The sample heat treated at 750°C shifted the potential towards the noble direction while the sample heat treated at 900°C was less noble when compared to both the as-cast and heat treated at 750°C samples, as shown Figure 4-74. A long passivation stage was observed in the potentiodynamic polarisation curves, indicating that good passivation protection was formed, as shown in Figure 4-75. The heat treated samples showed a decrease in corrosion resistance when compared to the as-cast condition. Table 4-32 shows the OCP and potentiodynamic polarisation results.

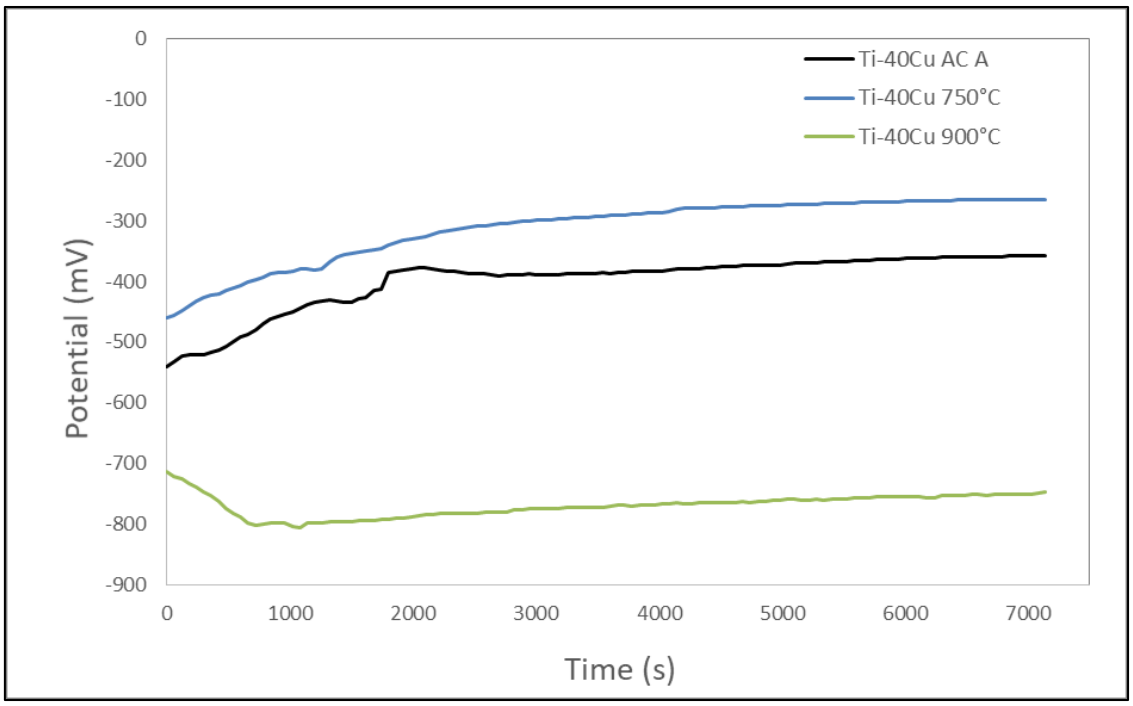


Figure 4-74. OCP of Ti-40Cu in PBS.

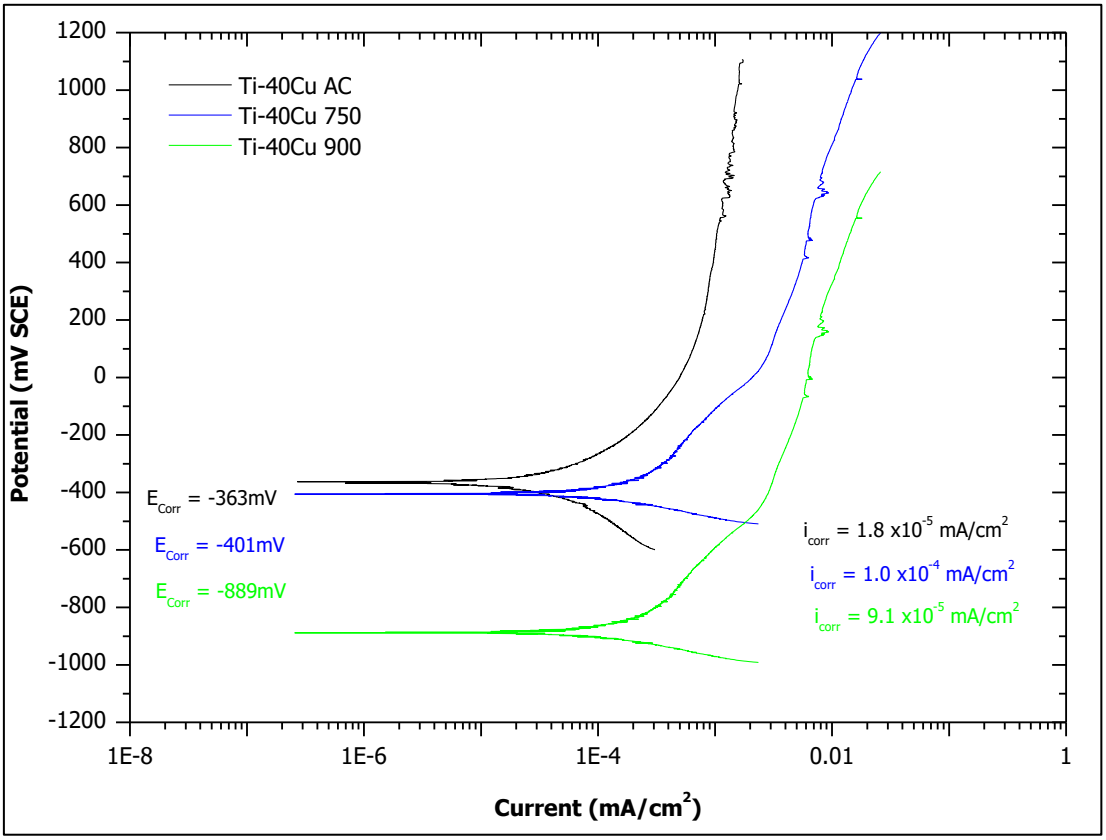


Figure 4-75. Potentiodynamic polarisation curves of Ti-40Cu in PBS.

Table 4-32. Corrosion tests results for Ti-40Cu.

Alloy		OCP (mV)	E_{Corr} (mV SCE)	I_{corr} (mA/cm²)	Corrosion Rates (mm/y)	
					Individual	Average
Ti-40Cu	As-cast	-448	-442	$2.0X10^{-05}$	0.00016	0.00017±0.000012
		-357	-363	$1.8X10^{-05}$	0.00018	
	750°C	-264	-401	$1.0X10^{-04}$	0.00090	0.00090±0.000000
		-265	-401	$1.0X10^{-04}$	0.00090	
	900°C	-748	-889	$9.1X10^{-05}$	0.00082	0.00086±0.000057
		-662	-803	$1.0X10^{-04}$	0.00090	

4.3.7 Ti-47Cu

Figure 4-76 and Figure 4-77 show the OCP and potentiodynamic polarisation curves in the PBS solution. The sample heat treated at 900°C was less noble compared to both the as-cast and 750°C heat treated samples, as shown in Figure 4-76. A long passivation stage was observed in the potentiodynamic polarisation curves, indicating that good passivation protection formed, as shown in Figure 4-77. The heat treated samples showed slight decreased corrosion rates compared to the as-cast sample. Table 4-33 shows the OCP and potentiodynamic polarisation results.

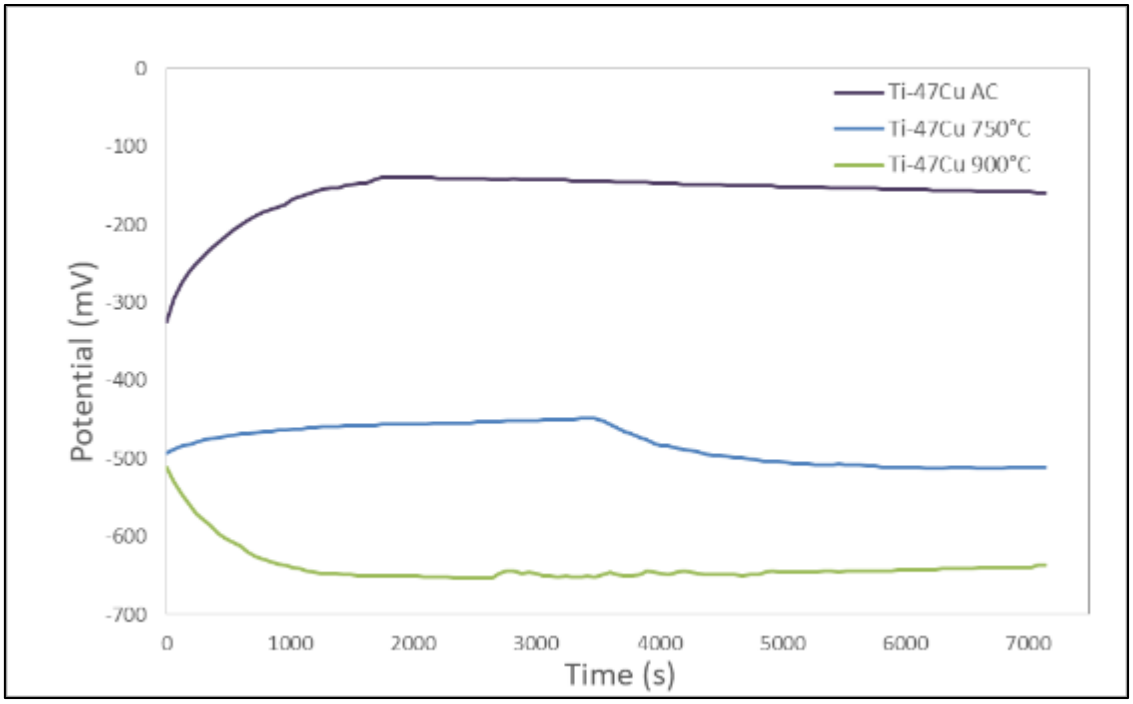


Figure 4-76. OCP of Ti-47Cu in PBS.

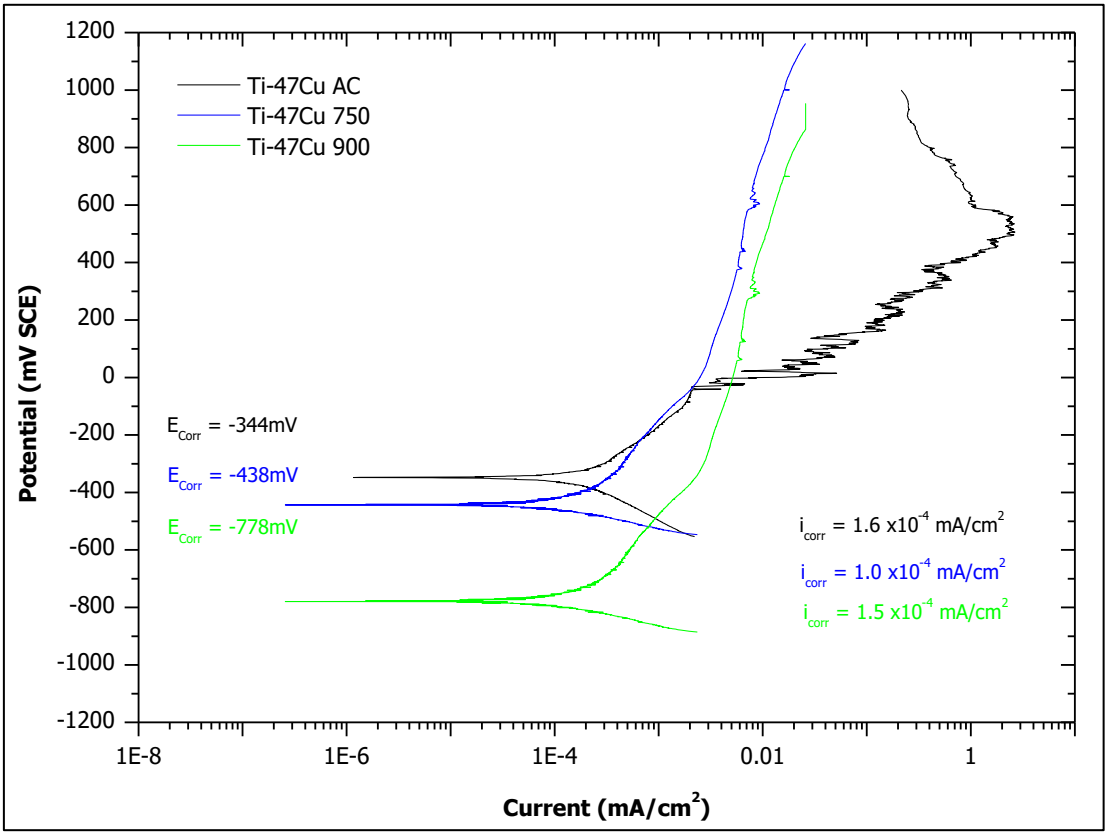


Figure 4-77. Potentiodynamic polarisation curves of Ti-47Cu in PBS.

Table 4-33. Corrosion tests results for Ti-47Cu.

Alloy		OCP (mV)	E_{Corr} (mV SCE)	I_{corr} (mA/cm²)	Corrosion Rates (mm/y)	
					Individual	Average
Ti-47Cu	As-cast	-159	-344	$1.6X10^{-04}$	0.00144	0.00198±0.000763
		-304	-244	$2.8X10^{-04}$	0.00252	
	750°C	-512	-438	$1.0X10^{-04}$	0.00108	0.00090±0.000127
		-304	-646	$1.2X10^{-04}$	0.00090	
	900°C	-636	-778	$1.5X10^{-04}$	0.00135	0.00126±0.000127
		-600	-736	$1.3X10^{-04}$	0.00117	

4.3.8 Ti-50Cu

Figure 4-78 and Figure 4-79 show the OCP and potentiodynamic polarisation curves in the PBS solution. The sample heat treated at 900°C was less noble compared to both the as-cast and 750°C heat treated sample, as shown in Figure 4-78. A long passivation stage was observed in the potentiodynamic polarisation curves, indicating that good passivation protection formed. At approximately 200 mV, for the as-cast sample a passive film broke down and re-passivation was observed at the increase in current. During as shown in Figure 4-79. The heat treated samples showed an order of magnitude increased corrosion rates compared to the as-cast sample. Table 4-34 shows the OCP and potentiodynamic polarisation results.

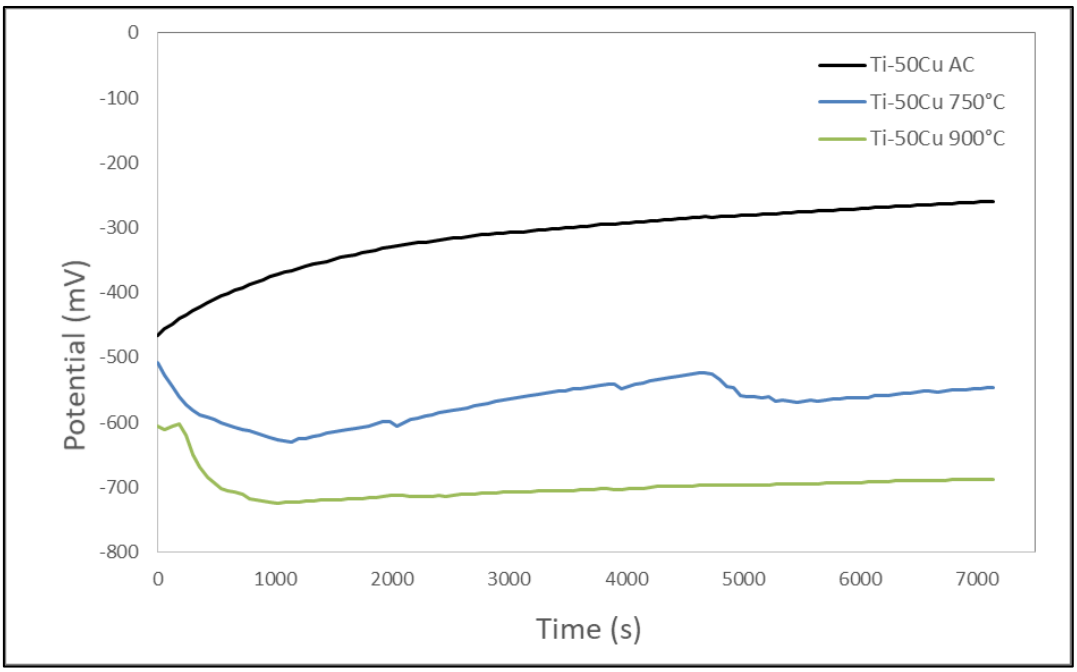


Figure 4-78. OCP of Ti-50Cu in PBS.

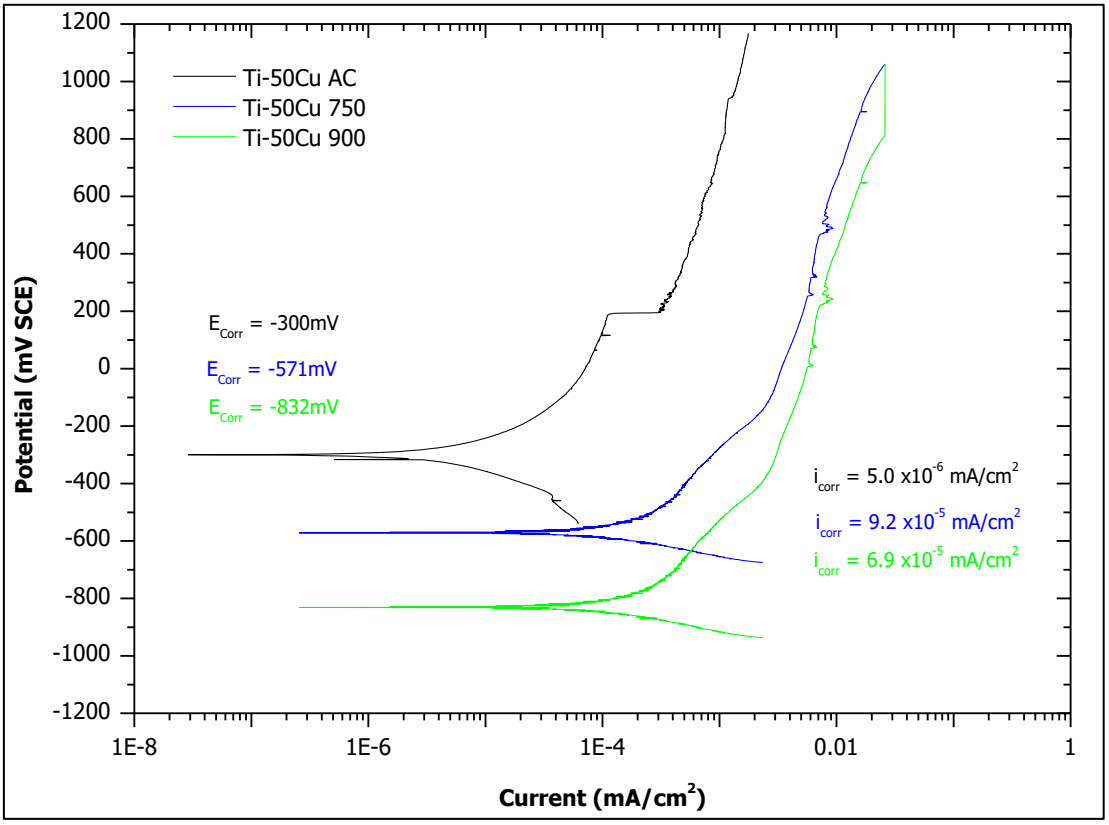


Figure 4-79. Potentiodynamic polarisation curves of Ti-50Cu in PBS.

Table 4-34. Corrosion tests results for Ti-50Cu.

Alloy		OCP (mV)	E_{Corr} (mV SCE)	I_{corr} (mA/cm²)	Corrosion Rates (mm/y)	
					Individual	Average
Ti-50Cu	As-cast	-260	-247	$6.4X10^{-06}$	0.00006	0.00005±0.000008
		-297	-300	$5.0X10^{-06}$	0.00005	
	750°C	-546	-571	$9.2X10^{-05}$	0.00083	0.00082±0.000006
		-427	-692	$9.1X10^{-05}$	0.00082	
	900°C	-688	-832	$6.9X10^{-05}$	0.00062	0.00068±0.000076
		-662	-803	$8.1X10^{-05}$	0.00073	

4.4.2 Immersion Testing

Mass-loss evaluations were performed after 30 days exposure in PBS. All the alloys showed weight gain after exposure indicating passivation. The as-cast samples showed a higher weight gain compared to the annealed samples. The samples annealed at 900°C showed the lowest weight gain, as shown in Figure 4-80. Table 4-35 shows all the results. Figure 4-81 to Figure 4-83 show the alloys after testing, and they appeared to have suffered no damage.

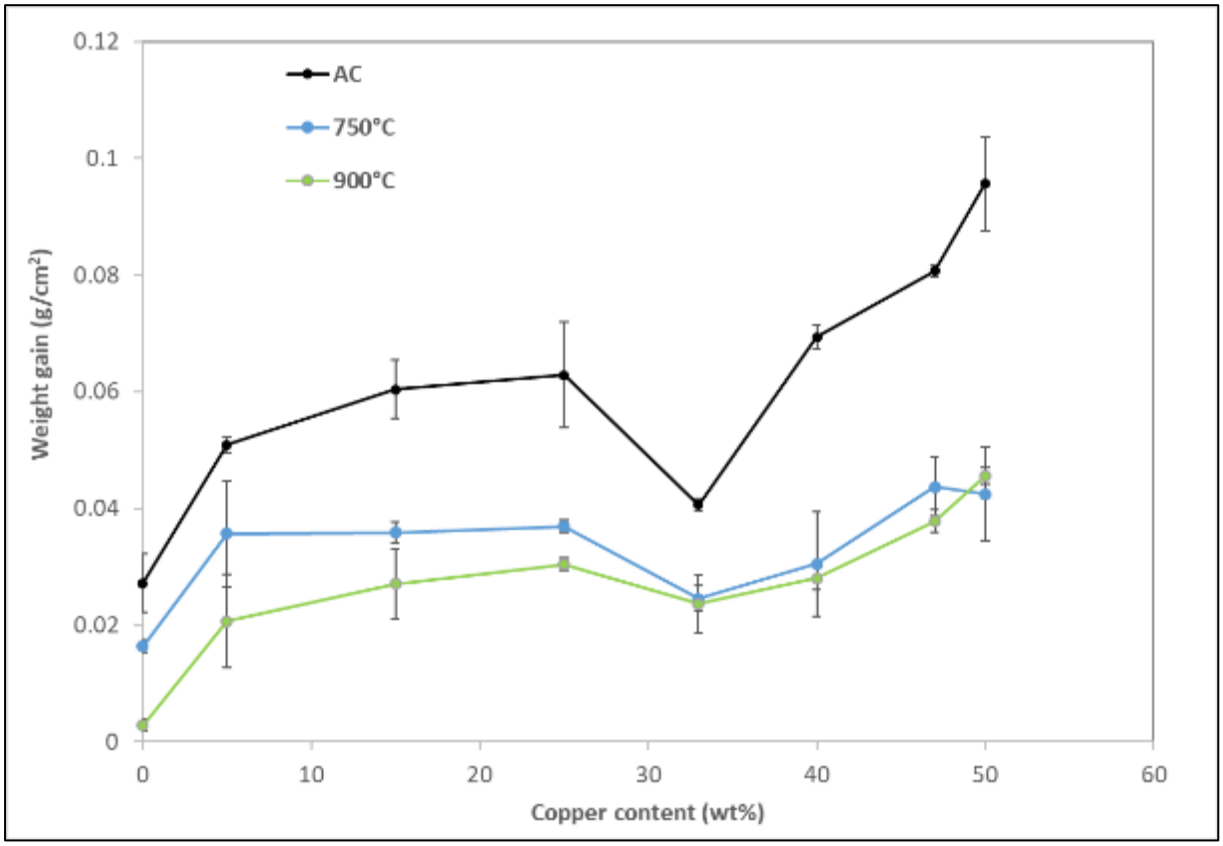


Figure 4-80. Immersion test results for all the alloys.

Table 4-35. Immersion test corrosion results of the alloys, after 720 h.

Alloy	Weight gain (g)	Weight gain (g/cm^2)
As-cast		
CP Ti	0.4103	0.0272±0.005
Ti-5Cu	0.3003	0.0509±0.001
Ti-15Cu	0.1746	0.0604±0.005
Ti-25Cu	0.4142	0.0629±0.009
Ti-33Cu	0.2726	0.0407±0.0011
Ti-40Cu	0.4478	0.0694±0.002
Ti-47Cu	0.5228	0.0807±0.001
Ti-50Cu	0.5007	0.0956±0.008
750°C		
CP Ti	0.0400	0.0164±0.001
Ti-5Cu	0.2144	0.0356±0.009
Ti-15Cu	0.3101	0.0358±0.0020
Ti-25Cu	0.0998	0.0369±0.001
Ti-33Cu	0.1009	0.0245±0.0021
Ti-40Cu	0.1003	0.0305±0.0001
Ti-47Cu	0.2055	0.0437±0.005
Ti-50Cu	0.3416	0.0425±0.008
900°C		
CP Ti	0.0032	0.0029±0.001
Ti-5Cu	0.0493	0.0207±0.008
Ti-15Cu	0.0858	0.0271±0.006
Ti-25Cu	0.0688	0.0305±0.001
Ti-33Cu	0.021	0.0236±0.0051
Ti-40Cu	0.1535	0.0280±0.0002
Ti-47Cu	0.1979	0.0378±0.002
Ti-50Cu	0.3005	0.0455±0.001

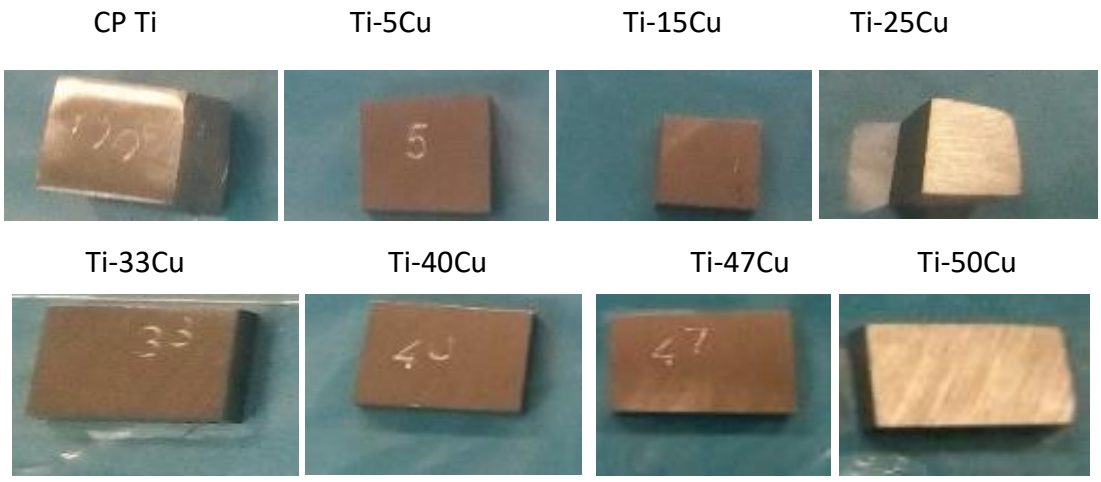


Figure 4-81. As-cast alloys after 30 days exposure in PBS solution.

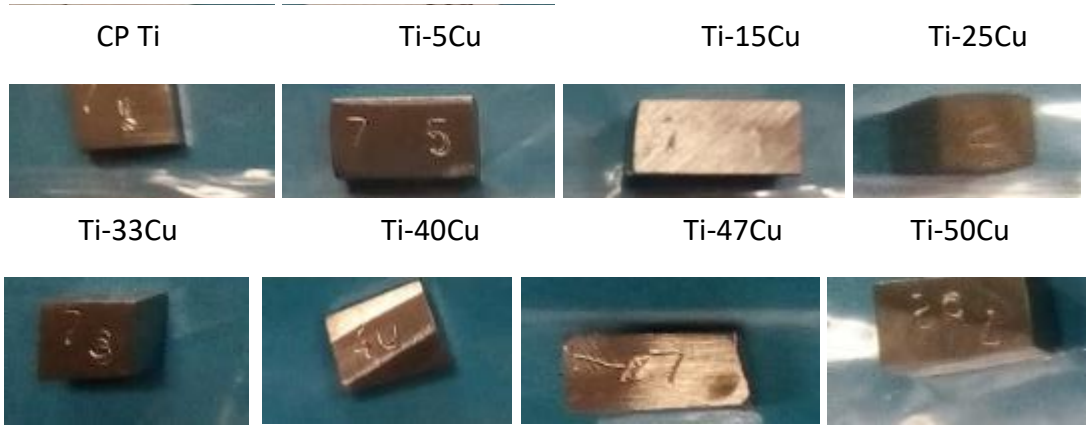


Figure 4-82. Alloys HT at 750°C after 30 days exposure in PBS solution.

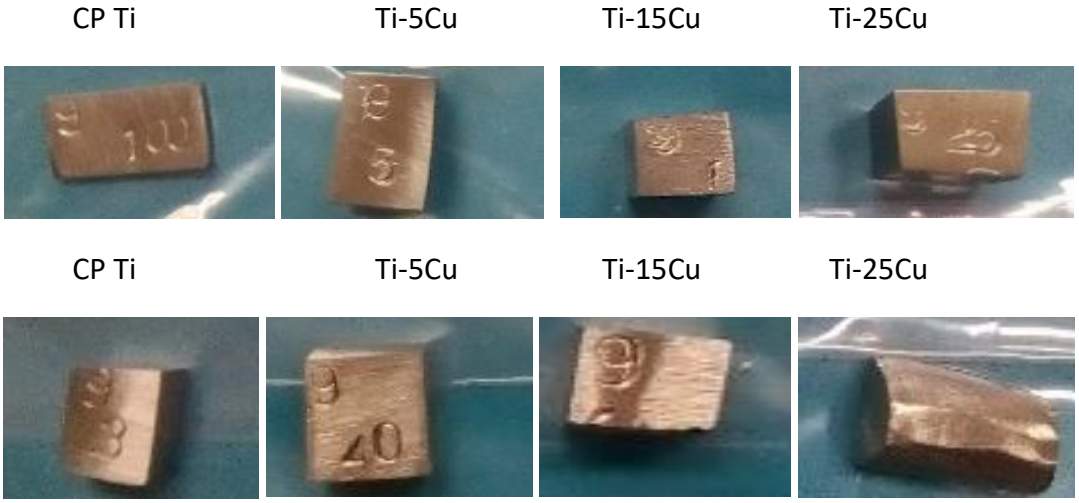


Figure 4-83. Alloys HT at 900°C after 30 days exposure in PBS solution.

4.5 Bacteria Testing

The alloys analysed were as-cast. The analysis after 2 and 6 hours were plotted to show the average antibacterial rate (R) for the alloys. The antibacterial rates after 2 hours were negative, except for Ti-33Cu with an antibacterial rate of 11.4%, as shown in Figure 4-84. The antibacterial rates after 6 hours were 12.2%, 5.9%, 5.9% and 7.7% for Ti-5Cu, Ti-15Cu, Ti-25Cu and Ti-33Cu respectively, as shown in Figure 4-85. Table 4-36 shows the antibacterial rate results of the alloys. The highest antibacterial rate was observed for the Ti-5Cu alloy, followed by Ti-33Cu. The Ti-15Cu and Ti-25Cu alloys had similar and low antibacterial rates after 6 hours.

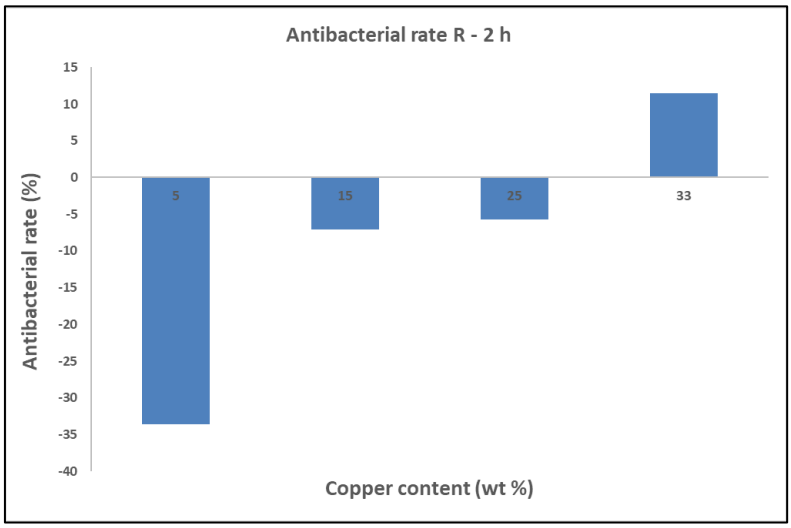


Figure 4-84. Antibacterial Rate (R) after 2 hours for the as-cast alloys.

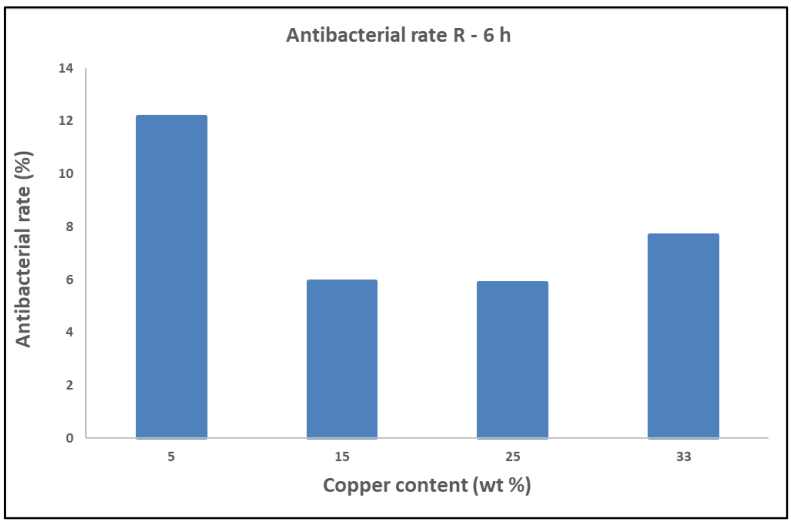


Figure 4-85. Antibacterial Rate (R) after 6 hours for the as-cast alloys.

Table 4-36. Antibacterial rate of the alloys as-cast.

Alloys	**Antibacterial rate (R) - (%) luminescence**	
	2 h	**6 h**
CP Ti	-	-
Ti-5Cu	-33.6	12.2
Ti-15Cu	-7.1	5.9
Ti-25Cu	-5.7	5.9
Ti-33Cu	11.5	7.7

Chapter 5: DISCUSSION

Materials characterisation

The CP Ti as-cast and annealed samples comprised basket-weave acicular microstructures. The basket weave structure is known as a Widmanstätten structure, and is characterised by long plate-like structures that are caused by the rapid growth of the incoherent interfaces that exist at the narrow edges (Brice, 2015). The EDX and XRD results showed (αTi), which indicates that the quenching was not sufficient enough to retain (βTi) and also not in agreement with Thermo-Calc predictions which were for equilibrium conditions. The CP (αTi) XRD peaks were observed at 2Θ = 62° and 74.5° but were absent from the modelled diffractogram with the closest being at 2Θ = 59° and 2Θ = 77°, this is because the modelled diffractogram was performed for pure titanium, whereas the phases in the alloys had some solid solution, even if in small amounts. Peaks for experimental alloys could be lost in the background. The modelled structures might not be totally respresntatative, as they did not appear as conventional unit cells (Figures 4-10 and 4-11).

The Ti-5Cu as-cast and annealed at 750°C comprised a dark (αTi) matrix and light Ti_2Cu precipitates, while the alloys annealed at 900°C had (αTi) surrounded by (αTi) + Ti_2Cu. Thermo-Calc prediction indicated that (βTi) would be present but (βTi) was not retained, because the quenching rate was insufficient. The EDX indicated that the light phase was Ti_2Cu, although the analyses included the surrounding (αTi) because the Ti_2Cu was fine. XRD analyses showed the dark phase was (αTi) and light phase was Ti_2Cu. According to the binary Ti-Cu phase diagram, Ti_2Cu precipitates in (αTi) matrix under equilibrium because of the sloping (αTi) solvus (Murray, 1987; Canale & Servant, Zhang, et al., 2016; 2002; Brice, 2015; Xu, et al., 2020). Thus, little copper can dissolve in the (αTi) solid solution in binary Ti-Cu at room temperature. According to the lever rule, 0.2 % mass fraction of Ti_2Cu was expected to precipitate.

The microstructures of Ti-15Cu and Ti-25Cu alloys comprised medium contrast (βTi) dendrites which may have formed first, followed by the light regions (sparse eutectic mixture of Ti_2Cu and βTi), which surrounded the dendrites. The (βTi) dendrites decomposed to (αTi) (dark contrast) and Ti_2Cu (light contrast). Ti-33Cu comprised dark contrast (βTi) dendrites

surrounded by Ti_2Cu (light contrast). The dendrites were fewer and smaller with more of Ti_2Cu (light contrast).

The EDX analyses indicated the dark dendrites to be (αTi) and the matrix to be Ti_2Cu which is in agreement with the XRD patterns which confirmed (αTi) and Ti_2Cu phases for both as-cast and annealed alloys. As well as there being more Ti_2Cu in the microstructure, the relative peak intensity of Ti_2Cu increased with more copper, indicating that more Ti_2Cu phase formed. Thermo-Calc™ predicted both (αTi) and (βTi) phases, as well as the Ti_2Cu phase.

For Ti-40Cu and Ti-47Cu, the titanium oxide dendrites solidified first and then Ti_2Cu nucleated on them and grew as dendrites surrounded by the TiCu phase. The Ti_2Cu dendrites in the Ti-40Cu sample show that it solidified congruently, rather than from a peritectic reaction from (βTi), and there was also a sparse TiCu + Ti_2Cu eutectic (Figure 4.44). The dark phase had less copper than the light phase, as would be expected from the contrasts. The dendrites became coarser with annealing. For Ti-50Cu, the titanium oxide dendrites solidified first and then TiCu Ti_2Cu nucleated on them and grew as needles, which were then surrounded by the TiCu + Ti_2Cu eutectic (Figure 4.56). The XRD patterns and EDX confirmed Ti_2Cu and TiCu intermetallic phases for both as-cast and annealed alloys. Thermo-Calc™ predicted the presence of both Ti_2Cu and TiCu including the (βTi) phase for Ti-40Cu.

The Ti_2Cu peak was observed at $2\Theta = 49.5°$ by Material Studio but in the XRD patterns of the samples shows this peak to appear at 51°. This may be due to the peak shift. The lattice distortion, due to defects, may cause a shift in the XRD peaks positions, depending on the type of strain in the crystal structure (Kumari, et al., 2015). However, the peak shift should be small since Ti_2Cu only has a narrow phase range.

Zhan et al. (2012) reported that Ti_3Cu was observed in Ti-25Cu annealed at 750 °C for 90 hours and not on the sample annealed at 805°C. They reported that Ti_3Cu precipitated in the dendritic Ti_{ss} phase with Ti_2Cu as the other phase, this was reported to be due to the annealing time being limited and fast quenching. Karlsson (1951) also reported the Ti_3Cu phase at 25 and 27.5 at. % Cu. In this work, during solidification the liquid solidified to (βTi) dendrites first, followed by Ti_2Cu in the Ti-25Cu and Ti-33Cu samples. The dendrites

subsequently transformed to (αTi) and Ti_2Cu in the solid state. No Ti_3Cu was observed by metallography, EDX and XRD analysis for all the alloys. Thermo-Calc™ also did not predict Ti_3Cu because it was not in the database used (database TTTI3). The Material Studio modelled XRD patterns of the phases were compared with the peaks observed on the samples by XRD analysis. Ti_2Cu and Ti_3Cu peaks observed by modelling were different. Ti_2Cu had the first peak at 2Θ = 22.5° while Ti_3Cu had it at 2Θ = 29.0°. Ti_2Cu had the high intensity peak at 2Θ = 45.5° while Ti_3Cu had the high intensity peak at 2Θ = 46° (Figure 4-12 and Figure 4-13). The experimental XRD results were similar for all the alloys showing initial Ti_2Cu peaks at 2θ = 19° which is in agreement with Mueller & Knott (1963). The high intensity peaks were at 2θ = 46°.

The phase diagram drawn using the Thermo-Calc software showed a congruent formation of Ti_2Cu without Ti_3Cu (Figure 4-1). Ansara et al. (2021) reported congruent formation of Ti_2Cu without Ti_3Cu, and a sparse (βTi) + Ti_2Cu eutectic (from the position of the eutectic point). Dyal Ukabhai et al. (2022) determined the temperatures of the reactions by DSC and also reported the formation of Ti_2Cu as congruent and also associated with L ↔ (βTi) + Ti_2Cu reaction. The position of the eutectic point was confirmed as being much closer to Ti_2Cu than (βTi), which gave a sparse eutectic. Thus, this work agrees with Ansara et al. (2021) and Dyal Ukabhai et al. (2022), and not with Canale and Servant (2002) who reported Ti_3Cu, nor with Murray (1987) who reported no Ti_3Cu and a peritectic formation of Ti_2Cu from (βTi), nor with Okomoto (2002) who reported Ti_3Cu and peritectic formation of Ti_2Cu. The Ti_2Cu p\hase was identified rather than Ti_3Cu because of the Cu/Ti ratio in the EDX analyses, and because of the 2Θ = 19° peak of Ti_2Cu was found. Ti_3Cu is assumed to be metastable (Ansara et al., 2021). This work also does not agree with Zhan et al. (2012) who found Ti_3Cu.

Hardness

The addition of copper into titanium increased the hardness of the alloys, while annealing the alloys at both temperatures decreased the hardness (Figure 5-1) because the microstructures coarsened. This was also observed by Liu, et al. (2014) and (Hayama, et al., 2014). The hardness reached a peak at Ti-25Cu. In titanium alloys, it is well known (Hayama, et al., 2014) that an increase in the content of the β stabilizing element causes hexagonal martensite to transform into orthorhombic martensite; however, the current XRD and metallography

results did not reveal this phenomenon. Further increase in copper content did not change the hardness significantly (almost remained constant), although a decrease was observed in the Ti-33Cu alloy. This decrease may have been due to inhomogeneity of the sample.

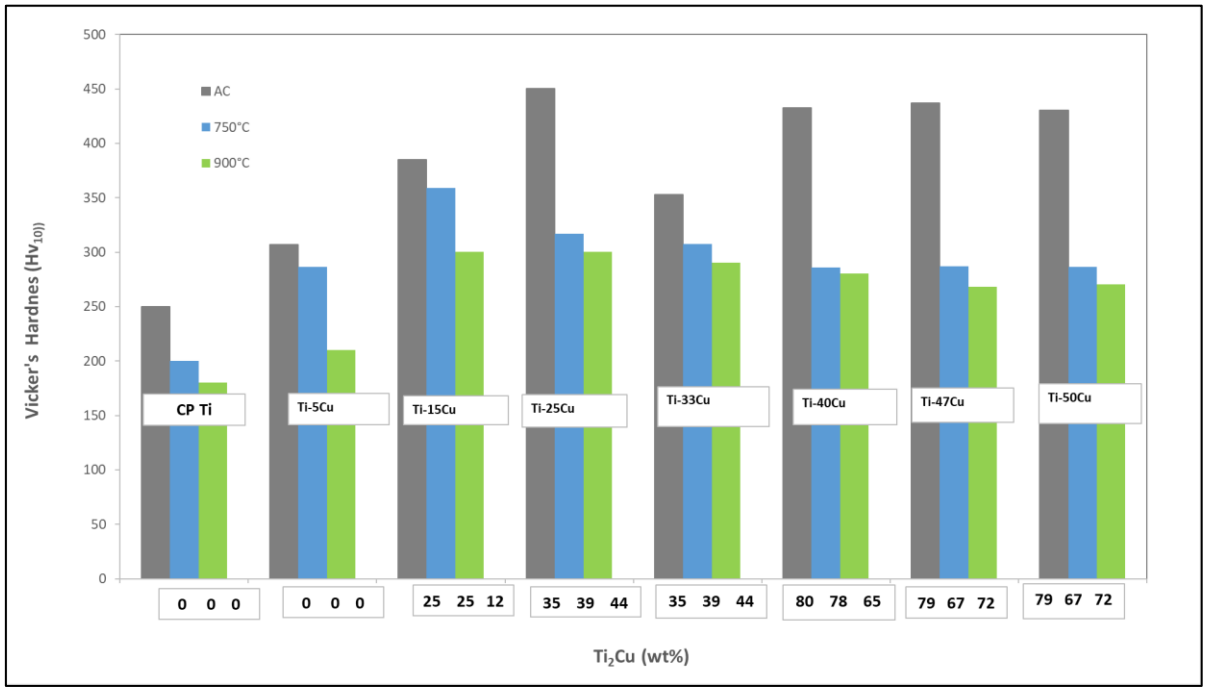


Figure 5-1. Effect of Ti_2Cu proportions on Vicker's hardness bar graph based on the samples.

With increasing copper content, the volume fractions of (αTi) and Ti_2Cu phases changed.

The alloys annealed at 900°C had lower hardness compared to the alloys annealed at 750°C and the as-cast condition, Figure 4-63. Hardness tends to be higher when a finely dispersed intermetallic phase in a phase matrix is obtained (Hayama, et al., 2014). The hardness decrease of the annealed samples was due to the precipitates coarsening (Božić, et al., 2008).

Corrosion Testing

The corrosion potential (mV) is reported as a function of time in an open circuit. The alloys in the series with the most active (negative) potentials would tend to undergo more significant corrosion, while the other alloys (with positive potential values) would generally suffer less attack. The OCP is used as a criterion for the corrosion behaviour (Mareci, et al., 2009). Compared with the CP Ti, the addition of copper shifted the OCP towards the noble positions for all the alloys in all conditions, except for Ti-25Cu annealed at 900°C. This indicates that Ti-

Cu alloys could suffer less corrosion compared to the CP Ti and this was also observed by Zhang et al. (2016). Annealing at 900°C shifted the potential towards the less noble positions, indicating that these alloys are expected to undergo more significant corrosion compared to the as-cast and alloys annealed at 750°C.

As-cast Ti-15Cu, Ti-33Cu, Ti-40Cu, Ti-47Cu and Ti-50Cu including the alloys annealed at 750°C Ti-15Cu, Ti-25Cu, Ti-33Cu, Ti-40Cu and Ti-47Cu rapidly increased to reach a near steady state at the initial stage of immersion, which is typically attributed to the growth and stabilisation of the passive film (Bao, et al., 2018; Wang, et al., 2019). As-cast CP Ti, Ti-5Cu,Ti-25Cu and Ti-33Cu, annealed at 750°C, CP Ti (as-cast and annealed), Ti-33Cu (as-cast and annealed) and Ti-50Cu (as-cast and annealed), including all the alloys annealed at 900°C showed an initial decrease in OCP suggesting that the characteristics of passive film changed in this medium (PBS), leading to a reduced corrosion resistance (Mareci, et al., 2009). Figure 5-2 to Figure 5-4 show the OCP of all the alloys.

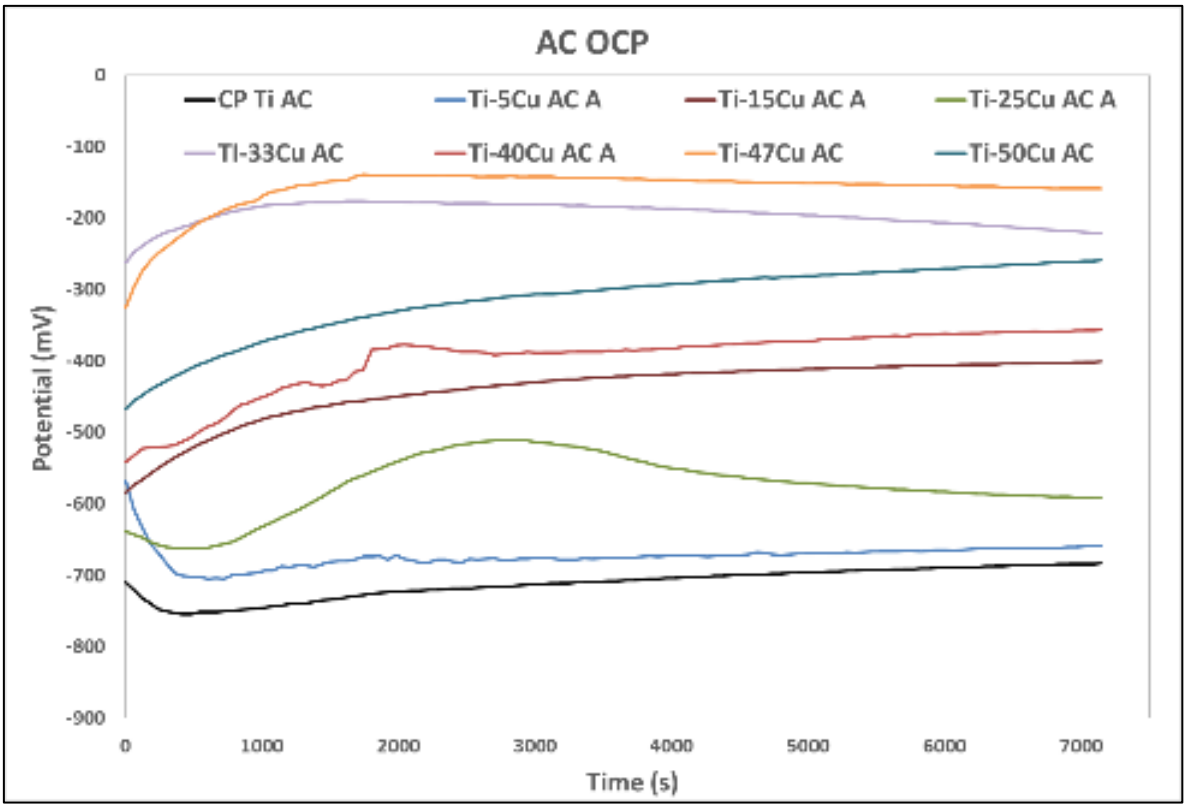


Figure 5-2.OCP of all the as-cast alloys.

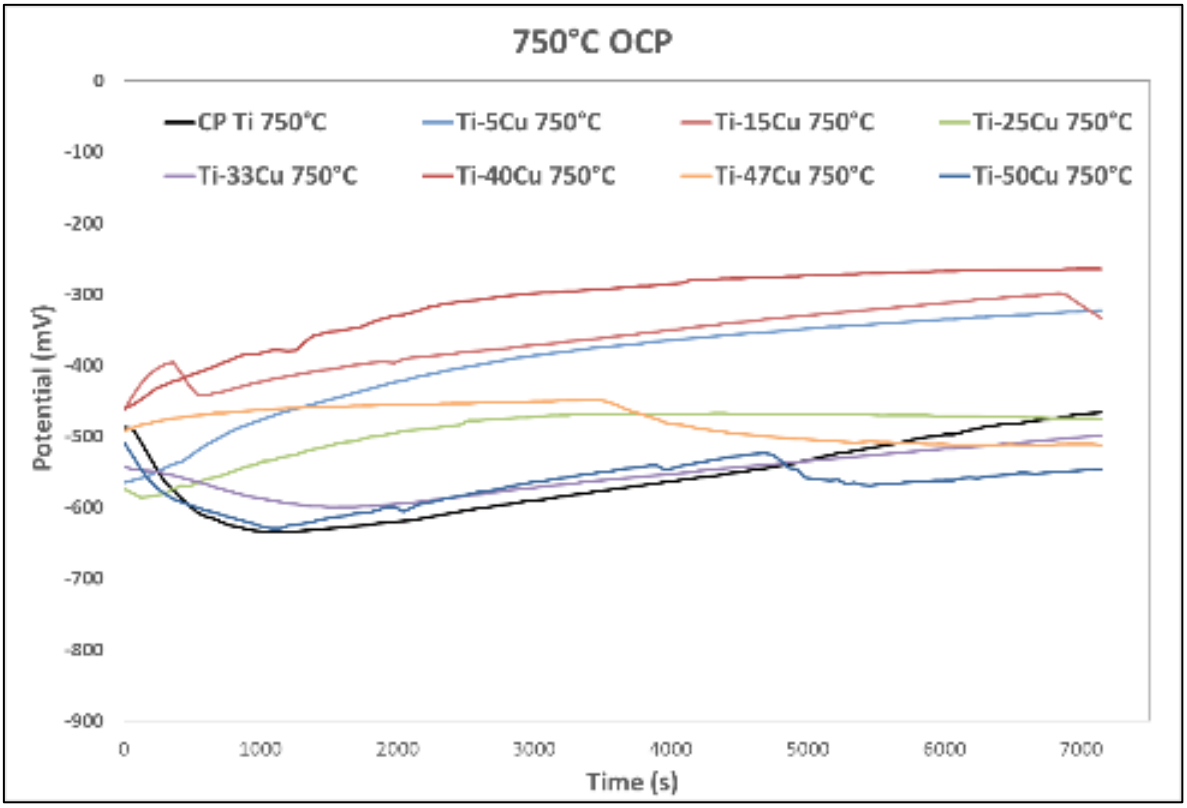


Figure 5-3. OCP of all the alloys annealed at 750°C.

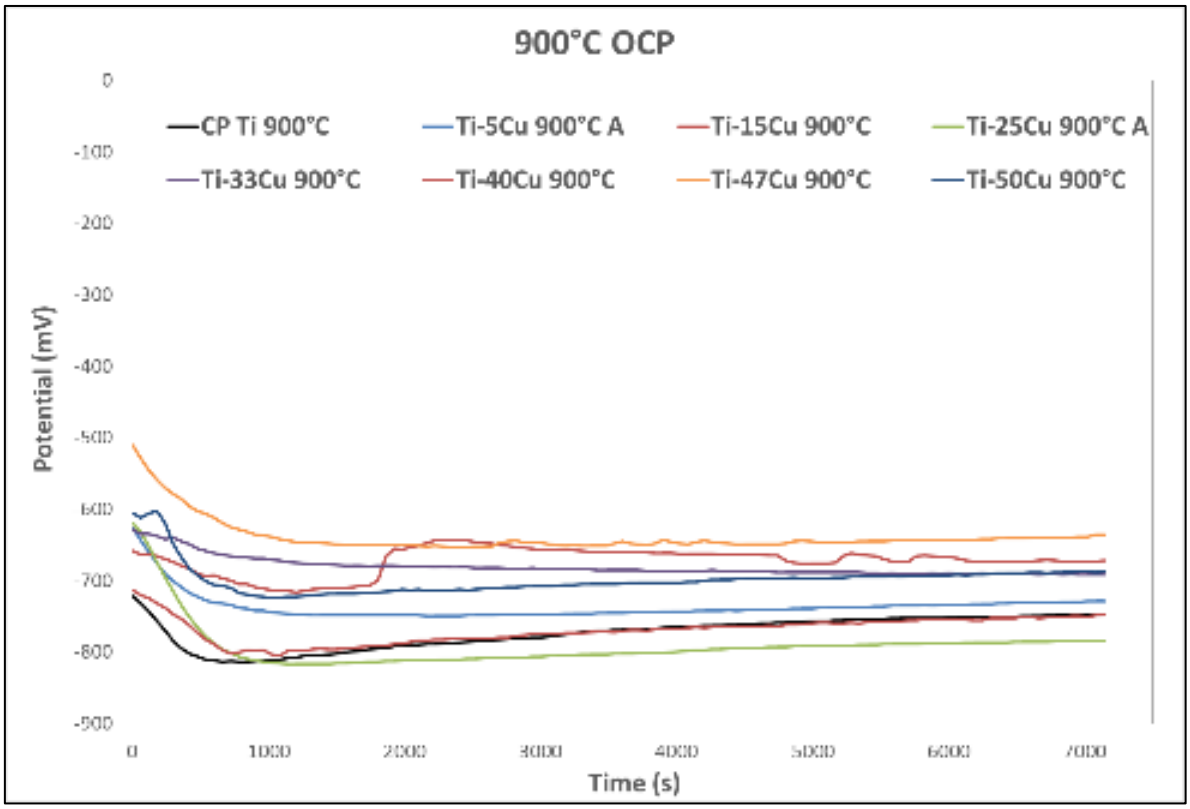


Figure 5-4. OCP of all the alloys annealed at 900°C.

The corrosion behaviour of alloys is mainly controlled by galvanic corrosion between titanium matrix and a secondary phase in the matrix (Zhang, et al., 2021). From the electrochemical viewpoint, the titanium rich regions (αTi) are expected to be nobler regions compared to the copper rich regions. Depending on the compositions, the Ti–Cu phase diagram shows that precipitation of Ti_2Cu intermetallic phase can occur in Ti–Cu alloys (Murray, 1987; Okamoto, 2002; Canale & Servant, 2002; Ansara & Ivanchenko, 2002; Brice, Xu, et al., 2020; Ansara, et al., 2021). In terms of corrosion resistance, intermetallic phases are nobler when compared to the metallic matrix (Osório, et al., 2010; Zhang, et al., 2021).

The microstructural characterization of Ti-5Cu as-cast and annealed hypo-eutectoid Ti–5Cu alloy revealed titanium phases, (αTi). The Ti_2Cu intermetallic phase was nobler than both the titanium (αTi), resulting in the lamellar Ti_2Cu (Figure 4-21 to Figure 4-23) surrounding and thus "enveloping" the titanium solid solution (less noble) thus providing corrosion protection, as shown in Figure 4-66 . Enveloping prevents the phase from being in contact with the corrosive liquid and thus giving the corrosion protection (Zhang, et al., 2021). Although Ti_2Cu formed on the (βTi) phase after annealing at 900°C, it still enveloped the titanium solid solutions, as shown in Figure 4-23. Annealing at 750°C shifted the potential towards noble position (-382±6 mV, Figure 4-66) indicating that it could suffer less corrosion attack compared to the as-cast (-679±10 mV, Figure 4-66) and the alloys annealed at 900°C (-755±9 mV, Figure 4-66). Therefore, the addition of 5 wt% copper (indicated by the green oval on Figure 5 5) resulted in low corrosion rates (average 0.00027±0.000000 mm/y as-cast, 0.00023±0.000038 mm/y at 750°C and 0.00026±0.000019 mm/y at 900°C) compared to all the alloys except for as-cast Ti-50Cu. This indicates that Ti-5Cu alloys had the highest corrosion resistance compared to all the other alloys. The long passivation stage in the Tafel curves observed for all the alloys (Figure 4-67) indicated good passivation on the surface, which showed that neither copper additions nor annealing reduced the passivation protection. Osório et al. (2010) indicated that with lower copper content, a more homogeneous and smoother oxide film formed which then resulted in low corrosion rates as observed in Ti-5Cu compared to the other alloys, as shown in Figure 4-67.

Ti-15Cu, Ti-25Cu and Ti-33Cu were hyper-eutectoid alloys. The microstructures were similar and comprised dark dendrites (βTi) and Ti_2Cu phases for the as-cast and annealed alloys.

Increased copper content resulted in increased fractions of Ti_2Cu. Increasing the volumetric fraction Ti_2Cu changes the cathode/anode ratio which then affects the electrochemical behaviour of the alloys, as shown in Figure 5-6. An unfavourable area ratio is a large cathode and small anode (Fontana & Greene, 1986). The as-cast and the alloys annealed at 750°C had OCP in the noble areas, while the alloys annealed at 900°C shifted the OCP towards less noble positions. This indicated that the samples annealed at 900°C would suffer more corrosion, followed by the samples annealed at 750°C and then the as-cast alloys would suffer less corrosion. The corrosion resistance decreased with increasing copper content in the as-cast and annealed conditions compared to CP Ti, which was attributed to more Ti_2Cu, resulting in an increased galvanic corrosion effect, as shown in Figure 5-6. Osório et al. (2010), Pina et al. (2016) and Zhang et al. (2016) also reported increased current density with increased copper content in Ti-Cu alloys. Although the galvanic corrosion effect was increased for these alloys in the as-cast and annealed conditions, especially for Ti-33Cu (corrosion of average 0.0050±0.000038 mm/y as-cast, 0.0117±0.000045 mm/y at 750°C and 0.0126±0.000000 mm/y at 900°C), as shown in Table 4-31; Bao et al. (2018) reported that high copper content could promote the copper ion release, and result in strong antibacterial ability. The Ti-33Cu alloys had the highest corrosion rate (indicated by the red oval in Figure 5-5). This may have been because the sample tested had a high volume fraction of Ti_2Cu and less (αTi), which may have created a large potential difference between the (αTi) matrix and the Ti_2Cu phase. Given the process of melting used, the sample sectioned from the as-cast alloy may have not been homogeneous hence the volume fraction of Ti_2Cu was higher.

Ti-40Cu, Ti-47Cu and Ti-50Cu alloys showed improved corrosion resistance compared to alloys Ti-15Cu, Ti-25Cu and Ti-33Cu, but less corrosion resistance than Ti-5Cu. Annealing also did not improve the corrosion resistance, as shown in Figure 5-6. This was observed in the OCP where the as-cast and the alloys annealed at 750°C had OCP in the noble positions while the alloys annealed at 950°C shifted the OCP towards less noble positions, as shown in Figure 5-2 to Figure 5-4.

The corrosion reaction consuming cathodic oxygen is according to Equation 5-1 (Xin, et al., 2022).

$$O_2 + 2H_2O + 4e^- \rightarrow 4OH^- \quad \text{Equation 5-1}$$

The anodic degradation of Ti_2Cu in SBF solution is a complex process and can be simplified as in Equation 5-2 (Xin, et al., 2022).

$$Ti_2Cu + 8OH^- \rightarrow 2TiO_2 + Cu^{2+} + 4H_2O + 10e^- \quad \text{Equation 5-2}$$

The copper ions (Cu^{2+}) released during corrosion/anodic reaction are required in liquid solution because they promote the antimicrobial activity (Li, et al., 2016; Fowler, et al., 2019; Jiao, et al., 2021).

When titanium is in the fully passive condition, corrosion rates are typically less than 0.02 mm/y and below the 0.13 mm/y maximum corrosion rate which is commonly accepted for biomaterial design and application (Bhola, et al., 2011). The potentiodynamic polarisation tests showed that corrosion rates obtained were very low, below 0.13 mm/y. The polarisation curves had the same shape and were typical of passive behaviour, which agreed with the immersion test results (Figure 4-80) which showed that all the alloys passivated. Thus, instead of mass-loss, the samples gained weight.

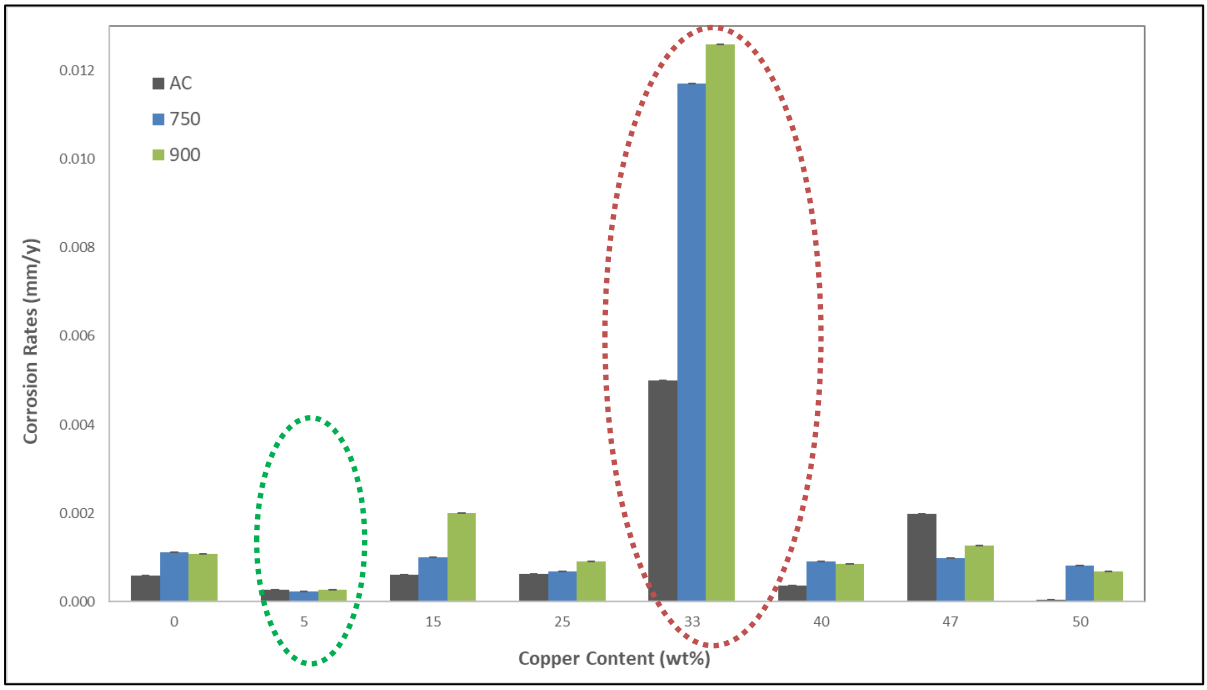


Figure 5-5. Summary of the corrosion rates: the green oval shows the lowest corrosion rates of Ti-5Cu and the red oval shows the highest corrosion rates of Ti-33Cu.

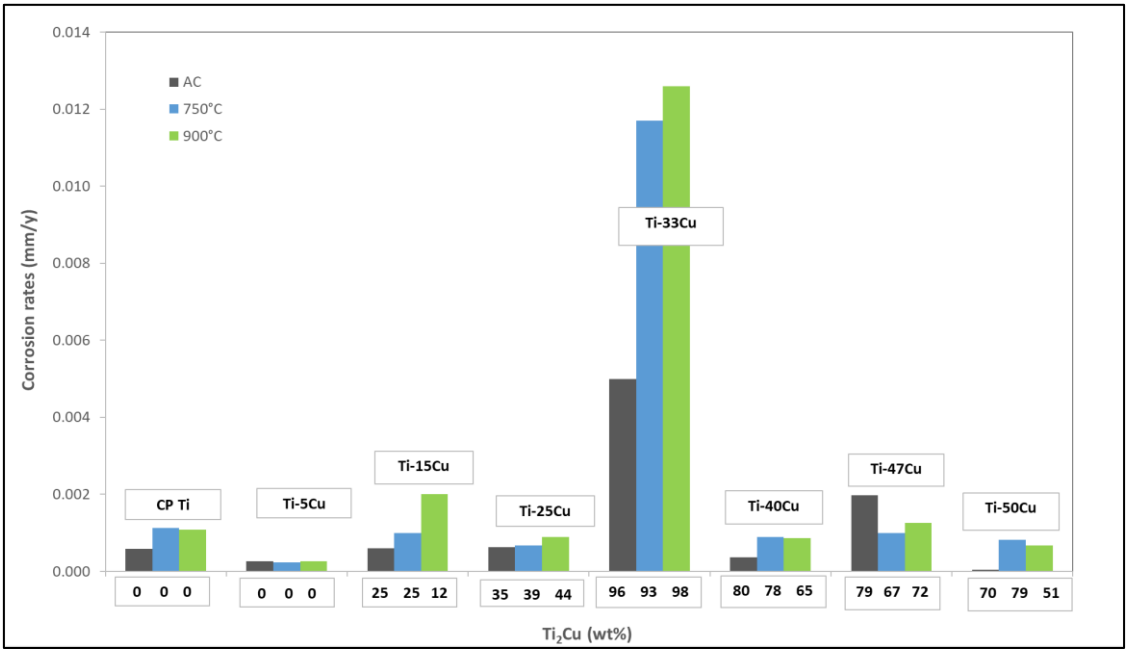


Figure 5-6. Effect of Ti_2Cu proportions on corrosion rates.

The highest antibacterial rate of 12.2% (Figure 4-85) was observed on the as-cast Ti-5Cu alloy after 6 hours indicating that it had exhibited strong antibacterial activity compared to all the other alloys. Tests performed by Zhang (2016) showed antibacterial rates of 90%; this is due to differences in the bacteria testing protocol which included: longer testing periods (18 h rather than 6 h), the use of *S. Aureus* instead of *S. Epidermidis*, and the difference in bacteria counting method used). However, while longer testing periods allow for longer exposures, the drawback of such tests is that the repeated addition of the growth medium (which ensures that the bacteria have sufficient food throughout the test) to the well plates could interfere with bacteria contact to the sample surface, in addition to interrupting the experiment. It is clear that more studies are required on all the alloys in the as-cast and annealed conditions to ascertain the influence of Ti_2Cu on antibacterial rate, and even Fowler et al. (2019), with their more extensive study came to this conclusion.

Chapter 6: CONCLUSIONS AND RECOMMENDATIONS

Both as-cast and annealed CP Ti samples comprised basket-weave acicular (αTi) microstructures. The (βTi) was not retained because the samples annealed at 900°C could not be quenched fast enough. As-cast and annealed Ti-5Cu samples comprised lamellar (αTi) and Ti_2Cu. Similar to Ti-5Cu, the microstructures of Ti-15Cu, Ti-25Cu and Ti-33Cu alloys comprised dark dendrites (αTi) and Ti_2Cu phases for the as-cast and annealed alloys. In Ti-40Cu and Ti-47Cu, the titanium oxide dendrites solidified first and then Ti_2Cu nucleated on them and grew as dendrites surrounded by the sparse Ti_2Cu + TiCu eutectic. In Ti-50Cu, TiCu was the true primary phase, growing as needles and was surrounded by the Ti_2Cu + TiCu eutectic. During casting great care was taken in melting to eliminate oxygen but the alloys showed that oxygen still remained. No Ti_3Cu phase was observed and the XRD peak at $2\theta = 19^\circ$ showed that Ti_2Cu was present, not Ti_3Cu. The Ti_2Cu solidified congruently, thus this work agreed with the phase diagram by Ansara et al. (2021). The addition of copper into titanium increased the hardness of the alloys, while annealing the alloys decreased the hardness.

Increasing the volume fraction of Ti_2Cu changed the cathode/anode ratio and affected the electrochemical behaviour of the alloys. The higher volume fraction of Ti_2Cu decreased the corrosion resistance, especially for Ti-33Cu, as shown in Figure 5-6. The potentiodynamic polarisation tests showed that the corrosion rates obtained were very low, below 0.13mm/y, which is an acceptable corrosion rate for biomaterial applications. This was indicated by the shape of the potentiodynamic scans and mass-loss testing which showed passivation of all the alloys. However, since copper ions in liquid solution promote antimicrobial activity, some corrosion is necessary to allow the copper ions to be available. Ti-5Cu showed excellent corrosion resistance compared to the other alloys, and Ti-33Cu showed lower corrosion resistance.

The Ti-Cu alloys of 5, 15, 25, 33, 40, 47 and 50 wt% copper were successfully cast and annealed followed by quenching. The quenching rate was insufficient, since the (βTi) phase was not retained after annealing at 900°C for the alloys up to ~40 wt% Cu. The following phases were obtained: (αTi), Ti_2Cu, Ti_2Cu and TiCu. Different microstructures with increased volume fractions of Ti_2Cu were obtained, which resulted in an increase in hardness. Alloy Ti-33Cu

showed the lowest hardness and highest corrosion, indicating that this alloy may have not been homogeneous after casting. The corrosion resistance derived by electrochemical testing showed acceptable corrosion resistance for all the alloys, while the immersion test showed that all alloys were passive when exposed to PBS solution at 37°C.

Future work

The analysis of Ti_2Cu phase proportions should be performed using image analysis or TEM to possibly improve the accuracy. The corrosion rates for the Ti-33Cu alloy needs to be investigated since they were unusually high for all heat treatments. A higher antibacterial rate and higher corrosion resistance was observed for the Ti-5Cu sample which makes this alloy the best alloy to consider for biomedical application but it is recommended that more bacteria tests be performed for longer time (18 hours) to obtain more reliable results.

REFERENCES

Adams, F. (2013). *National Council of Provinces Committee Economic and Business Development.* Accessed November 10, 2018, from https://pmg.org.za/committee-meeting/15437.

Adya, N., Alam, M., Ravindranath, T., Mubeen, A., Saluja, B. (2017). Corrosion in titanium dental implants:Literature review. *The Journal of Indian Prosthodontic Society,* 5(3), pp. 126-131.

Ananth, H., Kundapur, V., Mohammed, HS., Anand, M., Amarnath, GS., Mankar, S. (2015). A review on biomaterials in dental implantology. *International Journal of Biomedical Science*, 11(3), pp. 113-120.

Andrews, J. (2001). Determination of minimum inhibitory concentrations. *Journal of Antimicrobial Chemotherapy*, 48 (1), pp. 5-16.

Ansara, I., Ivanchenko ,V., Cornish, L., Ukabhai Dyal, K., Nape, K. (2021). Cu-Ti Binary Phase Diagram Evaluation, in MSI Eureka, Watson, A. (Ed.), MSI, *Materials Science International Services GmbH*, Stuttgart, Document ID: 20.11457.2.4.

ASTM NACE TM0169/G31—12a (2012). Standard Guide for Laboratory Immersion Corrosion Testing of Metals. Philadelphia: *ASTM International*. http://dx.doi.org/10.1520/G0031-12A

ASTMG5. (2013). Standard Reference Test Method for Making Potentiodynamic Anodic Polarization Measurements*, available from ASTM Headquarters Order PCN 12-700050-00.*

Baker, J., Sitthisa, S., Sengupta, M., Johnson, M., Jayaswal; R.K., Morrissey, J.A. (2010). Copper Stress Induces a Global Stress Response in Staphylococcus aureus and Represses sae and agr Expression and Biofilm Formation. *American Society for Microbiology,* 76(1), p. 150-160.

Bao, M., Liu, Y., Wang, X., Yang, L., Li, S., Ren, J. (2018). Optimization of mechanical properties, biocorrosion properties and antibacterial properties of wrought Ti-3Cu alloy by heat treatment. *Bioactive Materials*, 3(1), pp. 28-38.

Bhola, R., Bhola, S., Mishra, B., Olson, D. (2011). Corrosion in titanium dental implants/prostheses - A review. *Trends Biomater and artificial organs,* 25(1), pp. 34-46.

Bhola, S., Mishra, B. (2013). Effect of pH on the Electrochemical Properties of Oxides formed over β – Ti-15Mo and Mixed Ti-6Al-4V Alloys. *International Journal of Electrochemical Science,* 8, pp. 7075-7087.

Bowen, W., Burne, R., Wu, H., Koo, H. (2018). Oral Biofilms: Pathogens, matrix and polymicrobial interactions in microenvironments. *Trends in Microbiology,* 26(3), pp. 229-242.

Božić, D., Dimčić, O., Cvijović, I., Rajković, V. (2008). The combination of precipitation and dispersion hardening in powder metallurgy produced Cu–Ti–Si alloy. *Materials Characterisation,* 59(8), pp. 1222-1126.

Brice, D. (2015). *An assessment of uncommon titanium binary systems: Ti-Zn, Ti-Cu and Ti-Sb,* University of North Texas.

Bruellhoff, K., Fiedler, J., Möller, M., Groll, J., Brenner, R.E. (2010). Surface coating strategies to prevent biofilm formation on implant surfaces. *The International Journal of Artificial Organs*, 33(9), pp. 646-53.

Canale, P., Servant, C. (2002). Thermodynamic assessment of the Cu-Ti system taking into account the new stable phase $CuTi_3$. *Zeitschrift für Metallkunde,* 93, pp. 273-76.

Chaturvedi, T. (2009). An overview of the corrosion aspect of dental implants (Titanium and its alloys). *Indian Journal of Dental Research,* 20(1), pp. 91-98.

Codita, I., Caplan, D., Dragulescu, E.C., Lixandru, E.B., Coldea, L., Dragomirescu, C., Surdu-Bob, C., Badulescu, M. (2010). Antimicrobial activity of copper and silver Nano films on nosocomial bacterial species. *Roumanian Archives of Microbiology and Immunology*, 69, pp. 204-212.

Corrêa, J., Mori, M., Sanches, H.L., da Cruz, A.D., Poiate Jr,E., Poiate, I.A.V.P. (2015). Silver Nanoparticles in Dental Biomaterials. *International Journal of Biomaterials*, 2015, Article No. 485275.

Costa,R.C., Abdo, V.L., Mendes, P.H.C., Mota-Veloso, I., Bertolini, M., Mathew, M., Barão, V., Souza, J.G. (2021). Microbial Corrosion in Titanium-Based Dental Implants: How Tiny Bacteria Can Create a Big Problem? *Journal of Bio- and Tribo-Corrosion,* 7(4), Article No. 155.

Dyal Ukabhai, K., Curle, U.A., Masia, N.D.E., Smit, M., Mwamba, I.A., Norgren, S., Öhman-Mägi, C., Hashe, Cornish, L.A. (2022). Formation of Ti_2Cu in Ti-Cu Alloys. *Journal of Phase Equilibria and Diffusion*. 43, pp. 332-344.

Elias, C., Fernandes, D., Resende, C., Roestel, J. (2015). Mechanical properties, surface morphology and stability of a modified commercially pure high strength titanium alloy for dental implants. *Dental Materials,* 31(2), pp. eI-eI3.

Eliaz, N. (2019). Corrosion of Metallic Biomaterials: A Review. *Materials,* 12(3), 407.

Fais, L.M.G., Fernandes-Filho,R.B., Pereira-da-Silva, M.A., Vaz, L.G., Adabo, G.L. (2012). Titanium surface topography after brushing with fluoride and fluoride-free toothpaste simulating 10 years of use. *Journal of Dentistry,* 40(4), pp. 265-275.

Fischer, T.H., Almlof, J. (1992). General methods for geometry and wave function optimization. *Journal of Physical Chemistry*, 96(24), pp. 9768-9774.

Fontana, M., Greene, N.D. (1986). *Corrosion Engineering.* 3rd edn. Ohio: McGraw-Hill Book Company.

Fowler, L., Engqvist, H., Öhman-Mägi, C. (2019). Effect of Copper Ion Concentration on Bacteria and Cells. *Materials,* 12(22), Article No. 3798.

Francolini, I., Donelli, G. (2010). Prevention and control of biofilm-based medical-device-related infections. *FEMS Immunology and Medical Microbiology*, 59(3), pp. 227-238.

Geetha, M., Singh, A., Asokamani, R., Gogia, A. (2009). Ti based biomaterials, the ultimate choice for orthopaedic implants - A review. *FEMS Immunology & Medical Microbiology,* 58(3), pp. 397-425.

Gemelli, E., Camargo, N. (2007). Oxidation kinetics of commercially pure titanium. *Revista Matéria,* 12(3), pp. 525-531.

Gialanella, S., Malandruccolo, A. (2020). Titanium and Titanium Alloys. In: Aerospace Alloys. Topics in Mining, Metallurgy and Materials Engineering. Springer, Cham.

Gosavi, S., Gosavi, S., Alla, R. (2013). Titanium: A Miracle Metal in Dentistry. *Trends Biomaterial Artificial Organs,* 27(1), pp. 42-46.

Han, G., Lu, X; Xia, Q., Lei, B., Yan, Y., Shang, C.J. (2018). Face-centered-cubic titanium - A new crystal structure of Ti in a Ti-8Mo-6Fe alloy. *Journal of Alloys and Compounds,* 748, pp. 943-952.

Hansen, D. (2008). Metal Corrosion in the Human Body: The Ultimate Bio-Corrosion Scenario. *The Electrochemical Society Interface,* 17(2), pp. 31-34.

Hayama, A.O.F., Andrade, P.N., Cremasco, A., Contieri, R.J., Afonso, C.R.M., Caram, R. (2014). Effects of composition and heat treatment on the mechanical behaviour of Ti-Cu alloys. *Materials and Design,* 55, pp. 1006-1013.

Hohenberg, P., Kohn, W.(1964). Inhomogeneous Electron Gas. *Physical Review Journals Archives*, 1964, 136(3B), pp. B864-B871.

Hryniewicz, T., Rokicki, R., Rokosz, K. (2011). Magnetoelectropolished Titanium Biomaterial. In: *Biomaterials Science and Engineering.* USA: InTech, pp. 227-248.

Janus, A., Haagensen, I., Verotta, D., Huang, L., Spormann, A., Yang, K. (2015). New In Vitro Model To Study the Effect of Human Simulated Antibiotic Concentrations on Bacterial Biofilms. *Antimicrobial Agents and Chemotherapy*, 59(7), pp. 4074-4081.

Jiang, Y., He, Y., Liu, C. (2018). Review of porous intermetallic compounds by reactive synthesis of elemental powders. *Intermetallics,* 93, pp. 217-226.

Jiao, J., Zhang, S., Qu, X., Yue, B. (2021). Recent advances in research on antibacterial metals and alloys as implant materials. *Frontiers in Cellular and Infection Microbiology*, 11:693939 https://doi.org/10.3389/fcimb.2021.693939

Jorge, J,. Barão, V., Delben, J., Faverani, L., Queiroz, T., Assunção, W. (2012). Titanium in dentistry: Historical development, State of the art. *Indian Prosthodontic Society,* 13(2), pp. 71-77.

Karlsson, N. (1951). An X-Ray study of the phases in the Copper-Titanium system. *Journal of the Institute of Metals,* 79, pp. 391-405.

Khorasani, A., Goldberg, M., Doeven, E., Littlefair, G. (2015). Titanium in biomedical applications - Properties and fabrication: A review. *Journal of Biomaterials and Tissue,* 5(8), pp. 593-619.

Khoshnaw, F., Gubner, R. (2022). Part 1: General aspect of corrosion control, and corrosion prevention. *Corrosion Atlas Case Studies*, 2021 Edition, pp. xxv-xlii

Kikuchi, M., Takada, T., Kiyosoue, S., Yoda, M., Woldu, M., Cai, Z., Okuno, O., Okabe, T. (2003). Mechanical properties and microstructures of Ti-Cu alloys. *Dental Materials,* 19(3), pp. 174-181.

Kohn, W., Sham, L. (1964) Self-Consistent Equations Including Exchange and Correlation Effects. *Journal of Physics Review*; 140: A:1133.

Kumari, R., Sahai, A., Goswami, N. (2015). Effect of nitrogen doping on structural and optical properties of ZnO nanoparticles. *Progress in Natural Science: Materials International*, 25(4), pp. 300-309.

Li, M., Ma, Z., Zhu, Y., Xia, H., Yao, M., Chu, X., Wang, X., Yang, K., Yang, M., Zhang, Y., Mao, C. (2016). Towards a Molecular Understanding of the Antibacterial Mechanism of Copper-bearing Titanium Alloys against Staphylococcus aureus. *Advanced Healthcare Materials,* 5(5), pp. 557-566.

Liu, Y., Yang, C., Zhao, H., Qu, S., Li, X., Li, Y. (2014). Effect of Cu content on the antibacterial activity of titanium–copper sintered alloys. *Materials Science and Engineering*, 1(35), pp. 392-400.

Liu, R., Memarzadeh, K., Chang, B., Zhang, Y., Ma, Z., Allaker, R.P., Rn, L., Yang, K. (2016). Antibacterial effect of copper-bearing titanium alloy (Ti-Cu) against Streptococcus mutans and Porphyromonas gingivalis. *Scientific Report,* 6, Article No. 29985.

Liu, X., Chen, S., Tsoi, J., Matinlinna, J., (2017). Binary titanium alloys as dental implant materials—A review. *Regenerative Biomaterials,* 4(5), pp. 315-323.

Li, Y., Chen, N., Cui, H., Wang, F. (2017). Fabrication and characterization of porous Ti-10Cu alloy for biomedical application. *Journal of Alloys and Compounds,* 723, pp. 967-973.

Li, Y., Yang, C., Zhao, H., Qu, S., Li, X., Li, Y. (2014). New Developments of Ti-Based Alloys for Biomedical Applications. *Materials,* 4 March, 7(3), pp. 1709-1800.

Llor, C., Bjerrum, L. (2014). Antimicrobial resistance: risk associated with antibiotic overuse and initiatives to reduce the problem. *Therapeutic Advances in Drug Safety*, 5(6), pp. 229-241.

Manam, N.S., Harun, W.S.W., Shri, D.N.A., Ghani, S.A.C., Kurniawan, T., Ismail, M.H. (2017). Study of corrosion in biocompatible metals for implants: A review. *Journal of Alloys and Compounds,* 701, pp. 698-715.

Maphango, L. (2012). Overview of South Africa's titanium industry and global market review, Pretoria: Directorate : Mineral Economics.

Mareci, D., Chelariu, R., Gordin, D., Ungureanu, G., Gloriant, T. (2009). Comparative corrosion study of Ti–Ta alloys for dental applications. *Acta Biomaterialia,* 5(9), pp. 3625-3639.

Massalski, T.B., Okamoto, H., Subramanian, P.R., Kacprzak, L. (1991). ASM International, Materials Park, Ohio, USA, December, 3, pp. 628-629.

Materia, T., (2009). *Total Materia.* Accessed 6 June 2019, from https://www.totalmateria.com/page.aspx?ID=CheckArticle&site=ktn&NM=221

Mishler, O.P., Shiau, H.J. (2014). Management of peri-implant desease-A current appraisal. *Journal of Evidence-Based Dental Practice*, 14, Supplement, pp. 53-59.

Monkhorst, H.J., Pack, J.D. (1976). Special points for Brillouin-zone integrations. *Physical Review* B, 13(12), pp. 5188-5192.

Monsees, T.K. (2016). Biocompatibility and Anti-Microbiological Activity Characterization of Novel Coatings for Dental Implants: A Primer for Non-Biologists. *Frontiers in Materials,* 3, Article No. 40.

Mouritz, A.P. (2012). Corrosion of aerospace metals. *Introduction to Aerospace Materials.* Woodhead Publishing, pp. 498-520

Mueller, M., Knott, H. (1963). The Crystal Structures of Ti_2Cu, Ti_2Ni, Ti_4Ni_2O, and Ti_4Cu_2O. *Transactions of the Metallurgical Society of AIME,* 227, pp. 674-678.

Murray, J. (1987). The Cu-Ti (Copper-Titanium) system. *Bulletin of Alloy Phase Diagrams,* 4(1), pp. 81-95.

Naseem, M., Dubey, A.P., Mishra, T.K. (2020). Effect of Rehydration With Normal Saline Versus Ringer Lactate on Serum Sodium Level of Children With Acute Diarrhea and Severe Dehydration: A Randomized Controlled Trial. *Indian Pediatrics,* 57, pp. 519-522

Niinomi, M., Liu, Y., Nakai, M., Liu, H., Li, H. (2016). Biomedical titanium alloys with Young's moduli close to that of cortical bone. *Regenerative Biomaterials*, 3(3), pp. 173-185.

Noumbissi, S., Scarano, A., Gupta, S. (2019). A Literature Review Study on Atomic Ions Dissolution of Titanium and Its Alloys in Implant Dentistry. *Materials,* 12(3), Article No. 368.

Okamoto, H. (2002). Cu-Ti (Copper-Titanium). *Journal of Phase Equilibra,* 26(3), pp. 549-550.

Okazaki, Y., Gotoh, E. (2005). Comparison of metal release from various metallic biomaterials in vitro. *Biomaterials,* 26, pp. 11-21.

Oldani, C., Dominguez, A. (2012). Titanium as a Biomaterial for Implants. *InTech,* pp. 149-162.

Olsson, N. (2008). Mechanical properties, phases and structures of titanium alloys, Master of Science Thesis, Lund University, Stockholm, Sweden.

Osorio, R., Freire, M., Caram, C., Garcia, A. (2012). The role of Cu-based intermetallics on the pitting corrosion behavior of Sn–Cu, Ti–Cu and Al–Cu alloys. *Electrochimica Acta,* 77, pp. 189-197.

Osorio, R., Freire, M., Caram, C., Garcia, A. (2010). Electrochemical behavior of centrifuged cast and heat treated Ti–Cu alloys for medical applications. *Electrochimica Acta 55*, 55(10), pp. 759-770.

Özcan, M., Hämmerle, C. (2012). Titanium as a reconstruction and implant material in dentistry: Advantages and pitfalls. *Materials,* 5(9), pp. 1528-1545.

Perdew, J.P., Wang, Y. (1992). Accurate and simple analytic representation of the electron-gas correlation energy. *Physical Review, B45(23)*, pp. 13244-13249.

Pina, V., Amigó, V., Mũnoz, A. (2016). Microstructural, electrochemical and tribo-electrochemical characterisation of titanium-copper biomedical alloys. *Corrosion Science,* 109, pp. 115-125.

Porenczuk, A., Górski, B. (2021). Peri-implantitis: A Serious Problem of Dental Implantology. In: Chaughule, R.S., Dashaputra, R. (eds) Advances in Dental Implantology using Nanomaterials and Allied Technology Applications. Springer, Cham. https://doi.org/10.1007/978-3-030-52207-0_9

Prasad, S., Ehrensberger, M., Gibson, M.P., Kim, H., Monaco Jr, E.A. (2015). Biomaterial properties of titanium in dentistry. *Journal of Oral Biosciences, 57,* pp. 192-199.

Prathapachandra, J., Suresh, N. (2012). Management of peri-implantitis. *Dental Research Journal,* 9(5), pp. 516-521.

Refiloe, M. (2008). *An overview of South Africa's titanium mineral concentrate industry,* Pretoria: The Director: Mineral Economics, Mineralia Centre.

Rodrigues, D.C., Valderrama, T., Wilson, G., Palmer, K., Thomas, K., Sridhar, S., Adapalli, A., Burbano, M., Wadhwani, C. (2013). Titanium corrosion mechanisms in the oral environment: A retrieval study. *Materials*, 6(11), pp. 5258-5274.

Romanò, C.L., Scarponi, S., Gallazzi, E., Romanò, D., Drago, L. (2015). Antibacterial coating of implants in orthopaedics and trauma: a classification proposal in an evolving panorama. *Journal of Orthopaedic Surgery and Research*, 10, Article No. 157.

Roux, R., Van der Lingen, E., Botha, E., Botes, A. (2020). The fragmented nature of the titanium metal value chain. *The Journal of the Southern African Institute of Mining and Metallurgy,* 120(11), pp. 633-640.

Ryan, C.S., Kleinberg, I. (1995). Bacteria in human mouths involved in the production and utilization of hydrogen peroxide. *Archives of Oral Biology*, 40(8), pp. 753-763.

Schmidt, C., Anita, I., Claes, L. (2001). Proliferation and differentiation parameters of human osteoblasts on titanium and steel surfaces. *Journal of Biomedical Materials Research,* 54(2), pp. 209-215.

Schminke, B., Orde, F., Gruber, R., Schliephake, H. (2015). The pathology of bone tissue. *Journal of Dental Research,* 94(2), pp. 354-361.

Segall, M.D., Lindan P.L.D., Probert M.J., Pickard, C.J., Hasnip, P.J., Clark, S.J. (2002). First-principles simulation: ideas, illustrations and the CASTEP code. *Journal of Physics: Condensed Matter,* 14 (11), pp. 2717-2744.

Shirai, T., Tsuchiya, H., Shimizu, T., Ohtani, K., Zen, Y., Tomita, K. (2009). Prevention of pin tract infection with titanium-copper alloys. *Journal of Biomedical Matereials*, 91(1), pp. 373-380.

Smeets, E.W.F., Kroes, G. (2021). Performance of Made Simple Meta-GGA Functionals with rVV10 Nonlocal Correlation for H_2 + Cu(111), D_2 + Ag(111), H_2 + Au(111), and D_2 + Pt(111). *Journal of Physical Chemistry C*, 125(17), pp. 8993-9010.

Stopler, M.C. NORMAL SALINE (sodium chloride injection) drug. Accessed September 20, 2022, from https://www.rxlist.com/normal-saline-drug.htm#description.

Subramani, K., Jung, R., Molenberg, A., Hammerle, C. (2009). Biofilm on dental implants: a review of the literature. *International Journal of Oral Maxillofac Implants,* 24(4), pp. 616-626.

Swetha, B., Mathew, S., Murthy, B.V., Shruthi, N., Bhandi, S.H. (2015). Determination of biocompatibility: A review. *International Dental and Medical Journal of Advanced Research*, 1, pp. 1-6.

Takada, Y., Nakajima, H., Okuno, O., Okabe, T. (2001). Microstructure and corrosion behavior of binary titanium alloys with beta-stabilizing elements. *Dental Materials Journal,* 20(1), pp. 34-52.

Uhlmann, E., Schweitzer, L., Cunha, A., Polte, J., Huth-Herms, K., Kieburg, H., Hesse, B. (2019). Application of laser surface nanotexturing for the reduction of peri-implantitis on biomedical grade 5 Ti-6Al-4V dental abutments. Proc. SPIE 10908, *Frontiers in Ultrafast Optics: Biomedical, Scientific, and Industrial Applications* XIX, 109080A; https://doi.org/10.1117/12.2509701

Unosson, E., Tsekoura, E.K., Engqvist, H., Welch, K. (2013). Synergetic inactivation of Staphylococcus epidermidis and Streptococcus mutans in a TiO_2/H_2O_2/UV system. *Biomatterials*, 3(4), Article no. e26727.

Vanderbilt, D. (1990). Soft self-consistent pseudopotentials in a generalized eigenvalue formalism. *Physical Review* B, 41(11), pp. 7892-7895.

Vander Voort, G. (1999). *Metallography, Principles and Practice.* New York: Mc Graw-Hill.

Veritas, H., n.d. *Biocompatibility Definition.* Accessed 10 October 2018, from https://www.asminternational.org/documents/10192/1849770/06785G_Sample.pdf.

Wang, J., Zhang, S., Sun, Z., Wang, H., Ren, L., Yang, K. (2019). Optimization of mechanical property, antibacterial property and corrosion resistance of Ti-Cu alloy for dental implant. *Journal of Materials Science & Technology,* 35, pp. 2336-2344.

Weiss, E., Shalhav, M., Fuss, Z., (1996). Assessment of antibacterial activity of endodontic sealers by a direct contact test. *Endodontics & Dental Traumatology,* 12, pp. 179-184.

Wiria, F., Sing, S., Yeong, W.Y. (2017). *Selective laser melting of novel titanium-tantalum alloy as orthopedic biomaterial.* Texas, Proceedings of the 28th Annual International Solid Freeform Fabrication Symposium – An Additive Manufacturing Conference, pp. 2389-2397.

Xin, C., Wang, N., Chen, Y., He, B., Zhao, Q., Chen, L., Tang, Y. (2022). Biological corrosion behaviour and antibacterial properties of Ti-Cu alloy with different Ti_2Cu morphologies for dental applications. *Biological Design*, 215, Article No. 110540.

Xu, Y., Jiang, J., Yang, Z., Zhao, Q., Chen, Y., Zhao, Y. (2020). The effect of copper content on the mechanical and tribological properties of hypo-, hyper- and eutectoid Ti-Cu Alloys. *Materials,* 13, Article No. 3411.

Yang, Y., (2005). Investigation of the martensitic transformation and the deformation mechanisms occurring in the superelastic Ti-24Nb-4Zr-8Sn alloy. *Material Chemistry*. INSA de Rennes, 2015. English. NNT : 2015ISAR0002.

Zhang, E., Wang, X., Chen, M., Hou, B. (2016). Optimization of mechanical properties, biocorrosion properties and antibacterial properties of as-cast Ti–Cu alloys. *Biomedical Materials,* 11, Article No. 065001.

Zhang, E., Wang, X., Chen, M., Hou, B. (2016). Effect of the existing form of Cu element on the mechanical properties, bio-corrosion and antibacterial properties of Ti-Cu alloys for biomedical application. *Materials Science and Engineering*, 69, pp. 1210-1221.

Zhang, E., Zhao, X., Hu, J., Wang, R., Fu, S., Qin, G. (2021). Antibacterial metals and alloys for potential biomedical implants. *Bioactive Materials,* 6(8), pp. 2569-2612.

Zhang, E., Zheng, L., Liu, J., Bai, B., Liu, C. (2014). Influence of Cu content on the cell biocompatibility of Ti–Cu sintered alloys. *Materials Science and Engineering*, 46, pp. 148-157.

Zhang, E-L., Fu, S., Wang, R.X., Li, H-X., Liu, Y., Ma, Z-Q., Liu, G-K., Zhu, C-S., Qin, G-W., Chen, D.F. (2019). Role of Cu element in biomedical metal alloy design. *Rare Metals*, 38, pp. 476-494.

Zhan, Y., Peng, D., She, J. (2012). Phase Equilibria of the Cu-Ti-Er System at 773 K (500 C) and Stability of the $CuTi_3$ Phase. *Metallurgical and Materials Transactions ,* 43A, pp. 2012-4015.

Zohdi, H., Emami, M., Shahverdi, H. (2012). Galvanic corrosion behavior of dental alloys. In: *Environmental and Industrial Corrosion - Practical and Theoretical Aspects.* Iran: IntechOpen, pp. 157-168.

APPENDIX A: Individual hardness measurements

Alloy		Hardness (HV_{10})					
		Individual					Average
CP Ti	As-cast	252	255	252	243	248	250±5
	750°C	195	210	231	154	211	200±29
	900°C	192	185	172	172	180	180±9
Ti-5Cu	As-Cast	268	303	322	316	326	307±24
	750°C	339	269	269	289	266	286±31
	900°C	200	216	241	199	195	210±19
Ti-15Cu	As-Cast	382	378	378	389	398	385±9
	750°C	354	370	382	305	385	359±32
	900°C	299	219	319	359	306	300±51
Ti-25Cu	As-Cast	445	450	457	452	450	450±4
	750°C	301	321	306	351	306	317±20
	900°C	321	333	315	314	218	300±46
Ti-33Cu	As-Cast	359	357	338	350	362	353±10
	750°C	293	313	322	304	307	308±11
	900°C	291	289	307	300	265	290±16
Ti-40Cu	As-Cast	359	357	338	350	362	353±20
	750°C	282	258	313	269	309	286±24
	900°C	312	274	253	283	279	280±21
Ti-47Cu	As-Cast	359	357	338	350	362	353±19
	750°C	271	306	321	271	266	287±24
	900°C	234	276	260	298	272	268±23
Ti-50Cu	As-Cast	458	445	424	415	410	430±5
	750°C	283	274	298	293	285	287±9
	900°C	300	215	248	279	310	270±39

APPENDIX B: Corrosion scans (two per condition)

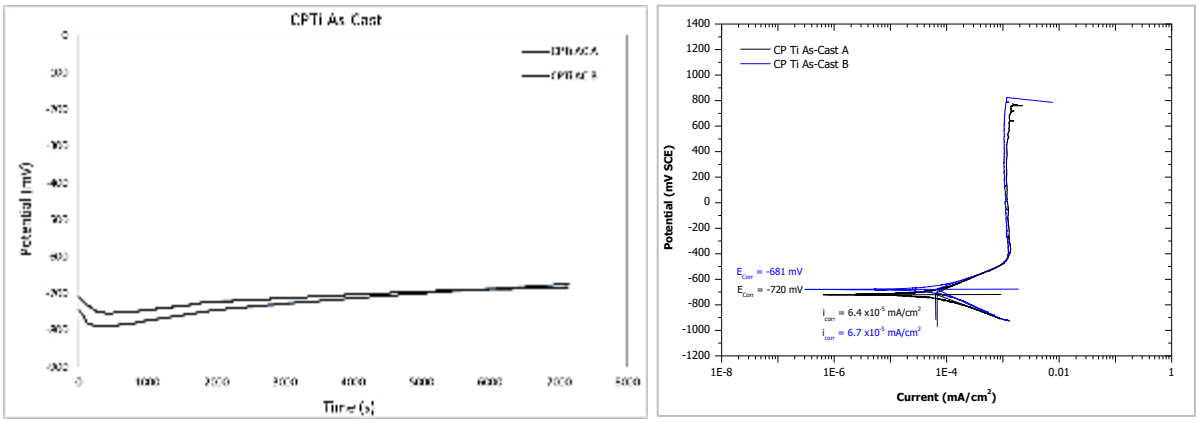


Figure B-0-1. OCP and potentiodynamic polarisation curves of CP Ti, as-cast in PBS.

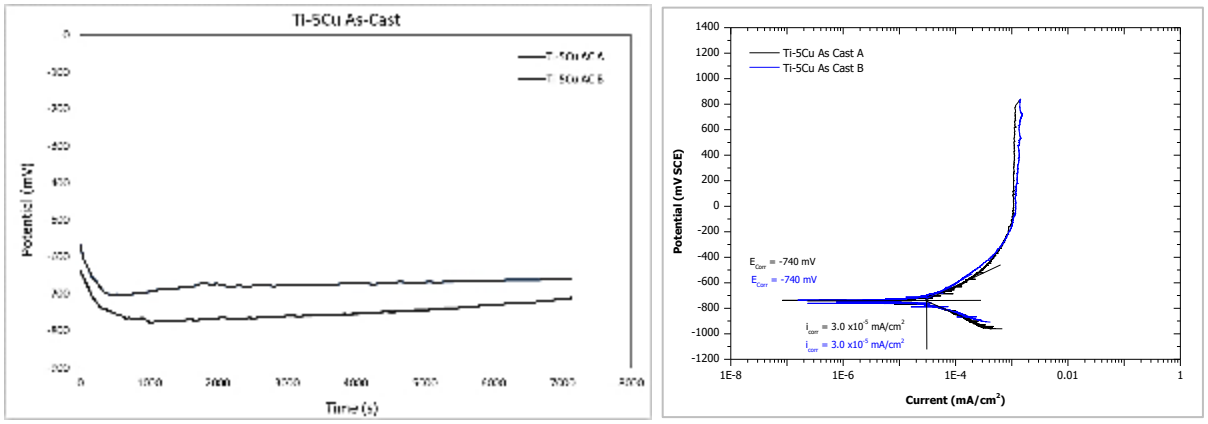


Figure B-0-2. OCP and potentiodynamic polarisation curves of Ti-5Cu, as-cast in PBS.

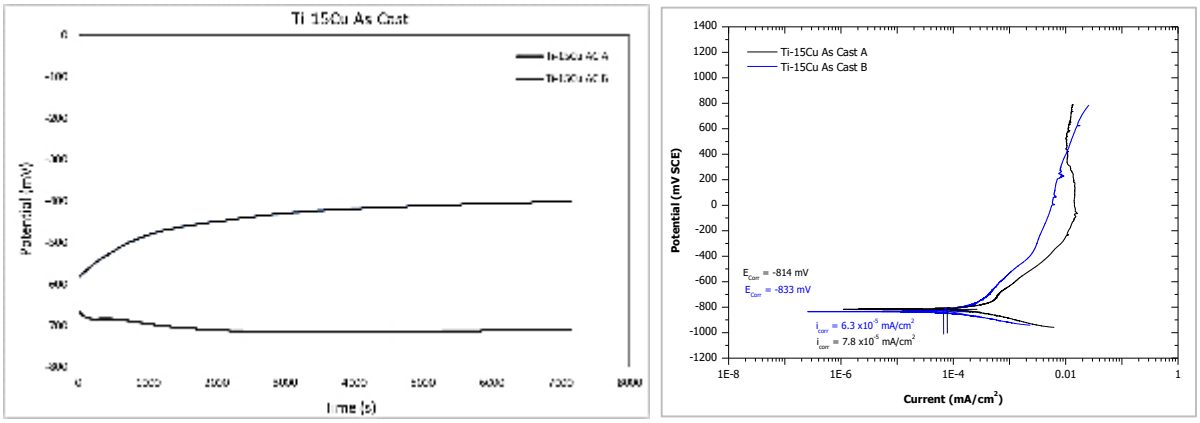


Figure B-0-3. OCP and potentiodynamic polarisation curves of Ti-15Cu, as-cast in PBS.

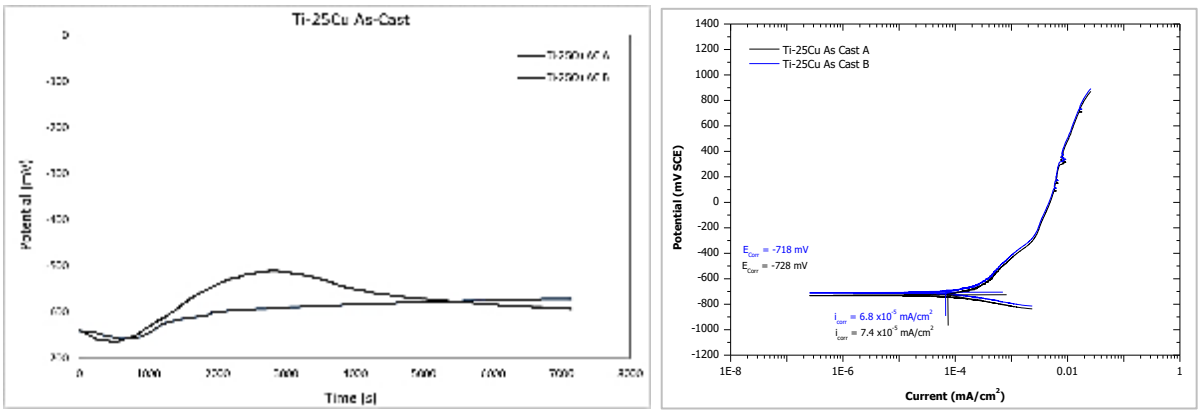


Figure B-0-4. OCP and potentiodynamic polarisation curves of Ti-25Cu, as-cast in PBS.

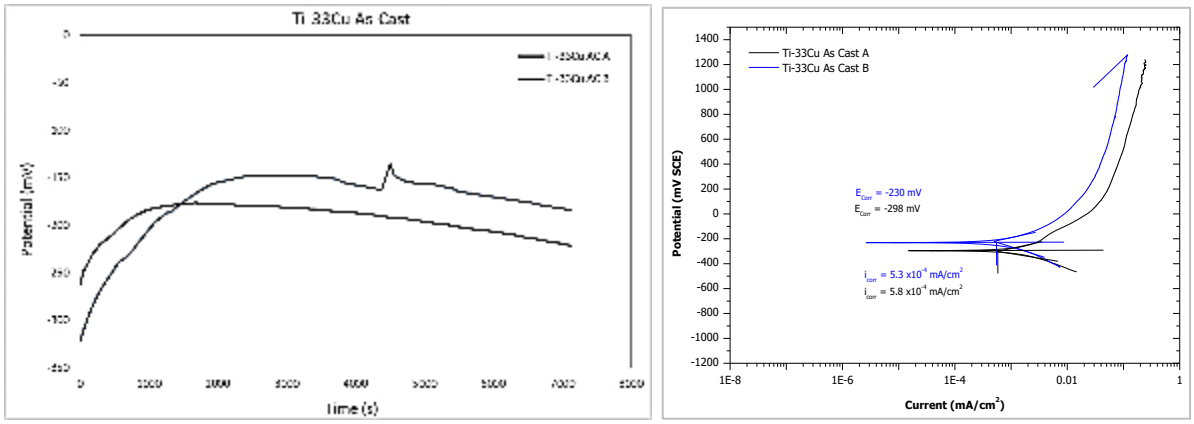


Figure B-0-5. OCP and potentiodynamic polarisation curves of Ti-33Cu, as-cast in PBS.

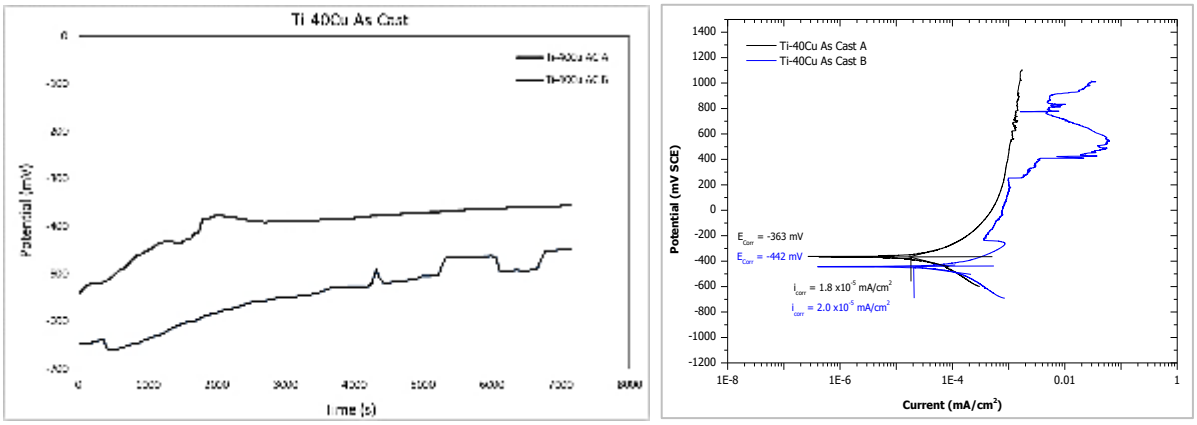


Figure B-0-6. OCP and potentiodynamic polarisation curves of Ti-40Cu, as-cast in PBS.

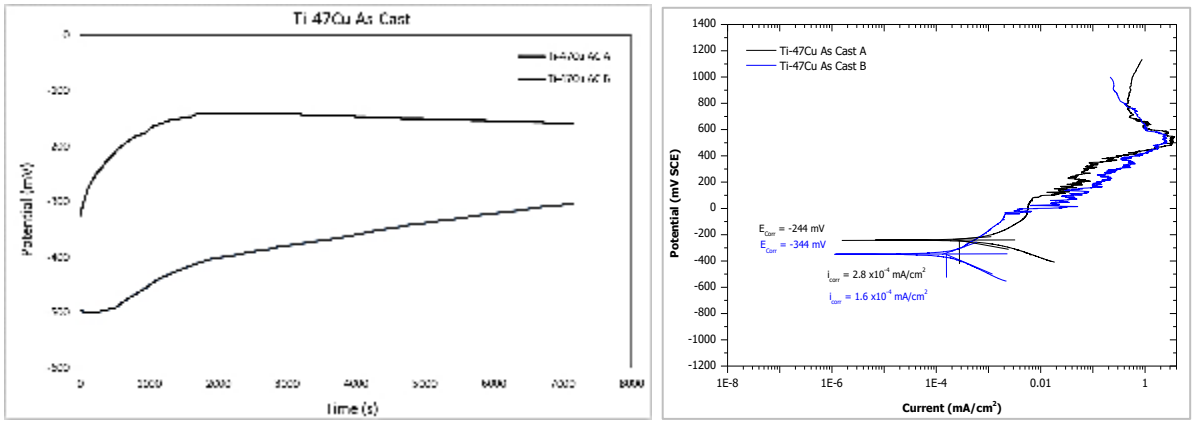


Figure B-0-7. OCP and potentiodynamic polarisation curves of Ti-47Cu, as-cast in PBS.

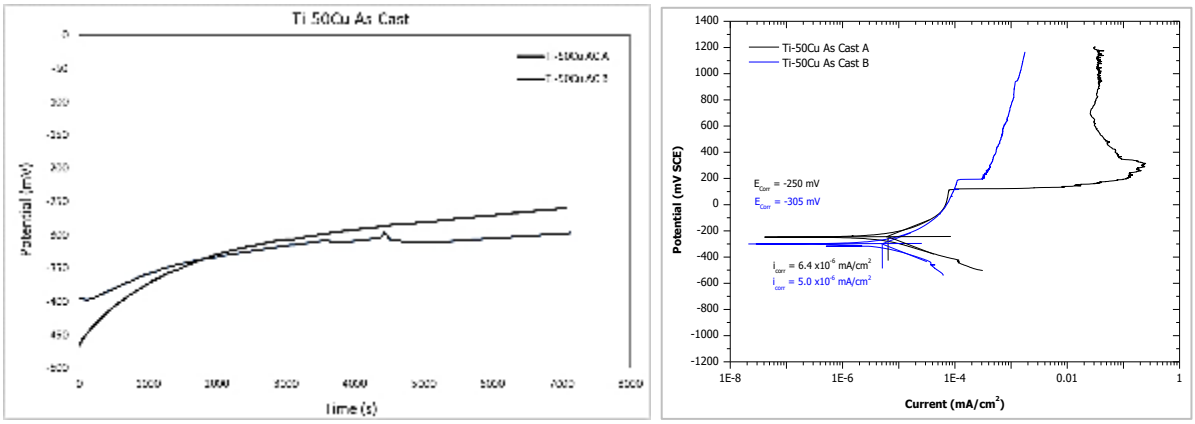


Figure B-0-8. OCP and potentiodynamic polarisation curves of Ti-50Cu, as-cast in PBS.

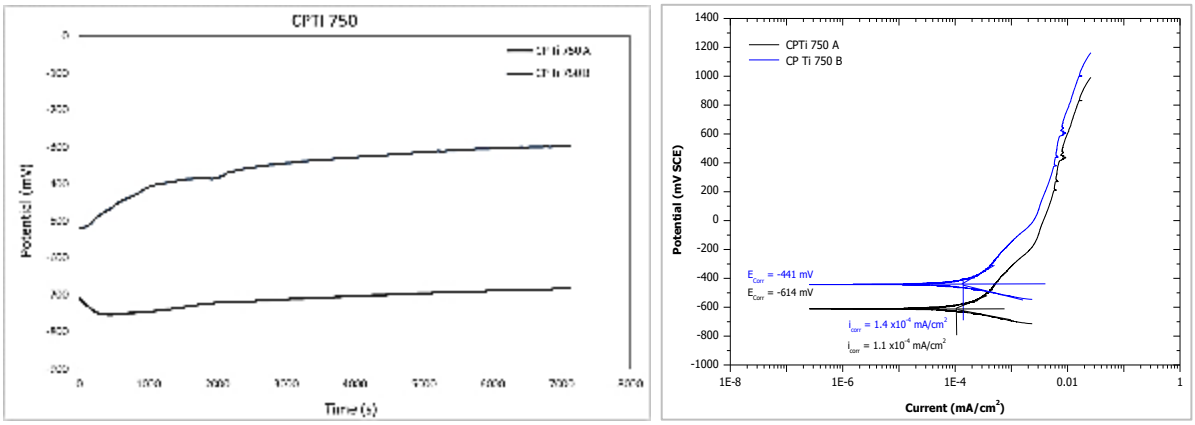


Figure B-0-9. OCP and potentiodynamic polarisation curves of CP Ti HT at 750°C in PBS.

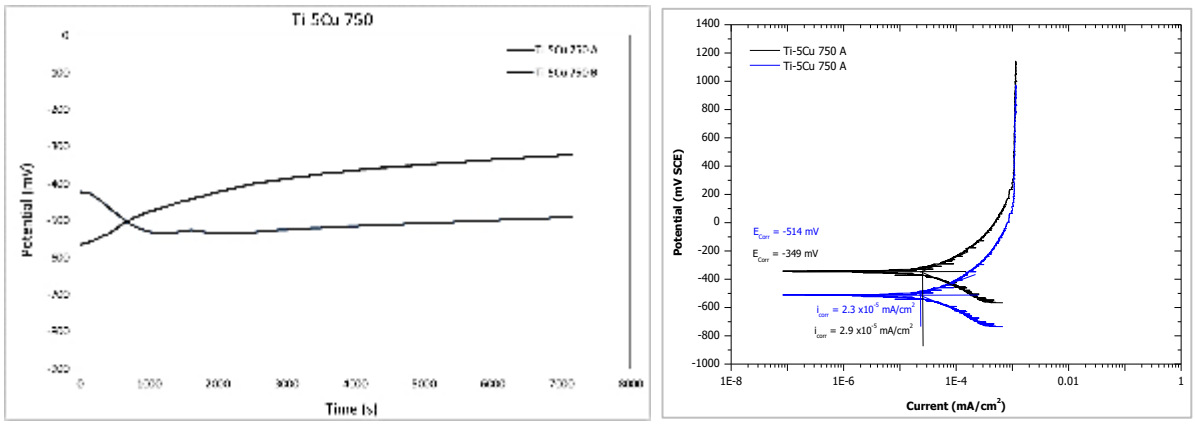


Figure B-0-10. OCP and potentiodynamic polarisation curves of Ti-5Cu HT at 750°C in PBS.

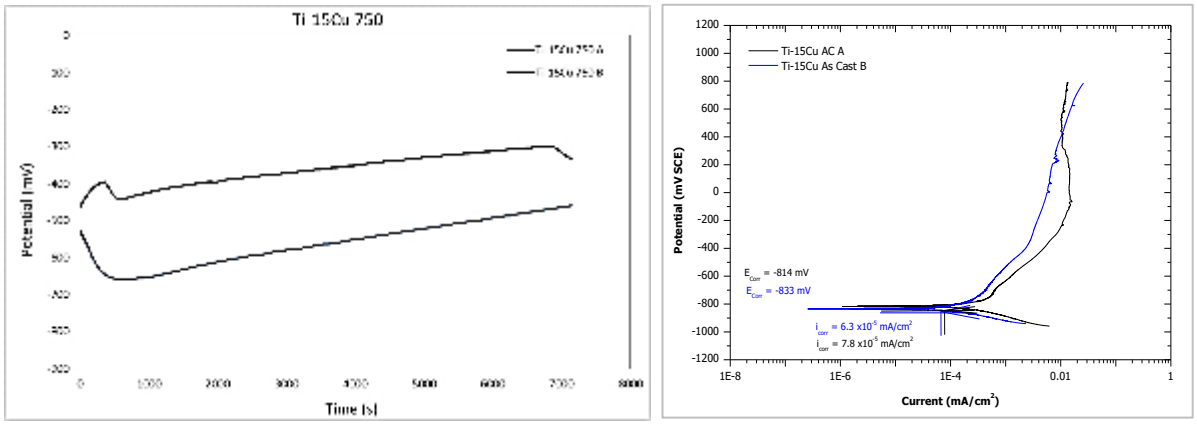


Figure B-0-11. OCP and potentiodynamic polarisation curves of Ti-15Cu HT at 750°C in PBS.

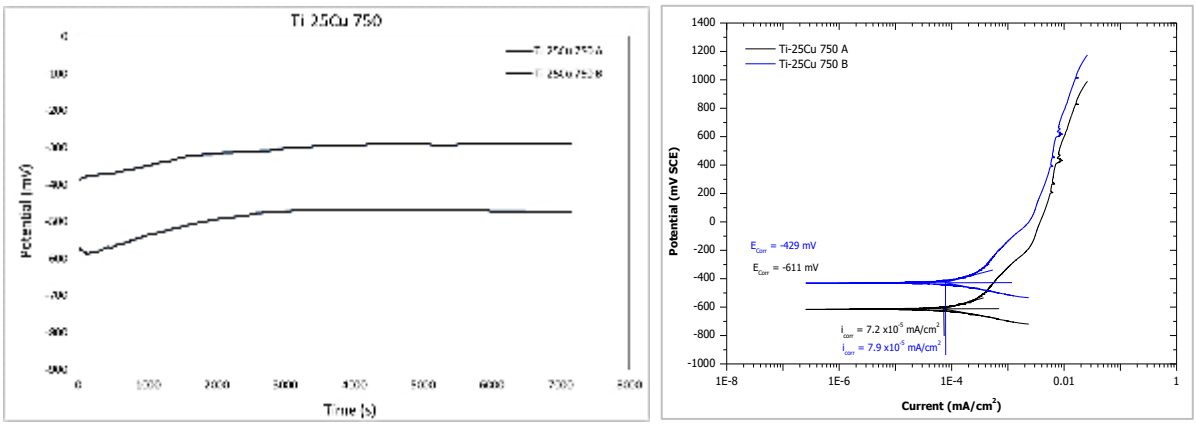


Figure B-0-12. OCP and potentiodynamic polarisation curves of Ti-25Cu HT at 750°C in PBS.

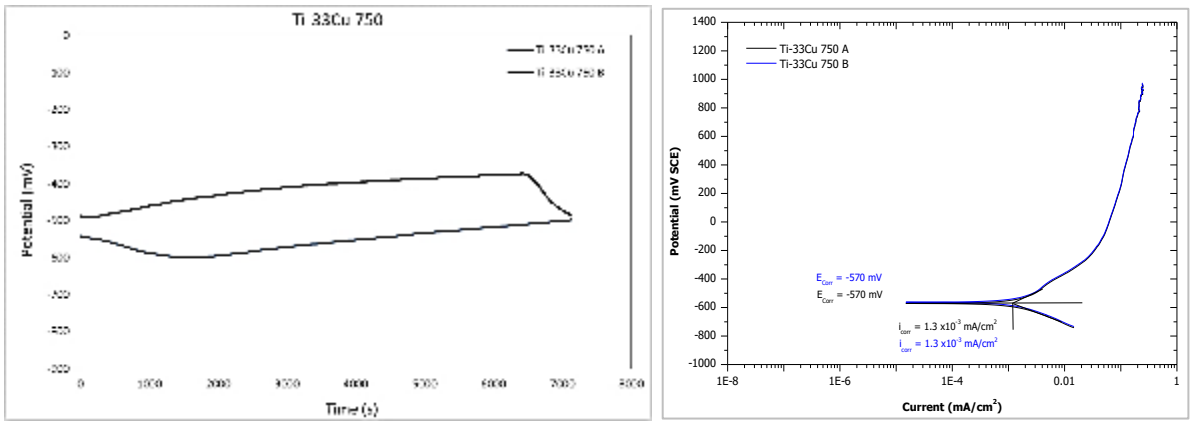


Figure B-0-13. OCP and potentiodynamic polarisation curves of Ti-33Cu HT at 750°C in PBS.

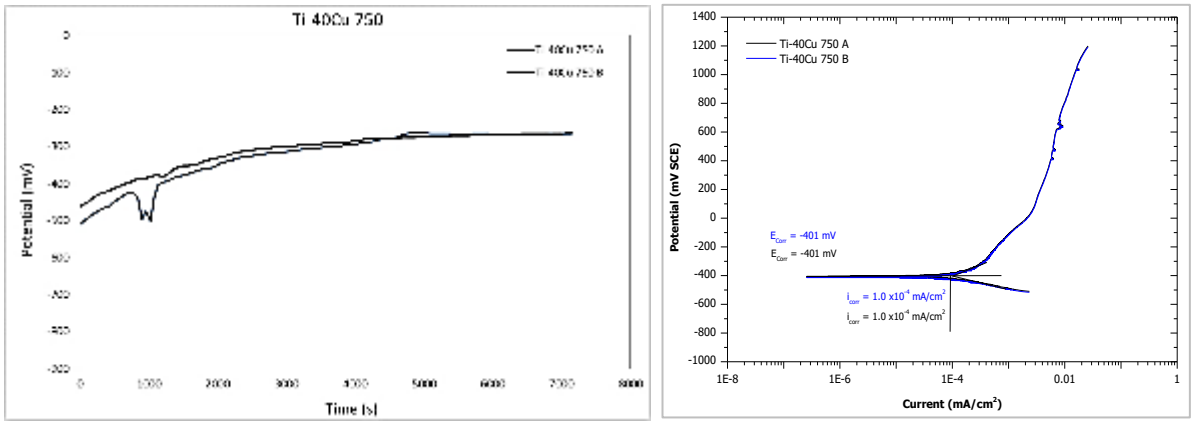


Figure B-0-14. OCP and potentiodynamic polarisation curves of Ti-40Cu HT at 750°C in PBS.

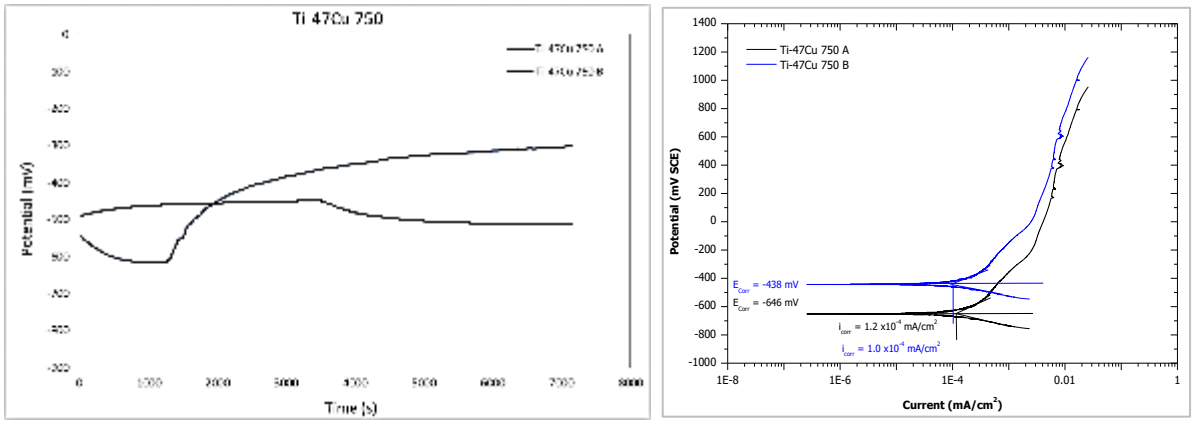


Figure B-0-15. OCP and potentiodynamic polarisation curves of Ti-47Cu HT at 750°C in PBS.

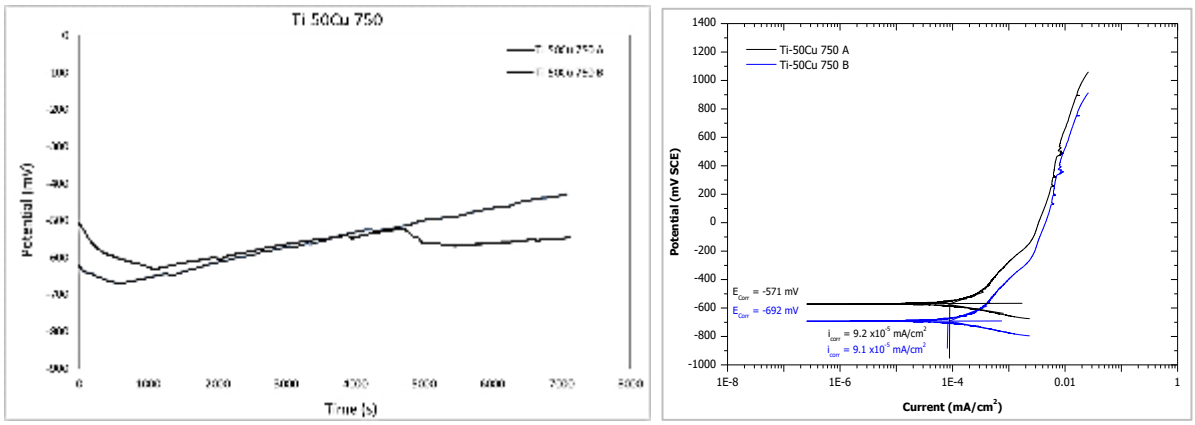


Figure B-0-16. OCP and potentiodynamic polarisation curves of Ti-50Cu HT at 750°C in PBS.

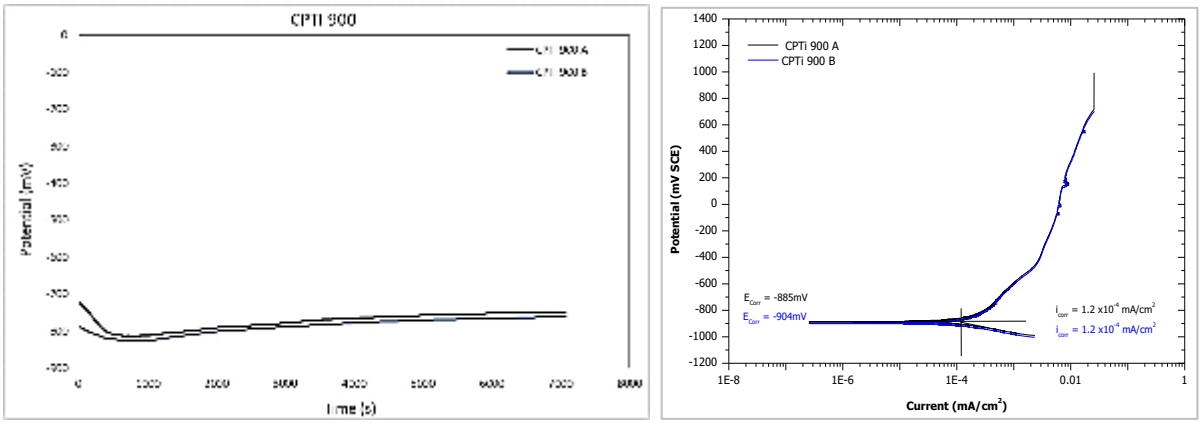


Figure B-0-17. OCP and potentiodynamic polarisation curves of CP Ti HT at 900°C in PBS.

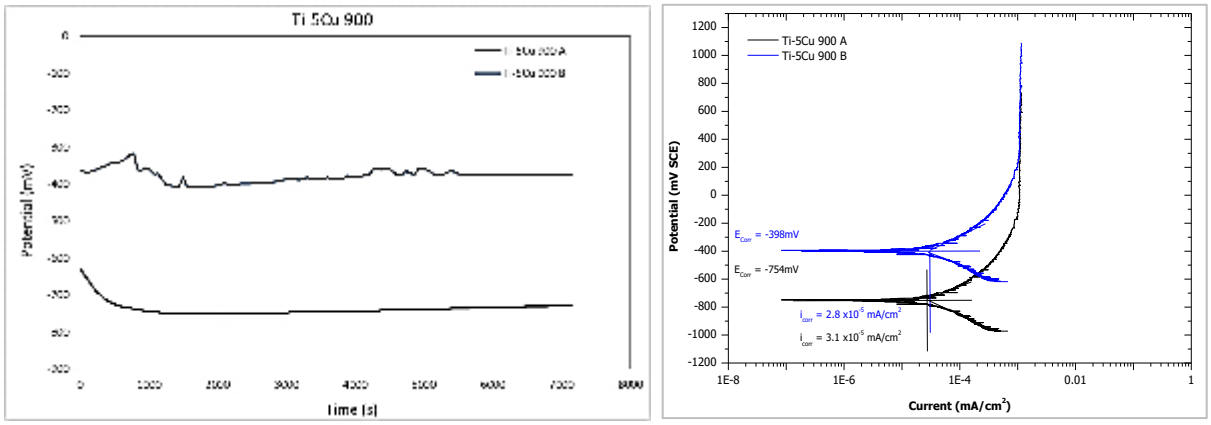


Figure B-0-18. OCP and potentiodynamic polarisation curves of Ti-5Cu HT at 900°C in PBS.

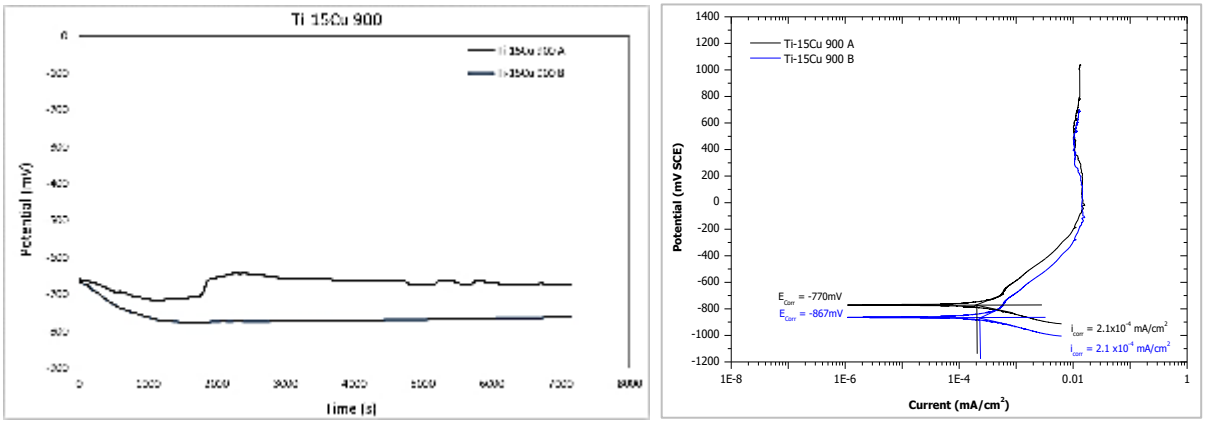


Figure B-0-19. OCP and potentiodynamic polarisation curves of Ti-15Cu HT at 900°C in PBS.

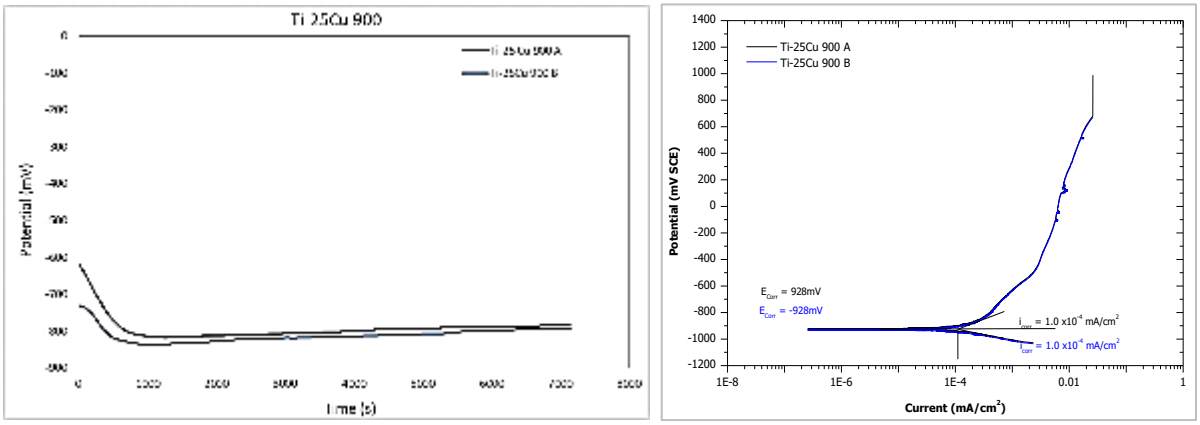


Figure B-0-20. OCP and potentiodynamic polarisation curves of Ti-25Cu HT at 900°C in PBS.

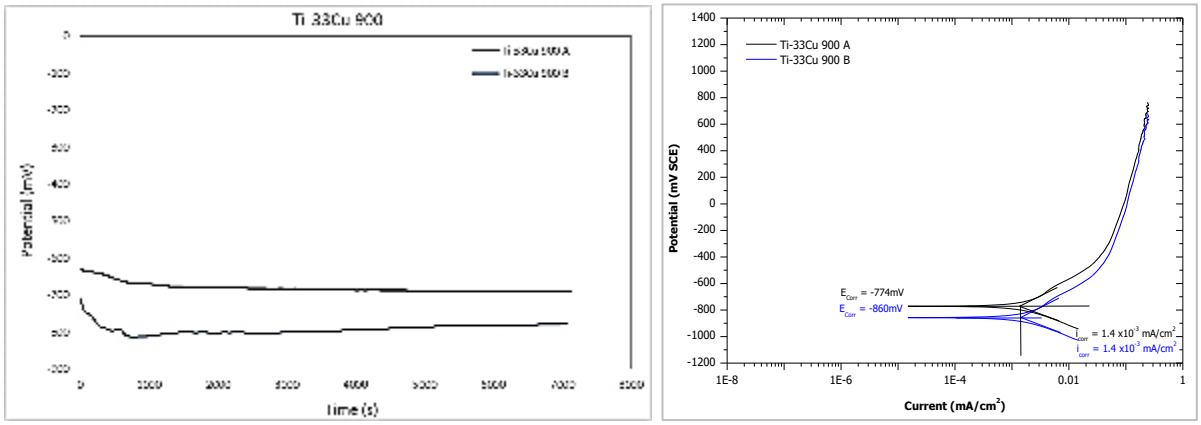


Figure B-0-21. OCP and potentiodynamic polarisation curves of Ti-33Cu HT at 900°C in PBS.

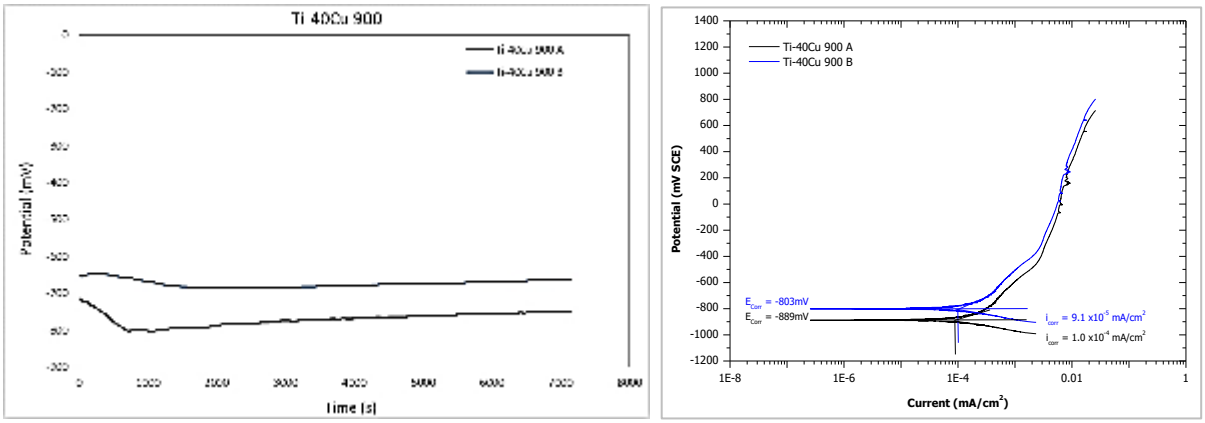


Figure B-0-22. OCP and potentiodynamic polarisation curves of Ti-40Cu HT at 900°C in PBS.

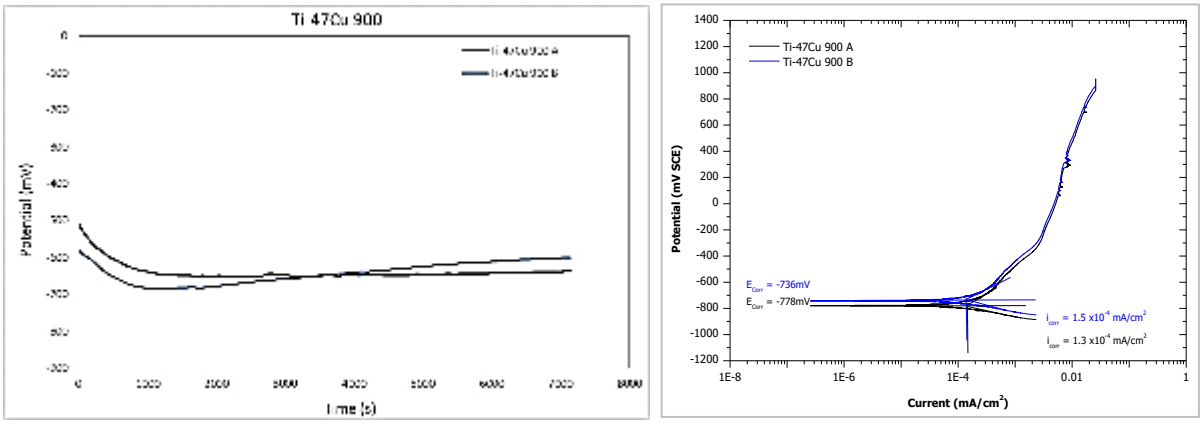


Figure B-0-23. OCP and potentiodynamic polarisation curves of Ti-47Cu HT at 900°C in PBS.

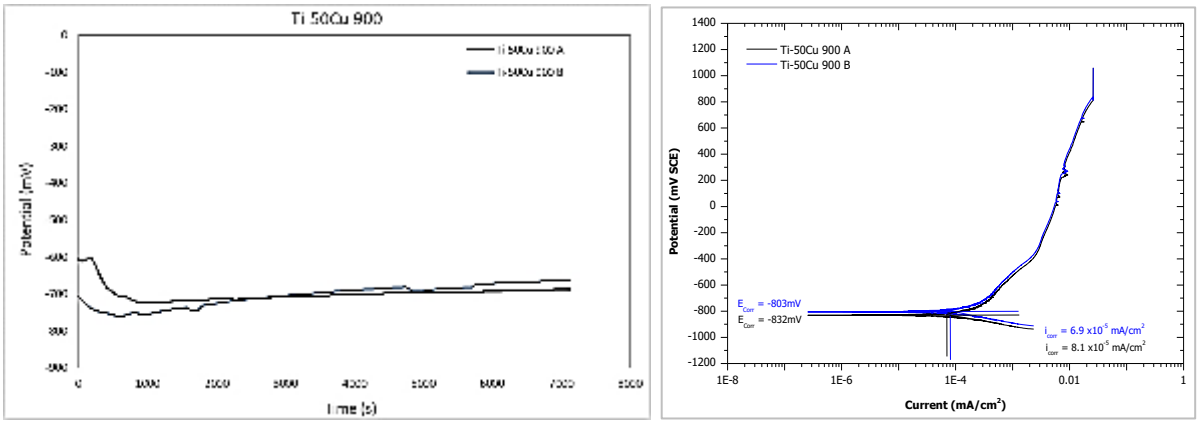


Figure B-0-24. OCP and potentiodynamic polarisation curves of Ti-50Cu HT at 900°C in PBS.

APPENDIX C: List of publications from this work

L. Fowler, N.D.E. Masia, L.A. Cornish, L.H. Chown, H. Engqvist, S. Norgren and C. Öhman-Mägi, Development of Antibacterial Ti-Cu_x Alloys for Dental Applications: Effects of Ageing for Alloys with Up to 10 wt% Cu, Materials 2019, Volume 12, p. 4017.

N.D.E. Masia, L.H. Chown, M. Smit, A.I. Mwamba and L.A. Cornish, Microstructural analysis of Ti-Cu alloys for dental implants applications, 56th Annual Conference of the Microscopy Society of Southern Africa Conference, Volume 48, p. 55, Club Mykonos, Langebaan, Western Cape, 1st – 5th December 2019.

N.G. Hashe, L. Fowler, S. Norgren, W.E. Goosen, C. Öhman Mägi, N.D. Masia, L.A. Cornish, J. Westraadt, L.H. Chown, S. Magadla, K.T. Nape, M. Mavundla and L. Spotose, A microstructural analysis of A Ti-Ta-Cu-Nb-Zr alloy, 56th Annual Microscopy Society of Southern Africa Conference, Volume 48, p. 30, Club Mykonos Resort, Langebaan, Western Cape, 1st – 5th December 2019.

K. Dyal Ukabhai, L. Fowler, K.T. Nape, M. Mavundla, L. Spotose, S. Magadla, N.D.E. Masia, D.E.P. Klenam, N.G. Hashe, C. Öhman Mägi, S. Norgren, L.H. Chown and L.A. Cornish, Effect of Different Copper Additions to Ti–10.1Ta–1.7Nb–1.6Zr (MASS%), 56th Annual Microscopy Society of Southern Africa Conference, Volume 48, p. 37, Club Mykonos Resort, Langebaan, Western Cape, 1st – 5th December 2019.

N.D.E. Masia, M. Smit, I.A. Mwamba, L. Fowler, L.H. Chown, S. Norgren, C. Öhman-Mägi, N.G. Hashe and L.A. Cornish, Corrosion Performance of Ti-Cu Alloys Targeted for Biomedical Applications, Conference of the South African Advanced Materials Initiative, Online Conference, 18 – 22 October 2021.

Dyal Ukabhai, K., Curle, U.A., Masia, N.D.E., Smit, M., Mwamba, I.A., Norgren, S., Öhman-Mägi, C., Hashe, Cornish, L.A. (2022). Formation of Ti2Cu in Ti-Cu Alloys. Journal of Phase Equilibria and Diffusion. 43, pp. 332–344.

materials

MDPI

Article

Development of Antibacterial Ti-Cu_x Alloys for Dental Applications: Effects of Ageing for Alloys with Up to 10 wt% Cu

Lee Fowler [1], Nomsombuluko Masia [2,3], Lesley A. Cornish [3], Lesley H. Chown [3], Håkan Engqvist [1], Susanne Norgren [1] and Caroline Öhman-Mägi [1,*]

1 Division of Applied Materials Science, Department of Engineering Sciences, The Ångström Laboratory, Uppsala University, Box 534, 751 21 Uppsala, Sweden; lee.fowler@angstrom.uu.se (L.F.); hakan.engqvist@angstrom.uu.se (H.E.); susanne.norgren@angstrom.uu.se (S.N.)

2 Advanced Materials Division, Mintek, Randburg 2124, South Africa; nomsombulukoh@mintek.co.za

3 School of Chemical and Metallurgical Engineering, and DST-NRF Centre of Excellence in Strong Materials, hosted by the University of the Witswatersrand, Johannesburg 2000, South Africa; lesley.cornish@wits.co.za (L.A.C.); lesley.chown@wits.co.za (L.H.C.)

* Correspondence: caroline.ohman@angstrom.uu.se

Received: 29 October 2019; Accepted: 28 November 2019; Published: 3 December 2019



Abstract: Peri-implantitis, a disease caused by bacteria, affects dental implants in patients. It is widely treated with antibiotics, however, with growing antibiotic resistance new strategies are required. Titanium-copper alloys are prospective antibacterial biomaterials, with the potential to be a remedy against peri-implantitis and antibiotic resistance. The aim of this study was to investigate Ti-Cu_x alloys, exploring how Cu content (up to 10 wt%) and ageing affect the material properties. Electron microscopy, X-ray diffraction, hardness testing, bacteriological culture, and electrochemical testing were employed to characterize the materials. It was found that alloys with above 3 wt% Cu had two phases and ageing increased the volume fraction of Ti_2Cu. An un-aged alloy of 5 wt% Cu showed what could be Ti_3Cu, in addition to the α-Ti phase. The hardness gradually increased with increased Cu additions, while ageing only affected the alloy with 10 wt% Cu (due to changes in microstructure). Ageing resulted in faster passivation of the alloys. After two hours the aged 10 wt% Cu alloy was the only material with an antibacterial effect, while after six hours, bacteria killing occurred in all alloys with above 5 wt% Cu. In conclusion, it was possible to tune the material and antibacterial properties of Ti-Cu_x alloys by changing the Cu concentration and ageing, which makes further optimization towards an antibacterial material promising.

Keywords: titanium alloys; copper; Ti_2Cu; Ti_3Cu; biomaterial; antibacterial

1. Introduction

Peri-implantitis is a disease caused by bacterial population of an implant surface, which results in local inflammation of soft tissue and ultimately implant loosening and failure [1]. The loss of bone tissue is often associated with the inflammation surrounding the implants, leading to revision surgeries often being troublesome to successfully accomplish [1]. The prevalence of peri-implantitis in the general population is estimated to be between 19% [2] and 28% [3]. Despite the discrepancy in prevalence data, it is generally agreed that the prevalence is under-estimated at present [1,3]. Nevertheless, the importance of the problem is clear and increasing, considering that the dental implant industry is estimated to have reached USD 5 billion in 2018 [1]. The bacteria responsible for the disease include: *Peptostreptococcus micros, Porphyromonas ginigivalis and Treponema denticola*, among others [4,5]. The fact

that these bacteria have virulent characteristic behavior [6], coupled with the increasing problems with antibiotic resistance [7], corroborate that an effective antibacterial solution is needed.

The effectiveness of bacterial colonization lies in the creation of biofilms [8], which have the ability to survive antibiotic treatments due to a multifaceted strategy of slower growth in the biofilm, poor penetration of antibiotics, and genetic variations in the bacteria [9,10]. The gram-positive *Staphylococcus epidermidis* is a biofilm forming bacteria, and is one of the most common bacteria in implant infections [11], making the bacteria a suitable strain for testing the antibacterial ability of biomaterials.

To date, much research has been focused on various approaches to reduce the bacterial burden correlated to implants, which include: surface treatments [12], the use of photochemical reactions [13], alloying of silver to titanium [14], and recently, the alloying of copper to titanium [15–17]. The antibacterial effect of Cu additions was found to be superior compared to silver [18]. The Ag appears to be effectual only at elevated temperatures [19], whereas Cu was found—using in vitro tests—to have antibacterial ability at ambient conditions [20]. For this reason, Cu is being investigated as an antibacterial element with increased frequency in thin films [21,22], ionic form [23,24], and in alloys [17,25,26]. In particular, Zhang et al. [27] have investigated the addition of Cu in titanium and found that there are discrepancies in the literature regarding required copper content and the mechanisms causing bacterial reduction. While success in antibacterial applications has been achieved with copper, the molecular process of bacterial death is not clear. However, it is hypothesized to be caused by Cu ions creating reactive oxygen species (ROS) via the Fenton reaction ($Cu^{+} + H_2O_2 \rightarrow Cu^{2+} + OH^{-} + \cdot OH$) [24], where ROS plays a role in the prohibition of bacteria 16SrRNA replication, resulting in bacteria death [28].

While it is important to understand the biological interactions in these systems, the antibacterial effect is only one aspect of successfully functioning antibacterial biomaterials. The mechanical properties are also important and should be considered, since implants experience mechanical loading in vivo. When excessive Cu is alloyed to Ti, intermetallic compounds (Ti_2Cu [29] and Ti_3Cu [30]) form, which can lead to brittleness [31]. While heat treatments of Ti alloys does allow some degree of ductility to be achieved in initially brittle materials, the resultant effect on microstructure and antibacterial properties must be assessed and understood. This inter-relationship between the various choices of compositions and heat treatments, and their impacts on mechanical properties and antibacterial effects, provide an opportunity for optimization of the final alloy. Therefore, the aim of the present study was to investigate these aspects (microstructural, mechanical and antibacterial) for different Ti-Cu alloys, to contribute to the understanding of these materials, and facilitate their future use as antibacterial biomaterials. The investigation only focused on alloys in the range 0 to 10 wt% Cu, since Cu ions released in this range of alloys did not show notable toxicity effects in previous works [15,23].

2. Materials and Methods

2.1. Production and Preparation of Alloys

Alloys of titanium and copper were produced in a range from 0 to 10 wt% Cu (Table 1). Titanium grade 4 (Sandvik AB, Stockholm, Sweden), "CPTi", and 99.9999% pure copper rods (365327-21.5G, Sigma Aldrich, St. Louis, MO, USA) were used to produce the alloy mixtures. Alloys were re-melted five times in an arc furnace, then re-melted and cast into rods in the same furnace (Series 5 Bell Jar, Centorr Vacuum industries, Nashua, New Hampshire, USA). Partial homogenization was achieved by turning over the melted alloys between each of the five melting events. Complete homogenization was achieved by heat treatments of the rods at 900 °C for 18 h, then 798 °C for 24 h and then finally, for half of the produced alloys, ageing at 400 °C for six hours. The annealing was done in vacuumed ampoules to reduce the oxygen contamination in the alloys, at a pressure of 1.333 mbar. All alloys were quenched into salt brine water by breaking the ampoules, to allow faster cooling. The alloy samples were cut into slices for analysis using a silicon carbide disk (150s, Struers, Ballerup, Denmark), to minimize

cutting damage. Following sectioning, the samples were embedded in Bakelite resin (PolyFast, Stuers, Ballerup, Denmark) for metallographic preparation.

Table 1. Ti-Cu_x samples used in the study.

Nominal wt% Cu	CPTi	1 wt% Cu	3 wt% Cu	5 wt% Cu	10 wt% Cu
Alloys heat treated at 798 °C (un-aged)	CPTi-798	1Cu798	3Cu798	5Cu798	10Cu798
Alloys aged at 400 °C	CPTi-400	1Cu400	3Cu400	5Cu400	10Cu400

The metallographic preparation of the samples included grinding and polishing for subsequent microstructural studies. The three-step metallographic procedure developed by Vander Voort [32] was adapted for the present study, further details are given in Table 2.

Table 2. Three-step metallographic preparation of Ti-Cu (All products sourced from Struers, except H2O2 sourced from BASF SE, Ludwigshafen, Germany).

Steps	1–Grind	2–Rough Polish	3–Final Polish
Surface	SiC–320P	MD–Dur cloth	MD–Floc cloth
Abrasive	-	6 µm diamond suspension	OP-S Si-Colloids and H_2O_2 (5:1) solution
Lubricant	Water	DP Lubricant Red	-
Speed (rpm)	200 contra	150 contra	150 contra
Duration (min)	Until planar	15 min	15 min

2.2. Microstructural Studies

The microstructures of the materials were studied by scanning electron microscopy (SEM)—using a LEO1550 SEM (ZEISS group, Oberkochen, Germany) equipped with an INCA AZtec Energy Dispersive X-ray Spectroscopy (EDX) system (Oxford Instruments, High Wycombe, UK). Images were taken with an Everhart-Thornley (HE-SE2 detector, ZEISS group, Oberkochen, Germany) and backscattered electron detector (BSD). To ensure that the microstructure was discernible in the SEM, the samples were etched in Kroll's Etchant: 2 mL HF, 4 mL HNO_3 and 100 mL distilled water, with etching times of 30 s using cotton swabbing [33].

The energy dispersive x-ray spectroscopy (EDX) analysis of the 5Cu798 sample was performed on a Merlin SEM (ZEISS group, Oberkochen, Germany) equipped with an Ultim-Max 100 mm^2 Silicon Drift Detector (Oxford Instruments, High Wycombe, UK) at a voltage of 15 kV and 8.5 mm working distance.

2.3. Hardness Studies

The hardness of the Ti-Cu_x alloys was measured using a Vickers Hardness tester (Duravision EMCO, Prufmaschinen GmbH, Kuchl, Austria) with a 9.8 centinewton load. The machine was calibrated before testing with a standard Vickers sample, and an average was taken from three indentations.

2.4. Phase Identification

All samples studied by X-ray diffraction were polished as specified by Vander Voort [32] (Table 2). X-ray diffraction (XRD) was performed on a D8 Advance TWIN-TWIN diffractometer (Bruker, AXS GmbH, Karlsruhe, Germany) with Cu Kα radiation ($K\alpha_1$ = 1.540598 Å with a Ni filter) and using the Bragg-Bretano experimental set-up. The detector system was a LynxEye XE PSD detector (Bruker, AXS GmbH, Karlsruhe, Germany). The EVA software suite (2015, Bruker) was used for phase analysis, while diffractogram plotting was done in Origin (2018b, OriginLab Corp., Northhampton, MA, USA). All crystallographic data were retrieved from the ICDD database PDF–4 + 2019 [34] and included PDF# 00-044-1294 (HCP-Ti), PDF# 00-015-0717 (Ti_2Cu) [35] and PDF# 00-055-0296 (Ti_3Cu).

2.5. Bacterial Luminescence by Direct Contact Test

The bacteria direct contact test has already been described [17], so only a summary is provided here. Staphylococcus epidermidis (XEN43) is a genetically modified bacterial strain that is bioluminescent due to the luxABCDE gene being bio-engineered into the bacterial genome [36,37]. Overnight bacterial inoculum of XEN43 was prepared a priori then seeded on the surface of sterile 5 mm diameter Ti-Cu_x alloys (both aged and un-aged) and allowed to attach. Tryptic soy broth (TSB, Fluke-Sigma Aldrich, Stockholm, Sweden) was then carefully added to the test wells. Periodic measurements of luminescence were recorded for the samples on a Hidex plate CHAMELEON V (425-106, Multilabel counter, Turku, Finland), and the mean was used to determine the antibacterial rate (R) after two- and six-hours of exposure, using Equation 2 [38]:

$$\mathrm{R} = \frac{N_{control} - N_{sample}}{N_{control}} \times 100\% \quad (1)$$

where $N_{control}$ = mean luminescence from the CPTi sample, and N_{sample} = mean luminescence for the Ti-Cu_x alloys [38].

2.6. Corrosion Testing

The corrosion testing was performed on all the samples at 37 ± 1 °C in a phosphate buffered saline (PBS) solution (containing 8 g/L sodium chloride, 0.2 g/L potassium chloride, 1.44 g/L sodium hydrogen phosphate, and 0.24 g/L potassium di-hydrogen phosphate) maintained at a pH of 7.4.

The sample preparation for the corrosion studies included mounting the samples (CPTi and Ti–Cu_x) of approximately 1 cm^2 in area, in non-conductive epoxy resin with a copper wire soldered to the samples for electrical connection. The samples were ground to 120 grit surface finishes using a SiC paper, then rinsed with de-mineralized water and degreased in acetone.

The electro-chemical testing was performed using a computer-driven Potentiostat (AutoTafel, ACM Instruments, Cark, Cumbria, England). Two graphite rods acted as counter-electrodes and a Haber-Luggin capillary made the junction with a saturated calomel reference electrode (SCE). All potential values were with respect to the SCE. Nitrogen was bubbled continuously during testing in order to remove all the oxygen and maintain an anaerobic condition.

After each sample was immersed in the solution, the open circuit potential against time curve was recorded for up to 4 h to determine the open-circuit potential (OCP). When the potential had reached a sufficiently stable value at four hours, a cyclic polarization scan was recorded from −250 mV to 1500 mV versus the corrosion potential at a scanning speed of 10 mV/min. The scan direction was not reversed.

2.7. Statistical Analysis

The statistical analysis for the bacterial luminescence measurements was done in Origin software (2018b, OriginLab Corp., Northhampton, MA, USA) at two and six hours, using a One-way ANOVA with a Tukey HSD Post-Hoc test, and with Levene's homogeneity of variance test. The same statistical test was also performed for the hardness with the exception that a Brown-Forsythe test for homogeneity of variance was performed. All tests had a statistical significance setting of $p = 0.05$.

3. Results

3.1. Microstructural Studies

Microstructures for the alloys were compared to determine any differences due to ageing. The microstructures of the alloys (both aged and un-aged) with less than 3 wt% Cu had a single-phase structure of α-Ti (the hcp solid solution of titanium) (Figure 1). However, the 1Cu798 showed peaks for the 2θ diffraction angle of the Ti_3Cu phase, at 20.9° and 23.4° (Figure 2). Those with equal to

and greater than 3 wt% Cu were all two-phased: Ti_2Cu and α-Ti (Figure 1). X-ray diffraction studies confirmed these findings (Figure 2), where HCP-Ti and Ti_2Cu peaks were identified, but peaks for the Ti_3Cu crystals were also observed at the 2θ diffraction angles of 20.9° and 23.4° for the alloys: 1Cu798, 3Cu798, 5Cu798, and 3Cu400.

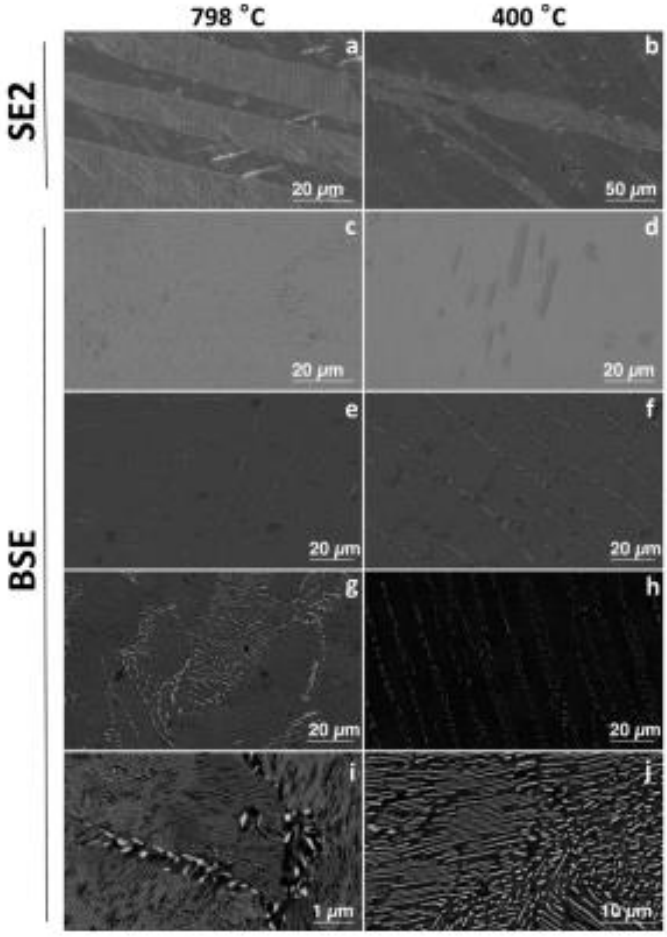


Figure 1. Secondary electron images of: (**a**) CPTi-798, (**b**) CPTi-400, and backscattered electron images of: (**c**) 1Cu798, (**d**) 1Cu400, (**e**) 3Cu798, (**f**) 3Cu400, (**g**) 5Cu798, (**h**) 5Cu400, (**i**) 10Cu798, and (**j**) 10Cu400.

Comparison of the 10 wt% Cu before and after ageing displayed that a larger volume fraction of Ti_2Cu precipitated due to this heat treatment. While an increase in Ti_2Cu with ageing was also found for the 5 and 3 wt% Cu, the volume fraction of precipitated Ti_2Cu was lower. In addition, these alloys had lamellar microstructures of Ti_2Cu and α-Ti (Figure 1).

3.2. EDX Study of Precipitates

Precipitates in the 5Cu798 sample were studied to determine the presence of variations in the Cu content for the individual phases in the alloy. Since it is known that the Ti_2Cu and Ti_3Cu crystals have an atomic % Cu concentration of 33% and 25%, respectively [29,30], point analysis of individual crystals was performed to ascertain which phase was present. For sample area 1 (Figure 3a), the atomic concentrations for precipitates 1 and 2 were 33.2 ± 1.1 and 34.1 ± 0.3, respectively (Table 3). For sample

area 2 (Figure 3b), the atomic concentrations for precipitates 3 and 4 were 31.5 ± 2.6 and 24.6 ± 0.5, respectively (Table 3).

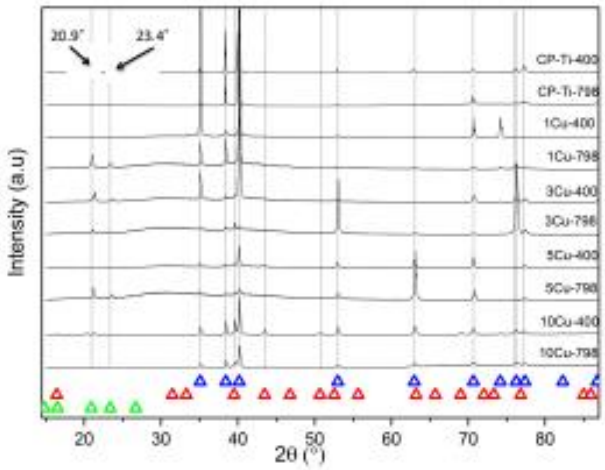


Figure 2. X-ray diffraction patterns of Ti-Cu_x alloys heat-treated at 798 °C, some aged at 400 °C: blue triangles indicate HCP-Ti, red triangles indicate Ti_2Cu and green triangles indicate Ti_3Cu. Note the peaks for Ti_3Cu at 20.9° and 23.4°.

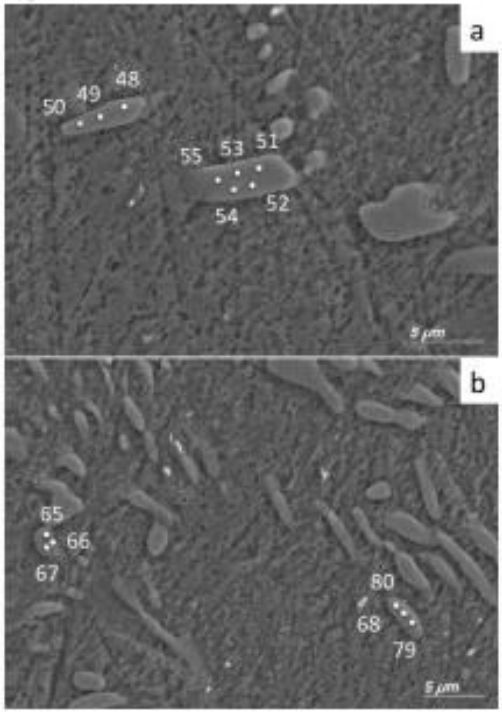


Figure 3. Positions of EDX spectral analyses of sample 5Cu798: (**a**) Sample area 1 with precipitate 1 (48, 49, 50) and precipitate 2 (51, 52, 53, 54, 55). (**b**) Sample area 2 with precipitate 3 (65, 66, 67) and precipitate 4 (68, 79, 80).

Table 3. EDX point spectral analyses of sample areas 1 and 2 (point spectral analysis correspond to points in Figure 3).

Precipitate (EDX Point Analyzed)	Atomic % Copper (Balance % Titanium)	Possible Phases
Precipitate 1 (48, 49, 50)	33.2 ± 1.1	Ti_2Cu
Precipitate 2 (51, 52, 53, 54, 55)	34.1 ± 0.3	Ti_2Cu
Precipitate 3 (65, 66, 67)	31.5 ± 2.6	Ti_2Cu
Precipitate 4 (68, 79, 80)	24.6 ± 0.5	Ti_3Cu

3.3. Bacterial Luminescence

At two hours, no significance in luminescence was found among the samples, except between CPTi-798 and the 1Cu400 and 3Cu400 samples, which had significantly higher values (Figure 4). However, the antibacterial rate of 10Cu400 (R = 12%) was higher than the other aged alloys at this time point. All other alloys had a negative R at this time point, indicating that more bacteria were found on these alloys than on the respective control.

For the un-aged alloys, it was found that after six-hours of exposure (Figure 5) the R for 10Cu798 (42%) was higher than that for 5Cu798 (7%). The alloys with lower Cu content still had negative R-values. The 10Cu798 alloy also had significantly lower luminescence than alloys 1Cu798, 3Cu798 and 1Cu400 ($p < 0.022$). At this time point, the 10Cu400 had lower luminescence than the samples CPTi-798, 1Cu798, 1Cu400, 3Cu798, and 3Cu400 ($p < 0.036$). Within the aged alloys, it was found that R for 10Cu400 (45%) was greater than that for the 5Cu400 (15%). As for the un-aged alloys, the 3Cu400 and 1Cu400 had negative R-values.

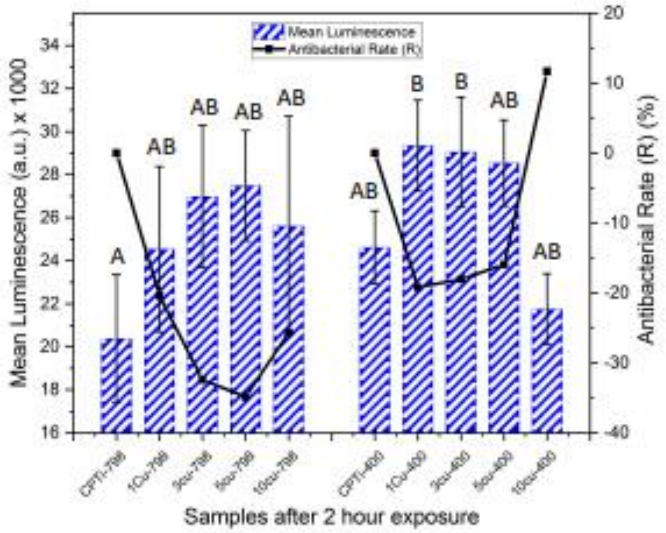


Figure 4. Mean luminescence counts (bars for standard deviation) of XEN 43 bacteria after two hours for all alloys, the negative controls were (CPTi), and the corresponding antibacterial rates are shown in black. Levene's Test: F (9,20) = 1.83, $p = 0.123$. One-way Anova: F = 3.176 ($p = 0.015$) with Tukey Test. Note: The same letters (e.g. "A" compared to "A") denotes being non-significantly different, while different letters (e.g. "A" compared to "B") denotes being statistically significantly different.

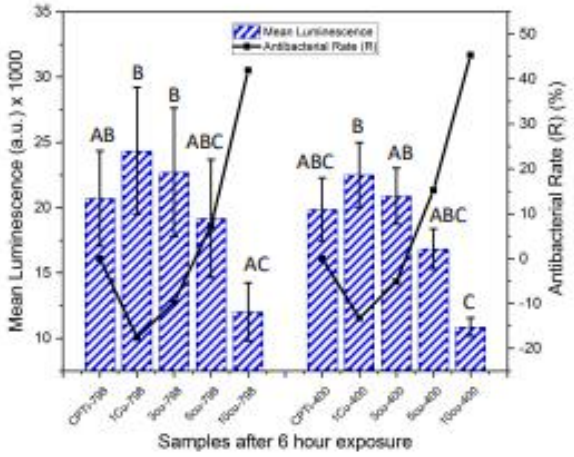


Figure 5. Mean luminescence counts (bars for standard deviation) of XEN 43 bacteria after six hours for all alloys, the negatives controls were CPTi, and the corresponding antibacterial rates are shown in black. Levene's Test: F (9,20) = 2.21, $p = 0.066$. One-way Anova: F = 5.697 ($p < 0.001$) with Tukey Test. Note: The same letters (e.g. "A" compared to "A") denotes being non-significantly different, while different letters (e.g. "A" compared to "B") denotes being statistically significantly different.

3.4. Hardness Tests

The effects of alloying Cu to Ti and ageing on hardness were investigated (Figure 6). The 10Cu798 alloy had the highest hardness (350 ± 12 Hv) of the alloys while the CPTi-400 alloy had the lowest (120 ± 3 H_V). The increased Cu addition to the CPTi correlated with a gradual augmentation in the Vicker's hardness, except for the 10Cu798 alloy with a hardness twice that of the 5Cu798 alloy (171 ± 7 H_V, $p < 0.0001$ in comparison with all other alloys). Ageing did not significantly affect the hardness of the alloys, except for 10Cu798, which was 1.9 times ($p < 0.0001$) harder than 10Cu400 (182 ± 1 H_V), and CPTi798 which had a 14% ($p < 0.021$) increase in H_V after ageing.

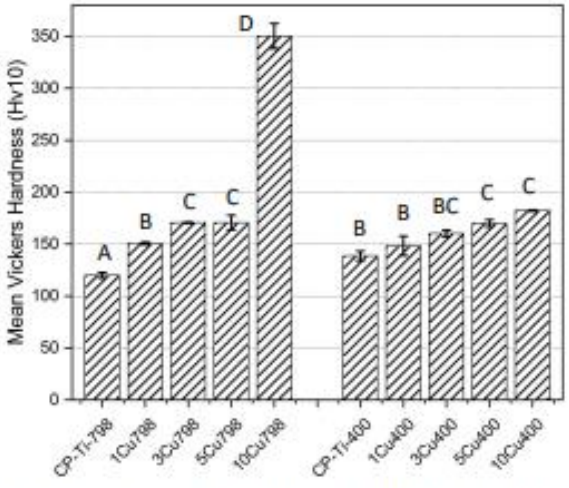


Figure 6. Mean Vickers hardness (bars for standard deviation) of all samples. Brown-Forsythe: F (9,20) = 1.413, $p = 0.2476$. One-way Anova: F = 368.92 ($p < 0.001$) with Tukey test. Note: The same letters (e.g. "A" compared to "A") denotes being non-significantly different, while different letters (e.g. "A" compared to "B") denotes being statistically significantly different.

3.5. Corrosion Tests

Corrosion studies were performed to determine the effect of the copper additions on the corrosion resistance, as well as the effect of ageing. The alloys were plotted in a single graph (Figure 7). The alloys aged at 400 °C showed a distinct corrosion profile after the anodic reaction took place. The aged alloys tended to passivate rapidly after the anodic reaction commenced. The un-aged alloys (quenched from 798 °C) clearly had a different corrosion profile trend, which indicated a gradual change in the passivation after the anodic reaction.

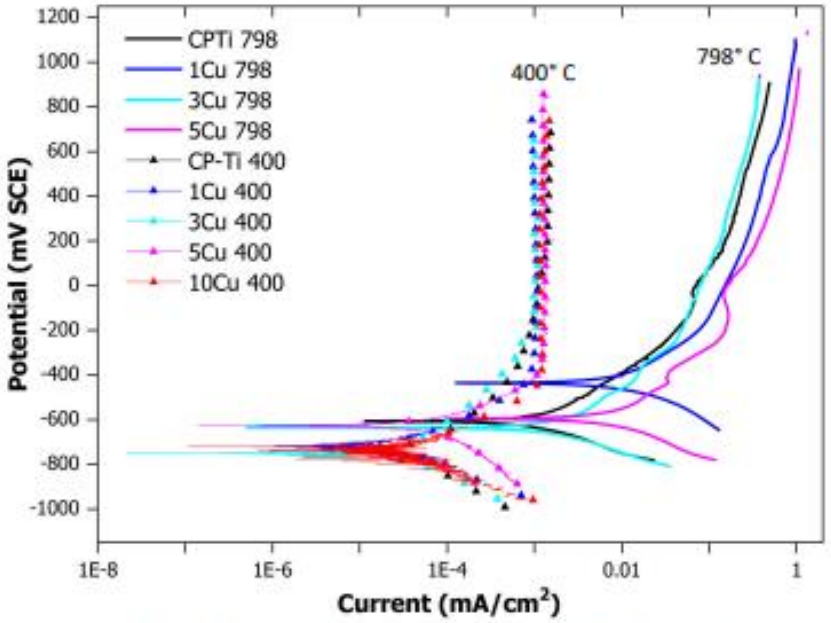


Figure 7. Corrosion plots for the aged (at 400 °C) and un-aged (quenched from 798 °C) alloys. The aged alloys are indicated with triangles to indicate the profile. Note: the 10Cu798 alloy was not included in the corrosion study.

4. Discussion

The present investigation focused on alloying up to 10 wt% of Cu into commercially pure titanium (a well-known implant material), where Cu has shown antibacterial potential in previous studies [17,20,38,39]. Its purpose was to determine the resultant microstructural and antibacterial characteristics of the materials, as a function of Cu addition and ageing heat treatments.

Microstructural and X-ray diffraction observations indicated no β-Ti in any of the alloys, despite a rapid quench (Figure 2). The reasons for this could be the active eutectoid transformation kinetics that drive transformation from $\beta - Ti \rightarrow \alpha - Ti + Ti_2Cu$ [40]. The two phases of α-Ti (HCP-Ti) and Ti_2Cu were observed as predicted in phase calculations [17]. The CPTi and 1Cu–except the 1Cu798 alloy that could have Ti_3Cu present–alloys were single-phase α-Ti alloys (Figures 1 and 2), while in alloys with higher Cu content (aged and un-aged) both α-Ti and Ti_2Cu were found. The ageing had a major effect on the microstructure and the Ti_2Cu precipitates had a larger volume fraction in the aged alloys. The ageing of the 10Cu798 alloy coarsened the Ti_2Cu from small precipitates to larger lamellar microstructures (Figure 1). A similar change occurred with ageing in the other two-phased alloys (5Cu798 and 3Cu798), but with coarsening of uniform lamellae of Ti_2Cu in the α-Ti phase.

α-Ti and Ti_2Cu were observed by X-ray diffraction, in addition to Ti_3Cu at 2θ angles of 20.9° and 23.4° for the 1Cu798, 3Cu798, 3Cu400, and 5Cu798 alloys. EDX measurements on a 5Cu798 sample confirmed that some of the precipitates had the expected 33 at% Cu for Ti_2Cu [35], while at least one

precipitate had compositions closer to 25 at% Cu, which is the expected composition for Ti_3Cu [30]. However, the results might have been affected by analyzing small areas, which resulted in collecting the signal from the surrounding phases. Although this study did not make use of a standard reference material for the analysis, the results gave insight into the variation of composition for the precipitates with Cu in the Ti-Cu_x alloys. It should however be noted that the precipitates with compositions closer to Ti_3Cu were in lower volume fractions—for the 5Cu798 alloy—relative to the precipitates with compositions close to 33 at% Cu. This lower volume fraction could be the reason for the absence of Ti_3Cu by X-ray diffraction in the 10 wt% Cu alloys, since it could have been below the detection limit for the technique. However, this was only a preliminary study on one alloy and further studies are needed to confirm the general presence of Ti_3Cu in Ti-Cu_x alloys.

As well as the microstructure, the hardness was also affected by Cu additions and ageing, and the 10Cu798 was twice as hard as the 10Cu400 alloy. The mechanism causing this could be the coarser lamellar structure in the 10Cu400 [41]. Ageing had a hardening effect on the CPTi-798 alloy as well, because the hardness was significantly higher for the CPTi-400 alloy.

The bacteria test gave an interesting result after two hours of exposure for the alloys, and 10Cu400 had an antibacterial rate R of 11%, while all the other Ti-Cu_x alloys had higher mean luminescence than CPTi. The reason for the higher luminescence could be that the bacteria underwent a stress response, which caused a rapid increase in population [23]. Comparison of the aged alloys at two hours and at six hours gave a similar trend for antibacterial rate (R). The 10Cu400 alloys seemed to be effectual at bacteria reduction already from two hours and thereafter increased, and at six hours the R was 46%. The 5Cu798 and 5Cu400 alloys after six hours had R values of 7% and 15%, respectively, although this was not significantly different from alloys with lower Cu content. The greater R at six hours for both aged (45%) and un-aged (42%) 10 wt% Cu alloys agreed with previous findings where a higher Cu content has been reported to yield a stronger antibacterial material [17,38]. The difference in R for the 10 wt% Cu alloys at two hours could be due to the larger amounts of Ti_2Cu in the aged alloy leading to higher Cu ion release rates as has been observed in studies on Ti-6Al-4V-5Cu alloys [28]. However, further studies on ion release from Ti-Cu_x are needed to support this conclusion. Additionally, direct contact of bacteria with a Cu rich surface—such as the 10Cu400 with higher volume fraction Ti_2Cu—could also have played a role in the antibacterial effect [24]. Thus, Cu ions and direct contact killing contributed to the antibacterial effect, and future studies could investigate how the amount and size of the Ti_2Cu phase influences copper ion release and the contact killing of bacteria.

The corrosion results indicated that alloying with Cu and ageing affected the corrosion rates and passivation rates. Alloying and ageing induced faster passivation for higher Cu contents, and decreased the corrosion rates. These results are in agreement with the findings of Zhang et al. [38] for an aged 4 wt% Cu alloy.

A limitation to the present study is that only alloys in the range of 0 to 10 wt% Cu were investigated. It has been demonstrated that a higher Cu content yields a better antibacterial response [17], however, an excess of copper can be harmful to the human body [42]. Previous studies [15,23] have reported that the Cu ions released from alloys with up to 10 wt% Cu did not have any notable toxic effects and were therefore the focus of the present study. Moreover, only two heat treatments were studied due to a necessary delimitation of the study. There are other heat treatments that could be tested, and future studies should further optimize the alloying process. The investigation on the presence of Ti_3Cu was a preliminary study and the results should not be viewed as conclusive due to only one alloy being characterized, the low number of precipitates characterized and the low resolution of the EDX technique. Another limitation is that the antibacterial ability of the alloys was only tested with one type of bacteria. However, the bacterium used, Staphylococcus epidermidis, is one of the most prevalent bacteria in implant infections and its use additionally allowed comparison with previous studies [23].

5. Conclusions

Both Ti_2Cu and Ti_3Cu were detected in Cu alloys using X-ray diffraction. A preliminary EDX study on the un-aged 5 wt% Cu alloy also indicated the presence of Ti_3Cu, however with the Ti_2Cu in majority. While the study of the Ti_3Cu was not quantitative in this investigation, it is recommended that future works focus on determination of this phase.

The hardness was reduced after ageing of the 10Cu798 alloy, as the microstructure changed from small precipitates to coarser lamellar microstructures. The alloys had good antibacterial rates above 5 wt% Cu (aged and un-aged) after six-hours of exposure, and the two-hour exposure was probably too short a duration for bacterial reduction to occur in most of the alloys. Ageing the alloys only ensured faster antibacterial rates after 2 hours, when the concentration of Cu was greater than 10 wt% Cu. The addition of Cu to Ti and ageing increased the corrosion resistance of the alloys, which could protect the biomaterial in vivo. However, since the ageing also lowered the hardness of the higher Cu content alloys, care should be taken to avoid over-ageing, and hence softening.

In conclusion, the un-aged 10 wt% Cu alloy was considered a suitable candidate material, which provided a good antibacterial effect, with superior hardness and corrosion protection. The ideal composition and heat treatment of these materials will however depend on the specific application envisioned, and will require further optimization.

Author Contributions: Conceptualization, H.E., S.N. and C.Ö.-M; Formal analysis, L.F., N.M., S.N. and C.Ö.-M; Funding acquisition, L.A.C., L.H.C., S.N. and C.Ö.-M; Investigation, L.F. and N.M.; Methodology, S.N. and C.Ö.-M; Project Administration, L.A.C., L.H.C., H.E., S.N. and C.Ö.-M; Resources, L.A.C., H.E., S.N. and C.Ö.-M; Supervision, L.A.C., L.H.C., H.E., S.N. and C.Ö.-M; Validation, L.F. and N.M.; Visualization, L.F. and N.M.; Writing-original draft, L.F.; Writing-review & editing, L.F., N.M., L.A.C., L.H.C., H.E., S.N. and C.Ö.-M.

Funding: This research was funded by the South African-Sweden Bilateral Scientific Research Cooperation program funded by the Swedish Foundation for International Cooperation in Research and Higher Education (STINT, GA SA2017-7127) and the South African National Research Foundation (NRF funding through STNT170905261815).

Acknowledgments: The authors thank Victoria Sternhagen for help with SEM imaging.

Conflicts of Interest: The authors declare no conflict of interest.

References

1. Alani, A.; Kelleher, M.; Bishop, K. Peri-implantitis. Part 1: Scope of the problem. *Br. Dent. J.* **2014**, *217*, 281–287. [CrossRef] [PubMed]
2. Atieh, M.A.; Alsabeeha, N.H.M.; Faggion, C.M.; Duncan, W.J. The frequency of peri-implant diseases: A systematic review and meta-analysis. *J. Periodontol.* **2013**, *84*, 1586–1598. [CrossRef] [PubMed]
3. Fransson, C.; Lekholm, U.; Jemt, T.; Berglundh, T. Prevalence of subjects with progressive bone loss at implants. *Clin. Oral Impl. Res.* **2005**, *16*, 440–446. [CrossRef] [PubMed]
4. Norowski, P.A.; Bumgardner, J.D. Biomaterial and antibiotic strategies for peri-implantitis: A review. *J. Biomed. Mater. Res.* **2009**, *88B*, 530–543. [CrossRef]
5. Hultin, M.; Gustafson, A.; Hallström, H.; Johansson, L.-Å.; Ekfeldt, A.; Klinge, B. Microbiological findings and host response in patients with peri-implantitis. *Clin. Oral Impl. Res.* **2002**, *13*, 349–358. [CrossRef] [PubMed]
6. Ladomersky, E.; Petris, M.J. Copper tolerance and virulence in bacteria. *Metallomics* **2015**, *7*, 957–964. [CrossRef]
7. Hawkey, P.M. The growing burden of antimicrobial resistance. *J. Antimicrob. Chemother.* **2008**, *62*, i1–i9. [CrossRef]
8. Arciola, C.R.; Campoccia, D.; Speziale, P.; Montanaro, L.; Costerton, J.W. Biofilm formation in Staphylococcus implant infections. A review of molecular mechanisms and implications for biofilm-resistant materials. *Biomaterials* **2012**, *33*, 5967–5982. [CrossRef]
9. Stewart, P.S. Mechanisms of antibiotic resistance in bacterial biofilms. *Int. J. Med. Microbiol.* **2002**, *292*, 107–113. [CrossRef]

10. Vasudevan, S.; Joseph, H.A.; Swamy, S.S.; Solomon, A.P. *Antibiotic Resistance in Biofilms*; ACS Symposium Series; Rathinam, N.K., Sani, R.K., Eds.; American Chemical Society: Washington, DC, USA, 2019; pp. 205–224. [CrossRef]
11. Zhang, Y.-Q.; Ren, S.-X.; Li, H.-L.; Wang, Y.-X.; Fu, G.; Yang, J.; Qin, Z.-Q.; Miao, Y.-G.; Wang, W.-Y.; Chen, R.-S.; et al. Genome-based analysis of virulence genes in a non-biofilm-forming Staphylococcus epidermidis strain (ATCC 12228). *Mol. Microbiol.* **2003**, *49*, 1577–1593. [CrossRef]
12. Spriano, S.; Bosetti, M.; Bronzoni, M.; Vernè, E.; Maina, G.; Bergo, V.; Cannas, M. Surface properties and cell response of low metal ion release Ti-6Al-7Nb alloy after multi-step chemical and thermal treatments. *Biomaterials* **2005**, *26*, 1219–1229. [CrossRef]
13. Unosson, E.; Tsekoura, E.K.; Engqvist, H.; Welch, K. Synergetic inactivation of Staphylococcus epidermidis and Streptococcus mutans in a TiO2/H2O2/UV system. *Biomatterials* **2013**, *3*, e26727. [CrossRef]
14. Unosson, E.; Morgenstern, M.; Engqvist, H.; Welch, K. In vitro antibacterial properties and UV induced response from Staphylococcus epidermidis on Ag/Ti oxide thin films. *J. Mater. Sci. Mater. Med.* **2016**, *27*, 49. [CrossRef]
15. Bai, B.; Zhang, E.; Dong, H.; Liu, J. Biocompatibility of antibacterial Ti–Cu sintered alloy: In vivo bone response. *J. Mater. Sci. Mater. Med.* **2015**, *26*, 265. [CrossRef]
16. Zhang, E.; Li, F.; Wang, H.; Liu, J.; Wang, C.; Li, M.; Yang, K. A new antibacterial titanium–copper sintered alloy: Preparation and antibacterial property. *Mater. Sci. Eng. C.* **2013**, *33*, 4280–4287. [CrossRef]
17. Fowler, L.; Janson, O.; Engqvist, H.; Norgren, S.; Öhman-Mägi, C. Antibacterial investigation of titanium-copper alloys using luminescent Staphylococcus epidermidis in a direct contact test. *Mater. Sci. Eng. C.* **2019**, *97*, 707–714. [CrossRef]
18. Codiță, I.; Caplan, D.M.; Drăgulescu, E.-C.; Lixandru, B.-E.; Coldea, I.L.; Dragomirescu, C.C.; Surdu-Bob, C.; Bădulescu, M. Antimicrobial activity of copper and silver nanofilms on nosocomial bacterial species. *Roum. Arch. Microbiol. Immunol.* **2010**, *69*, 204–212.
19. Russel, A.D.; Hugo, W.B. 7 Antimicrobial activity and action of silver. *Progr. Med. Chem.* **1994**, *31*, 351–370. [CrossRef]
20. Michels, H.T.; Noyce, J.O.; Keevil, C.W. Effects of temperature and humidity on the efficacy of methicillin-resistant Staphylococcus aureus challenged antimicrobial materials containing silver and copper. *Lett. Appl. Microbiol.* **2009**, *49*, 191–195. [CrossRef]
21. Stranak, V.; Wulff, H.; Rebl, H.; Zietz, C.; Arndt, K.; Bogdanowicz, R.; Nebe, B.; Bader, R.; Podbielski, A.; Hubicka, Z.; et al. Deposition of thin titanium–copper films with antimicrobial effect by advanced magnetron sputtering methods. *Mater. Sci. Eng. C* **2011**, *31*, 1512–1519. [CrossRef]
22. Jäger, E.; Schmidt, J.; Pfuch, A.; Spange, S.; Beier, O.; Jäger, N.; Jantschner, O.; Daniel, R.; Mitterer, C. Antibacterial silicon oxide thin films doped with zinc and copper grown by atmospheric pressure plasma chemical vapor deposition. *Nanomaterials* **2019**, *9*, 255. [CrossRef]
23. Fowler, L.; Engqvist, H.; Öhman-Mägi, C. Effect of Cu ion concentration on bacteria and cells. *Materials* **2019**, *12*, 3798. [CrossRef]
24. Mathews, S.; Hans, M.; Mücklich, F.; Solioz, M. Contact killing of bacteria on copper is suppressed if bacterial-metal contact is prevented and is induced on iron by copper ions. *Appl. Environ. Microbiol.* **2013**, *79*, 2605–2611. [CrossRef]
25. Ke, Z.; Yi, C.; Zhang, L.; He, Z.; Tan, J.; Jiang, Y. Characterization of a new Ti-13Nb-13Zr-10Cu alloy with enhanced antibacterial activity for biomedical applications. *Mater. Lett.* **2019**, *253*, 335–338. [CrossRef]
26. Liu, C.; Zhang, E. Biocorrosion properties of antibacterial Ti–10Cu sintered alloy in several simulated biological solutions. *J. Mater. Sci. Mater. Med.* **2015**, *26*, 142. [CrossRef]
27. Zhang, E.-L.; Fu, S.; Wang, R.-X.; Li, H.-X.; Liu, Y.; Ma, Z.-Q.; Liu, G.-K.; Zhu, C.-S.; Qin, G.-W.; Chen, D.-F. Role of Cu element in biomedical metal alloy design. *Rare Met.* **2019**, *38*, 476–494. [CrossRef]
28. Li, M.; Ma, Z.; Zhu, Y.; Xia, H.; Yao, M.; Chu, X.; Wang, X.; Yang, K.; Yang, M.; Zhang, Y.; et al. Toward a molecular understanding of the antibacterial mechanism of copper-bearing titanium alloys against staphylococcus aureus. *Adv. Healthc. Mater.* **2016**, *5*, 557–566. [CrossRef]
29. Kumar, K.C.H.; Ansara, I.; Wollants, P.; Delaey, L. Thermodynamic optimisation of the Cu-Ti system. *Zeitschrift Für Metallkunde* **1996**, *87*, 666–672.
30. Canale, P.; Servant, C. Thermodynamic assessment of the Cu–Ti system taking into account the new stable phase CuTi3. *MEKU* **2002**, *93*, 273–276. [CrossRef]

31. Appel, F.; Oehring, M. γ-titanium aluminide alloys: Alloy design and properties. In *Titanium and Titanium Alloys*, 1st ed.; Leyens, C., Peters, M., Eds.; Wiley-VCH Verlag GmbH & Co. KGaA: Weinheim, Germany, 2003; pp. 89–152. [CrossRef]
32. Voort, G.V. Materials characterization & testing: Microstructure of titanium and its alloys. *Ind. Heat.* **2006**, *73*, 82–84.
33. Nadai, L.; Katona, B.; Terdik, A.; Bognar, E. Chemical etching of titanium samples. *Periodica Polytechnica Mech. Eng.* **2013**, *57*, 57. [CrossRef]
34. PDF-4+ 2019, ICDD. (n.d.). Available online: http://www.icdd.com/index.php/pdf-4/ (accessed on 10 May 2019).
35. Mueller, M.H.; Knott, H.W. The crystal structures of Ti2 Cu, Ti2 Ni, Ti4 Ni2 O, and Ti4 Cu2 O. *Trans. Metallurg. Soc. AIME* **1963**, *227*, 674–678.
36. Vuong, C.; Kocianova, S.; Yu, J.; Kadurugamuwa, J.L.; Otto, M. Development of real-time in vivo imaging of device-related *staphylococcus epidermidis* infection in mice and influence of animal immune status on susceptibility to infection. *J. Infect. Dis.* **2008**, *198*, 258–261. [CrossRef]
37. Wiedmer, D.; Petersen, F.C.; Lönn-Stensrud, J.; Tiainen, H. Antibacterial effect of hydrogen peroxide-titanium dioxide suspensions in the decontamination of rough titanium surfaces. *Biofouling* **2017**, *33*, 451–459. [CrossRef]
38. Zhang, E.; Ren, J.; Li, S.; Yang, L.; Qin, G. Optimization of mechanical properties, biocorrosion properties and antibacterial properties of as-cast Ti–Cu alloys. *Biomed. Mater.* **2016**, *11*, 065001. [CrossRef]
39. Bai, B.; Zhang, E.; Liu, J.; Zhu, J. The anti-bacterial activity of titanium-copper sintered alloy against Porphyromonas gingivalis in vitro. *Dent. Mater. J.* **2016**, *35*, 659–667. [CrossRef]
40. Donthula, H.; Vishwanadh, B.; Alam, T.; Borkar, T.; Contieri, R.J.; Caram, R.; Banerjee, R.; Tewari, R.; Dey, G.K.; Banerjee, S. Morphological evolution of transformation products and eutectoid transformation(s) in a hyper-eutectoid Ti-12 at% Cu alloy. *Acta Mater.* **2019**, *168*, 63–75. [CrossRef]
41. Soffa, W.A.; Laughlin, D.E. High-strength age hardening copper–titanium alloys: Redivivus. *Progr. Mater. Sci.* **2004**, *49*, 347–366. [CrossRef]
42. Bull, P.C.; Thomas, G.R.; Rommens, J.M.; Forbes, J.R.; Cox, D.W. The Wilson disease gene is a putative copper transporting P–type ATPase similar to the Menkes gene. *Nat. Genet.* **1993**, *5*, 327–337. [CrossRef]



© 2019 by the authors. Licensee MDPI, Basel, Switzerland. This article is an open access article distributed under the terms and conditions of the Creative Commons Attribution (CC BY) license (http://creativecommons.org/licenses/by/4.0/).

MICROSTRUCTURAL ANALYSIS OF TI-CU ALLOYS FOR DENTAL APPLICATIONS

NDE Masia[1, 2, 3], LH Chown[2, 3], M Smit[1], AI Mwamba[1, 3] & LA Cornish[2, 3]

[1]Advanced Materials Division, Mintek, Randburg, [2]School of Chemical and Metallurgical Engineering, University of the Witwatersrand, Johannesburg[3], DST-NRF Centre of Excellence in Strong Materials, hosted by the University of the Witwatersrand, Johannesburg

Titanium has been the material of choice in several disciplines of dentistry, due to its excellent characteristics such as biocompatibility, osseointegration, high wear and corrosion resistance, low compatibility issues and high strength. Corrosion of titanium dental implants causes implant failure and can trigger peri-implantitis [1]. Avoiding bacterial adhesion on the implant surface can be achieved by applying hydrophilic coatings, but these can inhibit tissue integration [2]. Antibiotics can also be employed, but high doses may result in deleterious side-effects and bacterial resistance when used for a long term [3]. Copper bearing titanium alloys have been reported to possess excellent antibacterial properties. They are also reported to provide adequate biocompatibility, reasonable corrosion resistance and comparatively low melting temperatures, which greatly favour casting procedures [4]. The shape and size of Ti_2Cu phase significantly influences the antibacterial properties and mechanical properties, as well as corrosion properties [5]. Heat treatment, such as annealing and ageing, could significantly improve the mechanical properties, corrosion resistance and antibacterial rate due to the redistribution of copper and size distribution of Ti_2Cu precipitates. This study assessed the effect of the Ti_2Cu compound and its proportions on the corrosion resistance, and to compare them to the commercial pure titanium (Grade 4).

The Thermo-Calc program with TTTI3 (Ti-alloy database) was used to predict the phases. Ti-Cu alloys at different compositions such as 15, 25, and 47 wt % copper were produced in a button arc melting furnace. They were studied in the as-cast and annealed conditions (900°C water quenched). The microstructures was observed using optical microscopy. Compositional analyses were performed using an electron probe microanalyser, and the phases were identified by X-ray diffraction. Corrosion resistance was determined by potentiodynamic polarisation in a phosphate buffered saline (PBS) solution at 37°C in a pH of 7.4 while purging with nitrogen gas.

Thermo-Calc predicted only equilibrium alpha, beta and Ti_2Cu while XRD showed Ti_3Cu in Ti-25Cu in the as-cast condition and not after annealing. CP Ti consisted of a lamellar α Ti microstructure. Ti-15Cu and Ti-25Cu had similar microstructures consisting of eutectoid (lamellae) α Ti and Ti_2Cu with α Ti islands; except for that XRD indicated the presence of Ti_3Cu instead of Ti_2Cu in Ti-25Cu in the as-cast condition. Ti-47Cu consisted of a dual phase structure Ti_2Cu and TiCu with some substrate copper. Figures 1-2 shows the microstructures. In both the as-cast and annealed conditions CP Ti had the lowest corrosion rates while Ti-47Cu had the highest rates. The addition of copper decreased the corrosion resistance however the corrosion rates are still within the acceptable range for biocompatibility of metallic implants. Annealing at 900°C improved the corrosion resistance.

References

1. Rodrigues, D., Valderrama, T. G., Palmer, K., Thomas, K., Sridhar, S., Adapalli, A. and Wadhwani, C. (2013) Materials, 5258-5274.
2. Francolini, I., and Donelli, G. (2010). FEMS Immmology and Medical Microbiology,59, 227-238.
3. Andrews, J. (2001,). Journal of Antimicrobial Chemotherapy, Suppl.S15-16.
4. Osório, W., Cremasco, A., Andrade, P., Garcia, A., and Caram, R. (2010), Electrochimica Acta, 55(10),759-770.
5. Zhang, E., Wang, X., Chen, M., and Hou, B. (2016). Materials Science and Engineering,69, 1210-1221.

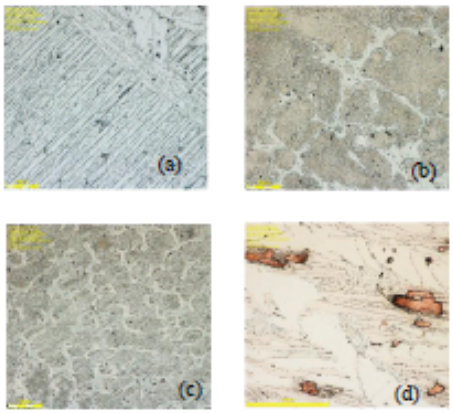


Figure 1. Ti-Cu alloys microstructures in the as-cast condition (a) CP Ti (b) Ti-15Cu (c) Ti-25Cu (d) Ti-47Cu

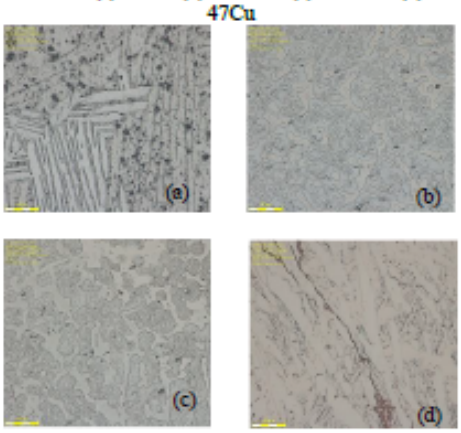


Figure 2. Ti-Cu alloys microstructures in the as-annealed condition (a) CP Ti (b) Ti-15Cu (c) Ti-25Cu (d) Ti-47Cu

Corresponding author: *nomsombulukoh@mintek.co.za*

A MICROSTRUCTURAL ANALYSIS OF A Ti-Ta-Cu-Nb-Zr ALLOY

N.G. Hashe[1], L. Fowler[2], W.E. Goosen[3], S. Norgren[2], N.D. Masia[4], L.A. Cornish[4], C. Öhman-Mägi[2], L.H. Chown[4], S. Magadla[1], K.T. Nape[4], M. Mavundla[4] and L. Spotose[4]

[1]Department of Physics, Nelson Mandela University, Port Elizabeth, [2]Department of Engineering Science, Uppsala University, Uppsala, Sweden, [3]CHRTEM, Nelson Mandela University, Port Elizabeth, [4]School of Chemical and Metallurgical Engineering, and DST-NRF Centre of Excellence in Strong Materials, hosted by the University of the Witwatersrand, Johannesburg

Titanium and its alloys are used in the medical industry as implants because of their biocompatibilities and excellent mechanical and physical properties[1]. The Ti-6Al-4V alloy is used as an implant material due to its high corrosion resistance and excellent biocompatibility[1]. However, there are concerns about the toxicity of aluminium and vanadium[2]. The other concern is the formation of the adherent biofilms around the surface area of the implants[3]. Therefore, the current research is aimed at replacing V and Al with Ta, Nb and Zr to produce a biocompatible alloy with antibacterial[4] and osseointegrative properties that has a similar microstructure to that of an alpha-beta Ti-6Al-4V alloy.

The Ti-10.1Ta-1.7Nb-1.6Zr (wt%) alloy produced by Stenlund *et al.*[5] was studied further. Titanium and Zr sponges were mixed with Ta and Nb wires and compressed into a 7 kg lump, which was melted four times in vacuum in an Electron Beam furnace for homogeneity. The Ti-10.1Ta-1.7Nb-1.6Zr alloy was mixed with 3 mass% Cu and the mixture was melted five times in a custom built arc-furnace. Annealing was done in a sealed quartz-ampoule at 1.333 mbar (after flushing) in a conventional furnace. Heat treatment was done at 980 °C for 10 hours, followed by 798 °C for 6 hours, with a final rapid salt-brine water quench. The annealing temperatures were chosen to obtain the alpha Ti (hcp) and beta Ti (bcc)[5]. After heat treatment, the samples were prepared metallographically and analysed by scanning electron microscopy (SEM) and X-ray diffraction (XRD).

Backscattered SEM imaging (Fig. 1) shows that the microstructure of the Ti-Ta-Cu-Nb-Zr alloy was lamellar, which are reported to have a high fatigue crack propagation resistance and high fracture toughness[6]. There were small, irregular regions of a much darker phases (indicated by a white arrow) , within the dark phase (indicated by a white star). Energy dispersive spectroscopy (EDX) showed the light contrast phase (indicated by a black arrow) had more Ta and Cu, with less Nb than the dark phase. However, the Nb content was less than 1 mass%, so the results were too near the detection limit to be reliable. The dark phase was identified as alpha Ti since it had more Ti. The small regions of the darkest phase were too small to analyse accurately with EDX.

The XRD patterns only showed alpha-Ti (Fig, 2). The pattern for the heat treated samples also showed apparent preferred orientation, which was surprising considering that the pattern from the as-cast sample was more random. Further work is required to identify the darkest phase, and XRD needs to be repeated with a more suitable X-ray source in order to quantify the phases present in the material.

References:
1. Geetha, M. *et al.* (2009) Prog. Mat. Sci. 54, 397.
2. Niinomi M. and Nakai M. (2011) Int. J. Biomater. 2011, 1.
3. Lorenzetti, M. *et al.* (2015) Appl. Mater. Interfaces 7, 1644.
4. Magadla, S. *et al.* (2019) Euromat 2019 Abstracts, 2288.
5. Stenlund, P. *et al.* (2015) Acta Biomat. 20, 165.
6. Filip, R. *et al.* (2003) J. Mat. Proc. Techn. 133, 84.

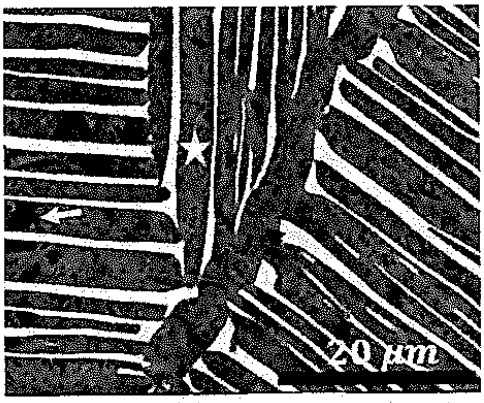


Figure 1. SEM-BSE image showing the typical microstructure of Ti-Ta-Nb-Zr-Cu alloy with three phases.

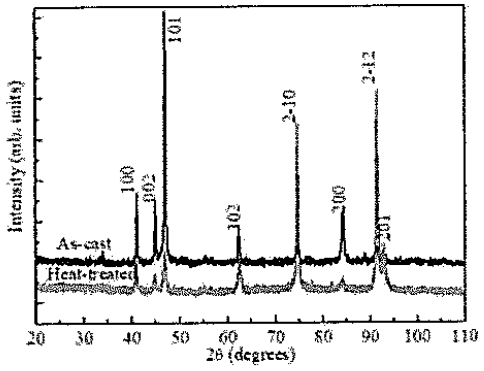


Figure 2. XRD patterns of the as-cast and heat treated Ti-Ta-Cu-Nb-Zr alloy, showing only alpha-Ti.

Corresponding author: nobom.hashe@mandela.ac.za

EFFECT OF DIFFERENT COPPER ADDITIONS TO Ti–10.1Ta–1.7Nb–1.6Zr

K. Dyal Ukabhai[1], L. Fowler[2], K.T. Nape[1], M. Mavundla[1], L. Spotose[1], S. Magadla[3], N.D. Masia[1,4], D.E.P. Klenam[1], N.G. Hashe[3], C. Öhman Mägi[2], S. Norgren[5], L.H. Chown[1] and L.A. Cornish[1]

[1]Sch. Chem. & Met. Eng. and DST-NRF CoE Strong Materials, hosted by U.Witwatersrand, [2]Dept of Eng. Sciences, Ångström Lab. Uppsala University, Sweden, [3]Dept Physics, Nelson Mandela University, Port Elizabeth, [4]Advanced Materials Division, Mintek, Randburg, [5]Sandvik Coromant R&D, Stockholm, Sweden

Commercially pure titanium is popular for bone-anchored dental devices, while the stronger Ti-6Al-4V alloy is preferred for higher load applications. However, Al and V are potentially toxic, giving reason to develop new (α+β) alloys without these elements, but with similar proportions of the two phases: (αTi) (brackets denote the solid solution based on Ti with that structure) and (βTi), for similar mechanical properties to Ti-6Al-4V. Stenlund *et al.*[1] undertook computer calculations to derive "TTNZ", an (α+β) alloy with similar phase proportions to Ti-6Al-4V, but without Al or V: Ti-10.1Ta-1.7Nb-1.6Zr (in wt%). The alloy was manufactured from Ti and Zr sponge, and Ta and Nb wire, which were mixed, compressed, then melted in vacuum in an electron beam furnace to generate a homogeneous alloy.

Around 7% of patients with dental implants suffer from peri-implantitis within 10 years due to infection[2]. Copper is known to have antimicrobial properties[3]. Liu *et al.*[4] studied sintered Ti–*x*Cu alloys (x = 2, 5, 10 and 25 wt%) using XRD and SEM, and the antibacterial activity was assessed. The Ti_2Cu phase was found in all alloys. A Cu-rich phase formed in alloys with >5wt% Cu, which were also the best alloys for antibacterial activity.

This study used TTNZ samples made in the same way as Stenlund *et al.*[1] with nominal 1, 3, 5 and 10 wt% Cu added. The samples were prepared metallograpically, and studied using XRD and SEM-EDX after Vickers hardness tests ($HV_{0.1}$). XRD showed only (αTi) and (βTi) in the 0 and 1 wt% Cu TTNZ-Cu alloys, but the 3, 5 and 10 wt% Cu alloys had increasing amounts of Ti_3Cu[5], instead of the more commonly-reported Ti_2Cu[4]. SEM-EDX gave the copper content of Ti_3Cu as 28.1±0.3 to 29.7±1.1 at.% Cu. Increased Cu changed the microstructures from mainly (βTi) with small amounts of precipitated (αTi) for 0 and 1 wt% Cu (Fig. 1) to more equal amounts of the two phases with 3 wt% Cu (Fig. 2). Further increase in Cu increased the Ti_3Cu proportions. The 10 wt% Cu alloy had a totally different microstructure (Fig. 3), with fewer and shorter (αTi) laths, and Ti_3Cu precipitated on the prior (βTi) grain boundaries. Hardness increased with copper addition up to 5 wt% Cu, but 10 wt% Cu had lower hardness due to its different microstructure. The hardnesses were: 145±8, 182±6, 200±10, 201±8 and 178±8 $HV_{0.1}$ for 0, 1, 3, 5 and 10 wt% Cu respectively. Although most of the hardness indentations were square, Fig. 2 shows there was less plastic deformation of the harder Ti_3Cu phase. The lower hardness of the 10 wt% Cu alloy indicated too much copper had been added.

References:
1. Stenlund, P. *et al.* (2015) Acta Biomat. 20, 165.
2. Derks, J. *et al.* (2015) J. Dent. Res. 94(3), 44S.
3. Grass, G., Rensing, C. and Solioz, M. (2011) Appl. Environ. Microbiol. 77, 1541.
4. Liu, J. *et al.* (2014) Mat. Sci. & Eng. C35, 392.
5. Canale, P. and Servant, C. (2002) Z.Metallkd. 93(4), 273.

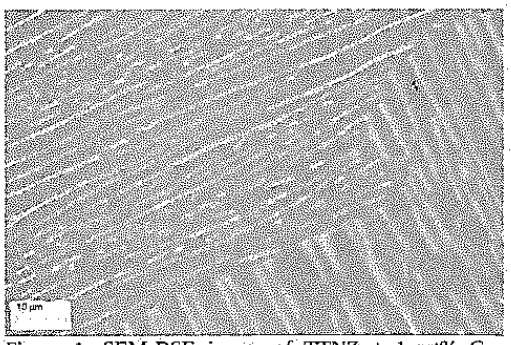


Figure 1. SEM-BSE image of TTNZ + 1 wt% Cu, showing light contrast (βTi) and dark contrast (αTi).

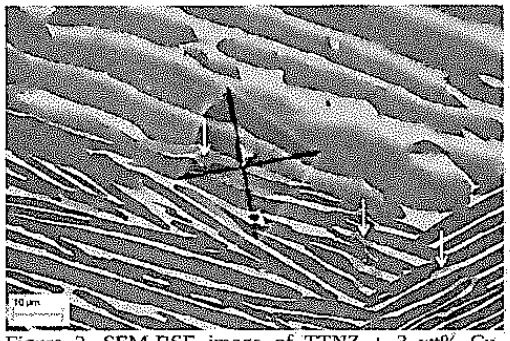


Figure 2. SEM-BSE image of TTNZ + 3 wt% Cu, showing a hardness indentation with light (βTi), dark (αTi) and medium contrast Ti_3Cu (shown by arrows).



Figure 3. SEM-BSE image of TTNZ + 10 wt% Cu: light (βTi), dark (αTi) and medium contrast Ti_3Cu.

Corresponding author: lesley.cornish@wits.ac.za

Corrosion Performance of Ti-Cu Alloys Targeted for Biomedical Applications

N.D.E. Masia[1,2,3,a*], M. Smit[1,b], I.A. Mwamba[1,c], L. Fowler[4,d], L.H. Chown[2,3,e], S. Norgren[4,f], C. Öhman-Mägi[4,g], N. Hashe[5,h], L.A. Cornish[2,3,i]

[1] Advanced Materials Division, Mintek, Randburg 2125, South Africa

[2] School of Chemical and Metallurgical Engineering, University of the Witwatersrand, Johannesburg 2050, South Africa

[3] DST-NRF Centre of Excellence in Strong Materials, hosted by the University of the Witwatersrand, Johannesburg 2050, South Africa

[4]Division of Applied Materials Science, Department of Engineering Sciences, The Ångström Laboratory, Uppsala University, Box 534, 751 21 Uppsala, Sweden

[5]Department of Physics, Nelson Mandela University (NMU), Port Elizabeth, South Africa

[a]nomsombulukoh@mintek.co.za*,[b]melanies@mintek.co.za,[c]alainm@mintek.co.za, [d]fowler.lee8@gmail.com, [e]dlesleyhchown@gmail.com, [f]susanne.m.norgren@sandvik.com, [g]caroline.ohman@angstrom.uu.se, [h]Nobom.Hashe@mandela.ac.za, [i]lesley.cornish@wits.ac.za

Abstract. The Thermo-Calc™ program and TTTI3 database were used to predict the phases in Ti-Cu with 5, 25, and 40 wt% Cu. Based on the predicted results, experimental work was conducted and the Ti-Cu alloys were produced in a button arc furnace, and characterised in the as-cast and the annealed condition (900°C) followed by water quenching. Microstructures and compositions were determined using an electron probe micro-analyser, and the phases were identified by X-ray diffraction. The corrosion performance was measured by potentiodynamic polarisation in a phosphate buffered saline solution at 37°C at 7.4 pH while purging with nitrogen gas. The Ti-5Cu and Ti-25Cu alloys comprised (αTi) and Ti_2Cu phases, the Ti-40Cu alloy comprised Ti_2Cu and TiCu. Although the addition of copper decreased the corrosion performance by down to 75%, the corrosion rates were still within the acceptable range (0.02-0.13 mm/y) for biocompatibility of metallic implants. Annealing at 900°C did not improve the corrosion performance.

1. Introduction

Commercially pure titanium (CP Ti) and titanium alloys are widely used in dental implant applications due to their good mechanical strength, successful osseointegration, high strength-to-weight ratio and resistance to corrosion [1, 2, 3]. Corrosion of titanium dental implants is associated with implant failure and is considered as a trigger factor for peri-implantitis [4], which is an inflammatory disease affecting the surrounding tissues of the implant, predominately the bone [4, 5]. It is caused by the adhesion of pathogenic biofilms on the implant surface and peri-implant tissues, resulting in bone loss and destruction of soft tissues [4]. Surgical and non-surgical treatments performed to control peri-implantitis have been

ineffective, and avoiding bacteria adhesion with hydrophilic coatings inhibits tissue integration [6, 7]. An alternative approach to antibacterial treatment are gels containing carvacrol and thymol [8], while others studied the antimicrobial affinity of different inorganic ions [7]. Silver and copper have emerged as promising alloying elements for antibacterial materials [7]. However, silver may lead to DNA damage and cannot kill bacteria at lower pH levels and temperatures [7, 9]. Due to these limitations, addition of copper is being studied. Addition of copper to titanium alloys which increases antibacterial properties has more potential [10]. The antibacterial property was associated with preferential copper ion release from the Ti-Cu alloys due to the galvanic corrosion between phases with copper and the titanium matrix. This galvanic coupling is strong and stable for copper contents above 5 wt%. They also obtained higher corrosion resistance of Ti-Cu alloys compared to CP Ti [11]. It was thought that the phases with copper such as Ti_2Cu played a very important role in the strong antibacterial behavior [12]. Heat treatment, such as annealing and ageing, could also significantly improve the mechanical properties, corrosion resistance and antibacterial rate due to the redistribution of copper and size distribution of Ti_2Cu precipitates [13]. Although Ti-Cu alloys have high corrosion resistance due to TiO_2 formed on the surfaces, they are not immune to corrosion. The aim of this study was to assess the effect of the Ti_2Cu compound and its proportions on the corrosion resistance, to see whether there was a degradation or improvement, and to relate the effect to the amounts of Ti_2Cu. Grade 4 CP Ti was selected due to its higher tensile strength and yield strength than Grades 1 to 3.

2. Materials and Experimental Procedure

2.1 Material Selection and Preparation

CP Titanium Grade 4 (15mm diameter rod, Multi Alloys (Pty) Ltd) and high purity copper (SAE CA110 - 3 mm thick plate, Meglan Trading CC) were the starting materials, and Table 1 shows their compositions. Ti-Cu alloys of 5, 25, and 40 wt% Cu were produced in a button arc melting furnace, with a high-energy arc at high temperatures on a water-cooled copper hearth. Two melts of each alloy were prepared: one melt was left as-cast and the other was annealed. The annealing was done in sealed quartz ampoules (each sample being in a separate ampoule) at 1.333 mbar in an induction furnace at 900°C for 2 h, followed a fast water quench (by crushing the amploules on quenching) to retain the (βTi) phase. Figure 1 shows the alloys on the Ti-Cu phase diagram [9].

Table 1. Chemical compositions of titanium and copper as starting materials.

	Elements (wt%)							
	N	**C**	**O**	**Fe**	**Ag**	**H**	**Cu**	**Ti**
Titanium Gr 4	0.05	0.08	0.4	0.5	-	0.015	-	98.96
SAE CA110	-	-	0.04	-	0.05	-	99.91	-

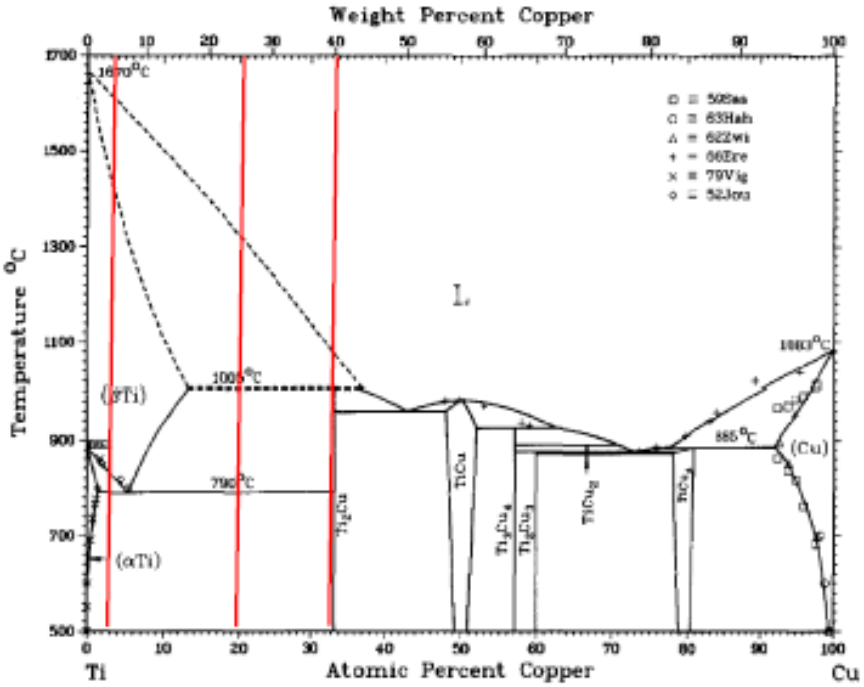


Figure 1. Ti-Cu phase diagram *[14]*.

2.2 Material Characterisation

Characterisation was performed on all the alloys in the as-cast and annealed conditions to study the basic features before corrosion testing. Chemical composition and microstructures were analysed using a JEOL 8230 electron probe microanalyser, with a combination of up to 5 wavelength dispersive X-ray spectroscopy (WDS) detectors and an energy dispersive X-ray spectroscopy (EDS) detector. Analyses were performed at 20 kV, 30 nA, and calibrated using pure metal reference standards. X-ray diffraction (XRD) was performed using a Bruker D8 Advance powder diffractometer, with a Linxeye detector using Fe filtered Co-Kα radiation. This method uses the net intensity of the main peaks of the phases, and identification is based on the crystal structure of phases that occur in amounts of >3 mass %. Amorphous phases are not detected, so the phases specified may not necessarily have the compositions deduced.

3. Electrochemical Testing

The corrosion tests were performed at 37±1°C (human body temperature) in a phosphate buffered saline (PBS) solution at pH 7.4. The PBS solution was chosen due to its buffer properties and because it has similar ion concentration to some human body fluids (isotonic) [15]. **Error! Reference source not found.** shows the composition of the PBS solution. Electrochemical tests were open circuit potential (OCP) and potentiodynamic polarization tests. Potentiodynamic tests were undertaken according to the ASTM-G5-2013 Standard, using a PC driven "ACM Gill AC" potentiostat. The alloys were sectioned into 10x10mm samples and were inserted in a sealed PVC holder. One graphite rod acted as a counter-electrode and a

Haber-Luggin capillary made the junction with a saturated calomel reference electrode (SCE). All potential values were measured with respect to the SCE. Nitrogen was bubbled continuously through the solution during testing to create an anaerobic environment, simulating conditions in the mouth.

Table 2.Chemical composition of the PBS solution.

Reagents (g)			
Sodium chloride (NaCl)	Potassium chloride (KCl)	Sodium hydrogen phosphate (Na_2HPO_4)	Potassium dihydrogen phosphate (KH_2PO_4)
8	0.2	1.44	0.24

The OCP was determined when the electrodes were immersed in the solution and the potential was recorded as a function of time. It was recorded at two hours when the potential was stable (at equilibrium). When the OCP was stable, potentiodynamic polarisation tests were done for each alloy. Each scan was from –250 mV to +1500 mV versus the corrosion potential at a scanning speed of 10 mV/min. The corrosion current densities were determined by Tafel extrapolation of the rate-determining segment of the polarisation curve, and the corrosion rates were calculated using Equation 1:

$$\text{Corrosion rate (mm/y)} = 0.009 \times I_{Corr} \times EW/d \qquad \text{Equation 1}$$

where mm/y = millimetres per year, EW = equivalent weight of the corroding species in grams (g), d = density of the corroding species (g/cm^3), and I_{Corr} = corrosion current density ($\mu A/cm^2$).

4. Results and Discussion

4.1 Thermo-Calc Results

Thermo-Calc predicted the equilibrium phases: liquid, BCC (βTi), HCP (αTi), Ti_2Cu and TiCu. Figure 2 to Figure *4* show the mole fractions of phases as a function of temperature for all the alloys. Ti-5Cu and Ti-25Cu alloys were predicted to comprise BCC (βTi), HCP (αTi) and Ti_2Cu phase, while the Ti-40Cu alloy was predicted to comprise BCC (βTi), Ti_2Cu and TiCu.

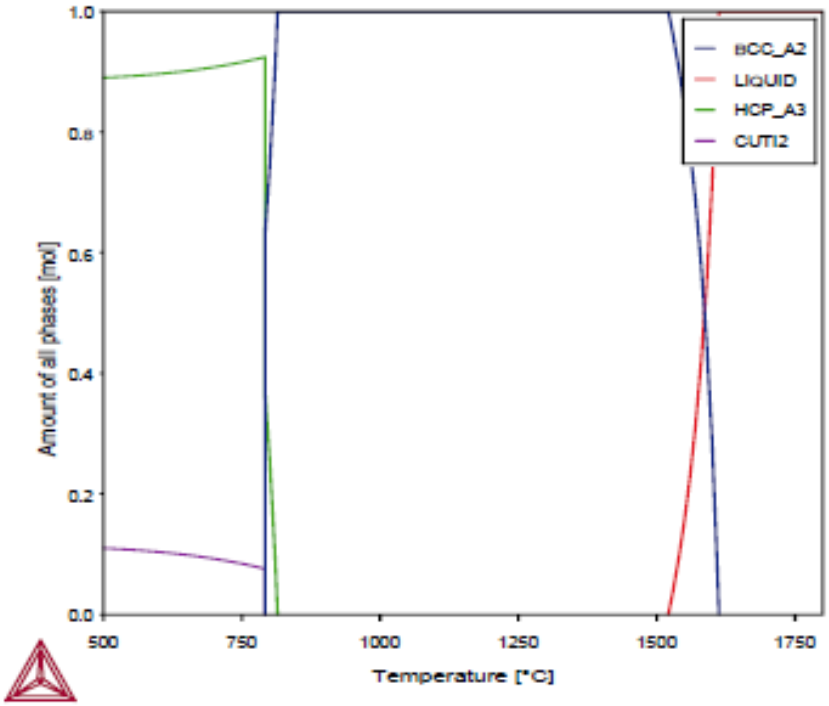


Figure 2. Phase proportion diagram for Ti-5Cu.

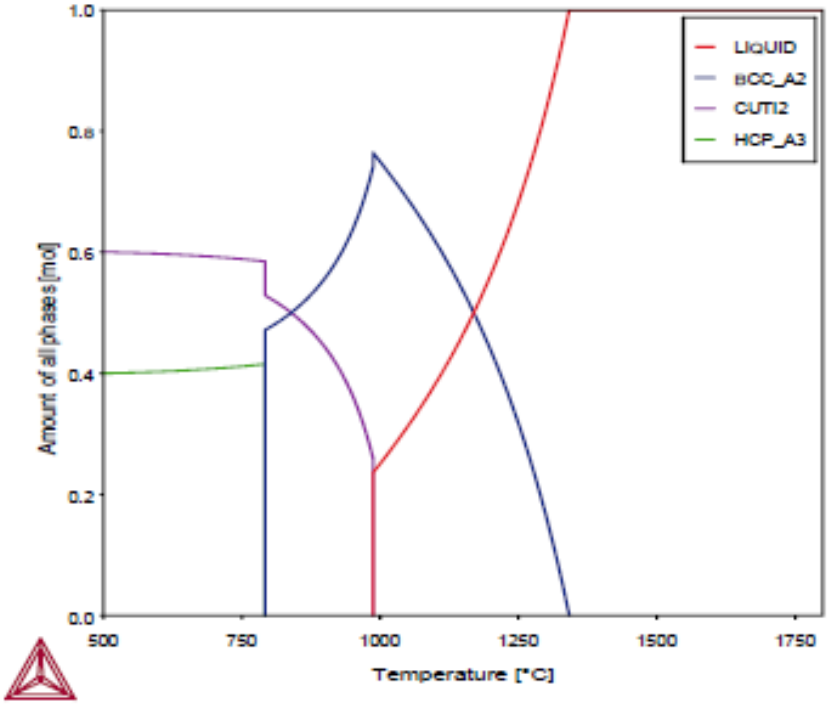


Figure 3. Phase proportion diagram for Ti-25Cu.

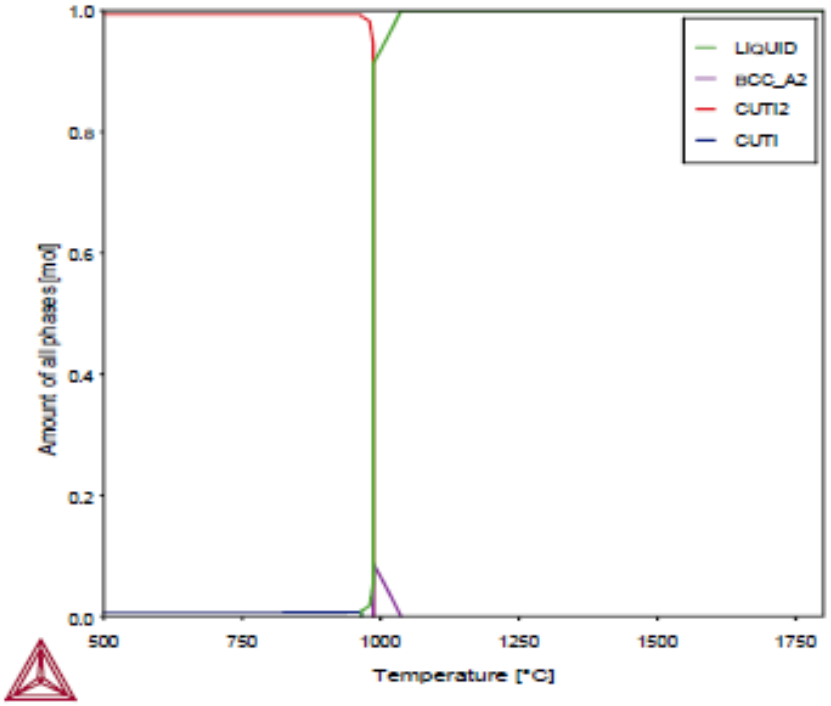


Figure 4. Phase proportion diagram for Ti-40Cu.

4.2 Microstructures and analyses

SEM-BSE images show differences in average atomic number: higher average atomic number phases have lighter contrasts [16]. Copper appears lighter since it has a higher atomic number than titanium. As-cast Ti-5Cu comprised lamellar (αTi) + (βTi), whereas the annealed alloy had (αTi) precipitated in (βTi), Figure 5. The EDX analysis indicated that the dark phase was (αTi), and light phase was (βTi), Table 3, which was retained [17], and agreed with XRD for both as-cast and annealed alloys, Figure 8.

Ti-25Cu alloys comprised dark dendrites in a Ti_2Cu matrix, Figure 6 and Table 3. After annealing at 900°C, light precipitates occurred inside the dendrites. The EDX analysis indicated the dark dendrites to be (βTi) instead of (αTi) and the matrix to be Ti_2Cu. The XRD patterns confirmed (αTi) and Ti_2Cu phases for both as-cast and annealed alloys, Figure 9.

Ti-40Cu comprised small oxide dendrites inside the Ti_2Cu dendrites, which were surrounded by the TiCu matrix, Figure 7. The dark phase had less copper than the light phase, Table 3. The XRD patterns confirmed Ti_2Cu and TiCu phases for both as-cast and annealed alloys, Figure 10. As well as there being more Ti_2Cu in the microstructure, the relative peak intensity of Ti_2Cu increased with more copper, indicating that more Ti_2Cu phase formed, Figure 8 to Figure 10.

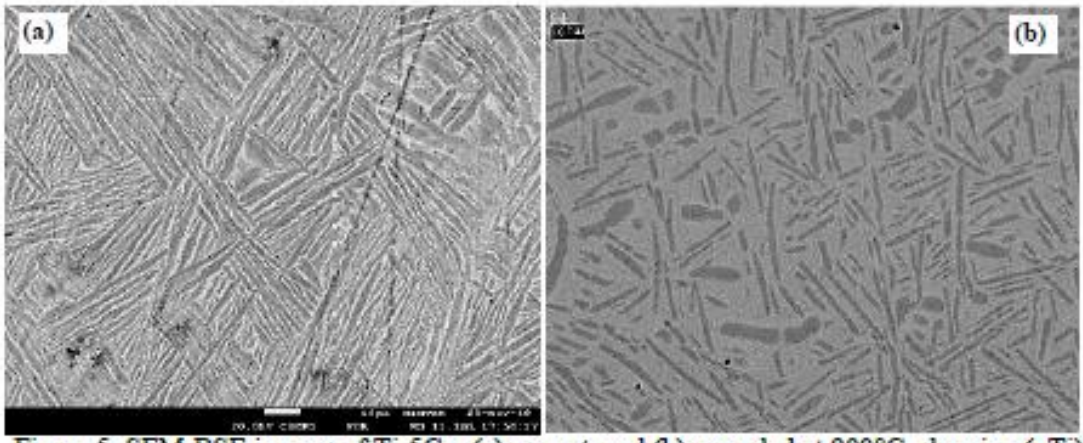


Figure 5. SEM-BSE images of Ti-5Cu: (a) as-cast, and (b) annealed at 900°C, showing (αTi) (dark contrast) and (βTi) (light contrast).

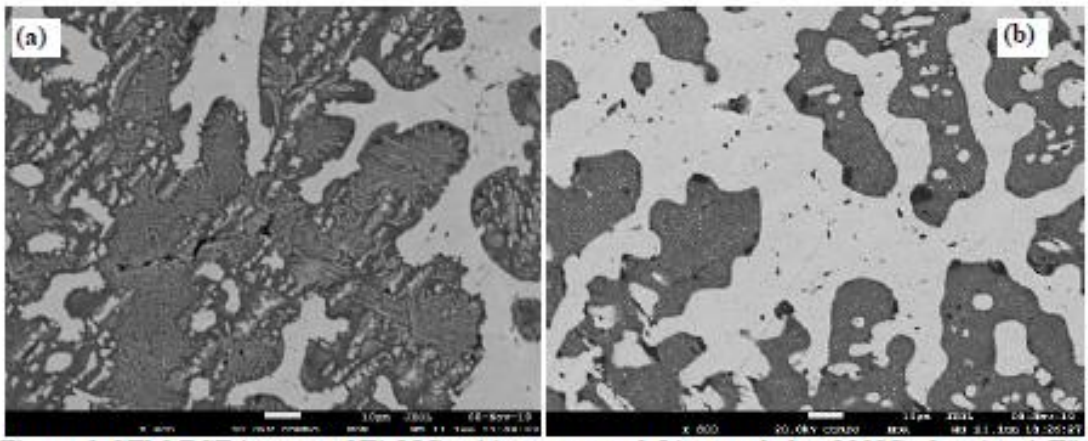


Figure 6. SEM-BSE images of Ti-25Cu: (a) as-cast, and (b) annealed at 900°C, showing (αTi) (dark contrast) and Ti_2Cu (light contrast).

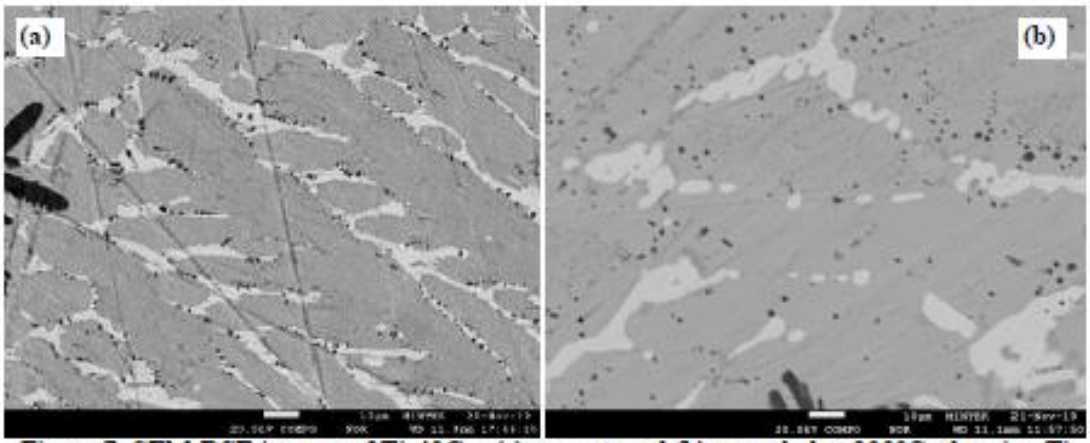


Figure 7. SEM-BSE images of Ti-40Cu: (a) as-cast, and (b) annealed at 900°C, showing Ti oxides (very dark contrast), Ti_2Cu (medium contrast) and TiCu (light contrast).

Table 3. EDX analyses.

Alloy	Cu (wt%)			
	Phase		As-cast	900°C
Ti-5Cu	Overall		4.6±0.9	4.7±1.0
	Dark	(αTi)	2.3±0.5	2.7±0.9
	Light	(βTi)	6.2±0.9	6.8±2.1
Ti-25Cu	Overall		26.2±2.0	24.9±3.8
	Dark	(βTi)	11.3±0.1	12.0±1.7
	Light	Ti_2Cu	37.0±0.5	38.0±0.1
	Precipitates in dendrites		None	18.1±1.5
Ti-40Cu	Overall		39.1±5.2	39.5±8.2
	Dark	Ti_2Cu	39.5±0.2	38.6±0.9
	Light	TiCu	55.6±0.2	56.2±0.1

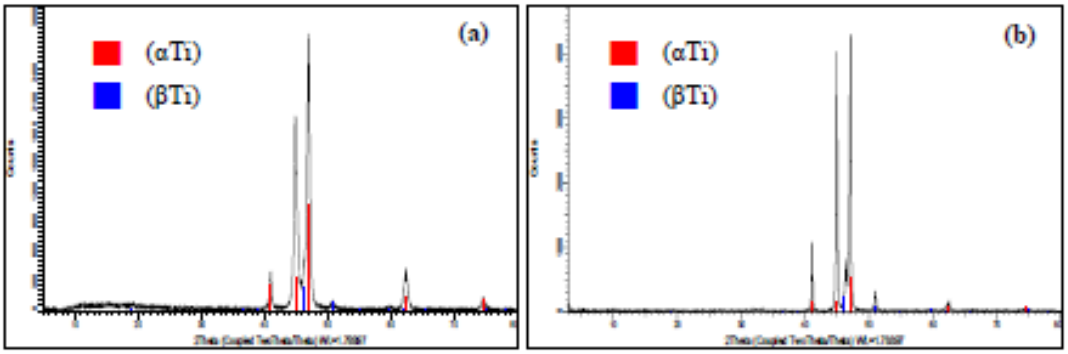


Figure 8. XRD patterns of Ti-5Cu: (a) as-cast, and (b) annealed at 900°C.

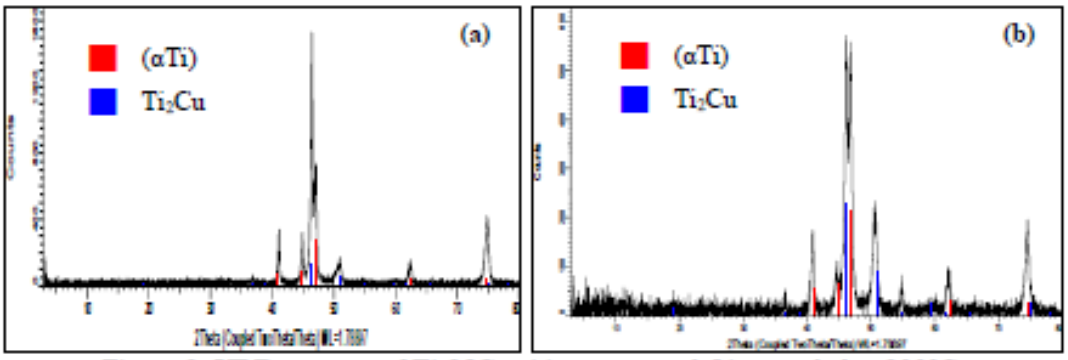


Figure 9: XRD patterns of Ti-25Cu: (a) as-cast, and (b) annealed at 900°C.

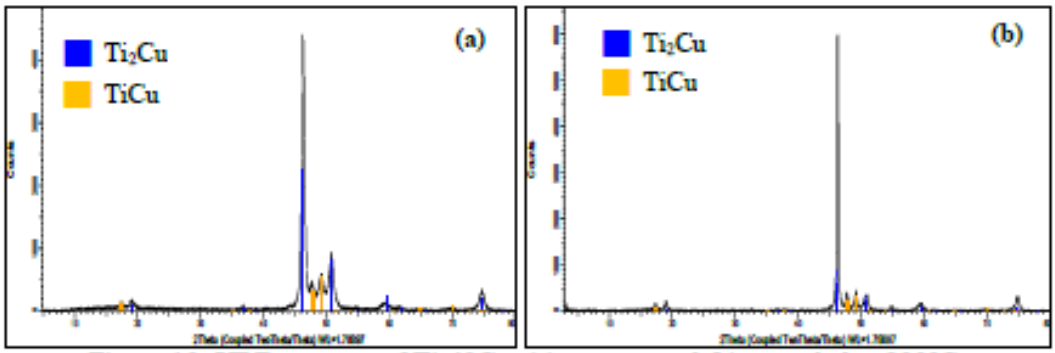


Figure 10: XRD patterns of Ti-40Cu: (a) as-cast, and (b) annealed at 900°C.

5. Electrochemical Testing

Figure 11 and
Table *4* show the OCP results. At two hours the OCP of the samples stabilised, although alloys Ti-25Cu and Ti-40Cu in the as-cast condition showed an initial increase in OCP, indicating that the passive layer was formed quickly on the surfaces. Higher copper additions shifted OCP in more noble positions (The OCP shift in the noble direction for the alloys suggests the formation of a passive film that reduces the corrosion rate) than for Ti-5Cu, while annealing at 900°C shifted the OCP towards less noble positions.

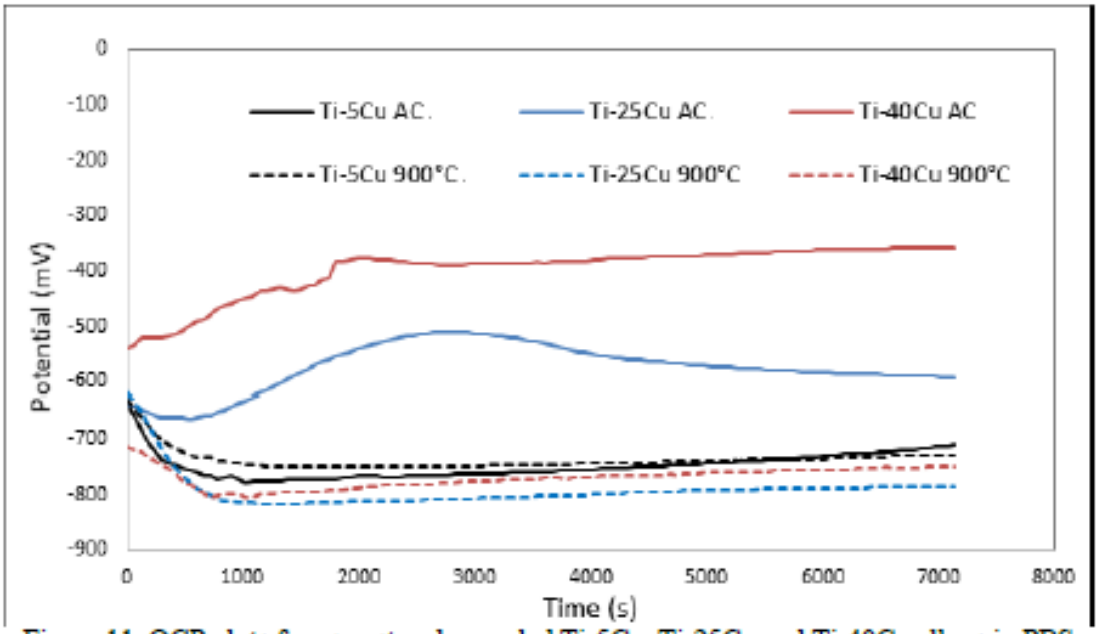


Figure 11. OCP plots for as-cast and annealed Ti-5Cu, Ti-25Cu and Ti-40Cu alloys in PBS solution.

Figure 13 shows the potentiodynamic polarisation scans. **Error! Reference source not found.** shows the corrosion rates obtained and

Table 4 gives the overall results. Ti-25Cu and Ti-40Cu alloys in both the as-cast and annealed conditions showed an increase in corrosion rate, with Ti-25Cu alloy showing a higher corrosion rate than the other alloys. This indicates that increasing copper content in the alloys decreased the corrosion resistance. Previously [18], the corrosion rate of as-cast CP Ti was 0.00059 mm/y, thus as-cast Ti-25Cu had the highest corrosion rate. The effect of alloy copper content associated with the intermetallic compounds has also been observed for Ti–Cu alloys by Osório et al. [19], who concluded, for their alloys, that with increased alloy copper content, the volumetric fraction of Ti_2Cu also increased, i.e., with lower copper content, a more homogeneous and smoother oxide film formed [19]. The impedance parameters made it clear that an intact passive titanium oxide film had been formed.

The annealed Ti-25Cu and Ti-40Cu alloys had higher corrosion rates, but alloy Ti-5Cu had a slightly reduced corrosion rate. Pina et al.[15] also reported increased current density with increased copper content in Ti-Cu alloys. The corrosion rate of CP Ti annealed at 900°C was 0.00108 mm/y [18] which was lower than Ti-25Cu and Ti-40Cu, although their corrosion rates were still acceptable for biomaterial applications [20]. All samples showed an active to passive behaviour, with no pitting breakdown. A long passivation stage in the Tafel curves of all the alloys indicated good passivation protection on the surface, which showed that neither copper additions nor annealing reduced the passivation protection. No pitting or localised attack was observed after testing. Ti-5Cu alloy at both conditions had higher corrosion resistance than the other alloys. The potentiodynamic polarisation tests showed that corrosion rates obtained were very low, below 0.13mm/y which is an acceptable corrosion rate for biomaterial design and application [20]. However, since Cu ions in liquid solution promote the antimicrobial activity, some corrosion is necessary to allow the Cu ions to be available [21].

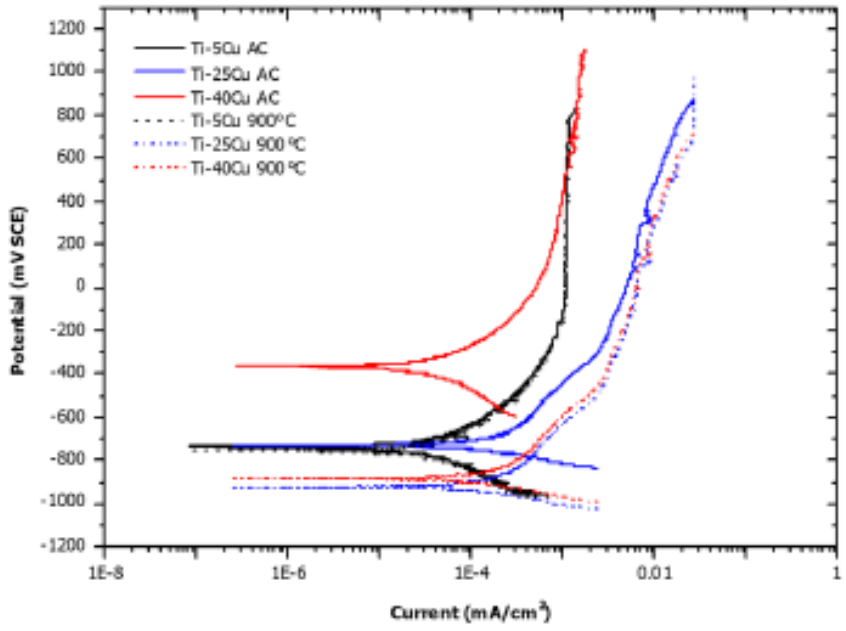


Figure 12. Potentiodynamic polarisation scans of as-cast and annealed Ti-5Cu, Ti-25Cu and Ti-40Cu alloys in PBS solution.

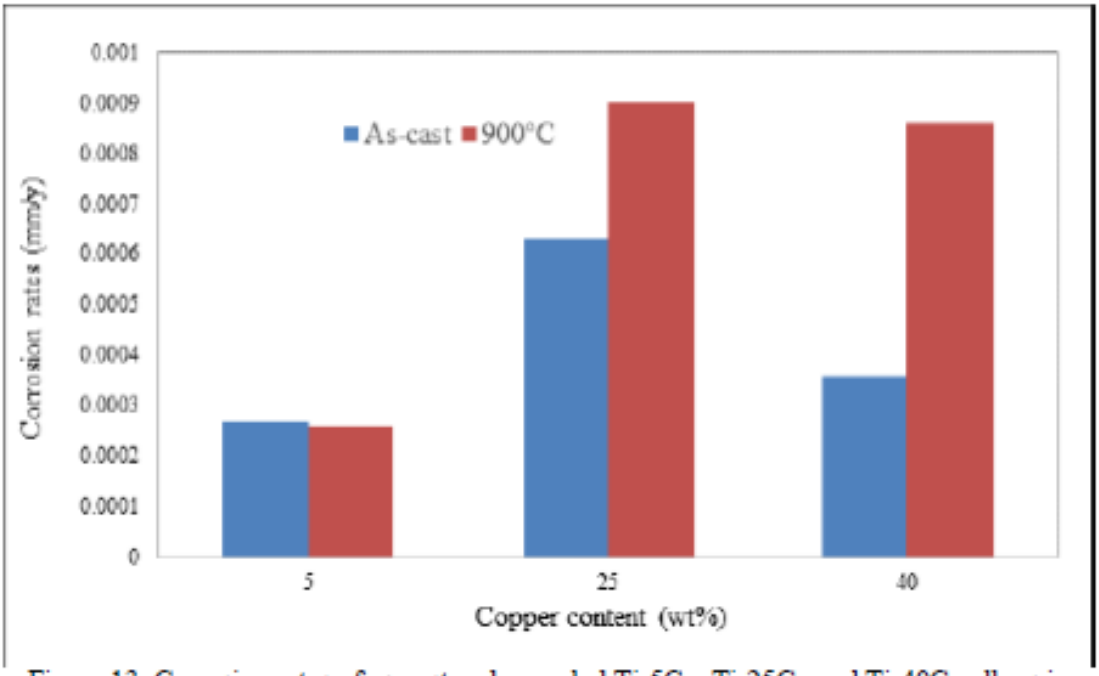


Figure 13. Corrosion rates of as-cast and annealed Ti-5Cu, Ti-25Cu and Ti-40Cu alloys in PBS solution.

Table 4. Potentiodynamic polarisation corrosion rates of as-cast and annealed Ti-5Cu, Ti-25Cu and Ti-40Cu alloys in PBS solution.

Samples		OCP (mV SCE)	E_{corr} (mV SCE)	i_{corr} (mA/cm^2)	Corrosion rates (mm/y)	
					Individual	Average
Ti-5Cu	As-cast	-711	-740	3.0×10^{-5}	0.00027	0.00027±0.0
		-659	-740	3.0×10^{-5}	0.00027	
	Annealed at 900°C	-729	-754	2.8×10^{-5}	0.00025	0.00026±0.0
		-374	-398	3.1×10^{-5}	0.00028	
Ti-25Cu	As-cast	-592	-728	7.4×10^{-5}	0.00067	0.00063±0.0
		-571	-718	6.8×10^{-5}	0.00061	
	Annealed at 900°C	-784	-928	1.0×10^{-4}	0.00090	0.00090±0.0
		-792	-928	1.0×10^{-4}	0.00090	
Ti-40Cu	As-cast	-357	-363	4.0×10^{-5}	0.00036	0.00036±0.0
		-448	-442	3.9×10^{-5}	0.00035	
	Annealed at 900°C	-748	-889	9.1×10^{-5}	0.00082	0.00086±0.0
		-662	-803	1.0×10^{-4}	0.00090	

6. Conclusions

This study assessed the corrosion performance of Ti-Cu Alloys targeted for biomedical applications, and the following conclusion were made:

- XRD gave similar results to Thermo-Calc: where Ti-5Cu and Ti-25Cu comprised (αTi) and Ti_2Cu, while Ti-40Cu comprised Ti_2Cu and TiCu.
- The as-cast Ti-5Cu alloy had a lamellar (αTi) and (βTi) microstructure, and after annealing (αTi) was precipitated in (βTi). Ti-25Cu alloys comprised dark (αTi) dendrites in a Ti_2Cu matrix and after annealing, light precipitates occurred inside the dendrites. Ti-40Cu comprised small oxide dendrites inside the Ti_2Cu dendrites, which were surrounded by the TiCu matrix, for both as-cast and annealed alloys.
- All samples showed active-to-passive behaviour without pitting breakdown. Long passivation stages existed for all alloys, indicating that copper did not destroy the passivation protection. The best alloy was Ti-5Cu. The corrosion rates were very low, below 0.13 mm/y, which although higher than Grade 4, is still an acceptable corrosion rate for biomaterial design and application. It is unlikely that improvements need to be made to this because some Cu in solution is needed for the antimicrobial properties. The corrosion performance of CP Ti alloyed with copper was acceptable for biomedical implants. The next stage of this work should include mechanical properties, anti-bacterial testing, then osseointergration studies.

7. Acknowledgments

The authors would like to acknowledge Mintek, University of the Witwatersrand, Uppsala University, NRF and Nelson Mandela University for assistance during the project and approval to publish this work.

8. References

[1] C. Schmidt, I. Anita and L. Claes, "Proliferation and differentiation parameters of human osteoblasts on titanium and steel surfaces," *Journal of Biomed Mater Res,* vol. 54, p. 209–215, 2001.

[2] S. G. S. Gosavi and R. Alla, "Titanium: A Miracle Metal in Dentistry," *Trends Biomaterial Artificial Organs,* vol. 27, no. 1, pp. 42-46, 2013.

[3] H. e. a. Ananth, "A Review on Biomaterials in Dental Implantology," *International Journal of Biomedical Science* , vol. 11, no. 3, pp. 113-120, 2015.

[4] D. Rodrigues, P. Valderrama, T. Wilson, K. Palmer, A. Thomas, S. Sridhar, A. Adapalli, M. Burbano and C. Wadhwani, "Titanium Corrosion Mechanisms in the Oral Environment: A Retrieval Study," *Materials,* vol. 6, pp. 5258-5274, 2013.

[5] M. Soler, S. Hsu, C. Fares, F. Ren, R. Jenkins, L. Gonzaga, A. Clark, E. O'Neill, D. Neal and J. Esquivel-Upshaw, "Titanium Corrosion in Peri-Implantitis," *Materials,* vol. 13, no. 23, p. 5488, 2020.

[6] J. Prathapachandran and N. Suresh, "Management of peri-implantitis," *Dental Research Journal,* vol. 9, no. 5, p. 516–521, 2012 .

[7] L. Fowler, O. Janson, H. Engqvist, S. Norgren and C. Öhman-Mägi, "Antibacterial investigation of titanium-copper alloys using luminescent Staphylococcus epidermidis in a direct contact test," *Mater Sci Eng C Mater Biol Appl,* vol. 97, pp. 707-714, 2019.

[8] M. Memara, P. Raei, N. Alizadeh, M. Aghdam and H. Kafil, "Carvacrol and thymol: strong antimicrobial agents against resistant isolates," *Medical Microbiology,* vol. 28, p. 63–68, 2017.

[9] K. Bruellhoff, J. Fiedler, M. Möller, J. Groll and R. Brenner, "Surface coating strategies to prevent biofilm formation on implant surfaces," *The International Journal of Artificial Organs,* vol. 33, no. 9, pp. 646-53, 2010.

[10] E. Zhang, X. Wang, M. Chen and B. Hou, "Effect of the existing form of Cu element on the mechanical properties,bio-corrosion and antibacterial properties of Ti-Cu alloys for biomedical application," *Materials Science and Engineering C,* vol. C, no. 69, pp. 1210-1221, 2016.

[11] J. Liu, F. Li, C. Liu, H. Wang, B. Ren and K. Yang, " Effect of Cu content on theantibacterial activity of titanium-copper sintered alloys," *Mater. Sci. Eng. CMater. Biol.,* no. App.35, p. 392–400, 2014.

[12] E. Zhang, X. Wang, M. Chen and B. Hou, "Effect of the existing form of Cu element on the mechanical properties, bio-corrosion and antibacterial properties of Ti-Cu alloys for biomedical application," *Materials Science and Engineering C,* no. 69, p. 1210–1221, 2016.

[13] M. Bao, Y. Liu, X. Wang, L. Yang, S. Li, J. Ren, G. Qin and E. Erlin Zhanga, "Optimization of mechanical properties, biocorrosion properties and antibacterial properties of wrought Ti-3Cu alloy by heat treatment," *Bioactive Materials,* vol. 3, no. 1, pp. 28-38, 2018.

[14] J. Murray, "The Cu-Ti (Copper-Titanium) system," *Bullet of Alloy Phase Diagrams,* vol. 4, no. 1, pp. 81-95, 1983.

[15] S. Cabeza, P. Zubiaur, G. Garcés, C. Andrade and P. Adeva, "Corrosion Behaviour of Mg98.5Nd1Zn0.5 (at. %) Alloy in Phosphate Buffered Saline Solution," *Metals,* vol. 10, no. 148, pp. 1-16, 2020.

[16] A. Nanakoudis, "https://www.thermofisher.com/blog/microscopy/sem-signal-types-electrons-and-the-information-they-provide/," ThermoFisher, 21 November 2019. [Online]. [Accessed 16 September 2021].

[17] D. Brice, "AN ASSESSMENT OF UNCOMMON TITANIUM BINARY SYSTEMS:Master of Science (Material Science and Engineering)," UNIVERSITY OF NORTH TEXAS, USA, 2015.

[18] N. Masia, L. Chown, M. Smit, A. Mwamba and L. Cornish, "Influence of copper on the corrosion properties of Grade 4 titanium for biomedical applications [Poster}," University of witwatersrand, Johannesburg, 2019.

[19] W. Osórioa, F. C. R. Caramb and A. Garcia, "The role of Cu-based intermetallics on the pitting corrosion behavior of Sn–Cu, Ti–Cu and Al–Cu alloys," *Electrochimica Acta,* vol. 77, p. 189–197, 2012.

[20] R. Bhola, S. Bhola, B. Mishra and D. Olson, "Corrosion in Titanium Dental Implants/Prostheses - A Review," *Trends Biomater. Artif. Organs,* pp. 34-46, 2011.

[21] j. Jiao, S. Zhang, X. Qu and B. Yue, "Recent Advances in Research on Antibacterial Metals and Alloys as Implant Materials," *Frontiers in Cellular and Infection Microbiology,* vol. 11, no. Article 693939, pp. 1-19, 2021.

J. Phase Equilib. Diffus. (2022) 43:332–344
https://doi.org/10.1007/s11669-022-00964-7

Formation of Ti_2Cu in Ti-Cu Alloys

K. Dyal Ukabhai[1,2] · U. A. Curle[3] · N. D. E. Masia[1,2,4] · M. Smit[4] · I. A. Mwamba[4] · S. Norgren[5] · C. Öhman-Mägi[6] · N. G. Hashe[7] · L. A. Cornish[1,2]

Submitted: 5 April 2022 / in revised form: 28 April 2022 / Accepted: 8 May 2022 / Published online: 19 June 2022
© ASM International 2022

Abstract One of the major issues with dental implants is failure due to bacterial infection, and additions of copper are known to improve the antimicrobial properties of Ti alloys. There are inconsistencies in the Ti rich area of the Cu-Ti binary phase diagram, hence the need to find out if Ti_2Cu or Ti_3Cu is formed, and to identify the type of formation of Ti_2Cu. Four alloys: 20, 33, 40 and 50 Cu (mass%) were produced by arc melting and studied using SEM, XRD and DSC. The reactions were derived, and the temperatures of the reactions were determined by DSC. The formation of Ti_2Cu is congruent, and no Ti_3Cu was found.

Keywords binary system · differential scanning calorimetry (DSC) · Ti-Cu · Ti_2Cu

1 Introduction

Biomedical materials are commonly used as structures and implants in humans, to replace lost or diseased biological structures and so improve the quality of life.[1–3] They are used for stents, heart valves, cardiac stimulators, knee replacements, hip replacements, dental screws etc... Titanium and its alloys are widely used in many industries, including biomedical use due to their excellent properties,

✉ K. Dyal Ukabhai
669011@students.wits.ac.za

U. A. Curle
ucurle@csir.co.za

N. D. E. Masia
nomsombulukoh@mintek.co.za

M. Smit
melanies@mintek.co.za

I. A. Mwamba
alainm@mintek.co.za

S. Norgren
susanne.norgren@iprod.lth.se

C. Öhman-Mägi
caroline.ohman@angstrom.uu.se

N. G. Hashe
Nobom.Hashe@mandela.ac.za

L. A. Cornish
lesley.cornish@wits.ac.za

[1] School of Chemical and Metallurgical Engineering, University of the Witwatersrand, Johannesburg, South Africa

[2] DSI/NRF, Centre of Excellence in Strong Materials, Johannesburg, South Africa

[3] Advanced Materials Engineering, Manufacturing Cluster, Council for Scientific and Industrial Research, Pretoria, Gauteng, South Africa

[4] Mintek, Randburg, South Africa

[5] Department of Mechanical Engineering Sciences, Lund University, Lund, Sweden

[6] Division of Applied Materials Science, Department of Engineering Sciences, The Ångström Laboratory, Uppsala University, Uppsala, Sweden

[7] Department of Physics, Nelson Mandela University (NMU), Gqeberha, South Africa

such as good mechanical properties, strong corrosion resistance, and excellent biocompatibility.[4] The two most used alloys in the biomedical field are commercially pure titanium (CP-Ti) and Ti-6Al-4V, which have been used for fracture fixation plates, femoral hip stems, fasteners, wires, and screws.[5] Although Ti-6Al-4V was originally designed for the aerospace industry, due to its good mechanical properties, it gained interest in the biomedical field.[6] The issue with this alloy is that it contains toxic elements V and Al, and the alloy has a significantly higher elastic modulus than bone.[4] CP-Ti does not have sufficient strength for load bearing implant applications and is expensive.[6]

Every day, more than 14 million people globally suffer from the pain of postoperative infection; 60% of the bacterial infections are related to the use of medical devices.[7,8] The two most common bacteria associated with implant infections are *Staphylococcus aureus* and *Staphylococcus epidermidis*.[9,10] In external fixtures like dental screws, pin tract infection is one of the common problems experienced.[11] Pin tract infections in external fixtures can cause loosening, osteomyelitis, and loss of the fixation.[12] Osteomyelitis, also known as bone infection, is characterized by the progressive inflammatory destruction and new apposition of bone.[13] The application of antibacterial biomaterials is a good way to resolve this problem,[14] and copper is one of the more promising alloying elements for clinical applications because of its low toxicity and high cytocompatibility (ability to be inert with cells in the body).[15] Copper has been used since 2000 BC to sterilize water and wounds. The Aztecs used copper oxide for treating skin conditions, and copper sulphate was used in Africa and Asia for healing sores and skin diseases.[16]

Copper is a β-stabilizer, and the addition of Cu decreases the melting point of the Ti-Cu alloy.[17] Silver behaves similarly to Cu in Ti-alloys, although it is too expensive to use in industrial applications,[18] and it is not a strong β-stabilizer.[19] Takahashi et al.[18] observed that Ti-Cu alloys had higher strength than Ti-Ag alloys, they also noted that Ti-Cu alloys had higher tensile strength, yield strength, and hardness than CP-Ti. Kraft et al.[20] and Masse et al.[21] found that Ag has toxic effects on human cells.

Zhang et al.[14,22], Aoki et al.[23], Liu et. al [8,24] and Kikuchi et al.[25] found that the addition of Cu improved the antibacterial properties of Ti-alloys. Titanium alloys with 1 (mass%) and 5 (mass%) Cu had good antibacterial properties compared to CP-Ti and showed reduced occurrence of pin tract infections,[26] which was attributed to the release of Cu ions and fine Ti_2Cu precipitates.[14] Zhang et al.[22] also found that at least 5 (mass%) Cu was needed for antibacterial properties, which are related to Cu ion release in the Ti-Cu alloys. Zhang et al.[14,27] also attributed high strength and strong antibacterial ability to Cu content and fine Ti_2Cu precipitates.

These small additions of Cu to Ti promoted interest in the Ti-rich end of the Ti-Cu phase diagram. There are several versions of the phase diagram, even for high Ti contents. Copper is recognized as a β-stabilizer for Ti alloys[17] via a eutectoid reaction[28] to form Ti_2Cu and (αTi), or to form Ti_3Cu and (αTi)[29] which is now recognised as metastable.[30] There are two reported reactions to form Ti_2Cu: congruently, with an associated L $\leftrightarrow$ Ti_2Cu + (βTi) eutectic reaction, or peritectically: L + (βTi) $\leftrightarrow$ Ti_2Cu. Figure 1 shows some of the most recent of phase diagrams, with the latest and complete different versions.[30–33]

Resolving the phase diagram has been difficult because of several problems. One problem is that titanium is very reactive with oxygen, so there are very few liquidus data for high Ti contents at high temperatures. Another problem is that the Ti_2Cu and Ti_3Cu phases have very similar XRD patterns which makes them difficult to distinguish. For Co Kα radiation, the only differences are that Ti_2Cu has a 44% intensity peak at $2\theta = 19.094°$ and a 14% intensity peak at $2\theta = 36.717°$,[34] whereas Ti_3Cu has a 15% intensity peak at $2\theta = 24.845°$ and a 6% intensity peak at $2\theta = 35.424°$.[35] Except for the 44% intensity peak Ti_2Cu, the other differentiating peaks have very small intensities, and are likely to be lost in the background. Additionally, the eutectic data summarised by Murray[36] were mixed up, which might have led to confusion where the earlier papers could not be accessed.

The aim of this work was to deduce whether Ti_2Cu or Ti_3Cu formed, and to identify whether the formation of Ti_2Cu was congruent or peritectically from (βTi). Four alloys: 20, 33, 40 and 50 Cu (mass%) were studied in the as-cast condition to understand the solidification reactions.

2 Previous Work

The first phase studies were done by Laves and Wallbaum[37] and at $\geq$ 50 at.% Ti, the solid phases were TiCu, Ti_2Cu, metastable Ti_3Cu, (βTi) and (αTi). Murray[30] reviewed the available data up to 1985. Subsequently, the Cu-Ti system was studied using several techniques over different temperature and composition ranges, and Predel[38] reviewed the available data to 1992, with similar interpretations to Murray.[30] Studying the Cu-Fe-Ti system, Alisova et al.[39] found the tetragonal Ti_2Cu compound and deduced its solidification as congruent.

Several thermodynamic assessments were performed.[36,40–46] Kumar et al.[47] thermodynamically reassessed the system, including all the phases except for Ti_3Cu. They[47] did not use several results,[39,48,49] nor

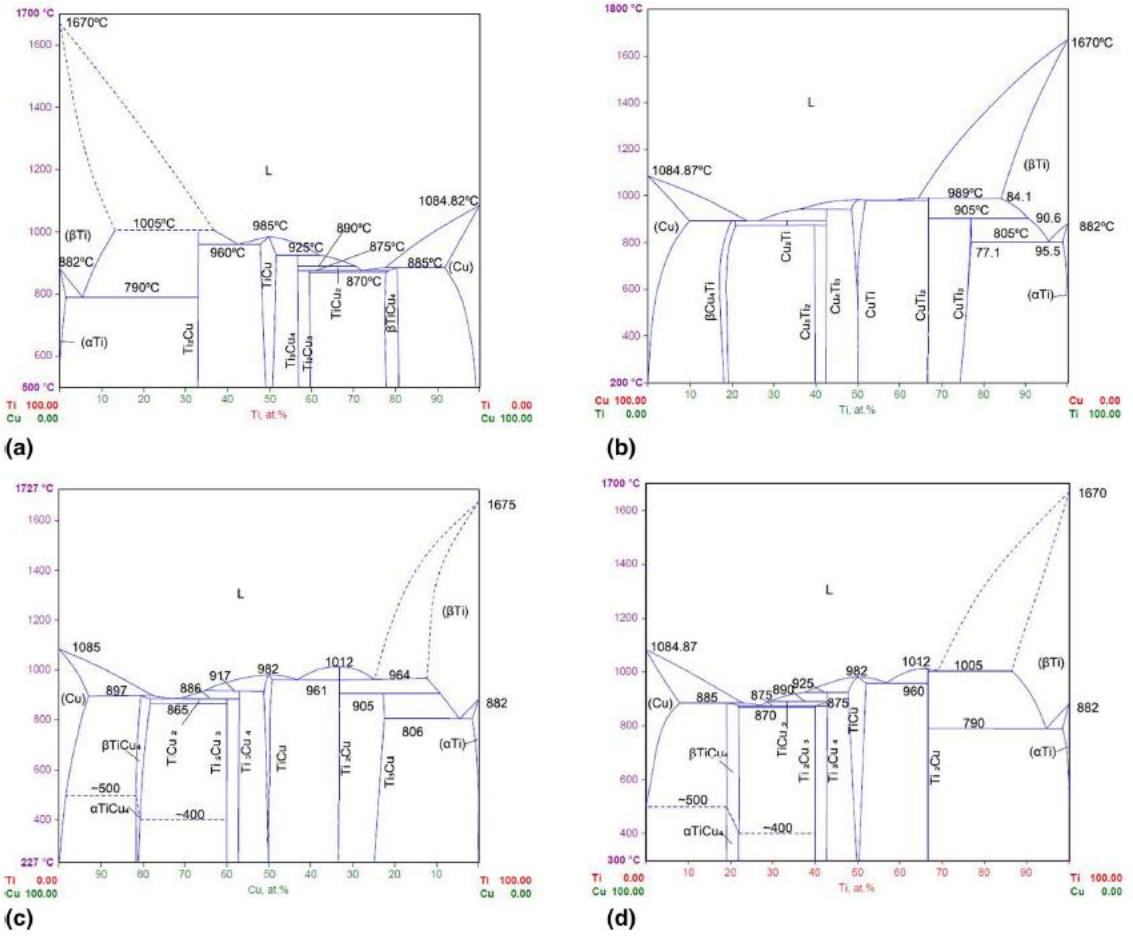


Fig. 1 Selected complete Ti-Cu phase diagrams (a) Peritectic formation of Ti_2Cu without Ti_3Cu[30] (b) Peritectic formation of Ti_2Cu and stable Ti_3Cu[31] (c) Congruent formation of Ti_2Cu and stable Ti_3Cu[32] and (d) Showing congruent formation of Ti_2Cu without Ti_3Cu[33]

certain thermodynamic analyses,[50–52] and the calculated phase diagram had peritectic (incongruent) formation of $TiCu_2$. The calculated enthalpies of formation of TiCu, Ti_3Cu_4, Ti_2Cu_3 and $TiCu_4$ were in excellent agreement with subsequent measurements by Colinet et al.,[53] whereas those for $\beta TiCu_2$ disagreed. The enthalpies of mixing of liquid alloys were more positive than those determined by Kleppa and Watanabe.[54] Later more data were produced,[55,56] as well as more thermodynamic analyses by Turchanin et al.[57] Subsequently, the Ti_3Cu phase was found experimentally by Canale and Servant[29] and formed from a peritectic reaction between (βTi) and Ti_2Cu. However, the microstructure shown had much porosity, which suggested non-equilibrium cooling, Turchanin[58] derived the temperature dependence of the integral enthalpy of mixing in the liquid phase and noted that the models for the solid solutions of Kumar et al.[47] gave positive deviations from ideality, which was contrary to the way the components mix. Later Turchanin et al.[59] undertook a thermodynamic assessment of the system, using the ideal associated solution (IAS) model,[57,58,60] and obtained good agreement with the experimental data, especially those they selected as being the most self-consistent,[39,48,49,61,62] rather than.[53,54,63] This was surprising, since other results of Kleppa and co-workers[54,64] are usually well regarded, and hydrogen should have reduced any oxidation problems of titanium. The curved liquidus of (βTi)[59] is unusual but was stated to be consistent with the interaction of the components. As part of a calculation of the Cu-Sn-Ti system, Wang et al.[65] used the assessment of Kumar et al.[47] with the experimental data of Colinet et al.[53] and first principles calculations of Ghosh[66,67] to reassess the parameters of $TiCu_2$. This produced a phase diagram like Kumar et al.,[47] but with more symmetrical

enthalpies across the system, and with TiCu as the phase with the lowest enthalpy.

Intermetallic compounds were reported experimentally by many authors.[29,34,35,39,48,49,55,61,62,68–72] Using Cu-Ti diffusion couples, $TiCu_4$, $TiCu_2$, Ti_2Cu_3, Ti_3Cu_4, TiCu and Ti_2Cu were found in the temperature ranges investigated,[73–75] and the same phases were also found after melting elemental powders in a zirconia crucible in a vacuum resistance furnace.[76]

Using earlier results,[39,48,49,61,62,68] Turchanin et al.[59] confirmed that $TiCu_2$ has a negligible solubility range, and only TiCu had a larger composition range. Karlsson[35] and Raub[69] identified TiCu to comprise two phases based on composition, although Eremenko et al.[48,62] demonstrated that it was single-phase, or at least related to one structure.[59]

Eremenko et al.[48] described Ti_2Cu with a composition range of $0.67 \leq x_{Ti} \leq 0.70$, agreeing with Rostoker.[77] The Ti_3Cu phase was reported by Karlsson,[35] although Ence et al.[70] interpreted this as contaminated Ti_2Cu after being melted in refractory crucibles, although it was reported by Lutjering and Weissmann.[78] and Canale and Servant[29] Thermal analysis for the Ti-25Cu (mass%) composition had a thermal arrest near 985°C,[68] which was between reported formation temperatures for Ti_2Cu and Ti_3Cu.[29] Karlsson[35] admitted that complete equilibrium could not be obtained and reported ordering below 650°C. Ti_3Cu has been reported as being stable,[29] since it was found Ti_3Cu in slow quenched samples (5 $K.min^{-1}$ cooling rate) instead of the expected TiCu, and in samples annealed for 15 days at 820°C.[29] Calculated enthalpies of formation[29] were lower than the calculated Meidema values,[79] although they[29] were on the edge of the hull, only just showing stability (and favouring metastability). Since Ti_3Cu is formed from a peritectoid reaction, it could be missed in samples cooled from higher temperatures, which might be adding to the confusion in deciding its stability. Using diffusion couples,[73–75] only Ti_2Cu was reported and not Ti_3Cu, although TiCu was also found. Klotz and Liu[80] did not find Ti_3Cu after annealing a Cu-Ti diffusion couple component at 800°C for 864 h, which again shows that this phase is not stable.

Most authors accept only one TiCu phase, although Eremenko et al.[49] and Andrieux et al.[81] found a higher temperature phase after annealing single-phase as-cast TiCu at 827°C for 300 h. This phase was not found in x-ray studies, although a layered microstructure was reported, and the electrical resistance changed. However, Wei and Wang[82] found evidence of ordered TiCu after ageing and using transmission electron microscopy (TEM).

Fast cooling changes the phases, so that Zwicker[83,84] found martensite in high Ti content alloys, and Vigier et al.[85] found martensite in Ti-2.4Cu (mass%). Metastable transformations were identified in alloys with up to 5.2 at.% Cu.[86,87] Studying eutectoid decomposition, Franti et al.[88] found both bainite and pearlite in the Ti-Cu system. Deveraj et al.[89] studied the competing martensitic, bainitic and eutectoid transformations in a hypoeutectoid Ti-5Cu (mass%) alloy, finding that fast cooling gave mixed microstructures of nanoscale bainite comprising non-equilibrium Ti_2Cu and martensitic α plates, whereas near-equilibrium cooling gave eutectoid microstructures. Ti alloys have different phases with non-equilibrium cooling, and with Cu, (βTi) decomposes eutectoidally to form the α' and ω phases,[90] and 11 at.% Cu stabilised (βTi) as a metastable phase.[91]

Several versions of the phase diagram exist,[29–31,36,38,46–48,59–62,68,72,92–97] the main types shown in (Fig. 1),[30–33] and the main differences are the peritectic formation of Ti_2Cu[30,31,36,38,46,47,68,72,94,96] (Fig. 1a and b) or congruent formation of Ti_2Cu[48,59,60,62] (Fig. 1c and d), and the presence of Ti_3Cu[29,31] (Fig. 1b and c). However, there are few reported data points at high temperature for the Ti-rich part of the phase diagram; all are below 1030°C, except values of Joukainen et al.[68] which could support a liquidus associated with a peritectic reaction, and the others are indeterminate for either peritectic or congruent formation of Ti_2Cu, which are very close in temperature anyway. Contamination was possible from either refractory crucible[61] or from arc melting,[62] so it is difficult to resolve this. Although Shull et al.[98] found a peritectic microstructure in a 30 at.% Cu alloy, Eremenko et al.[62] found a eutectic microstructure for a 31 at.% alloy. However, fast cooling can give the appearance of a peritectic reaction because a halo of the other phase is formed around the primary phase.[99] Additionally, a sparse eutectic could also be difficult to discern since there would be only a small proportion of one phase. Although the eutectic composition of (βTi) + Ti_2Cu has been shown to nearly midway between the two products,[32] considering the different formation temperatures of (βTi) and Ti_2Cu it is more likely to be closer to Ti_2Cu, and then the proportions of the phases would be unequal and possibly difficult to identify as a eutectic.[33]

Using thermal analysis, Alisova et al.[39] found Ti_2Cu had a single heat effect at 1012 ± 3°C, which suggested congruent melting and a eutectic reaction $L \leftrightarrow (\beta\ \text{Ti}) + Ti_2Cu$,[62] instead of the peritectic reaction.[30] The eutectic reaction was reported by several researchers,[39,48,61,62,100] with an associated congruent melting of Ti_2Cu.[39,48,61,62] Zhan et al.[101] undertook metallographic studies on 75 Ti: 25 Cu alloys which were as-cast, and annealed at 750°C, 805°C and 850°C, well as thermal analysis of the sample which had been annealed at 750°C. They identified Ti_3Cu, but they analysed small areas of the phase (which would have suffered pick-up from the surrounding (αTi)), did not

show the differentiating Ti_2Cu/Ti_3Cu XRD peaks, and their scanning rate of 20°C.min^{-1} would have shifted the reaction temperature. Their as-cast microstructure appeared like a sparse eutectic, but as they were using Canale and Servant,[29] they interpreted it as peritectic formation of Ti_2Cu. However, most authors interpret the reaction as eutectic L ↔ (β Ti) + Ti_2Cu,[29–31,36,38,46,47,65,68,72,94,96] which agrees with Kleppa and Watanabe[54] who stated that the enthalpy of mixing was highly exothermic, contributing to the high stability of the liquid phase with respect to the crystalline phases, hence promoting the eutectic (and possibly peritectic) points below the melting points of the pure elements. However, Colinet et al.[53] measured more positive enthalpies of mixing of liquid alloys than those determined by Kleppa and Watanabe,[54] and Pietrokowsky and Maticich[102] observed peritectic microstructures, although on fast cooling, where the peritectic reaction can occur instead of the more stable eutectic.[99] Measured temperatures of the Ti_2Cu reactions are given in Table 1. The values of Eremenko et al. were different in the two papers, and the later values are given.[48,62] The compositions of the liquid for the L → (βTi) + Ti_2Cu were reported as: 31 at.% Cu[48,62] and ~31 at.% Cu.[61] The eutectic temperatures of L → Ti_2Cu + TiCu were reported as: 960°C at 43 at.% Cu[61,68] and 980°C at 43 at.% Cu.[48]

Yamane et al.[72] studied the Ti-rich phase equilibria, up to 25 at.% Cu at different pressures, finding that the eutectoid decomposition temperature decreased with increasing pressure. The peritectic temperature L + (βTi) ↔ Ti_2Cu increased by about 50°C, and the composition of copper in (βTi) increased by 4 at.%. However, they supported peritectic formation of Ti_2Cu.

Turchanin et al.[59] reviewed the available data prior to undertaking an assessment, also considering the liquidus data, where most of the solid-liquid boundaries were only studied by Joukainen et al.[68] They[59] produced a phase diagram like Ansara and Ivachenko,[32] but including the two $TiCu_4$ phases,[30,36,103] $TiCu_3$ as a stable phase,[29] and with the (βTi) liquidus drawn smoothly. However, the curved liquidus of (βTi)[59] is as already mentioned unusual, even though it was stated to be consistent with the interactions of the components.

The activity of Cu in (βTi) was studied using a triple Knudsen cell.[104] De Boer et al.[105] calculated heats of formation for hypothetical compositions, including TiCu and Ti_2Cu. Eremenko et al.[49] studied the heats of fusion of TiCu. Enthalpies of formation of Ti_2Cu were TiCu were determined by solution calorimetry in liquid aluminium.[53]

Table 1 shows the results of various investigations of the high Ti end of the Cu-Ti phase diagram.

3 Experimental Procedure

Samples of 10 g each were prepared using pure (99.9%) elemental powders of Ti and Cu from Sigma Aldrich. The powders were weighed, mixed and cold compacted and then melted in a button arc-furnace, in an argon atmosphere on a water-cooled copper hearth with a titanium oxygen-getter which was melted before melting each sample. The samples were melted 5 times to promote homogeneity, and the samples were inverted before each melt.

The as-cast samples were cut using a Struers automatic cutting machine with an Accutom diamond cutting wheel. Standard metallographic preparation method was followed,

Table 1. Reaction temperatures of different investigations with calculated values are shown in italic

Reference	Reaction type for formation of Ti_2Cu	Formation T of Ti_2Cu	Eutectic T: Ti_2Cu + (βTi)	Formation T of Ti_3Cu	Eutectoid T: (βTi) → Ti_3Cu +(αTi)	Eutectoid T: (βTi) → Ti_2Cu +(αTi)	Ti_3Cu present?
68	Peritectic	995	…	…	…	798	N
61	Congruent & eutectic	1015±10	1009	…	…	…	N
36, 30	*Peritectic*	*1005±10*	…	…	…	*790±10*	*N*
48	Congruent & eutectic	1010±5	1003±3	…	…	800±5	N
94	Peritectic	990	…	…	…	798	N
98	Peritectic	1005±10	…	…	…	…	N
47	*Peritectic*	*1000*	…	…	…	*799*	*N*
59	*Congruent & eutectic*	*1009*	*958*	…	…	*1065K*	*N*
32	*Congruent & eutectic*	*1012*	*964*	*905*	*806*	…	*Y*
29 - exp	Peritectic	1002[72]	…	890	790	…	Y
29 - calc	*Peritectic*	*989*	…	*905*	*805*	…	*Y*
65	*Peritectic*	*990*	…	…	…	*788*	*N*
101	Peritectic	~1002	…	…	805	…	Y

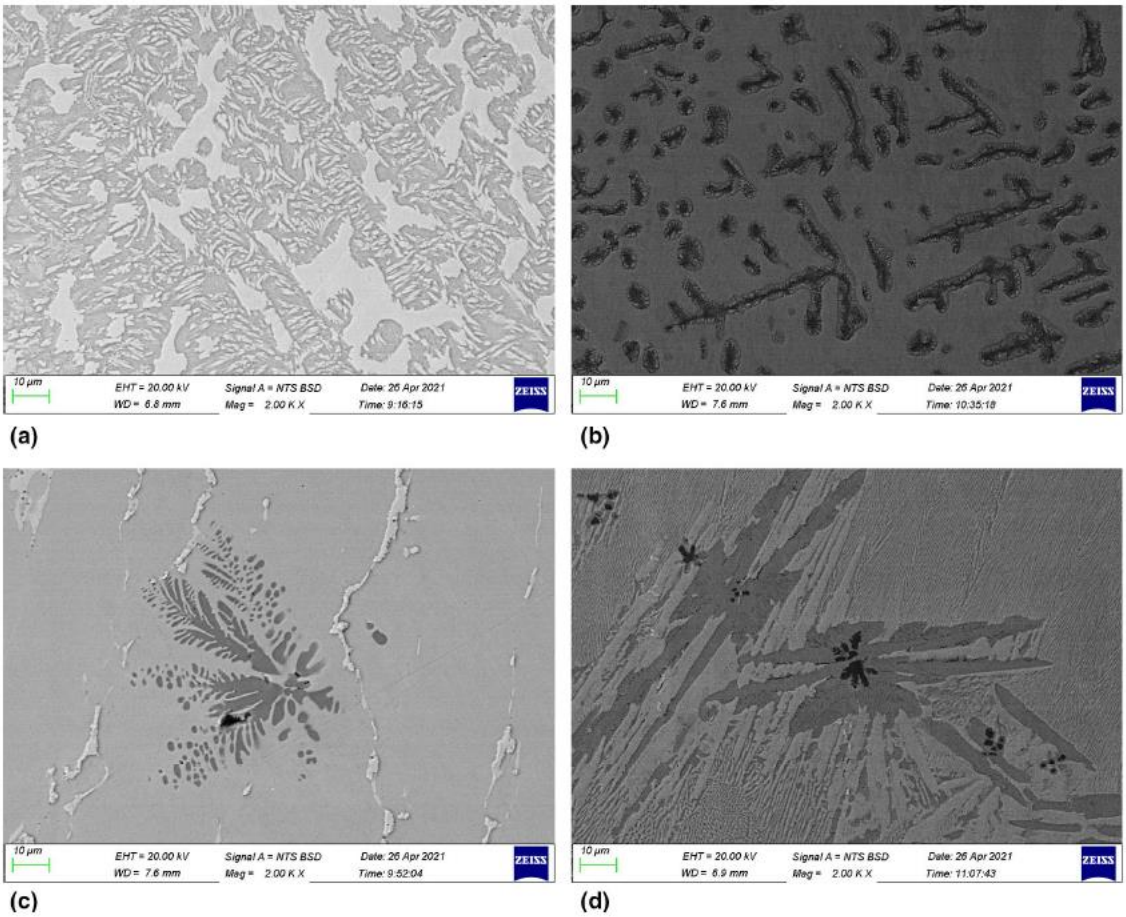


Fig. 2 SEM-BSE images of the Ti-Cu alloys (a) Ti-20Cu (mass%): original (βTi) dendrites which had decomposed to (αTi) (dark) + Ti_2Cu (light), with sparse (βTi) (now transformed to (αTi) + Ti_2Cu eutectic. (b) Ti-33Cu (mass%): original (βTi) dendrites which had decomposed to (αTi) (dark) + Ti_2Cu (light), with sparse (βTi) (now transformed to (Ti) + Ti_2Cu eutectic (c) Ti-40Cu (mass%): TiO_2 (dark) with major Ti_2Cu (medium) dendrites surrounded by small amounts of sparse Ti_2Cu + TiCu (light) eutectic and (d) Ti-50Cu (mass%): TiO_2 (dark) with Ti_2Cu (medium) needles, surrounded by TiCu needles (light) and Ti_2Cu + TiCu (light) eutectic

grinding down to P4000 and polishing with colloidal silica. XRD was done using a Bruker D2 diffractometer, with Co radiation, a step size of 0.026°, and scanning for 1 hour from 2θ = 20° to 120°. The peaks were checked using Diffrac Plus EVA program and ICDD (International Centre for Diffraction Data) PDF2 (Powder Diffraction File) 2020 release database.

The samples were etched using Kroll's regent. Scanning electron microscopy was done on a ZEISS Sigma 300 VP SEM (after first checking on an optical microscope) to study the microstructures and analyse the compositions of the phases and overall (area) composition of the alloys. For each phase a minimum of five analyses was done and the averages were reported with standard deviations.

Differential scanning calorimetry (DSC) tests were done to confirm the phases being formed using a Netzsch STA 449F3 Jupiter Simultaneous Analyser, in accordance with: MSM-LM-WP-660 with alumina crucibles. The heating rate was 20°C.min^{-1} under an argon atmosphere.

4 Results

Backscattered electron micrographs are shown in Fig. 2, with a higher magnification micrograph of Ti-33Cu (mass%) given in Fig. 3. EDX analyses are given in Table 2, and Fig. 4 shows the EDX spectra for Ti-40Cu and Ti-50Cu (mass%).

The XRD patterns are shown in Fig. 5, and the phases identified by XRD agree with the compositions analysed by SEM. There were some small peaks for the Ti-33Cu (mass%) which matched with those of TiCu, confirming the existence of that phase, even though the sample was inhomogeneous. The DSC curves are shown in Fig. 6.

Ti-20Cu (mass%) (Fig. 2a) showed a bimodal microstructure. The dark (βTi) dendrites formed first, followed by the lighter grey interdendritic areas, and although the dendrites were irregular, they did not seem to have experienced peritectic reaction. There were smaller dark areas within the lighter interdendritic areas, and these were identified as evidence of a sparse eutectic reaction. The dendrites subsequently transformed to (αTi) (dark contrast) and Ti_2Cu (light contrast) (Table 2). The XRD pattern (Fig. 5a) showed that (αTi) and Ti_2Cu phases were present. The unidentified peak at $2\theta = \sim 37$ is Ti_2Cu. Fig. 6 shows that 3 transformation took place when the sample was heated during DSC tests (Table 3).

Figure 2(b) shows a very fine microstructure of Ti-33Cu (mass%), with fewer and smaller dendrites than in Fig. 2(a) and more of the lighter matrix, and a reaction that occurred within the dendrites, which initiated from the phase interface (Fig. 3). The compositions of the different areas were very different (Table 2). The XRD pattern (Fig. 5) showed that there were two phases present: (αTi) and Ti_2Cu. Two transformation reactions (Table 3) took place on heating the sample (Fig. 6).

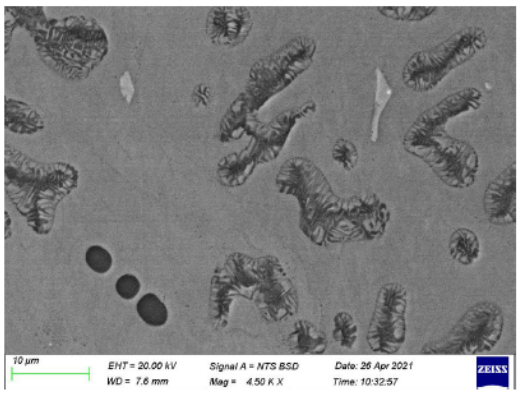


Fig. 3 SEM-BSE image of Ti-33Cu (mass%) at higher magnification, showing: Ti_2Cu (light area in dendrite), (Ti) (dark area in dendrite) and Ti_2Cu (matrix). The lightest areas were TiCu

For Ti-40Cu (mass%), the dark TiO_2 phase formed first as small dendrites and nucleation of Ti_2Cu occurred on these (Fig. 2c). Most of the sample was the medium contrast Ti_2Cu, with only a small amount of interdendritic TiCu (Table 2). The XRD pattern (Fig. 5c) indicated TiCu and Ti_2Cu, with some TiO_2. The dark regions (Fig. 2c) were too small to analyse accurately using EDX, although O was found in the EDX analysis of the sample (Fig. 3), and TiO_2 was identified by XRD (Fig. 4c). Thus, the dark phase was identified as TiO_2. Only one reaction took place, as shown on Fig. 6(c).

In the Ti-50Cu (mass%) sample, small TiO_2 dendrites solidified first (Fig. 2d), and the Ti_2Cu needles nucleated on these. Instead of the eutectic forming next, there were TiCu needles, which was due to the fast cooling and allowed the Cu-rich composition to return to the eutectic composition so that the Ti_2Cu + TiCu eutectic could form naturally. Unlike the Ti-40Cu (mass%) sample, this Ti_2Cu + TiCu eutectic was not sparse. Fig. 6(d) shows that three transformation peaks were present (Table 3).

The DSC reaction peaks are listed in Table 3 and have been matched with their reactions from the as-cast microstructures and to be self-consistent. The wide and highest temperature negative peak of the Ti-20Cu (mass%) sample was assumed to be the oxide peak. Strangely, it was the only unidentified peak from all four samples, although the Ti-33Cu (mass%) sample also showed a shallow dip at the same temperature.

5 Discussion

Although great care was taken on melting to eliminate oxygen, there was obviously some left in at least the Ti-40Cu (mass%) (Fig. 2c) and Ti-50 Cu (Fig. 2d) samples,

Table 2. EDX results of the as-cast alloys

Alloy		Overall	(αTi)	Ti_2Cu	TiCu
Ti-20Cu (mass%)	Ti	79.7 ± 1.6	82.1 ± 2.6	61.9 ± 0.9	…
	Cu	20.3 ± 1.6	17.9 ± 2.6	38.1 ± 0.9	…
Ti-33Cu (mass%)	Ti	68.8 ± 0.7	98.0 ± 1.8	61.8 ± 1.9	…
	Cu	31.2 ± 0.7	2.0 ± 1.8	38.2 ± 1.9	…
Ti-40Cu (mass%)	Ti	62.3 ± 0.9	…	63.0 ± 0.4	45.2 ± 1.9
	Cu	37.7 ± 0.9	…	37.0 ± 0.4	54.8 ± 1.9
Ti-50Cu ((ass%)	Ti	50.4 ± 1.4	…	60.6 ± 1.4	45.2 ± 1.7
	Cu	49.6 ± 1.4	…	39.4 ± 1.4	54.8 ± 1.7

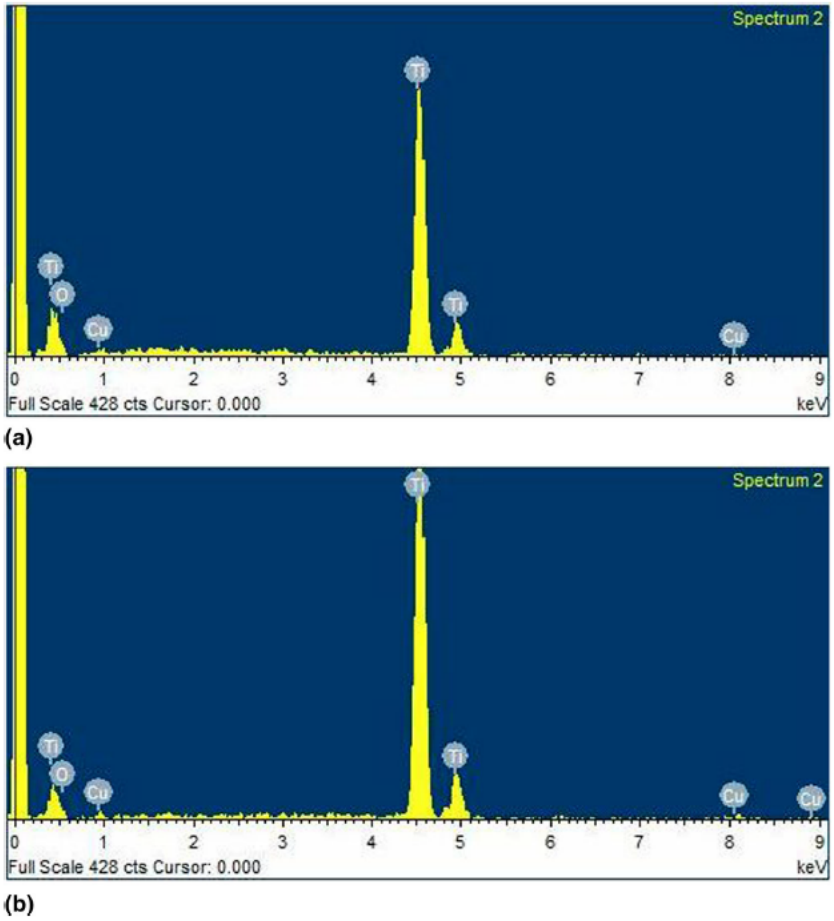


Fig. 4 EDX spectra for (a)Ti-40 Cu and (b)Ti-50 Cu (mass%) showing a peak for oxygen

because the phase that formed first was the TiO_2, which formed as dendrites, and the true primary phase nucleated on them. The oxygen content was also shown by the EDX results of these samples in Fig. 3. Apart from this, the analysed phases were as expected (Table 2), and these agreed with the XRD results (Fig. 4). The Ti_2Cu phase was identified rather than Ti_3Cu because of the Cu/Ti ratio in the EDX analyses, and because of the $2\theta = 19.094°$ peak of Ti_2Cu was found.

The microstructures of the as-cast samples should reveal the casting history, even if the phase compositions were not at equilibrium, although it was difficult to differentiate between a (βTi) + Ti_2Cu eutectic or a L + (βTi) → Ti_2Cu peritectic reaction for the Ti-20Cu (mass%) (Figure 2a) and Ti-33Cu (mass%) (Fig. 2c) samples, because there was neither a clear eutectic reaction, nor a clear peritectic reaction. However, the prior (βTi) dendrites of Ti-20 Cu were quite clear, even with fast cooling from arc melting, which suggested a eutectic reaction rather than a peritectic reaction (Fig 2a), which would have reacted with the edges. These dendrites then decomposed eutectoidally to give (αTi) + Ti_2Cu. The Ti-33 Cu sample was less clear, and the proportion of the (βTi) dendrites was less, giving more surrounding Ti_2Cu, which was part of the sparse eutectic. The eutectoid transformation was less clear because it started at the (βTi)/Ti_2Cu interface and then grew inwards (Fig. 3) much more clearly than in the Ti-20Cu (mass%) sample. The occurrence of small amounts of TiCu in Ti-33Cu (mass%) (Fig. 3) can only be explained by local inhomogeneity.

The Ti-40Cu (mass%) sample solidified to mainly Ti_2Cu, with a minor about of TiCu, so the expected Ti_2Cu + TiCu eutectic was not clear. Only one sample, Ti-50Cu (mass%), clearly showed the Ti_2Cu + TiCu eutectic, but even in this sample, the eutectic was suppressed until precipitation of TiCu occurred (thus decreasing the oversaturation of Cu) allowing the liquid composition to be nearer to that of the Ti_2Cu + TiCu eutectic. It was

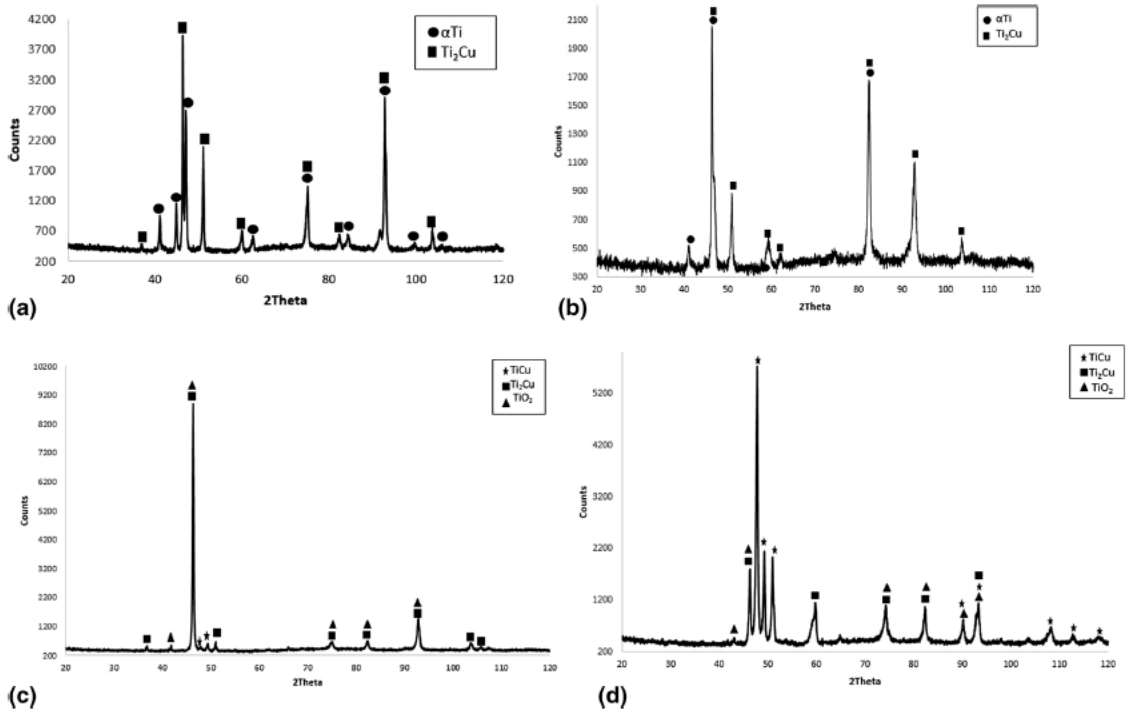


Fig. 5 XRD patterns for Ti-Cu alloys: (a) Ti-20Cu, (b) Ti-33Cu, (c) Ti-40Cu and (d) Ti-50Cu (mass%)

surprising that in Ti-50Cu (mass%), both Ti_2Cu and TiCu took the form of needles, because in Ti-40Cu (mass%), the Ti_2Cu grew as coarse dendrites. However, since the phase was the major phase, its real morphology could have been hidden as it grew so coarse. The fast cooling from arc melting could also have promoted needles rather than dendrites.

The fast cooling of the DSC scans (20°C min^{-1} rate) would give lower temperature peaks than equilibrium values, so the values of the peaks were only used as a guide. The DSC results for Ti-40 Cu clearly revealed one major peak (Fig. 6c), showing that the formation of Ti_2Cu is congruent, which means that the reaction involving (βTi) and Ti_2Cu is eutectic rather than peritectic. The reason why no clear eutectic structure was observed in Ti-20Cu (mass%) (Fig. 2a) and Ti-33Cu (mass%) (Fig. 2b), apart from the fast cooling from arc melting,[99] is that firstly the eutectic is sparse, since the eutectic point is much nearer Ti_2Cu than (βTi), which would give a much lower fraction of (βTi).[33] This gives a shallower and more likely (βTi) liquidus than Turchanin et al.[59] Also, the eutectic point being near to Ti_2Cu could mean it might be missed or misinterpreted in earlier reported thermal analyses. Thus, the samples agree with the phase diagram of Ansara et al.[33], and with the researchers who found congruent melting of Ti_2Cu and a eutectic reaction to form (βTi) + Ti_2Cu,[48,59,60,62] without any Ti_3Cu, so disagreeing with Canale and Servant[29] and Okamoto.[31]

6 Conclusions

By using as-cast samples to study the solidification microstructures the reactions were derived, even if the compositions were not equilibrium values. The temperatures of the reactions were determined by DSC and showed that there was a single peak for the Ti-33Cu (mass%) sample, showing that the formation of Ti_2Cu is congruent,

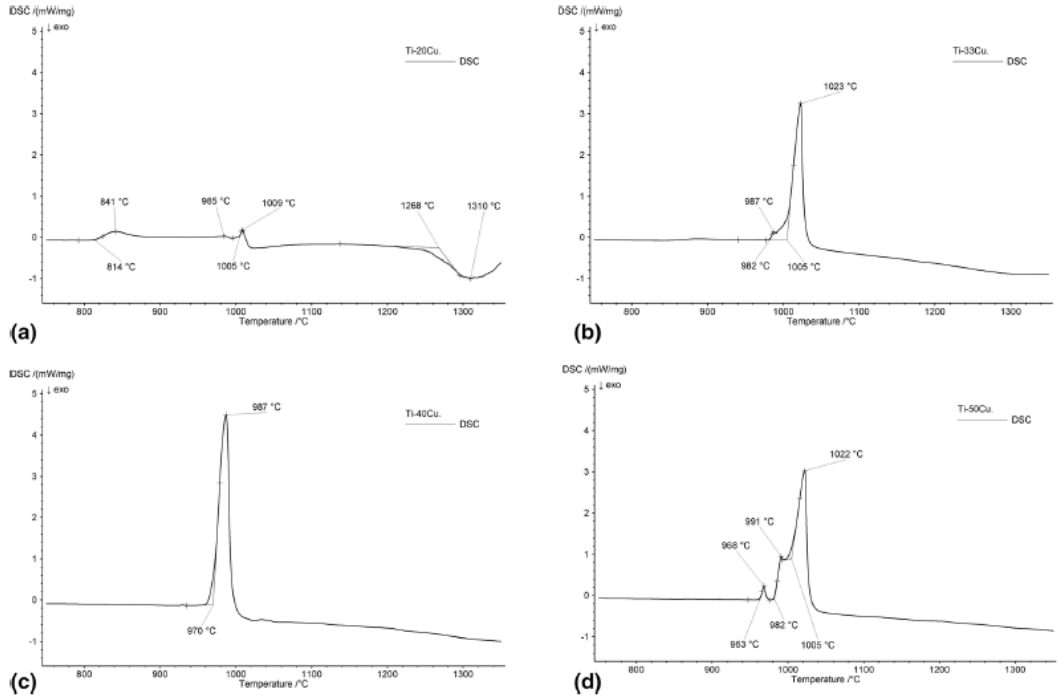


Fig. 6 DSC curves for Ti-Cu alloys recorded on heating: (a) Ti-20Cu, (b) Ti-33Cu, (c) Ti-40Cu and (d) Ti-50 Cu

Table 3. Onset and peak temperatures of DSC results

Alloy (mass%)	Onset temperature (°C)	Peak temperature (°C)	Reaction
Ti-20Cu	814	842	$(\beta Ti) \leftrightarrow (\alpha Ti) + Ti_2Cu$
		985	$L \leftrightarrow (\beta Ti) + Ti_2Cu$ (Small peak)
	1005	1009	$L \leftrightarrow (\beta Ti)$ (Liquidus)
	1271 (1238?)	1310	Reaction to form oxide?
Ti-33Cu	982	987	$L \leftrightarrow (\beta Ti) + Ti_2Cu$
	1005	1023	$L \leftrightarrow (\beta Ti)$ (Liquidus)
Ti-40Cu	970	987	$L \leftrightarrow Ti_2Cu$
Ti-50Cu	963	968	$L \leftrightarrow TiCu + Ti_2Cu$
	982	991	(Small peak)
	1005	1022	$L \leftrightarrow Ti_2Cu$ (Liquidus)

and it has an associated $L \leftrightarrow (\beta Ti) + Ti_2Cu$ reaction. The position of the eutectic point was confirmed as being much closer to Ti_2Cu than (βTi), which gave a sparse eutectic that was often difficult to discern clearly. No Ti_3Cu was found, and this phase is assumed to be metastable, and has been misinterpreted.

Acknowledgements The Department of Science and Innovation and National Research Foundation, South Africa are acknowledged, as well as the Swedish Foundation for International Cooperation in Research, Edson Muhuma of Mintek is thanked for melting the samples. Department of Science and Innovation, South Africa. National Research Foundation, South Africa

References

1. M. Long, and H.J. Rack, Titanium Alloys in Total Joint Replacement—A Materials Science Perspective, *Biomater.*, 1998, **19**(18), p 1621–1639.
2. M. Geetha, A.K. Singh, R. Asokamani, and A.K. Gogia, Ti based Biomaterials, the Ultimate Choice for Orthopaedic Implants: A Review, *Prog. Mater. Sci.*, 2009, **54**(3), p 397–425.
3. M.A.H. Gepreel, and M. Niinomi, Biocompatibility of Ti-alloys for Long-Term Implantation, *J. Mech. Biomed. Mater.*, 2013, **20**, p 407–415.
4. L.C. Zhang, and L.Y. Chen, A Review on Biomedical Titanium Alloys: Recent Progress and Prospect, *Adv. Eng. Mater.*, 2019, **21**, p 1801215.

5. D. Lijima, T. Yoneyama, H. Doi, H. Hamanaka, and N. Kurosaki, Wear Properties of Ti and Ti–6Al–7Nb Castings for Dental Prostheses, *Biomater.*, 2003, **24**(8), p 1519–1524.
6. N. Olsson, *Mechanical properties, phases and structures of titanium alloys, Master of Science Thesis*. Stockholm, Sweden, 2008.
7. H. Hu, W. Zhang, Y. Qiao, X. Jiang, X. Liu, and C. Ding, Antibacterial Activity and Increased Bone Marrow Stem Cell Functions of Zn-Incorporated TiO_2 Coatings on Titanium, *Acta Biomater.*, 2012, **8**, p 904–915.
8. J. Liu, F. Li, C. Liu, H. Wang, B. Ren, K. Yang, and E. Zhang, Effect of Cu Content on the Antibacterial Activity of Titanium–Copper Sintered Alloys, *Mater. Sci. Eng. C*, 2014, **35**, p 392–400.
9. E. Barth, Q.M. Myrvik, W. Wagner, and A.G. Gristina, In Vitro and In Vivo Comparative colonization of *Staphylococcus aureus* and *Staphylococcus epidermidis* on Orthopaedic Implant Materials, *Biomater.*, 1989, **10**, p 325–328.
10. G.R. Persson, and S. Renvert, Cluster of Bacteria Associated with peri-implantitis, *Clin. Implant Dent. Relat. Res.*, 2014, **16**(6), p 783–793.
11. J. Mahan, D. Selgison, S.L. Henry, P. Hynes, and J. Dobbins, Factors in Pin Tract Infections, *Orthopedics*, 1991, **14**, p 305–308.
12. E. Guerado, J. RamonCano, and F. Fernandez-Sanchez, Pin Tract Infection Prophylaxis and Treatment, *Injury*, 2019, **50**(1), p S45–S49.
13. D.P. Lew, and F.A. Waldvogel, Osteomyelitis, *N. Engl. J. Med.*, 1997, **336**, p 999–1007.
14. E. Zhang, X. Wang, M. Chen, and B. Hou, Effect of the Existing form of Cu Element on the Mechanical Properties, Bio-corrosion and Antibacterial Properties of Ti-Cu Alloys for Biomedical Application, *Mater. Sci. Eng. C*, 2016, **69**, p 1210–1221.
15. L.G.X. Jin, E. Liu, F. Yu, X. Shu, and H. Wang, Microstructure, Corrosion and Tribological and Antibacterial Properties of Ti-Cu Coated Stainless Steel, *J. Mech. Behav. Biomed. Mater.*, 2015, **50**, p 23–32.
16. G. Borkow, and J. Gabbay, Copper An Ancient Remedy Returning to Fight Microbial, Fungal and Viral Infections, *Curr. Chem. Biol.*, 2009, **3**, p 272–278.
17. L.P. Luzhnikov, V.M. Novikova, and A.P. Mareev, Solubility of Beta Stabilisers in Alpha-Ti, *Met. Sci. Heat Treat.,* 1963, **5**(2), p 78-81, translated from *Metall. Term. Obrab. Met.*, 1963, **2**, p 13-16.
18. M. Takahashi, M. Kikuchi, and Y. Takada, Mechanical Properties and Microstructures of Dental Cast Ti-Ag and Ti-Cu Alloys, *Dental Mater.*, 2002, **21**(3), p 270–280.
19. O. Taguchi, Diffusion of Copper, Silver and Gold in α-Titanium, *Phil. Mag. A*, 1995, **72**(6), p 1649–1655.
20. C.N. Kraft, M. Hansis, S. Arens, M.D. Menger, and B. Vollmar, Striated Muscle Microvascular Response to Silver Implants: A Comparative in Vivo Study with Titanium and Stainless Steel, *J. Biomed. Mater. Res.*, 2000, **49**, p 192–199.
21. A. Masse, A. Bruno, M. Bosetti, A. Biasibetti, M. Cannas, and P. Gallinaro, Prevention of Pin Track Infection in External Fixation with Silver Coated Pins: Clinical and Microbiological Results, *J. Biomed. Mater. Res.*, 2000, **53**, p 600–604.
22. E. Zhang, F. Li, H. Wang, J. Liu, C. Wang, M. Li, and K. Yang, A New Antibacterial Titanium–Copper Sintered Alloy: Preparation and Antibacterial Property, *Mater. Sci. Eng. C*, 2013, **33**, p 4280–4287.
23. T. Aoki, I.C.I. Okafor, I. Watanabe, M. Hattori, Y. Oda, and T. Okabe, Mechanical Properties of Cast Ti-6Al-4V-XCu alloys, *J. Oral Rehab.*, 2004, **31**, p 1109–1114.
24. R. Liu, K. Memarzadeh, B. Chang, Y. Zhang, Z. Ma, R.P. Allaker, L. Ren, and K. Yang, Antibacterial Effect of Copper Bearing Titanium Alloy (Ti-Cu) Against *Streptococcus mutans* and *Porphyromonas gingivalis*, *Sci. Rep.*, 2016, **6**, p 29985.
25. M. Kikuchi, Y. Takada, S. Kiyosue, M. Yoda, M. Woldu, Z. Cai, O. Okuno, and T. Okabe, Mechanical Properties and Microstructures of Cast Ti-Cu Alloys, *Dental Mater.*, 2003, **19**, p 174–181.
26. T. Shirai, H. Tsuchiya, T. Shimizu, K. Ohtani, Y. Zen, and K. Tomita, Prevention of Pin Tract Infection with Titanium-Copper Alloys, *J. Biomed. Mater. Res. B Appl. Biomater.*, 2009, **91**, p 373–380.
27. Z. Zhang, G. Zheng, H. Li, L. Yang, X. Wang, G. Qin, and E. Zhang, Anti-Bacterium Influenced Corrosion Effect of Antibacterial Ti-3Cu Alloy in *Staphylococcus aureus* Suspension for Biomedical Application, *Mater. Sci. Eng. C*, 2019, **94**, p 376–384.
28. R.F. Bunshah, D. Osterberg, E. Ence, and H. Margolin, Further Studies on Active-Eutectoid Alloys of Titanium, *U.S. Dept Comm. Office Tech. Serv.* , PB Rept., 1960, 161964, p 1–73.
29. P. Canale, and C. Servant, Thermodynamic Assessment of the Cu-Ti System Taking into Account the New Stable Phase $CuTi_3$, *Z. Metallkd.*, 2002, **93**, p 273–276.
30. J.L. Murray, Cu-Ti (Copper-Titanium), *Phase Diagrams of Binary Copper Alloys*, ASM; P.R. Subramanian et al. (Eds), 1994, p 447–460.
31. H. Okamoto, Cu-Ti (Copper-Titanium), *J. Phase Equilib.*, 2002, **23**(6), p 549–550.
32. I. Ansara and V. Ivanchenko, Cu-Ti Binary Phase Diagram Evaluation, in MSI Eureka, Effenberg, G. (Ed.), MSI, Materials Science International Services GmbH, Stuttgart 2002, Document ID: 20.11457.1.0.
33. I. Ansara, V. Ivanchenko, L. Cornish, K. Ukabhai, and K. Nape, Cu-Ti Binary Phase Diagram Evaluation, in *MSI Eureka*, Watson, A. (Ed.), MSI, Materials Science International Services GmbH, Stuttgart (2021), Document ID: 20.11457.2.4.
34. M.H. Müller, and H.W. Knott, The Crystal Structures of Ti_2Cu, Ti_2Ni, Ti_4Ni_2O, and Ti_4Cu_2O, *Trans. Metall. Soc. AIME*, 1963, **227**, p 674–678.
35. N. Karlsson, An X-Ray Study of the Phases in the Copper Titanium System, *J. Inst. Met*, 1951, **79**, p 391–405.
36. J.L. Murray, The Cu-Ti (Copper-Titanium) System, *Bull. Alloy Phase Diagrams*, 1983, **4**(1), p 81–95.
37. F. Laves, and H.J. Wallbaum, On the Crystal Chemistry of Titanium Alloys (in German), *Naturwissenschaften*, 1939, **27**(40), p 674–675.
38. B. Predel, Cu-Ti (Copper-Titanium), *Cr-Cs - Cu-Zr*, Madelung, O. (Ed.), *Springer Materials: Landolt-Börnstein New Series* IV/5, 1998, **5D**, p 1-7.
39. S.P. Alisova, N.V. Lutskaya, A.N. Kobylkin, and P.B. Budberg, TiFe-Ti_2Cu Section of the Ti-Fe-Cu System. Conditions of the Formation of Ti_2Fe Compound, *Russ. Metall.*, 1994, **5**, p 121–123, Transl. from *Izv. Ross. Akad. Nauk*, 1993, **5**, p 170-172.
40. L. Kaufman, and H. Bernstein, *Computer Calculation of Phase Diagrams*. Academic Press, New York, 1970.
41. L. Kaufman, Coupled Phase Diagrams and Thermochemical Data for Transition Metal Binary Systems-III, *Calphad*, 1978, **2**(2), p 117–146.
42. N. Saunders, Phase Diagram Calculations for Eight Glass Forming Alloy Systems, *Calphad*, 1985, **9**(4), p 297–309.
43. N. Saunders, and A.P. Miodownik, Evaluation of Glass Forming Ability in Binary and Ternary Metallic Alloy Systems: An Application of Thermodynamic Phase Diagram Calculations, *Mater. Sci. Technol.*, 1988, **4**(9), p 768–777.
44. K. Zeng, Z. Jin, and P. Huang, Optimization and Calculation of the Titanium-Copper Phase Diagram, *C-MRS Int. Symp. Proc.*, 1990, **5**, p 851–855.

45. K. Zeng and Z. Jin, Thermodynamic Calculation for the Ti-Cu Alloy System Liquid Phase (in Japanese), *Xiyou Jinshu Cailiao Gongcheng (Rare Met. Mater. Eng.)*, 1990, **4**, p 9-12.
46. K. Zeng, Zh. Jin, and P. Huang, Optimization and Calculation of the Ti-Cu Phase Diagram, *C-MRS Int. Symp. Proc.*, Beijing, Meeting Date 1990, 1991, **5**, p 851-855.
47. H. Kumar, I. Ansara, P. Wollants, and L. Delaey, Thermodynamic Optimisation of the Cu-Ti System, *Z. Metallkd.*, 1996, **87**(8), p 666–672.
48. V.N. Eremenko, Y.I. Buyanov, and N.M. Panchenko, Polythermal and Isothermal Sections of the System Titanium-Copper-Silver. Part II, *Sov. Powder Metall. Met. Ceram.* (Engl. Transl.), 1970, **9**(5), p 410-414.
49. V.N. Eremenko, R.N. Mogilevskii, V.M. Sergeenkova, and V.M. Petyukh, The Heat of Fusion and Range of Homogeneity of the Intermetallic TiCu (Engl. Transl.), *Russ. Metall.*, 1987, **6**, p 171-173. Transl. from, *Izv. Akad. Nauk SSSR, Met.*, 1987, **6**, 165-168.
50. M.A. Turchanin, and I.V. Nikolaenko, Enthalpies of Solution of Titanium, Zirconium and Hafnium in Liquid Copper, *J. Alloys Compd.*, 1996, **236**, p 236–242.
51. M.A. Turchanin and S.V. Porokhnaya, Heat of Formation of Liquid Copper Alloys with 3d-Transition Metals, *Powder Metall. Met. Cer.*, 1996, **35**(7–8), p 378–388, translated from *Powder Met.*, 1996, **7–8**, p 64–75.
52. M.A. Turchanin, S.V. Porochnia and I.V. Nikolaenko, Calorimetric Investigation of Liquid Copper Alloys with IIIa- and IVa-Metals, *Fifth International School Phase diagrams in Materials Science*, Katsyvely, Crimea, Ukraine, September 23–29, 1996, Abstracts, p 120.
53. C. Colinet, A. Pasturel, and K.H.J. Buschow, Enthalpies of Formation of Ti-Cu Intermetallic and Amorphous Phase, *J. Alloys Compd.*, 1997, **247**(1–2), p 15–19.
54. O.J. Kleppa, and S. Watanabe, Thermochemistry of Alloys of Transition Metals: Part III Copper-Silver, -Titanium, -Zirconium, and -Hafnium at 1373 K, *Metall. Trans. B*, 1982, **13**(3), p 391–401.
55. V.E. Oliker, A.A. Mamonova, and T.I. Shaposhnikova, Structure and Phase Composition of the Ti-Cu Diffusion Zone, *Powder Metall. Met. Cer.*, 1996, **35**(3-4), p 173-175, Transl. from *Poroshkovaya Metallurgiya*, 1996, **384**(3/4), p 67-70.
56. S. Nararjuna, and D.S. Sarma, On the Variation of Lattice Parameter of Cu Solid Solution with Solute Content in Cu-Ti Alloys, *Scr. Mater.*, 1999, **41**(4), p 359–363.
57. M.A. Turchanin, P.G. Agraval, A.N. Fesenko, and A.R. Abdulov, Thermodynamics of Liquid Alloys and Metastable Phase Transformations in the Copper - Titanium System, *Powder Metall. Met. Ceram.*, 2005, **44**(5-6), p 259-270, Transl. from *Poroshkovaya Metallurgiya*, 2005, **443**(5-6), p 67–80.
58. M.A. Turchanin, Phase Equilibria and Thermodynamics of Binary Copper Systems with 3d-Metals. VII. Concentration-Temperature Dependences of the Thermodynamic Functions of Mixing for Liquid Alloys of Copper and Transition Metals, *Powder Metall. Met. Ceram.*, 2007, **46**(11–12), p 565–581.
59. M.A. Turchanin, P.G. Agraval, and A.R. Abdulov, Thermodynamic Assessment of the Cu-Ti-Zr System. I. Cu-Ti System, *Powder Metall. Met. Ceram.*, 2008, **47**(5-6), p 344–360, Transl. from *Poroshkovaya Metallurgiya*, 2008, **461**(5-6), p 84–94.
60. M.A. Turchanin, *Thermodynamics of Liquid Copper Alloys with Transition Metals (in Russian), Abstract of Thesis*, Taras Shevchenko Kiev University, Kiev, Ukraine, 2007, p 1–34.
61. W. Trzebiatowski, J. Berak, and T. Romotowski, The Copper-Titanium System (in Polish), *Rocz. Chem.*, 1953, **27**, p 426–437.
62. V.N. Eremenko, Yu.I. Buyanov, and S.B. Prima, Phase Diagram of the System Titanium-Copper, *Sov. Powder Metall. Met. Ceram.* (Engl. Transl.), 1966, **5**(6), p 494–502, Translated from *Poroshk. Metall.*, 1966, **6**(42), p 77–87.
63. M. Arita, R. Kinaka, and M. Someno (1979) Application of the Metal hydrogen Equilibration for Determining Thermodynamic Properties in the Ti-Cu System. *Metall. Trans., A*; **10**(5):529–534.
64. O.J. Kleppa, and S. Watanabe, Enthalpies and Entropies of Solution of First Row Transition Metals in Liquid Copper, *Solid State Commun.*, 1983, **46**(11), p 799–801.
65. J. Wang, C. Liu, C. Leinenbach, U.E. Klotz, P.J. Uggowitzer, and J.F. Löffler, Experimental Investigation and Thermodynamic Assessment of the Cu–Sn–Ti Ternary System, *Calphad*, 2011, **35**, p 82–94.
66. G. Ghosh, First-Principles Calculations of Structural Energetics of Cu-TM (TM = Ti, Zr, Hf) Intermetallics, *Acta Mater.*, 2007, **55**(10), p 3347–3374.
67. G. Ghosh, S. Vaynman, M. Asta, and M.E. Fine, Stability and Elastic Properties of $L1_2$-(Al, Cu_3(Ti, Zr) Phases: Ab Initio Calculations and Experiments, *Intermetallics*, 2007, **15**(1), p 44–54.
68. A. Joukainen, N.J. Grant, and C.F. Floe, Titanium-Copper Binary Phase Diagram, *Trans. AIME*, 1952, **194**, p 766–770.
69. E. Raub, P. Walter, and H. Engel, Alloys of Titanium with Copper, Silver and Gold (in German), *Z. Metallkd.*, 1952, **43**, p 112–118.
70. E. Ence, and H. Margolin, A Study of the Ti-Cu-Zr System and the Structure of Ti_2Cu, *Trans. Met. Soc. AIME*, 1961, **221**, p 320–322.
71. K. Schubert, About Titanium-Copper and Titanium-Silver Systems (in German), *Z. Metallkd.*, 1965, **56**(3), p 197–199.
72. T. Yamane, S. Nakajima, H. Araki, Y. Minamino, S. Saji, J. Takahashi, and Y. Miyamoto, Partial Phase Diagrams of the Titanium-Rich Region of the Ti-Cu System under High Pressure, *J. Mater. Sci. Lett.*, 1994, **13**(3), p 162–164.
73. A. Dziadon, and M. Konieczny, Structural Transformations at the Cu-Ti Interface During Synthesis of Copper-Intermetallics Layered Composite, *Kovove. Mater*, 2004, **42**, p 42–50.
74. B.S. Bokstein, V.I. Vnukov, E.V. Golosov, M.I. Karpov, Y.R. Kolobov, D.A. Kolesnikov, V.P. Korzhov, and A.O. Rodin, Structure and Diffusion Processes in Laminated Composites of a Cu-Ti System, *Russ. Phys. J.*, 2009, **52**, p 811–815.
75. Y.Q. Song, S.C. Li, and G.H. Du, Study on Formation Mechanism of Ti/Cu Solid Phase Interface Diffusion Solution Layer, *Rare Metal Mater. Eng.*, 2009, **38**, p 1188–1192.
76. Y. Fan, J. Fan, and C. Wang, Formation of Typical Cu-Ti Intermetallic Phases Via a Liquid-Solid Reaction Approach, *Intermetallics*, 2019, **113**, 106577.
77. W. Rostoker, Observation on the Occurrence of Ti_2X Phases, *Trans. AIME*, 1952, **194**, p 209–210.
78. G. Lutjering, and S. Weissmann, Mechanical Properties and Structure of Age-Hardened Ti-Cu Alloys, *Metall. Trans.*, 1970, **1**, p 1641–1649.
79. F. De Boer, R. Boom, W.C. Mattens, A.R. Miedema, and A.K. Niessen, *Cohesion in Metals and Transition Metal Alloys* North Holland, Amsterdam, 1988, p 126
80. U.E. Klotz, C. Liu, P.J. Uggowitzer, and J.F. Loeffler, Experimental investigation of the Cu-Ti-Zr system at 800 °C, *Intermetallics*, 2007, **15**, p 1666–1671.
81. J. Andrieux, O. Dezellus, F. Bosselet, M. Sacerdote-Peronnet, C. Sigala, R. Chiriac, and J.C. Viala, Details on the Formation of Ti_2Cu_3 in the Ag-Cu-Ti System in the Temperature Range 790 to 860°C, *J. Phase Equilib. Diffus.*, 2008, **29**(2), p 156–162.
82. Y. Wei and X. Wang, A New Ordered Phase Forming During Aging in Cu-Ti Alloys, *Chin. Sci. Bull.*, 1997, **42**(19), p 1671–1672.

83. U. Zwicker, Tempering and Mechanical Properties of Copper-Titanium Alloys (in German), *Z. Metallkd.*, 1962, **53**, p 709–714.
84. U. Zwicker, Investigations on the Effect of Oxygen Addition on Cu-Ti Alloys by the Use of the Electron Microprobe (in German), *Mikrochim. Acta*, 1967, pp. 116–122.
85. G. Vigier, J.M. Pelletier, and J. Merlin, Determination of Copper Solubility in Titanium and Study of Ti-Cu Solid Solution Stability by Thermoelectric Power Measurements, *J. Less-Common Met.*, 1979, **64**(2), p 175–183.
86. L.P. Srivastava, and J.G. Parr, *Trans. TMS-AIME*, 1962, **224**, p 1295–1297.
87. J. Zhao, and M.R. Notis, Phase Transformation Kinetics and the Assessment of Equilibrium and Metastable States, *J. Phase Equilib.*, 1993, **14**(3), p 303–315.
88. G.W. Franti, J.C. Williams, and H.I. Aaronson, A Survey of Eutectoid Decomposition in Ten Ti-X Systems, *Metall. Trans. A*, 1978, **9**(11), p 1641–1649.
89. A. Devaraj, S. Nag, B.C. Muddle, and R. Banerjee, Competing Martensitic, Bainitic, and Pearlitic Transformations in a Hypoeutectoid Ti-5Cu Alloy, *Metall. Mater. Trans. A*, 2011, **42**(5), p 1139–1143.
90. A.V. Dobromyslov, Phase Transformation in Binary Titanium-Base Alloys with Metals of the I, IV-VIII Groups, *Mater. Sci. Forum*, 2007, **546–549**, p 1349–1354.
91. A.V. Dobromyslov, and V.A. Elkin, Martensitic Transformation and Metastable Beta-Phase in Binary Titanium Alloys with d-Metals of 2–6 Periods, *Scr. Mater.*, 2001, **44**(6), p 905–910.
92. M. Hansen, D.J. McPherson, and W. Rostoker, Constitution of Titanium Alloy Systems, WADC Techn. Rep. 53-41, *Armour Res. Found. Illinois Inst. Techn., Wright-Patterson Air Force Base*, Ohio, 1953, p 129–136.
93. U. Zwicker, E. Kalsch, T. Nishimura, D. Ott, and H. Seilstorfer, The Effect of Additions on the Equilibria of Cu-Rich Cu-Ti Alloys (in German), *Metall.*, 1966, **20**(12), p 1252–1255.
94. U. Zwicker, Binary Systems (in German), *Tiran und Titanelegierungen*, 1974, **21**, p 562–575.
95. P. Franke and D. Neuschütz, Cu-Ti (Copper-Titanium), Binary systems. Part 3: Binary Systems from Cs-K to Mg-Zr, *Springer Materials: Landolt-Börnstein New Series* IV/9B, 2005, **19B3**, p 1–5.
96. T.B. Massalski, Ed., *Binary Alloy Phase Diagrams* 2nd edn. ASM International, Metals Park, 1990
97. H. Okamoto, Comment on Cu-Ti (Copper-Titanium), *J. Phase Equilib.*, 1994, **15**(5), p 566–567.
98. R. Shull, A. McAlister, and J. Murray, J., 1982, quoted by J.L. Murray. *The Cu-Ti (Copper-Titanium) System*, 1983.
99. G.A. Chadwick, *Metallography of Phase Transformations.* Butterworths, London, 1972.
100. A.R. Abdulov, *Thermodynamic Properties of Cu-Ti-Zr, Cu-Ni-Ti, Cu-Fe-Ti Liquid Alloys and Modeling of Their Glass-forming Ability* (in Russian), Abstract of Thesis, Taras Shevchenko Kiev University, Kiev, Ukraine, 2008, p 1–20.
101. Y. Zhan, D. PengJia, and S. She, Phase Equilibria of the Cu-Ti-Er System at 773 K (500 A degrees C) and Stability of the CuTi3 Phase, *Metall. and Mater. Trans. A.*, 2012, **43**(11), p 4015–4022.
102. P. Pietrokowsky and J.R. Maticich, The Use of the Electron-Microprobe Analyzer in the Study of Binary Metal Alloys Systems, X-ray and X-ray Microanalysis, *3rd Int. Symp.*, 1963, p 591–602.
103. R.C. Ecob, J.V. Bee, and B. Ralph, The Cellular Reaction in Dilute Copper-Titanium Alloys, *Phys. Status Solidi A, Appl. Mater*, 1979, **52**, p 201–201.
104. J.V. Hackworth, M. Hoch, and L. Gegel, Thermodynamics of Titanium Alloys: I. Development of a Triple Knudsen Cell and Its Use to Study the Activity of Copper in the Ti-Cu System, *Metall. Trans.*, 1971, **2**(7), p 1799–1805.
105. F.R. De Boer, R. Boom, and A.R. Miedema, Enthalpies of Formation of Liquid and Solid Binary Alloys Based on 3d Metals I, Alloys of Sc, Ti, V, *Physica B/C*, 1980, **101**(3), p 294–319.

Publisher's Note Springer Nature remains neutral with regard to jurisdictional claims in published maps and institutional affiliations.